UNIVERSITÀ
DEGLI STUDI
FIRENZE

DIPARTIMENTO
DI INGEGNERIA
INDUSTRIALE

DOTTORATO DI RICERCA IN

"*Ingegneria Industriale e dell'Affidabilità*"

CICLO *XXX*

COORDINATORE Prof. Maurizio De Lucia
REFERENTE Prof. Mario Tucci

DEVELOPMENT AND DESIGN OF PMSM CONTROL SYSTEMS FOR AUTONOMOUS UNDERWATER VEHICLES

Settore Scientifico Disciplinare ING-IND/13

Dottorando
Ing. *Libero Paolucci*

Tutore
Prof. *Benedetto Allotta*

Anni 2015/2017

Dedico questo lavoro alla mia bellissima famiglia,
il più grande e bel regalo che la vita potesse farmi.

Ringraziamenti

Un grande ringraziamento al Professor Benedetto Allotta capo del Laboratorio di Modellazione Dinamica e Meccatronica (MDM Lab) del Dipartimento di Ingegneria Industriale dell'Università degli Studi di Firenze, che è stato mio tutor di dottorato ed al Professor Andrea Rindi per l'opportunità di poter collaborare nel loro gruppo di ricerca. Vorrei ringraziare tutti i membri di MDM Lab con cui in questi anni ho lavorato e che mi hanno aiutato a crescere professionalmente ed umanamente. In particolare ringrazio i Dott.ri Riccardo Costanzi, Pierluca D'Adamio, Francesco Fanelli, Emmanuele Galardi, Jonathan Jelli, Niccolò Monni, Alessandro Ridolfi e l'Ing. Marco Natalini per il valido supporto offerto durante l'intero lavoro di dottorato. Un ringraziamento inoltre al Professor Matthias Nienhaus del Laboratory of Actuation Technology (LAT) of the Saarland University per avermi messo a disposizione il suo laboratorio di ricerca, ai suoi collaboratori, con speciale riferimento al Dott. Emanuele Grasso per il grande supporto ed esperienza che ha voluto mettermi a disposizione e agli Ingg. Stefano Fabbri, e Niklas Köenig.
Grazie infine a tutte le persone che in questi anni mi hanno sostenuto nel raggiungimento di questo importante obbiettivo. Grazie per la vostra amicizia, per il supporto, per le critiche e per gli incoraggiamenti.

Firenze, 12 Marzo 2017

Libero

Abstract

Underwater vehicle propulsion is usually performed exploiting hydraulic or electrically operated propellers and hydraulic or electrically operated ducted jet propulsors. Electrical motor propulsion is in general the most flexible solution and it is growing in popularity because of its high efficiency both at high and low advance speed, quick and simple deployment, low costs and encumbrance. In the present work, the advantages of Permanent Magnet Synchronous Motors (PMSM) for underwater propulsion are highlighted. In particular sensorless control of PMSM permits reduced costs high reliability and performances. As a test case, the development of the MARTA AUV propulsion system has been developed. It is an Observation Class AUV for subsea archeology purposes. Several motor control techniques are presented with the relative test results. In particular, the author focused the research in the development of a technique able to perform a reliable rotational speed and torque estimation. This indeed would permit the exploitation of a vehicle dynamic model for the navigation algorithm. Pool and field tests for the identification of the dynamic parameters of the vehicle and of the propellers are presented. Finally, an off-line preliminary validation of a navigation algorithms based on a dynamic model is presented with encouraging results. In particular, the possibility to operate a position estimation of the vehicle less dependent on the on board sensors was highlighted. This involves obvious benefits in terms of cost reduction and reliability of the system.

Contents

List of Figures

Introduction

The present work deals with the study of underwater propulsion systems applied to small size underwater mobile robots developed and built by the Mechatronics and Dynamic Modeling Laboratory (MDM Lab) of the Department of Industrial Engineering of the Florence University. The laboratory carries out a scientific activity concerning underwater robotics since 2010. The main projects the laboratory has worked on so far, regard the development of Autonomous Underwater Vehicles (AUV) for inspections of valuable underwater sites of archaeological interest. In these years, two main projects have been carried out: THESAURUS (TecnicHe per l'Esplorazione Sottomarina Archeologica mediante l'Utilizzo di Robot aUtonomi in Sciami) [11] founded by Regione Toscana and ARROWS (ARchaeological RObot systems for the World's Seas) [12] an European funded project (www.arrowsproject.eu). Other AUVs developed by the MDM Lab are the Turtle and the FeelHippo vehicles which were designed for student competitions [13],[14],[15],[16], SAUC-e and euRathlon. The laboratory has also worked on a Remotely Operated Vehicle (ROV) called Nemo [17] which has been realized and successfully employed for the monitoring, before the rescuing operation, of the Costa Concordia wreck, Isola del Giglio, Italy. Research activities performed by MDM Lab include: vehicle design and control [18], swarm localization [11] and navigation [19], underwater communication [20], 2D and 3D geometric computational vision image/video representation [21], annotation and retrieval, visual servoing [22],[23],[24],[25].

The need of developing new solutions in underwater robotics applications is due to the growing importance of off-shore activities in the Oil and Gas field or in general off-shore activities for energy production, and in many other fields of application, such as biology, geology, archeology, etc.

The work concerning this PhD thesis has been carried on during the years 2015/2017 and has been intended as a support for the ARROWS and ARCHEO-SUb projects.
ARROWS (ARchaeological RObot systems for the World's Seas) was an FP7 European project which started in 2012 and lasted three years. The main purpose of the project was to adapt and develop low cost autonomous underwater vehicle technologies to significantly reduce the cost of archaeological operations, covering the full extent of archaeological campaign. The activities of interest concerned the development of vehicles able to perform fast and low cost horizontal surveys of large areas of interest, the design of semi-automated data

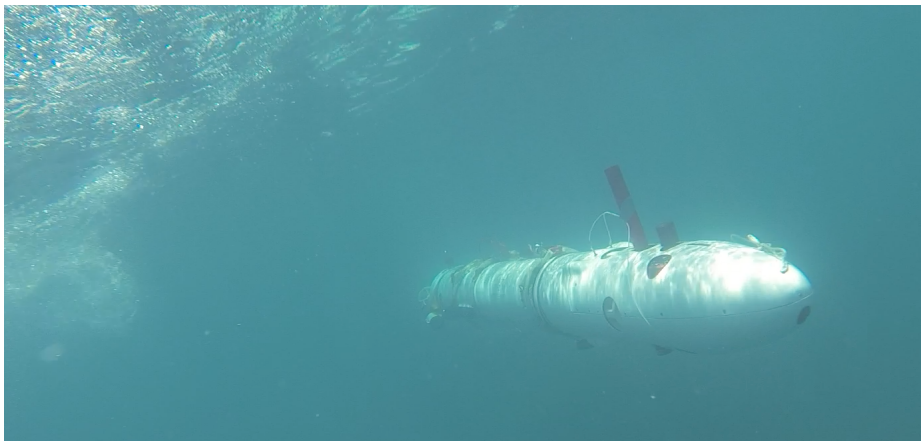

Figure 1: The TifOne AUV performing sea tests during the final demos of the ARROWS project [1].

analyzing tools for underwater mapping and site and object relocation. Additive tasks concerned the development of small agile underwater robots able to perform shipwreck penetration and internal mapping, soft excavation for diagnosis and excavation of fragile objects [1]. The MDM Lab of the University of Florence worked in the project as coordinator and the main activity has concerned the development of MARTA AUV, which is an autonomous underwater vehicle characterized by high modularity and adaptability to the different kinds of archaeological mission. The laboratory worked in each phase of the vehicle development, from the mechanical design to the navigation and localization algorithms design, the computer vision and the underwater communication. The vehicle is composed of several modules, each one dedicated to a particular task (e.g. propulsion, sensor payloads, power supply, etc.). This way, MARTA AUV can be customized according to the mission profile to perform [12]. ARCHEOSUb (Autonomous underwater Robotic and sensing systems for Cultural HEritage discOvery conservation and in SiTu valorization) [26] project aims to develop products and services in support of the discovery of new Underwater Cultural Heritage (UCH) sites and of the surveying, conservation, protection, and valorization of new and existing ones. The project started in 2017 and it is in its initial phases; it involves the development of small AUVs designed to be sent to sites of interest, relying on in-situ underwater sensor network nodes for accurate localization. Additional tasks of the project are the development of real time communication of multimedia data and localization services for divers [26].

Underwater vehicle propulsion is usually performed exploiting hydraulic or electrically operated propellers and hydraulic or electrically operated ducted jet propulsors [27]. Hydraulic solutions are generally used when high torques generation is required, although these systems suffer for poor energy conversion efficiency, high encumbrances and weight. Concerning turbojet propellers they

are mainly used when high advance speed are required because their efficiency fades at low speed and they involve complex mechanical design. Electrical motor propulsion is in general the most flexible solution and it is growing in popularity because of its high efficiency both at high and low advance speed, quick and simple deployment, low costs and encumbrance. The electric motors used for these applications are mainly DC motors with permanent magnets and induction motors [27].

Hence the work has been focused on the selection of an optimal propulsion system according to the vehicle type and application. The study has regarded motor selection, optimal control technique, propeller shape and size selection. The solutions have been deeply investigated and tested both with test bench and in field campaigns.

The first part of the work is described in chapter 2 and deals with Permanent Magnet Synchronous Motors (PMSM) structure, principle of operation, mathematical modeling and control. In chapter 3 various PMSM sensorless control techniques are described. These techniques have been studied and implemented in order to test their functionality in chapter 4. This part of the work has been carried out in cooperation with the Laboratory of Actuation Technology (LAT) of the Saarland University. In particular their support has concerned the design and implementation of the test bench electronics for the algorithm development and validation. An overview of the various test bench solution, and motor drive prototypes which have been designed during my thesis activities is shown in chapter 5. Finally in chapter 6 experimental results performed in laboratory and in field are presented.

Chapter 1

Underwater Vehicle Propulsion: State of the Art

One of the most important research topic of the MDM Lab research group of the Florence University is the design and development of underwater vehicles both autonomous (Autonomous Underwater Vehicle), and remotely operated (Remotely Operated Vehicle). In particular the activity is mainly concentrated in Observation Class and Mid Sized [27] ROVs and AUVs for underwater archaeologist purposes. Since 2010, the laboratory has designed and realized several AUVs like the Typhoon-class [28], MARTA AUV [1], and the two didactic purpose vehicles Turtle [14] and FeelHippo [15]. The laboratory activity has also concerned the design of an Observation Class ROV called Nemo ROV [17] used by the University of Florence to monitor the Costa Concordia wreck. The design of an efficient, reliable and cost effective customized propulsion system for these vehicles hence is of key importance in order to maximize vehicle advance speed, maneuverability and reliability.

There are two main families of actuators: Electrically or hydraulically driven propeller and ducted jet propulsion (either electrically or hydraulically driven) [27]. System type selection is made according to vehicle size, task and operating conditions. When high torques are required, hydraulic systems are used while Ducted jet propulsion is used to achieve high advance speed. Although the most common is the electrically actuated propeller due to its versatility, efficiency and easy deployment.

1.1 Hydraulically Driven Propellers

Hydraulic actuation is generally implemented when high torques are needed. This although come at the expenses of efficiency, weight and costs. The hy-

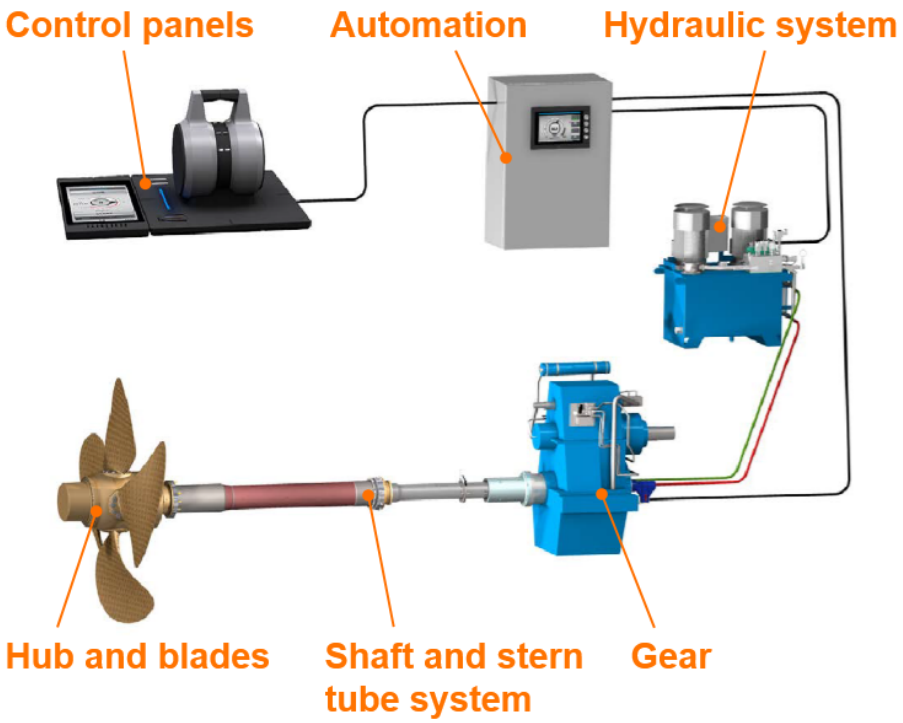

Figure 1.1: Hydraulic propulsion scheme [2].

draulic pumps which power these systems are indeed electrically driven, hence the conversion from electrical to mechanical to hydraulic power involves losses which affect the overall efficiency. Other losses are due to hydraulic lines and components [29]. Also these systems are in general more complex and have more parts with respect to electric ones. As a consequence, more maintenance is needed and the consequences of a system failure could be severe especially in terms of pollution and system recovery. Hydraulic system are also quite heavy and cumbersome compared to electric ones.

Thus the high energy losses, costs and of hydraulic systems are justified just in case the application requires high mechanical force. This, in general, is the case when dealing with big vehicles or when manipulation tasks are required from the vehicle and electrical actuators can not comply with the system requirements. In this case, also if electric actuation would be sufficient for vehicle propulsion, it is sometimes preferred the hydraulic one. Indeed if the electric vehicle has to have a hydraulically powered tool, then a lot of the electric vehicle benefit would be lost in the heavy-duty hydraulic system. For small size Observation Class vehicles like MARTA AUV, hydraulic propulsion is thus not advisable because of it is poor efficiency, high weight and dimension. Vehicles exploiting hydraulic propulsion are: Atom Work Class ROV by SMD and the

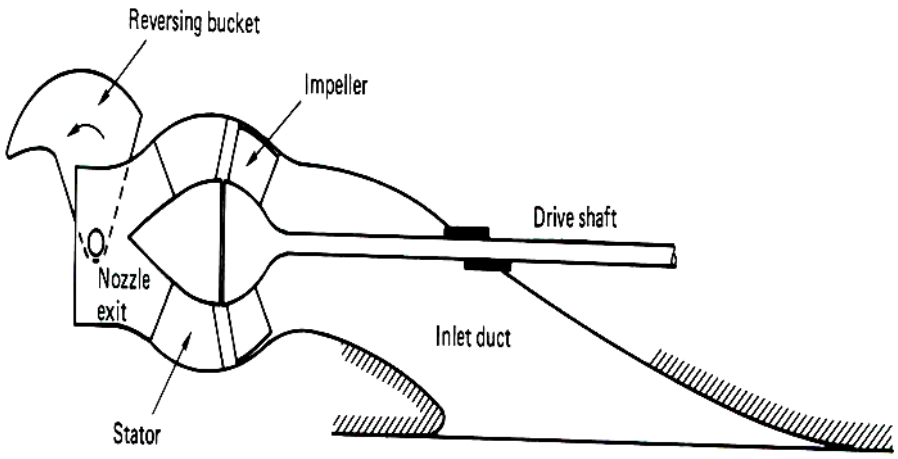

Figure 1.2: Hydraulic propulsion scheme [3].

UHD ROV Heavy Work Class by Schilling Robotics.

1.2 Electrically and Hydraulically Driven Ducted Jet Propulsors

Waterjet propulsion is applied on a wide range of small high-speed vehicles. It reaches top efficiency at high advance speed while at lower speed efficiency fades. It is often applied where other propulsion forms can not be used for some reason: typically for reasons of efficiency, cavitation extent, noise or immersion and draught. The three main component of the waterjet are shown in figure 1.2: an inlet duct, a pump and a nozzle exit. The principle of operation of these systems is that water is drawn through a ducting system by an internal pump which adds energy after which the water is expelled aft at high velocity. The thrust is generated as a result of the momentum increase imparted to the water [10].

It can be actuated both hydraulically and electrically, and great maneuverability can be reached with these systems, although with respect to propeller actuated ones it is generally heavier, more complex and costly. Electrically based waterjet propulsion is exploited by the Black Shadow by Rotinor, the Sonobot by EvoLogics or the Seabob F7 by Seabob. Observation Class vehicles like MARTA AUV require high maneuverability but, generally, at low advance speed which as highlighted above is not an efficient working condition for waterjets. Furthermore, because of its cost and complexity, simpler actuation system are preferred.

1.3 Electrically Driven Propellers

Concerning small and middle size AUV and ROV propulsion, electrically driven propellers are by far the most used because of the simplicity of implementation, efficiency and versatility. They operate efficiently over a wide range of advance speed and the design simplicity reduces costs, maintenance and dimensions. They are actuated with several electrical motors types according to the power source, vehicle dimension and torque requirements. On observation-class ROV systems, the DC motor, due to its power, availability, variety, reliability, and ease of interface is the most popular. Permanent Magnet Synchronous Motor (PMSM), however, is more efficient and reliable [30] and it is widely used for underwater thrusters [27]. As an example the Typhoon vehicles, the Folaga AUV, the REMUS AUVs, the Nemo ROV, the BlueROV2 ROV are moved with PMSM actuated thrusters. Other motors which are commonly used are the induction motors which although, as the PMSM, involve more complex driving techniques with respect to the DC one. Observation-class AUVs are mainly actuated with electrically operated propellers since low advance speed and operational torques are generally required for these kind of vehicles. Other examples of Observation Class and Mid Sized electrically actuated AUVs are the SPARUS II AUV produced by Girona University [31], the SeaCat AUV produced by Atlas Elektronik [32], the Folaga AUV produced by Graaltech [33] and the REMUS AUVs fleet produced by Kongsberg [34].

Chapter 2

Permanent Magnet Synchronous Motor Structure and Characteristics

Permanent Magnet Synchronous Motors are becoming increasingly popular for both industrial and consumer applications thanks to their high efficiency, compact form, reduced noise operation, high reliability, and low maintenance [30]. All of these positive characteristics came at the expense of an increased complexity for what concerns the driving techniques.

The principle of operation is the same of the brushed DC motor; a directional magnetic field is generated by the permanent magnets of the rotor and it interacts with a rotational magnetic field generated by the stator coils. Differently from the Brushed DC motor in which the voltage commutation from a coil to another is mechanical and it is performed automatically, in a PMSM, coil switching is operated through an electronic control and it depends on rotor position. For this reason, in order to operate a correct control of phase voltages, it is necessary to know the mutual position between rotor and stator.

This can be obtained by placing sensors on the rotor shaft or by estimating the rotor position through measurements of the motor electrical quantities. The first approach named Sensored Control, generally exploits a three-phase inverter which requires a rotor position sensor with which the inverter generates the right commutation sequence on motor phases. For low demanding applications, Hall sensors are used, while for high demanding application such as position control or high dynamic speed control, resolvers and absolute position sensors are used. Position sensors increase cost, motor size and the overall mechanic complexity, they are often temperature sensitive, limiting the operation of the motor. Also system reliability is affected by the introduction of additive wiring

which connects the motor to the control logic. This limits the use of PMSM in harsh conditions such as high operational temperatures or underwater operation. PMSM sensorless control exploits measurements of stator and current voltages in order to estimate the position of the rotor with respect to the stator. Clearly there are some drawbacks concerning the use of such techniques such as limited operational speed range, motor parameters dependence, higher implementation complexity concerning both the control electronics and algorithm and higher need of customization according to the application and kind of motor. PMSM control is generally operated starting from a DC voltage source. Although the control voltage and current which are supplied to the motor are not continuous waveforms. If a motor control is preformed through mutually shifted square waves on the three phases (the Six Step commutation technique), in this work, they will be referred to as Brushless DC motors (BLDC); if a motor control is performed through continuous waveforms (such as Field Oriented Control), they will be referred to as Brushless AC Motors (BLAC). A sensorless control approach is therefore convenient when low budget, high reliability and harsh operational condition are required. This is the case of MARTA AUV where cost reduction and low encumbrances are important design requirements. For these reasons this PhD work has been focused on the research, development and implementation of a sensorless PMSM control solution which could be integrated in an underwater vehicle. The aim of the work has been the development of a small size motor drive, highly reliable and able to perform sensorless speed and torque estimation over a wide speed range.

2.1 Physical Laws Related to Electric Motor Operation

Conversion from electrical to mechanical power is usually achieved thanks to the interaction between current and magnetic field according to the Lorenz force law,

$$\boldsymbol{F} = i\boldsymbol{l} \times \boldsymbol{B}, \tag{2.1}$$

where F is the force produced on a straight wire on which the current i runs, l is the wire length B is the magnetic field density which crosses the wire and the symbol $\times$ here is intended as the vector product. Considering a coil in which a current $\frac{i}{2}$ runs, crossed by a uniform induced field B as shown in figure 2.1 it is possible to use the force F to generate a rotational torque. According to figure 2.1 the generated torque is:

$$\tau = ilBd\cos\theta. \tag{2.2}$$

According to (2.2) it is easy to understand that if the angle between the coil and the the magnetic field density B is $\theta = 0$ the torque is maximum while it is zero when $\theta = \frac{\pi}{2}$. Equation (2.2) could be explained through magnetic fields

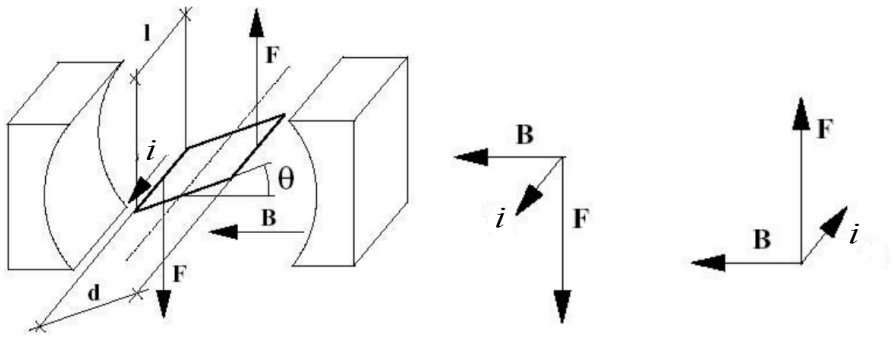

Figure 2.1: Coil in a constant magnetic field [4].

interactions. The current running through a straight wire indeed generates a magnetic field according to the Biot-Savart law:

$$\boldsymbol{B}_c = \frac{\mu_0 \boldsymbol{i}}{2\pi r} \times \boldsymbol{r}, \tag{2.3}$$

where μ_0 is the magnetic permeability in vacuum, r is the distance of a generic point from the wire and $\boldsymbol{r}$ identifies the direction of the point with respect to the wire. According to (2.3), inside the plane of the coil of figure 2.1, current $\boldsymbol{i}$ generates a magnetic field directed orthogonally with respect to $\boldsymbol{d}$ and $\boldsymbol{l}$. The magnet generated field $\boldsymbol{B}$ and the coil generated one $\boldsymbol{B}_c$ are orthogonal when $\theta = 0$ and they are parallel when $\theta = \frac{\pi}{2}$. Hence (2.2) essentially quantifies the force generated by the fact that the two magnetic fields tend to align.
In figure 2.1, $\boldsymbol{B}$ is produced through a couple of magnets; a directional field however can be generated by two parallel coils. In that case the directional field $\boldsymbol{B}$ is generated by a current i_s through these coils.
The interaction between magnetic fields and coils generate another important effect described by Lenz's law which is called electromotive force ϵ,

$$\epsilon = -\frac{d}{dt}\Lambda, \tag{2.4}$$

where:

$$\Lambda = Bld\sin\theta = \Lambda_m \sin\theta. \tag{2.5}$$

This means that a variation of the magnetic flux linkage Λ through a coil provokes a voltage drop at its terminals. According to these laws it is possible to explain the operation of an electrical motor.

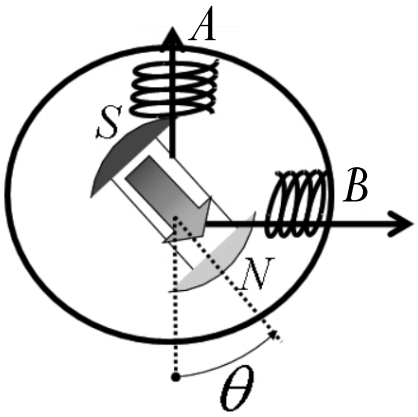

Figure 2.2: Scheme of a Permanent Magnet Synchronous Motor.

2.2 Permanent Magnet Synchronous Motor, Principles of Operation and Mathematical Model

PMSM, usually is composed by a stator with three phases corresponding to three windings and a rotor with permanent magnets. The principle of operation is the following: a directional magnetic field is generated by the permanent magnets of the rotor and it interacts with a rotational magnetic field generated by the stator coils. The stator rotational magnetic field is generated by switching from a coil to another and it is performed through a control electronics; this means that each winding is supplied by a different phase and each of it is controlled with a different waveform. The simplest scheme of a PMSM is shown in figure 2.2 [35].

It is a two phases PMSM. The stator coils are energized by the phases in a way to generate a rotational magnetic flux. According to (2.2) the maximum torque is delivered when the rotor and stator magnetic flux are orthogonal. This although requires the control system to know the mutual orientation between the rotor and the stator. For this reason an optimal commutation can be performed when knowing the rotor position while it turns so that the power is switched to each phase at the right time. It must be said that there are applications in which motor control is performed in open loop but this leads to some disadvantages which will be illustrated later. A rotational magnetic flux is obtained by processing a DC voltage and generating phase shifted voltage waveforms. According to figure 2.2 the power must be switched to winding A when $\theta = \pm\frac{\pi}{2}$ and to winding B when $\theta = \pi$ or $\theta = 0$. Figure 2.3 roughly illustrates the polarity of the voltage signals (V_A and V_B) which have to be delivered to each phase according to the rotor position. It is also shown the back electromo-

tive force (BEMF) induced in the coils terminals during the complete rotation. V_A and V_B can have different waveform according to the driving technique.

The equivalent circuit of a two coils motor like the one in figure 2.2 is shown in figure 2.4.

The two voltage generators V_A and V_B are the inverter generated signals, R_A and R_B are the resistance of the two stator windings, L_A and L_B model the coil inductance and the magnetic interactions between the two coils. ϵ_A and ϵ_B model the BEMF induced in the stator coils by the flux linkage generated by the rotor magnet.

BEMF behavior is dependent on motor geometry. Factors influencing its shape are: magnet geometry, magnetization, stator core geometry, and the winding distribution. All of these characteristics are related to the motor itself, and do not depend on the driving voltage. It varies from a sinusoidal to a trapezoidal waveform. For description purposes, in formulas, a sinusoidal approximation will be used.

According to the number of magnetic poles n_p, back electromotive force frequency is $\omega_e = n_p\omega_r$, where ω_r is the rotor angular speed while ω_e is called electrical speed. Concerning the rotor position, $\theta_e = n_p\theta_r$, where θ_r is the rotor angle while θ_e is called electrical angle and identifies the stator flux direction with respect to a stationary reference frame.
Referring to the motor represented in figure 2.2 has one magnetic pole, thus it is possible to express BEMF as

$$\begin{aligned} \epsilon_A &= \frac{d}{dt}\Lambda_m \sin(\theta_e) = \Lambda_m \omega_e \cos(\theta_e), \\ \epsilon_B &= \frac{d}{dt}\Lambda_m \sin(\theta_e - \frac{\pi}{2}) = \Lambda_m \omega_e \cos(\theta_e - \frac{\pi}{2}). \end{aligned} \tag{2.6}$$

Where Λ_m has been defined in (2.5). It is possible to express a mathematical model of the PMSM through the following equations:

$$\begin{aligned} V_A &= R_A i_A + \frac{d}{dt} L_A i_A + \epsilon_A, \\ V_B &= R_B i_B + \frac{d}{dt} L_B i_B + \epsilon_B. \end{aligned} \tag{2.7}$$

For what concerns the electromechanical torque,

$$\tau_{tot} = \tau_A + \tau_B = \frac{W}{\omega_r} = \frac{1}{\omega_r}(i_A\epsilon_A + i_B\epsilon_B). \tag{2.8}$$

Where W is the electric power. (2.8) can also be written as [35],

$$\tau_{tot} = \tau_A + \tau_B = \Lambda_m i_A \cos(\theta_e) + \Lambda_m i_B \cos(\theta_e - \frac{\pi}{2}). \tag{2.9}$$

Assuming, i_A and i_B sinusoidal with equal modulus i and shifted of $\frac{\pi}{2}$

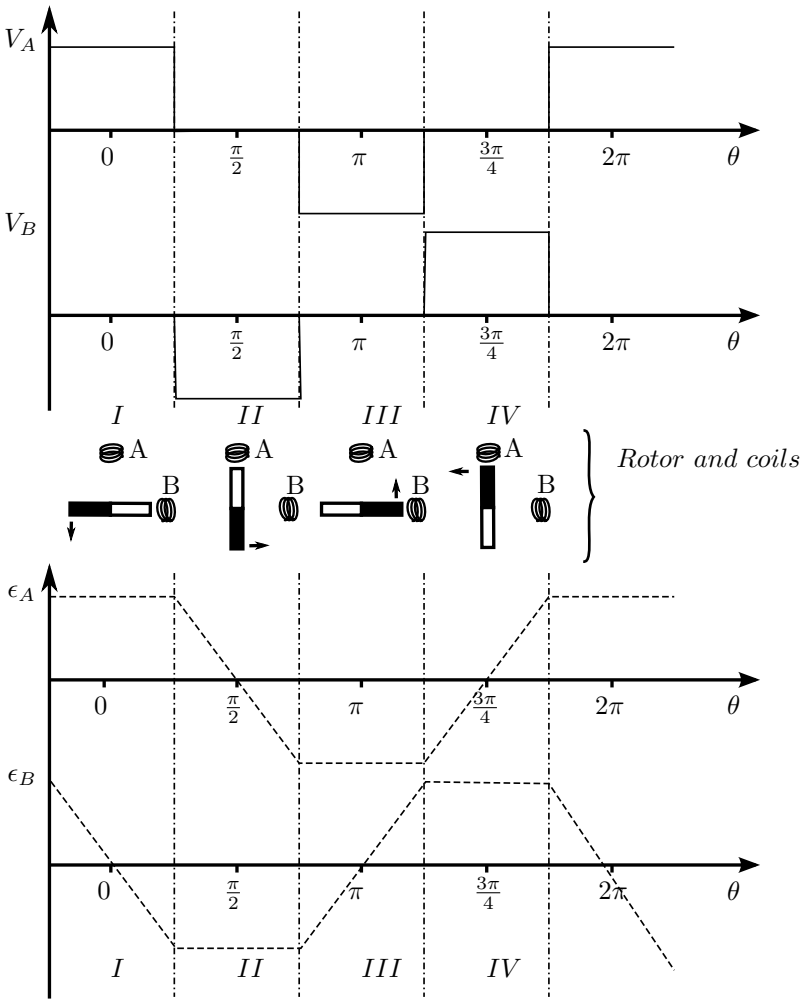

Figure 2.3: Induced back electromotive force on the two coils.

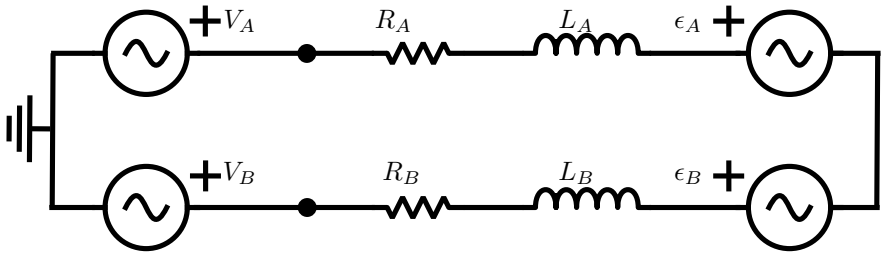

Figure 2.4: Equivalent motor circuit.

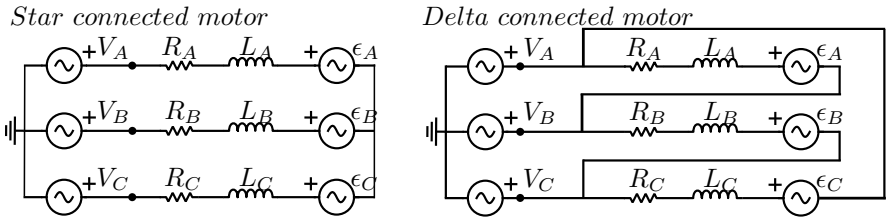

Figure 2.5: Electrical scheme of star and delta connected motors.

$$\begin{aligned} i_A &= i\cos(\theta_e), \\ i_B &= i\cos(\theta_e - \frac{\pi}{2}). \end{aligned} \tag{2.10}$$

(2.9) could be expressed as,

$$\tau_{tot} = \tau_A + \tau_B = \Lambda_m i\cos^2(\theta_e) + \Lambda_m i\cos^2(\theta_e - \frac{\pi}{2}) = \Lambda_m i, \tag{2.11}$$

which is the optimal condition in which generated torque is maximized.

As said at the beginning of the chapter normally PMSM have three phases and a number of magnet pole pairs which depends on motor types. The electric model of a three phase motor is shown in figure 2.5. Model components are totally equivalent to the two phase motor described in figure 2.4. Voltage equations of a three phase electrical motor are:

$$\begin{bmatrix} V_A \\ V_B \\ V_C \end{bmatrix} = \begin{bmatrix} R_{abc} \end{bmatrix} \begin{bmatrix} i_A \\ i_B \\ C \end{bmatrix} + \frac{d}{dt} \begin{bmatrix} L_{abc} \end{bmatrix} \begin{bmatrix} i_A \\ i_B \\ C \end{bmatrix} + \begin{bmatrix} \epsilon_A \\ \epsilon_B \\ \epsilon_C \end{bmatrix}. \tag{2.12}$$

In this case the voltage waveforms are shifted of $\frac{2\pi}{3}$rad instead of $\frac{\pi}{2}$rad Thus:

$$\begin{aligned} i_A &= i\cos(\theta_e), \\ i_B &= i\cos(\theta_e - \frac{2\pi}{3}), \\ i_C &= i\cos(\theta_e + \frac{2\pi}{3}). \end{aligned} \tag{2.13}$$

Also in this case, a balanced set of three phase currents has been assumed. For what concerns the BEMF waveform:

$$\begin{aligned} \epsilon_A &= \Lambda_m \omega_r \cos(\theta_e), \\ \epsilon_B &= \Lambda_m \omega_r \cos(\theta_e - \frac{2\pi}{3}), \\ \epsilon_C &= \Lambda_m \omega_r \cos(\theta_e + \frac{2\pi}{3}). \end{aligned} \tag{2.14}$$

The first term of (2.12) models stator coils resistance and, for a balanced three phase system, it is possible to assume $R_A = R_B = R_C = R_s$ [36]. Thus $\left[R_{abc}\right]$ is a $3 * 3$ diagonal matrix.

The second term of (2.12) model the fluxes and currents generated voltage drops due to phase inductances . The expression of $\left[L_{abc}\right]$ is:

$$L_{abc} = \begin{bmatrix} L_{aa} & M_{ba} & M_{ca} \\ M_{ab} & L_{bb} & M_{cb} \\ M_{ac} & M_{bc} & L_{cc} \end{bmatrix}. \tag{2.15}$$

Also in this case, assuming a balanced three phase system in (2.15) it is possible to assume the mutual inductance elements $M_{jy} = M_{yj}$. Diagonal elements of $\left[L_{abc}\right]$ represent phase self inductances and also in this case $L_{aa} = L_{bb} = L_{cc} = L_s$ can be assumed.

Stator phase voltages V_A, V_B, V_C in a three phase system, dimensionally, lie on a plane and they are usually shifted of $\frac{2\pi}{3}$rad; thus they generate a two-dimensional vector which can be expressed with a two-phase orthogonal stator frame $\boldsymbol{\alpha}$ and $\boldsymbol{\beta}$. This is done through a mathematical transformation called forward Clarke Transformation with which it is possible to express the same voltage vector by using two vectors instead of three. This simplifies motor model analysis and design of an appropriate driving technique by shrinking the dimension of motor equations from three to two. By applying the direct Clarke Transformation, a two-phase orthogonal stator axis called stationary reference frame is obtained [37]:

$$\begin{bmatrix} V_\alpha \\ V_\beta \end{bmatrix} = \frac{2}{3} \begin{bmatrix} 1 & -\frac{1}{2} & -\frac{1}{2} \\ 0 & \frac{\sqrt{3}}{2} & -\frac{\sqrt{3}}{2} \end{bmatrix} \begin{bmatrix} V_A \\ V_B \\ V_C \end{bmatrix} = \left[T_{abc/\alpha\beta}\right] \begin{bmatrix} V_A \\ V_B \\ V_C \end{bmatrix}. \tag{2.16}$$

The resulting voltage vector has the same amplitude and phase as the three phase reference frame resulting voltage vector. Motor equation can thus be expressed as a two phase motor just like the one presented at the beginning of the chapter:

$$\begin{bmatrix} V_\alpha \\ V_\beta \end{bmatrix} = \left[R^s\right] \begin{bmatrix} i_\alpha \\ i_\beta \end{bmatrix} + \frac{d}{dt} \left[L^s\right] \begin{bmatrix} i_\alpha \\ i_\beta \end{bmatrix} + \begin{bmatrix} \epsilon_\alpha \\ \epsilon_\beta \end{bmatrix}, \tag{2.17}$$

where $\left[R^s\right]$ and $\left[L^s\right]$ are the resistance and inductance matrices of the stationary reference frame:

$$\left[R^s\right] = \begin{bmatrix} R_s & 0 \\ 0 & R_s \end{bmatrix} = \left[T_{abc/\alpha\beta}\right] \left[R_{abc}\right] \left[T_{\alpha\beta/abc}\right], \tag{2.18}$$

$$\left[L^s\right] = \begin{bmatrix} L_\alpha & L_{\alpha\beta} \\ L_{\beta\alpha} & L_\beta \end{bmatrix} = \left[T_{abc/\alpha\beta}\right] \left[L_{abc}\right] \left[T_{\alpha\beta/abc}\right]. \tag{2.19}$$

The apex ^{s} recalls that the quantities are expressed in the stator reference frame and $\left[T_{\alpha\beta/abc}\right] = \left[T^T_{abc/\alpha\beta}\right]$. The expression of mutual and self inductance of $\left[L^s\right]$ is:

$$\begin{aligned} L_\alpha &= \frac{1}{2}\left[(L_q + L_d) + (L_q - L_d)\cos(2\theta_e)\right], \\ L_\beta &= \frac{1}{2}\left[(L_q + L_d) - (L_q - L_d)\cos(2\theta_e)\right], \\ L_{\alpha\beta} = L_{\beta\alpha} &= \frac{1}{2}\left[(L_q - Ld)\sin(2\theta_e)\right], \end{aligned} \tag{2.20}$$

L_d and L_q are the minimum and maximum self inductance of a single phase coil over an entire electrical rotor revolution:

$$\begin{aligned} L_d &= \frac{N^2}{2}\left(\frac{1}{\mathcal{R}_M}\right), \\ L_q &= \frac{N^2}{2}\left(\frac{1}{\mathcal{R}_m}\right), \end{aligned} \tag{2.21}$$

where $\mathcal{R}_M$ and $\mathcal{R}_m$ are the maximum and minimum flux reluctance over an entire electrical rotor revolution [38],[36]. it is interesting to note that according to (2.20) the value of these inductances depends on rotor position. Reluctance variation could be up to 200% when dealing with Internal Permanent Magnet Synchronous Motors (IPMSM) and $L_d > L_q$ while for Surface Mounted PMSM the variation is usually around 5%-15% and $L_d < L_q$ [38]. The expression of the torque in α and β reference frame is the same as (2.9);

$$\tau_{tot} = \tau_A + \tau_B + \tau_C = \frac{1}{\omega_r}(i_A\epsilon_A + i_B\epsilon_B + i_C\epsilon_C) = \frac{3}{2\omega_r}(i_\alpha\epsilon_\alpha + i_\beta\epsilon_\beta). \tag{2.22}$$

Another representation of the two phase reference frame is the synchronous reference frame which rotates at the electrical rotor speed. It is obtained by applying the Park Transformation to a stationary reference frame as defined in (2.23) [39]. It is defined by a two-phase orthogonal stator axis $\boldsymbol{d}$ and $\boldsymbol{q}$ with the $\bar{d}$ axis aligned with the rotor flux direction as shown in figure 2.6.

Since dq frame rotates synchronously with the rotor, the voltage and current space vector is fixed in magnitude and direction with respect to the rotor. Thus, it results as a static value and it has no sinusoidal behavior.

$$\begin{bmatrix} V_d \\ V_q \end{bmatrix} = \begin{bmatrix} \cos(\theta_e) & \sin(\theta_e) \\ -\sin(\theta_e) & \cos(\theta_e) \end{bmatrix} \begin{bmatrix} V_\alpha \\ V_\beta \end{bmatrix} = \left[T_{\alpha\beta/dq}\right] \begin{bmatrix} V_\alpha \\ V_\beta \end{bmatrix}, \tag{2.23}$$

Motor model expression in synchronous reference frame is thus:

$$\begin{bmatrix} V_d \\ V_q \end{bmatrix} = \left[R^r\right] \begin{bmatrix} i_d \\ i_q \end{bmatrix} + \frac{d}{dt}\left[L^r\right] \begin{bmatrix} i_d \\ i_q \end{bmatrix} + \begin{bmatrix} 0 \\ \epsilon_q \end{bmatrix}. \tag{2.24}$$

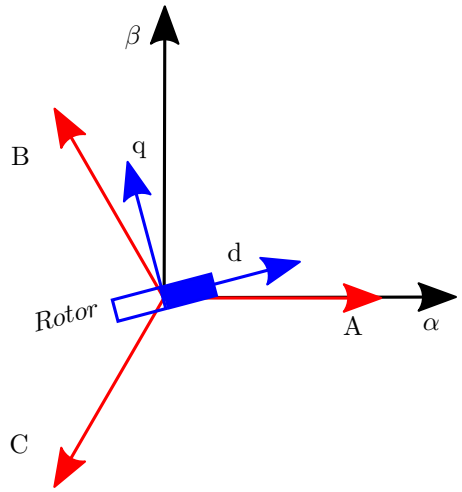

Figure 2.6: Stationary and synchronous reference frame.

Where the apex ^{r} means that the quantities are referred to the rotor (synchronous) reference frame. Resistance and inductance matrices in rotor reference frame are:

$$\left[R^r\right] = \begin{bmatrix} R_s & 0 \\ 0 & R_s \end{bmatrix}, \tag{2.25}$$

$$\left[L^r\right] = \begin{bmatrix} L_d & 0 \\ 0 & L_q \end{bmatrix}. \tag{2.26}$$

From (2.24) an expression of the direct V_d and quadrature V_q voltage component is obtained:

$$\begin{aligned} V_d &= R_s i_d + L_d \frac{d}{dt} i_d - \omega_e L_q i_q, \\ V_q &= R_s i_q + L_q \frac{d}{dt} i_q + \omega_e L_d i_d + \omega_e \Lambda_m. \end{aligned} \tag{2.27}$$

Torque expression is:

$$\tau_{tot} = \frac{3}{2\omega_r}\omega_e(\Lambda_m i_q + L_d i_d) - \frac{3}{2\omega_r}\omega_e L_q i_q = \frac{3}{2} n_p[\Lambda_m + (L_d - L_q) i_d] i_q. \tag{2.28}$$

In (2.28) electromechanical torque is expressed as a function of the i_d and i_q currents and it has two components. The first part of the expressions concerns the interaction between rotor flux and i_q. Since the d-axis of figure 2.6 is aligned along the flux direction, if a magnetic flux is generated along the q-axis the two fluxes tend to align. As a result, electromechanical torque is generated

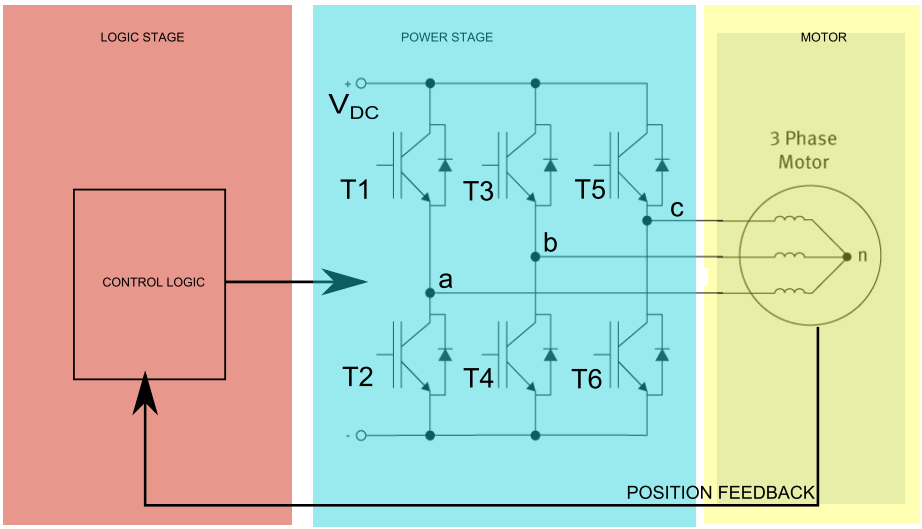

Figure 2.7: Three phase drive scheme.

proportionally to the current along the q-axis according to (2.2). For this reason the first component of (2.28) is called "alignment torque". The second part depends on motor salience and it is proportional both to i_d and i_q, it is called "reluctance torque".

2.3 Motor Drive Structure and Principle of Operation

PMSM are controlled with a specific electronics which is able to generate the appropriate voltage waveform to be applied on motor phases. In order to do this, motor drives include a logic stage which controls a power stage which physically delivers electrical power to the motor. Basically these devices, convert a continuous voltage into three phase sinusoidal voltage waveforms. The basic scheme of a PMSM drive is shown in figure 2.7. The power stage is called three phase H bridge and it is basically composed of 6 switches which are controlled by the logic stage. By alternating which switches are on, voltage and current flow can be directed in any desired direction.

To do this, the voltage and current waveform, have to be applied accordingly with the rotor position, in order to maximize the electromechanical torque which is generated. According to (2.2) it is possible to notice that the maximum torque is generated when rotor and stator generated fluxes are orthogonal. For this reason the rotor position has to be measured or estimated by the control logic. Thanks to rotor position information, the control logic imposes an optimal switching of the H bridge.

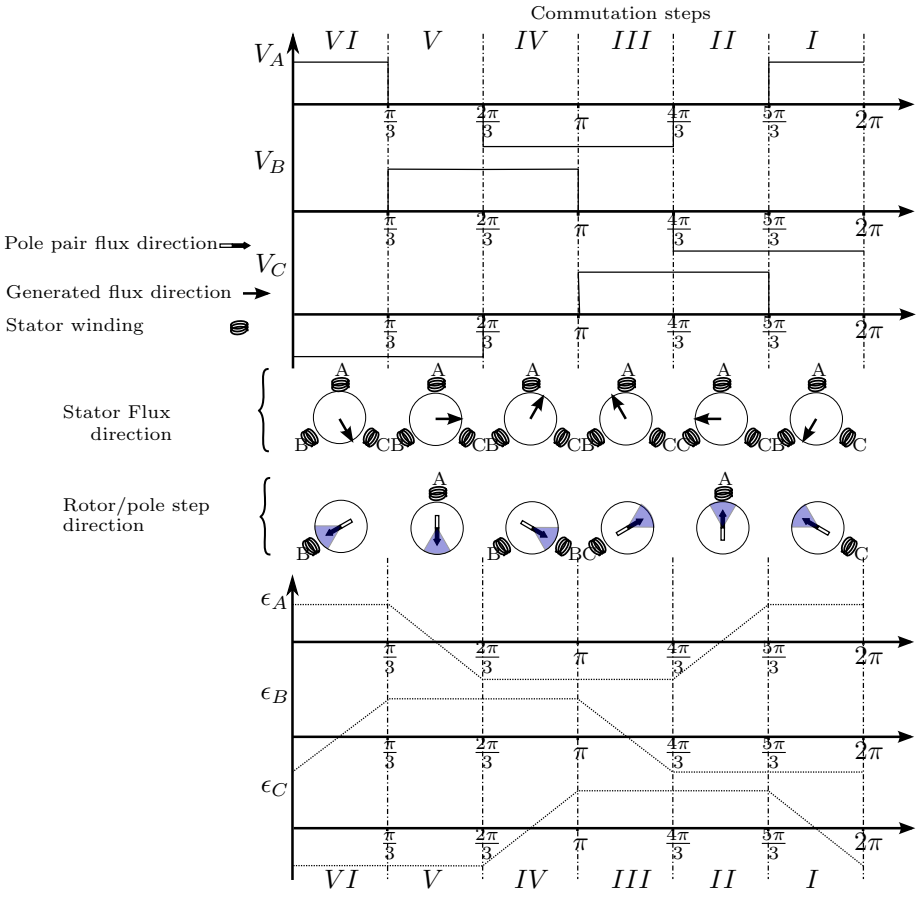

Figure 2.8: Six steps commutation technique.

2.4 Six Step PWM Commutation Technique

Motor driving signal could be of many different waveforms according to the driving technique. The six step commutation technique is one of the most used due to its simplicity of implementation and robustness.

In figure 2.8 the six voltage steps are schematically shown driving a motor with three windings and one magnetic pole pair during a complete electrical rotation. The six steps correspond to the six different voltage phase settings there illustrated. For this type of motor, switching from a step to another, will result in an electrical rotation of,

$$\Delta\theta_e = \frac{2\pi}{6}. \tag{2.29}$$

Voltage amplitude V_A, V_B and V_C is regulated by the duty-cycle of the

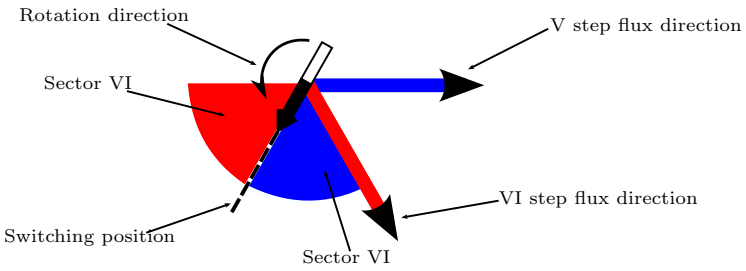

Figure 2.9: Generate flux direction and corresponding pole pair.

Pulse Width Modulation (PWM) which is imposed by the control electronics. By operating an optimal switching from a step to another, phase current peaks and torque ripple are minimized. In figure 2.8 it is shown the optimal phase voltage commutation according to a given phase voltage amplitude. In (2.11) it has been shown that given a two phase BLDC motor with sinusoidal BEMF, the optimal driving corresponds to condition (2.10), which means that the phase currents waveforms (i_A, i_B) and the BEMF (ϵ_A, ϵ_B) are in phase. For a three phase motor this condition corresponds to,

$$\begin{aligned} i_A &= i\sin(\theta_r), \\ i_B &= i\sin(\theta - \frac{2\pi}{3}), \\ i_C &= i\sin(\theta - \frac{4\pi}{3}). \end{aligned} \tag{2.30}$$

in phase with ϵ_A, ϵ_B and ϵ_C. Under the assumption that the phase current and voltage are in phase, the phase switching performed in figure 2.8 basically is an approximation of these conditions. The approximation consists in the fact that the phase voltage waveforms are squared, most of the times the BEMF waveform is not sinusoidal and phase inductive effects shift currents with respect to voltage.

In other words optimal switching means keeping the pole pair flux and stator flux the most possibly orthogonal in order to maximize the torque. So, since the stator generated flux can take six discrete directions, there will be a corresponding angular sector for the flux direction in which the applied torque is maximized. In figure 2.9 it is shown the sixth step of the stator flux direction and the corresponding angular sector in which the flux it is directed; when flux direction has reached the switching position, the system has to switch to the fifth step and the rotor will be moved to the next sector.

It is easy to understand that for a given rotor speed, there will be a corresponding switching rate. Nevertheless the rotor speed do not just depend on the switching rate, it also depends on the supplied voltage. The time the pole pair flux vector takes to go through a certain angular sector decreases when increasing the applied voltage. According to the voltage amplitude (V_A, V_B, V_C),

the control logic has to switch at a proper frequency so that an optimal "lock condition" is kept.

If the commutation frequency is too slow with respect to the applied voltage, commutation occurs late, resulting in high motor current and high torque ripple. If the commutation frequency is too fast with respect to the applied voltage,the motor can not accelerate fast enough to catch the next commutation, lock is lost and the motor spins down. Thus it is necessary to apply an optimal switching rate with respect to the applied voltage. This could be achieved through an open loop or a closed loop control technique.

Open loop technique could be based on a look-up table which regulates the phase voltage and the frequency according to the desired speed. This is made possible by knowing the characteristics and the behavior of a certain motor in nominal conditions. The problem of an open loop control is that, out of nominal conditions, motor operation is inefficient and unreliable. For these reasons open loop operation of a BLDC is used just in case of low demanding applications.

It is otherwise possible to use a closed loop regulation of the motor so as to maintain the motor in lock condition and being able to set and monitor the motor speed. In this case motor control can be performed also out of nominal conditions. The rotor position information, which is necessary to operate a closed loop control, can be gathered through position sensors or with sensorless techniques. In general BLDC motors driving is performed through Hall sensors which can sense the rotor position. More accurate techniques use rotational position encoders. Similar information can be gathered from the BEMF by sensing phase currents or voltage waveform on each phase or by measuring stator inductance variation according to rotor position. These techniques do not need position sensors and are thus called sensorless techniques. Their advantage is that eliminating position sensors the drive is simpler, lighter and cheaper.

2.5 Space Vector Pulse Width Modulation Commutation Technique

Space Vector Pulse Width Modulation (SVPWM) is a technique that optimize the switching pattern of the three phase inverter described in section 2.3 in order to generate a desired space vector voltage. With respect to the Six Step control technique with which it is possible to generate six discrete voltage vector directions, with the SVPWM, it is possible to generate a continuous rotating voltage vector as a composition of the six directions shown in figure 2.8. Otherwise, to generate a continuous rotating voltage vector, it would be necessary to operate the driver switches shown in figure 2.7 in their linear region. This would lead to a very accurate direction and amplitude control with low added noise. Although it would came at the expense of a very high power dissipation on the control electronics which means low overall efficiency. For this reason, with the SVPWM it is possible to exploit both the control accuracy of a linear power stage and the efficiency of the Six Step PWM control technique.

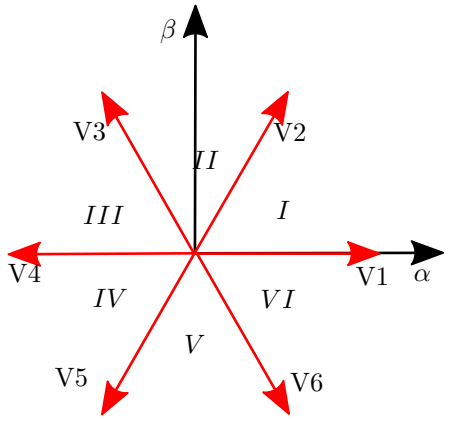

Figure 2.10: Discrete Voltage Vector directions $V_{1,2...6}$ and position sectors $I, II....VI$.

			Drive Switches Cfg (0 = OFF, 1= ON)					
Step	V_{step}	θ_{step}	T_1	T_2	T_3	T_4	T_5	T_6
1	V_1	$\theta_1 = 0^o$	1	0	0	1	0	1
2	V_2	$\theta_2 = 60^o$	1	0	1	0	0	1
3	V_3	$\theta_3 = 120^o$	0	1	1	0	0	1
4	V_4	$\theta_4 = 180^o$	0	1	1	0	1	0
5	V_5	$\theta_5 = 240^o$	0	1	0	1	1	0
6	V_6	$\theta_6 = 300^o$	1	0	0	1	1	0
7	V_7	-	0	1	0	1	0	1
8	V_8	-	1	0	1	0	1	0

Table 2.1: Driver switches configurations with respect to the different commutation steps.

Each of the above mentioned commutation step, corresponds to a certain configuration of the power stage and it is described in Table 2.1. The switches $T_{1,2...6}$ to which the table refers to, are shown in figure 2.7. It is possible to note that there are two more states/configurations in addition to the ones showed in figure 2.10 corresponding to a null voltage applied to the three motor phases.

In figure 2.10 each of these steps ($V_{1,2...6}$) are expressed with respect to the α, β stationary frame. Given a desired voltage vector direction and amplitude expressed in the same reference frame, it is possible to express it as a linear combination of a couple of two spatially adjacent steps V_i and $V_{i\pm1}$. To do this, appropriate weights have to be calculated in order to assign a duty-cycle to each of the steps. If θ_e and V_{ref} are the desired direction and voltage amplitude, V_i and V_j the two steps delimiting the sector of interest and V_{DC} the supply voltage, the following equations have to be solved: [35]

$$\begin{aligned} V_{ref}(\theta_e) &= V_i \cdot a_i + V_j \cdot a_j + V_7 \cdot a_7 + V_8 \cdot a_8, \\ V_{ref}\cos(\theta_e) &= V_{DC}(a_i \cos(\theta_i) + a_j \cos(\theta_j)), \\ V_{ref}\sin(\theta_e) &= V_{DC}(a_i \sin(\theta_i) + a_j \sin(\theta_j)), \\ a_i + a_j + a_7 + a_8 &= 1, \\ a_7 &= a_8. \end{aligned} \tag{2.31}$$

Once the weights a_i, a_j, a_7 and a_8 are calculated, it is possible to define the duty cycle corresponding to each state:

$$\begin{aligned} T_i &= T_s \cdot a_i, \\ T_j &= T_s \cdot a_j, \\ T_7 &= T_s \cdot a_7, \\ T_8 &= T_s \cdot a_8, \end{aligned} \tag{2.32}$$

where T_s is the PWM period. Differently from the Six Step commutation technique, by using the SVPWM, it is possible to operate an accurate position or torque control. It clearly requires a higher computational effort thus it is employed in more demanding applications. Also using the SVPWM control technique it is possible to operate the motor in open loop control but the resulting performance is lowered by poor electrical efficiency and dynamic performance.

2.6 Permanent Magnet Synchronous Motors: comparison with other motor topologies

The popularity of the Permanent Magnet Synchronous Motors in various field of application is due to their high energy efficiency, compact form, reduced noise operation, high reliability, and low maintenance [30]. Brushless DC (BLDC) motors and Brushless AC (BLAC) motors have basically the same structure and

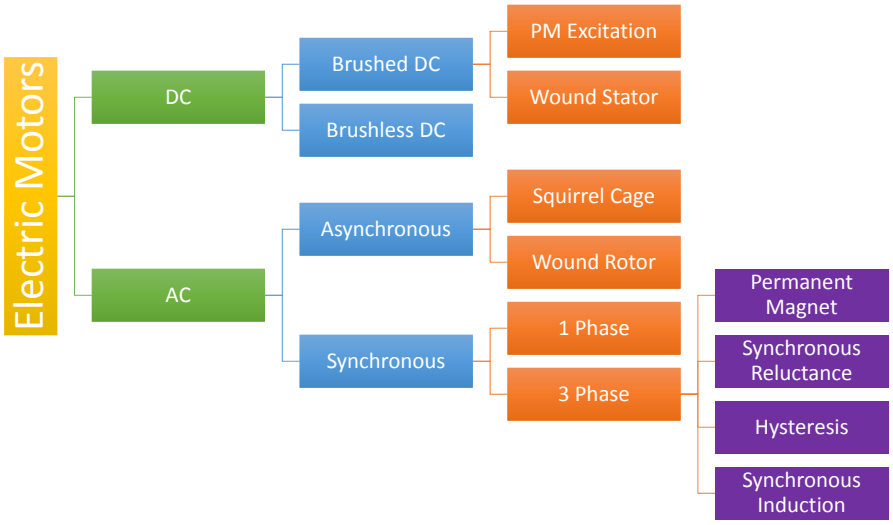

Figure 2.11: Most common electric motors on the market.

both are PMSM. By convention, BLDC motors are controlled with squared voltage waveforms mutually shifted on the three phases and the back electromotive force waveform that they induce on stator coils is approximately trapezoidal. BLAC motors instead are controlled with continuous voltage waveform and they produce a sinusoidal back electromotive force. In practical this difference means that the BLAC motor can reach higher performances regarding motor position, speed or torque control, efficiency and dynamic performance; they are generally also more expensive compared to the BLDC ones an more sophisticated techniques are required for their control. There are although several motors topologies present in the market, and the choice of the most suitable for a specific applications depends on many factors. In figure 2.11 a diagram of some of the most common electric motors is shown.

The Brushed DC Motor is one of the most common electric motor, it is widely used for commercial and industrial applications. Control techniques for these motors are extremely easy and they could be operated over a wide range of speed with considerable dynamic performance. As specified at the beginning of the chapter, they are often used in underwater propulsion on a wide range of vehicles. With respect to PMSM, these motors are easier to control and both the motor and control electronics are generally cheaper. The downsides associated with this kind of motor are, with respect to PMSM: limited speed range, low dynamic performance due to high rotor inertia, low heat dissipation, low power density, low reliability and high maintenance needs due to the creeping contacts

of the armature. Also efficiency in terms of energy conversion is around 15-23% lower with respect to PMSM [40].

Also induction motors are really common and widely available on the market: they feature a very simple design, low price and robustness. Concerning the control technique, they need an alternate voltage excitation hence it is more complex with respect to Brushed DC motors. Although differently from PMSM, rotor position is not required for operation. With respect to PMSM hence they are cheaper and easier to control; the drawbacks consist in lower power density due to the fact that permanent magnets produce more flux for their size than the magnetic energy produced the induction motor. Also overall efficiency is lower partially due to resistive losses in the copper bar and lower dynamic performance [41], [42].

Concerning the other kind of motors listed in the scheme of Figure 2.11 they are not of interest because they do not met the dynamic requirement of underwater propulsion.

Chapter 3

Sensorless Control Techniques for PMSM

Sensored control of PMSM is widely used in many field of application, for its reliability, precision and simplicity of operation [43]. Also concerning the underwater field of application [28] it has proven to be highly reliable, easy and quick commissioning, thanks to the many widely tested commercial applications that can be found on the market. Although the wiring required for position sensors and the sensor itself, represents an additional cost and encumbrance. The presence of additional electronics furthermore also constitutes a drawback in terms of maintenance and reliability. A simpler, cheaper, more reliable, and less cumbersome electronics would then be preferable when dealing with underwater applications where space saving and reliability are crucial. The work regarding this thesis was mainly focused on the improvement of the propulsion system of MARTA AUV which is an Observation Class AUV. The vehicle has been equipped with PMSM motors and it has the same propulsion setup as the Typhoon vehicle, with four thrusters for sway, heave, and pitch motion and two rear propellers for surge and yaw motion. MARTA AUV thruster configuration is shown in Figure 6.2.

In order to efficiently operate vehicle navigation it is useful to operate a precise speed or torque control of motor thruster. This can reduce navigation hardware costs, improve diagnostic vehicle capability and increase navigation accuracy. In general, speed control is operated through rotor position sensors; this is the case of the Typhoon vehicles whose motors are equipped with Hall position sensors. More advanced motor controllers as the BlueESC mounted on the BlueROV2 ROV, exploit sensorless control speed feedback but a speed control is not provided by the controller itself.

Also for the navigation strategy of MARTA AUV, speed measurement is necessary but, with respect to the Typhoons vehicles, in this case, a sensorless actuation system has been preferred, also for research purposes. The selection was made in order to avoid the additional wiring required for position sen-

sors and the sensor itself which represents an additional cost and encumbrance. The presence of additional electronics furthermore also constitutes an additional drawback in terms of maintenance and reliability. However, during this research activity, it has not been possible to find commercial solutions exploiting a sensorless speed and torque estimation for PMSM especially applied to underwater propulsion. On the other hand, customized solutions designed by industrial motor control factories would be extremely expensive. Hence this work thesis has been focused on the development of a complete propulsion solution exploiting a PMSM controlled with a sensorless technique able to perform speed and torque estimation. There are several kind of sensorless control techniques each of these has its pros and cons according to the field of application and to the operating conditions which are required.

3.1 Trapezoidal Control Sensorless Techniques

This family of techniques, is implemented in combination with the Six Steps commutation technique illustrated in section 2.4 and they are based on the observation of the BEMF waveform on the three phases during motor operation. Interest on motor generated BEMF behavior is due to the fact that its behavior depends on rotor position. In Figure 2.8 it is shown the waveform of the BEMF induced in each phase in an entire rotation. It is possible to notice that depending on the rotor position it could be positive or negative with respect to a reference voltage level called "star center level". When the BEMF signal crosses that level, it is called "zero crossing". Zero crossings could be used as a reference point to identify the rotor position; it can be seen that they occur when the magnet generated flux and coil induced flux are parallel. So once it is possible to detect them while the motor is turning, it is also possible to estimate the rotor position and, consequently, its speed and the acceleration. Zero crossing detection can be performed by sampling phases voltages during rotation. BEMF voltage measurements indeed are taken from phase terminals where the driving voltage is also delivered. So the BEMF can not be measured when a phase is energized, because the driving voltage would hide the information contained in it. Figure 2.8 shows that the Six Step commutation technique leave one phase floating at each commutation step. The BEMF induced in the floating phase, can then be measured on that phase.

The star center level represented in Figure 2.8 is a reference value which does not necessarily correspond to the ground level. However this level is necessary when wanting to detect the BEMF zero crossings. In a star connected motor it is available in the star center of it. For delta connected motors and for star connected motor in which the star center is not accessible this reference point has to be estimated.

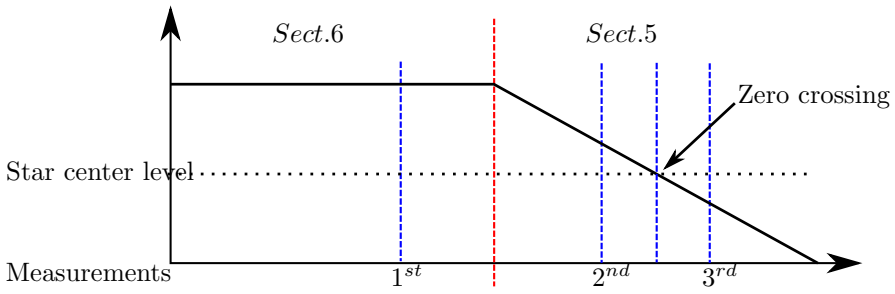

Figure 3.1: Phase readings during VI and V sector.

3.1.1 Sensorless Motor Control: Application Note 857 by Microchip technique

In the Application Note 857 by Microchip [5] it is described a sensorless control technique based on Six Step control. The motor speed is regulated by using voltage amplitude as a control reference quantity. So according to the applied voltage, the controller has to perform an optimal phase switching which represents the lock condition.

In this case the BEMF measurements are performed in just one of the motor phases and through this measurement the controller is able to track the optimal step switching ratio. By making the measurements on phase A, it is possible to see on Figure 2.8 that during drive sector VI and VI, phase settings are:

- Sector IV:
  Phase A: high
  Phase B.: floating
  Phase C: Low

- Sector V:
  Phase A: floating
  Phase B: high
  Phase C: low

The control performs three measurements during these sectors. The first reading is taken during sector VI when phase terminal A is actively driven high as shown in Figure 3.1. This is a measurement of the applied voltage V_{DC}. The next two readings are taken during sector 5 when phase terminal A is floating. In phase lock condition according to [5] criteria, while phase terminal A is switched from high to floating the ϵ_A has a zero crossing at $\frac{1}{2}$ of the commutation period. For this reason the second measurement is took at $\frac{1}{4}$ of the commutation period and the third reading is taken at $\frac{3}{4}$ of the commutation. With these readings it is possible to understand how the commutation frequency need to be adjusted in order to track the phase lock condition:

- Phase lock condition is respected if:

$Reading2 > \frac{V_{cc}}{2}$ and $Reading3 < \frac{V_{cc}}{2}$.

- Commutation frequency is too slow if:

$Reading2 < \frac{V_{cc}}{2}$.

Indeed it means that the zero crossing occurs too early and the phase switch occurs later, when the rotor has already reached the optimal switching position.

- Commutation frequency is too fast if:

$Reading3 > \frac{V_{cc}}{2}$.

This means that the phase commutation occurs when the rotor has not reached the switching position.

So every time the lock condition is not fulfilled the controller updates a commutation index which adjust the proper switching rate.

Since at standstill and low rotor speed BEMF waveform amplitude is too low to control the motor, the controller has to generate a startup routine. Initial switching is controlled in open loop by a look-up table in which according to the applied voltage it is defined the corresponding optimal switching frequency. When the motor turns fast enough the control is switched from the open loop to the closed loop control. The system control flow chart is shown in Figure 3.2. It is a very simple commutation technique and it is interesting to notice that this kind of control do not need a star center reference value to detect the zero crossing because it makes an estimation of it.

3.1.2 Sensorless Motor Control: Application Note 907 by Microchip Technique

In the application note 907 by Microchip [6] it is described a BEMF based technique for controlling a BLDC motors. It performs a zero crossing detection on the three phases. As shown in Figure 2.8, in an electrical revolution two zero crossings occur in each phase. Hence to perform sensorless control, the controller basically measures the time T between two subsequent zero crossings on two different phases. As shown in Figure 3.3 in optimal conditions T is equal to the time that has to elapse between two subsequent phase switchings. Thus after having measured the time elapsed between two subsequent zero crossings the controller is able to give the right phase switching frequency. The commutation after the second zero crossing indeed has to occur after $\frac{T}{2}$.

Also this method, needs a startup sequence since at standstill and low rotor speeds there is no detectable BEMF.

The rotor is initially turned in a lock position with two subsequent phase switching. Thanks to this positioning, the controller is supposed to know in

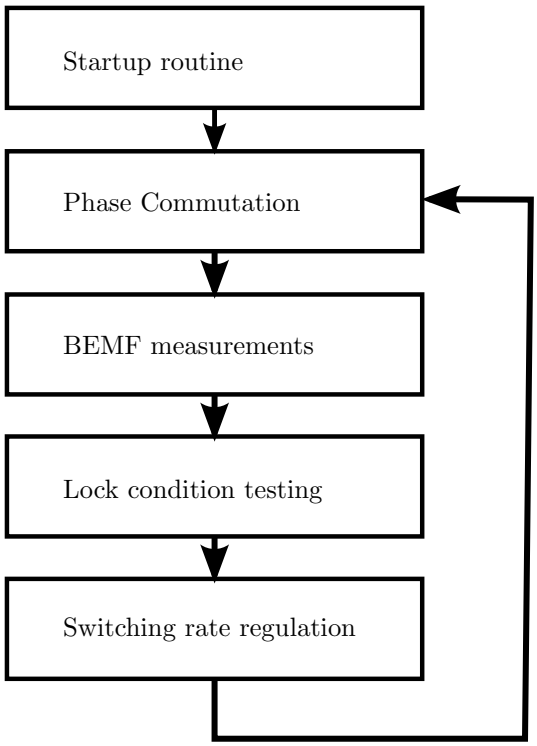

Figure 3.2: Flowchart of the AN857[5] control system.

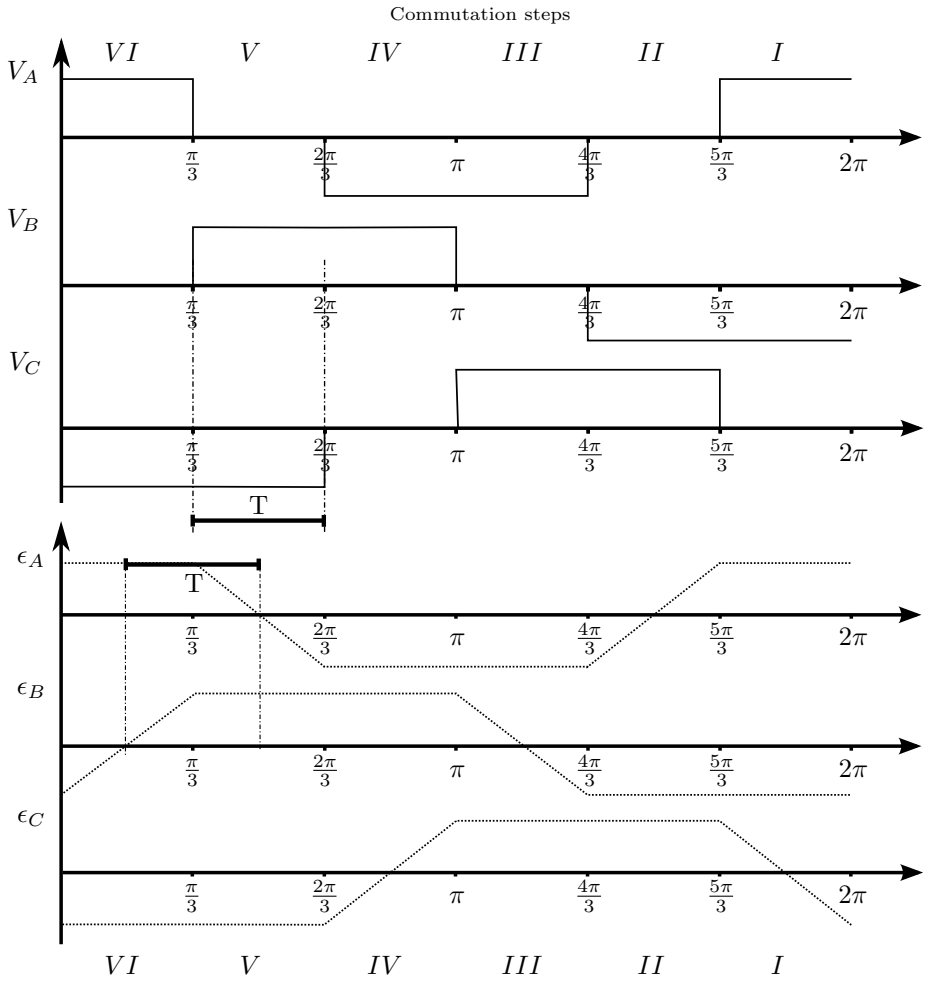

Figure 3.3: Time elapsed between two zero crossing when optimal phase commutation is performed.

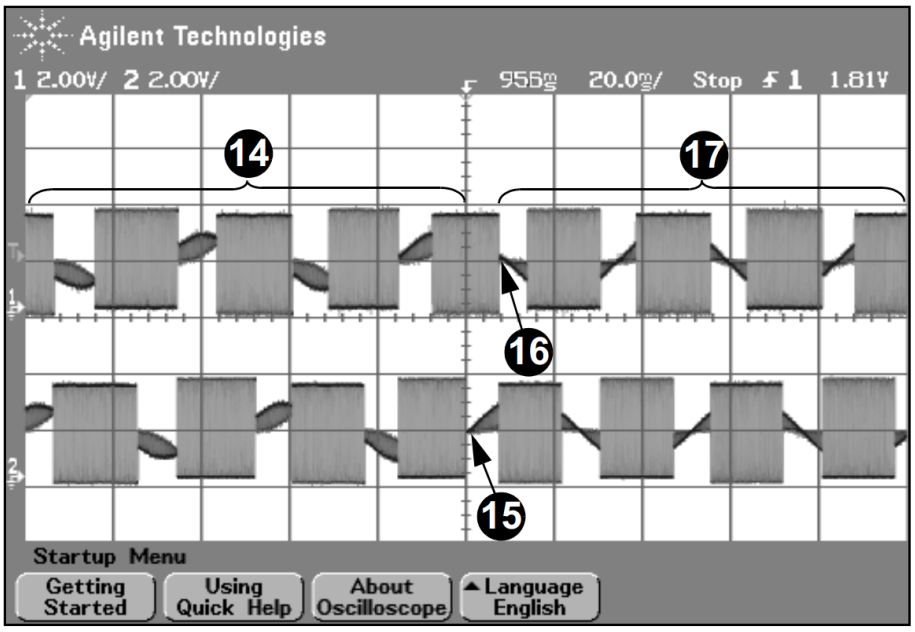

Figure 3.4: First start up method [6].

which position the rotor is. The startup sequence is composed of a first moment in which the phase switching frequency spins the motor at $\frac{1}{60}$ of the nominal motor speed. It is then accelerated until $\frac{1}{6}$ of the nominal speed. This is the speed from which the controller switches from open loop to closed loop operation. Of course the acceleration and the voltage delivered to the motor from the controller must be tuned according to the type motor and the operating conditions. A problem could be, that in open loop the switching frequency is not optimal, for this reason the BEMF zero crossings could occur when the corresponding phase energized. In this case, zero crossing can not be detected. According to [6] at constant speed, when driving the motor in open loop, the rotor is 90^o (electrical) in advance with respect to the optimal position; in this case BEMF zero crossing occur when the phases are energized. The Application Note 907 by Microchip illustrates two ways of switching from the open to the closed loop mode.

The first way suggests to accelerate the switching time in order to reduce the angular error previously described. By doing this, the BEMF zero crossings occur when the phases are not energized and the system can detect two subsequent zero crossings. In Figure 3.4 it is shown the acceleration phase (14) and the two first zero cross detections (15)(16). After them the motor starts to turn correctly (17) with the zero crossing occurring when the phase is not energized.

The second way illustrated in Note 907 by Microchip suggests to spin the motor in open loop at a certain speed (enough to generate sufficient BEMF)

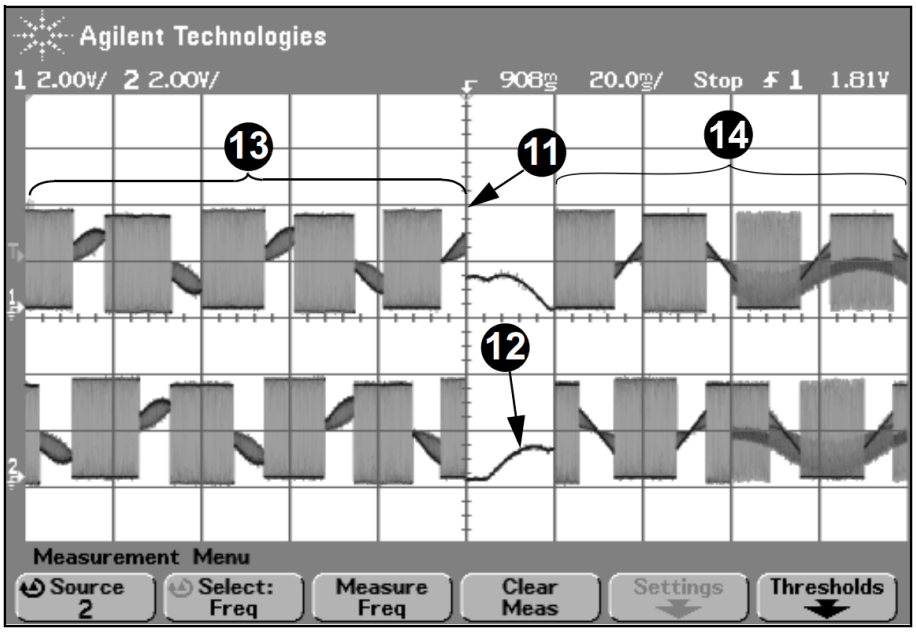

Figure 3.5: Second start up method [6].

and then to de-energize for a rotation the three phases thus making possible to detect the zero crossings. Of course this method is based on the assumption that the lack of spin to the rotor caused by the de-energization of the phases would not decrease significantly the rotor speed.

In Figure 3.5 it is shown the first part of the start up sequence (13) in which the rotor turns in an incorrect angular phase shift with respect to the correct one; in this part the zero crossings are not visible because they occur when the corresponding phase is not energized. In (11) phases are de-energized indeed it is possible to observe that BEMF signal has less ripple. It has to be noticed that being all the three phases de-energized, BEMF is no more shifted of a $\frac{1}{2}V_{DC}$ offset normally seen when the drive is on. Thus it should be set a threshold value at which the BEMF is compared (12). In this case the controller detects the BEMF zero crossings on the three phases, so that it could gather rotor direction, speed and position. The system is then transitioned to closed loop operation (14).
A flowchart of the application note 907 is shown in Figure 3.6

3.1.3 Sensorless Motor Control: InstaSPIN™-BLDC by Texas Instruments Technique

This technique is quite different from the previous ones because it is based on the measurement of the stator induced magnetic flux instead of the BEMF voltage.

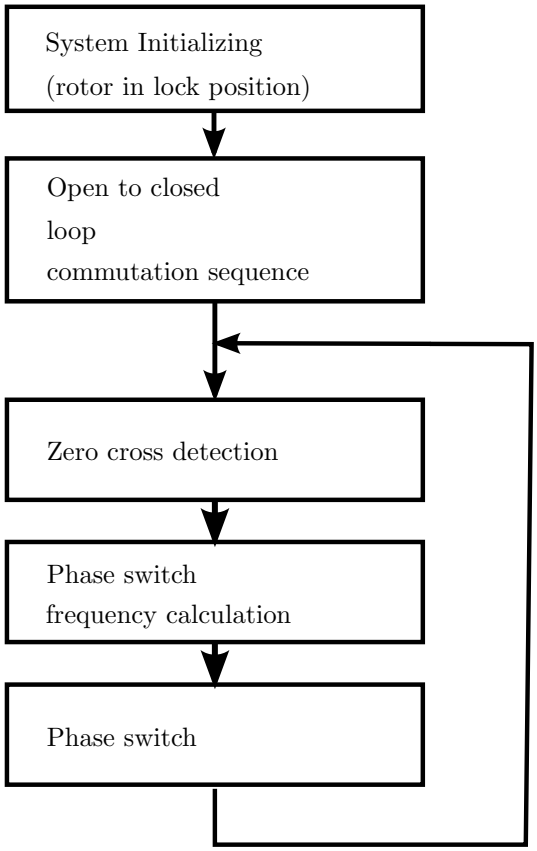

Figure 3.6: Flowchart of the Application Note 907 by Microchip control technique.

This means that the BEMF is still sensed but, an integration of it is performed, and the resulting quantity is magnetic flux.

During motor operation, the BEMF integration is performed at each step on the floating phase after the zero crossing has been detected. For this technique a star center reference has to be generated.

The integrated signal evolves quadratically as shown in Figure 3.7. Once integration has started the control switches to the next step when an optimal flux threshold is reached. The optimal threshold level depends on motor characteristics and has to be tuned in order to perform optimal switching. It is important to notice that this value is constant regardless of rotor speed. This is due to the fact that according to (2.6), the BEMF amplitude is proportional to the rotor speed. In Figure 3.8 it is schematically shown the BEMF integration at a certain speed ω_k and at $\frac{\omega_k}{4}$. In both cases, the integrated area is the same, so the switching threshold is also the same. The method has the big advantage that can control the motor even at a very low speed, when the produced BEMF has a really low amplitude. Furthermore, being flux an integration of the BEMF signal, it will be less noisy and, as a consequence, and easier to be measured. The phase switching is self regulated according to the applied voltage, and since it is not based on past information about rotor position, the optimal commutation frequency is constantly tracked. This makes the system robust for what concerns abrupt speed variations, and capable to optimize the energy consumption.

The startup sequence consists into two subsequent step that put the rotor in a certain position. After that, the system switches to the next step and starts to integrate the BEMF. When the result of the integration reaches the threshold value, the system switches to the next step and it can already operate in closed loop. A flowchart of the InstaSPIN$^{\text{TM}}$technique is shown in Figure 3.9

3.1.4 Considerations About Trapezoidal Control Sensorless Techniques

The main advantages of Trapezoidal Control Sensorless Techniques are the simplicity of implementation, low computational cost, simple and cheap hardware. They can be applied to a wide range of PMSM regardless of their structure and electrical characteristics and reliability. Their main drawback relies on limited performance. Dynamic performance in general is bounded by the fact that the switching control is not based on a rotor position estimation. The Six Step control technique does not allow a precise tracking of the orthogonality condition between the stator and rotor generated flux which is also the maximum torque generation condition. This influences the electrical efficiency. While it is quite easy to perform a speed control, with these techniques it is not practical to perform a torque control and in each case the accuracy is low. Concerning the technique illustrated in subsection 3.1.1 and in subsection 3.1.2, it has the main advantage of being extremely simple in terms of implementation and computational cost. Although they could fail facing abrupt speed changes because the step switching is based on a guess of what the optimal switching period is,

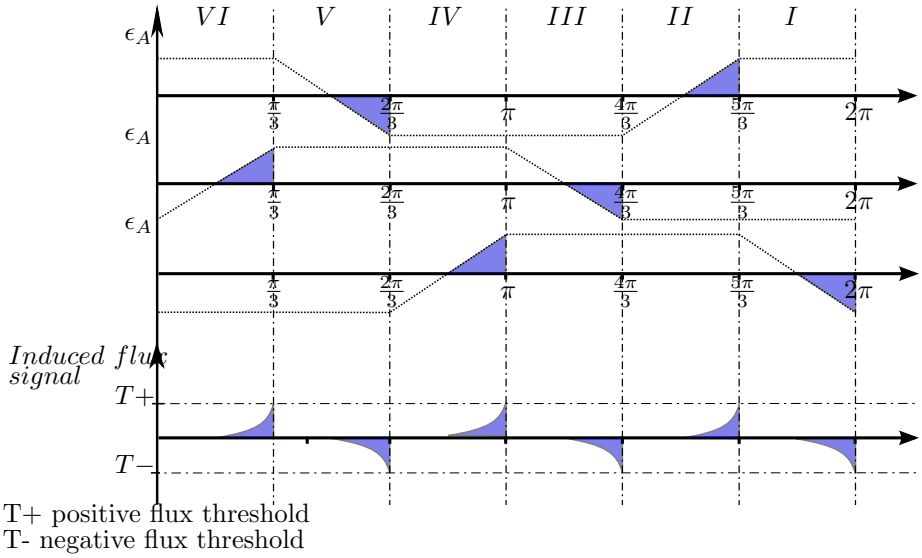

Figure 3.7: BEMF integration in InstaSPIN^{TM}technique.

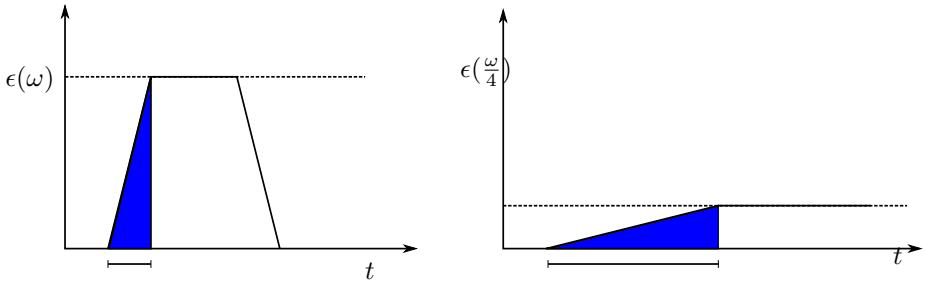

Figure 3.8: BEMF integration at two different speed.

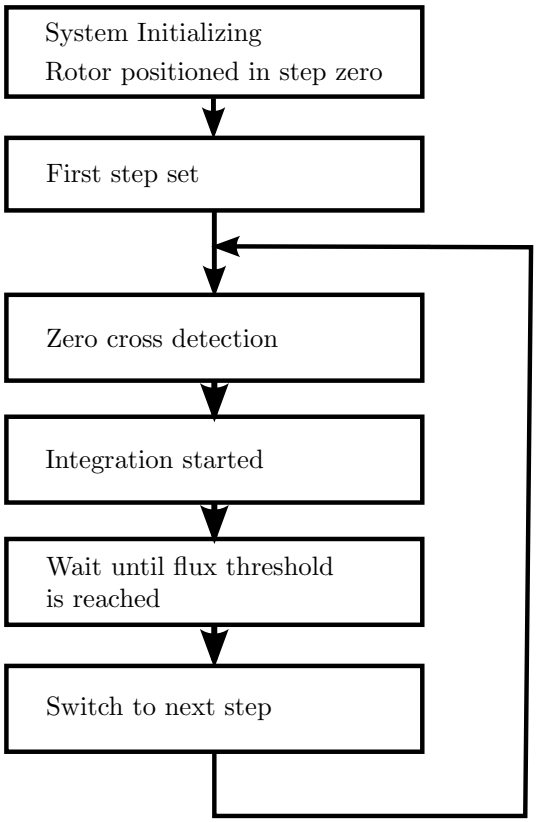

Figure 3.9: Flowchart of the InstaSPIN^{TM}technique.

according to previous commutation periods. The technique described in subsection 3.1.3, is the one that guarantees the best dynamic performance because it performs switching according to an estimation of the rotor position. Also it is the one that can operate the motor at the lower speed with respect to the other two, since it exploits an integration of the BEMF waveform instead of the BEMF itself.

3.2 Field Oriented Control (FOC) Techniques

Differently from trapezoidal control systems, in vector control based systems, stator quantities are represented by vectors and a continuous control on the amplitude and angle of these quantities is operated. This means that it is possible to control also electromagnetic transients, which is necessary for high-performance motor applications that are required to operate smoothly over the full speed range, generate full torque at zero speed and have high dynamic performance including fast acceleration and deceleration.

The most obvious solution, in order to achieve a more accurate control of motor quantities is the generation of three sinusoidal currents on the three phases and keep the rotor and stator generated magnetic flux orthogonal. The three currents vary smoothly as the rotor turns so that the resulting current space vector, which is proportional to the electromechanical torque, has constant magnitude and generates a constant torque. This minimizes the torque ripple and commutation spikes associated with trapezoidal commutation. To do this, a precise rotor position information and current measurements are necessary. They are needed to generate current reference signals and to operate a closed loop control of these currents. In Figure 3.10 [44] a diagram of the sinusoidal control is represented. Two of the motor winding are controlled in current by a separated control loop thanks to a PI controller. The current on the third phase, is imposed as the sum of the currents of the other two phases. The encoder measured position is fed to a look-up table, in order to synthesize two sinusoids phase shifted of $\frac{2\pi}{3}$rad one with respect to the other. The generated sine-waves amplitude is set proportional to the desired torque and fed to the two PI controllers which impose the desired currents on rotor windings by controlling the PWM generators. The illustrated technique represents a great improvement with respect to the trapezoidal control techniques in terms of position and torque control precision and smoothness. Although, with sinusoidal control, a motor can be efficiently operated only at low speed. This is due to the limited bandwidth and gain of PI controllers which have to operate a sinusoidal signal tracking. By increasing rotor speed, the current sinusoid frequency increase proportionally and reference signal tracking lose precision. This results in larger errors which perturbs the orthogonality condition between rotor and stator generated flux until they become parallel and no electromechanical torque is generated anymore. As a consequence, efficiency decreases and maximum speed is limited by the lack of generated torque.

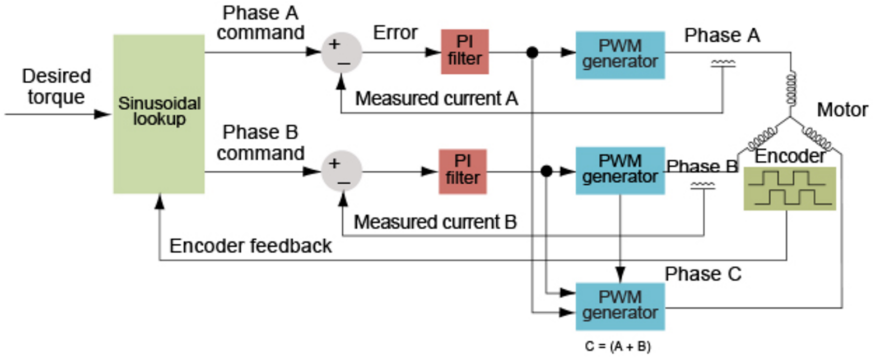

Figure 3.10: Sinusoidal control driver diagram.

Field Oriented Control (FOC) operates a control of the current space vector directly in the synchronous reference frame mentioned in (2.23). By doing this, it is possible to decouple torque and flux control in the PMSM. This means that on the d-axis, the stator current component controls rotor flux, and on the q-axis the current component controls rotor electromagnetic torque.

The two reference components are synchronous with the rotor electrical position. Hence, current space vector is fixed in magnitude and direction with respect to the rotor, this results in a two coordinates time invariant system. Thanks to this strategy, the control structure is totally similar to that of a field excitation DC machine but without the drawbacks of the DC motor mechanical commutations. With respect to the sinusoidal control above mentioned, in this case, the reference quantities do not oscillate at a frequency that is proportional to rotor speed so the controllers are not directly involved in the generation of the sinusoidal waveforms of phase currents and voltages. Therefore maximum speed is not limited by the frequency response of the current controllers, control tuning is simpler and higher performances can be achieved. Usually electrical angle between rotor and stator magnetic flux components are kept at $\frac{\pi}{2}$. This indeed is the condition to maximize the rotor electromechanical generated torque as explained in (2.2).
The classical diagram of a FOC is shown in Figure 3.11 [45]

Its structure is not really different from the Sinusoidal Control schematic of Figure 3.10 except for the fact that the controller output currents are not fed directly to the PWM generator but two transformations are operated before: the reverse Park Transformation from a two phase synchronous reference frame to a two phase stationary reference frame and the reverse Clarke Transformation from a two phase stationary reference frame to a three phase stationary reference frame. This as mentioned above, greatly simplifies and enhances motor control. Currents along the d and q axis, are imposed by setting a reference voltage on the to axis. To operate a separate control on torque and flux channels, the resulting currents along these axis, need to be mismatched. Currents expression along d and q axis, can be obtained by solving equations (2.27) with respect to

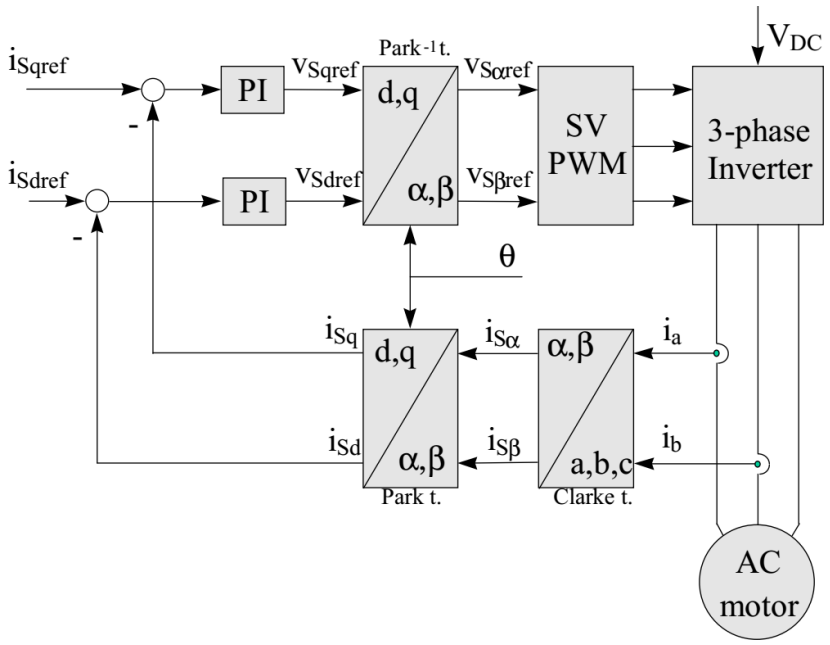

Figure 3.11: Field Oriented Control driver diagram.

i_d and i_q.

$$\frac{d}{dt}i_d = \frac{v_d}{L_d} - \frac{R_s}{L_d}i_d + \frac{\omega_e L_q}{L_d}i_q, \tag{3.1}$$

$$\frac{d}{dt}i_q = \frac{v_q}{L_q} - \frac{R_s}{L_q}i_q - \frac{\omega_e L_d}{L_q}i_d. \tag{3.2}$$

These expression, can be managed more easily in the frequency domain. Thanks to the Laplace transformation, the following expression of the synchronous reference frame currents is obtained:

$$i_d = \frac{v_d + \omega_e L_q i_q}{L_d s + R_s}, \tag{3.3}$$

$$i_q = \frac{v_q - \omega_e L_d i_d - \omega_e \Lambda_m}{L_q s + R_s}. \tag{3.4}$$

By eliminating the coupling terms between them a decoupling between torque and flux reference is achieved. It can be done by imposing the following voltages along d and q axis:

$$v_d = v_d^* - \omega_e L_q i_q, \tag{3.5}$$

$$v_q = v_q^* + \omega_e L_d i_d. \tag{3.6}$$

Consequently, the two resulting currents are no more dependent on the coupling component:

$$i_d = \frac{v_d}{L_d s + R_s}, \tag{3.7}$$

$$i_q = \frac{v_q - \omega_e \Lambda_m}{L_q s + R_s}. \tag{3.8}$$

Generally, the current component along the d-axis is set to zero while along the q-axis a current is imposed in order to set the desired electromechanical torque. According to (2.28) if i_d is set to zero, the "reluctance torque" component goes to zero resulting in:

$$\tau = \frac{3}{2} n_p \Lambda_m i_q = K_t i_q, \tag{3.9}$$

where K_t is called torque constant; it depends on motor geometry and construction quality. By estimating K_t a reference torque can be imposed.

The available sensorless techniques can be classified into two main categories [8]. The first and most common category of sensorless techniques is based on the fundamental model of the PMS machine. In this case the observation of the back

EMF induced in the machine coils by the rotor magnets is used in combination with observers to determine the rotor position. The observers are based on the state space model of the machine and can be divided into three types: deterministic observers (e.g. MRAS, Luenberger Observer), probabilistic observers (e.g. Kalman filter) and nonlinear observers (e.g. Sliding Mode Observer). Nevertheless, the back electromotive force induced by the rotor on the stator coils is null at zero speed, therefore these techniques are not capable of working at standstill and low speed ranges. The second category of techniques concerns the exploitation of motor magnetic anisotropies. These techniques are able to estimate the rotor position at standstill and low speeds, thus permitting the full speed range operation of the PMS machine. In fact, differently from back EMF based methods, these techniques provide the rotor position by using motor anisotropies like saliency, change of magnetic conductivity and saturation effects due to technological deviations. Among this category of techniques, signal injection based methods have been particularly exploited. These methods exploit the injection of high frequency voltage signals and require an observer for saliency tracking. In particular, the machine saliency create rotor/flux position-dependent harmonics in the high frequency stator currents which can be signal-processed to yield the required position. Several approaches have been realized and proposed in the scientific community for different kind of machines, as IPMSM and SPMSM (Interior and Superficial PMS motors), and anisotropies. These techniques have been also investigated on induction motors.

3.2.1 Sliding Mode Observer Based Rotor Position Estimation Technique

Most of the fundamental excitation based techniques described at the beginning of the chapter, are highly performing in terms of efficiency and control accuracy. One of the main concern regarding these techniques is low robustness facing motor parameters uncertainty and variation. The Sliding Mode Observer (SMO) technique due to its robustness is proposed to overcome these disadvantages. Several studies [46], [47], [48], [49] have demonstrated the robustness facing motor parameters variation and uncertainty of this technique.

SMO estimation is a model based technique, a preliminary identification of motor parameters is consequently necessary. The scheme of a SMO based FOC is shown in Figure 3.12.

The typical mathematical model of a PMSM in the two-axis $\alpha\beta$ stationary reference is described in (2.17). By solving it with respect to the derivative of the currents i_α and i_β and neglecting the mutual inductance components $M_{\alpha\beta}$ and $M_{\beta\alpha}$:

$$\frac{di_\alpha}{dt} = -\frac{R_s i_\alpha}{L_\alpha} - \frac{\epsilon_\alpha}{L_\alpha} + \frac{V_\alpha}{L_\alpha}, \tag{3.10}$$

$$\frac{di_\beta}{dt} = -\frac{R_s i_\beta}{L_\beta} - \frac{\epsilon_\beta}{L_\beta} + \frac{V_\beta}{L_\beta}. \tag{3.11}$$

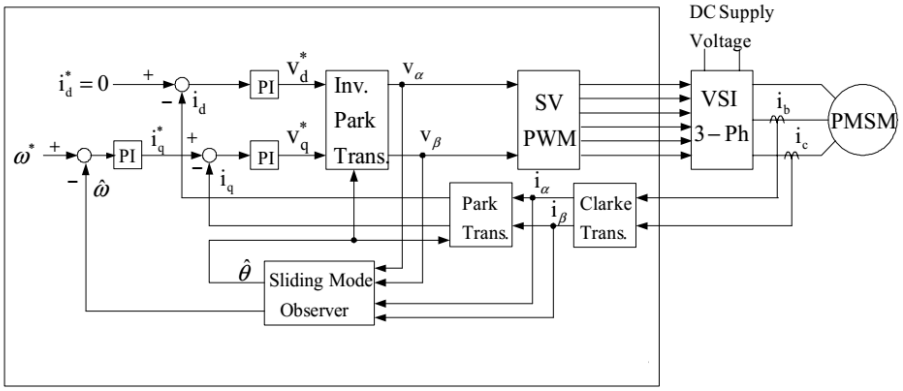

Figure 3.12: SMO based field oriented control scheme [7].

If an a priori knowledge of the parameters R and L characterizing the motor is available, it is possible to define an SMO estimator as [7]:

$$\frac{d\hat{i}_\alpha}{dt} = -\frac{R_s\hat{i}_\alpha}{L_\alpha} + \frac{V_\alpha}{L_\alpha} - \frac{l_1}{L_\alpha} sign(\bar{i}_\alpha), \tag{3.12}$$

$$\frac{d\hat{i}_\beta}{dt} = -\frac{R_s\hat{i}_\beta}{L_\beta} + \frac{V_\beta}{L_\beta} - \frac{l_1}{L_\beta} sign(\bar{i}_\beta), \tag{3.13}$$

where $\hat{i}_\alpha$ and $\hat{i}_\beta$ are the estimated currents and l_1 is a constant observer gain; $\bar{i}_\alpha$ and $\bar{i}_\beta$ are current estimation mismatches ($\bar{i}_\alpha = \hat{i}_\alpha - i_\alpha$, $\bar{i}_\beta = \hat{i}_\beta - i_\beta$) Once the estimator equations are defined it is possible to define a sliding surface as follows:

$$S = [S_\alpha, S_\beta]\,. \tag{3.14}$$

where,

$$S_\alpha = \hat{i}_\alpha - i_\alpha, \tag{3.15}$$

$$S_\beta = \hat{i}_\beta - i_\beta. \tag{3.16}$$

The error dynamics reaches zero when $S = 0$ which means that the observed currents converged to the measured ones. A condition has to be calculated to impose the error dynamics to converge on the sliding surface. It can be done by selecting an appropriate Lyapunov function:

$$V = \frac{1}{2}S^T S = \frac{1}{2}(S_\alpha^2 + S_\beta^2), \tag{3.17}$$

and by imposing the convergence condition:

$$S\dot{S} < 0. \tag{3.18}$$

To do that it is necessary to define the error dynamics from (3.11) and (3.13):

$$\frac{dS_\alpha}{dt} = -\frac{R_s}{L_\alpha}S_\alpha + \frac{\epsilon_\alpha}{L_\alpha} - \frac{l_1}{L_\alpha}sign(\bar{i}_\alpha), \tag{3.19}$$

$$\frac{dS_\beta}{dt} = -\frac{R_s}{L_\beta}S_\beta + \frac{\epsilon_\beta}{L_\beta} - \frac{l_1}{L_\beta}sign(\bar{i}_\beta). \tag{3.20}$$

It is then possible to compute (3.18). For sake of simplicity, let us consider $L_\alpha = L_\beta = L_s$:

$$\begin{aligned} S\dot{S} = &-\frac{R_s}{L_s}\left(\bar{i}_\alpha^2 + \bar{i}_\beta^2\right) + \frac{1}{L_s}\left(\epsilon_\alpha\bar{i}_\alpha - l_1\bar{i}_\alpha sign(\bar{i}_\alpha)\right) \\ &+ \frac{1}{L_s}\left(\epsilon_\beta\bar{i}_\beta - l_1\bar{i}_\beta sign(\bar{i}_\beta)\right) < 0. \end{aligned} \tag{3.21}$$

The condition described in (3.21) is fulfilled by imposing the following:

$$l_1 > max(|\epsilon_\alpha|, |\epsilon_\beta|). \tag{3.22}$$

When (3.22) and (3.22) are verified, the dynamics of the sliding surface and its derivative converge to zero:

$$\begin{pmatrix} S_\alpha \\ S_\beta \end{pmatrix} = \begin{pmatrix} \dot{S}_\alpha \\ \dot{S}_\beta \end{pmatrix} \approx \begin{pmatrix} 0 \\ 0 \end{pmatrix}. \tag{3.23}$$

By substituting (3.23) in (3.20) an estimation of the stator induced BEMF is obtained:

$$\begin{cases} 0 = \epsilon_\alpha - l_1 sign(\bar{i}_\alpha) \\ 0 = \epsilon_\beta - l_1 sign(\bar{i}_\beta) \end{cases} \Rightarrow \begin{cases} \epsilon_\alpha = l_1 sign(\bar{i}_\alpha) \\ \epsilon_\beta = l_1 sign(\bar{i}_\beta) \end{cases} \tag{3.24}$$

A description of the SMO operation, can be expressed by the schematic of Figure 3.13.

The technique used to estimate the Back EMF is called bang-bang control and, as shown in Figure 3.13 is implemented by using a $sign(\cdot)$ function. So signals ϵ_α and ϵ_β are square waves with a low frequency component consisting in the Back EMF signal and other higher frequency harmonics generated by the switching of the $sign(\cdot)$ function. Hence, it is necessary to reject these harmonics components in order to make the estimated signal exploitable. Signals ϵ_α and ϵ_β are filtered with a low pass filter in order to reject switching harmonics. Clearly the more accurate the filtering of this signal, the better the estimation of the Back EMF. For this reason, the cut-off frequency of the low pass filters

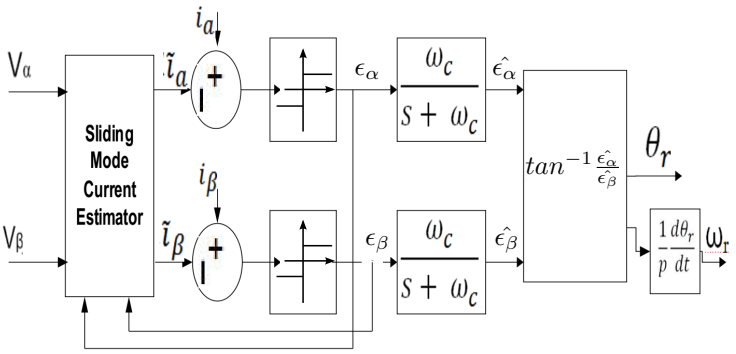

Figure 3.13: SMO estimator schematic.

is a very important parameter in order to optimize SMO based filter operation exploiting the bang-bang control.

Once BEMF signal estimations $\hat{\epsilon_\alpha}$ and $\hat{\epsilon_\beta}$ are available, it is necessary to extract rotor speed and position information from it. The expression of ϵ_α and ϵ_β is totally equivalent to ϵ_A and ϵ_B as defined in (2.6).

$$\epsilon_\alpha = \Lambda_m \omega_e \cos(\theta_e), \tag{3.25}$$

$$\epsilon_\beta = \Lambda_m \omega_e \cos(\theta_e - \frac{\pi}{2}). \tag{3.26}$$

They are two sinusoidal waveform, shifted of $\frac{\pi}{2}$ and the argument of the sinus is the electrical angle θ_e. It can be extracted from the two signals as:

$$\hat{\theta_e} = -tan^{-1}\left(\frac{\hat{\epsilon_\alpha}}{\hat{\epsilon_\beta}}\right). \tag{3.27}$$

As a consequence the electrical speed, can be computed as the time derivative of the estimated rotor position:

$$\hat{\omega}(t) = \frac{\hat{\theta_e}(t)}{dt}. \tag{3.28}$$

Since the BEMF signals are estimated thanks to the SMO observer of Figure 3.13, the chattering due to the $sign(\cdot)$ function introduce an unavoidable noise which makes this operation extremely inefficient. The estimation process can consequently be performed thanks to a PLL as the one in Figure 3.14[7]. The PLL guarantees good tracking performances to signal frequency and phase and it is robust facing system disturbances. The following Δe signal is obtained by processing the output of the SMO observer:

$$\Delta e = -\hat{\epsilon_\alpha}\sin(\hat{\theta_e}) - \hat{\epsilon_\beta}\cos(\hat{\theta_e}). \tag{3.29}$$

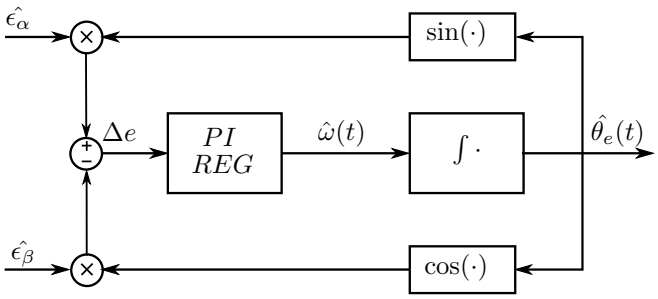

Figure 3.14: PLL schematic for rotor speed and position extraction.

By substituting (3.26) in (3.29) the following expression is obtained:

$$\begin{aligned}\Delta e &= \Lambda_m \omega_e \cos(\theta_e)\sin(\hat{\theta_e}) - \Lambda_m \omega_e \sin(\theta_e)\cos(\hat{\theta_e}),\\ &= -\Lambda_m \omega_e \sin(\hat{\theta_e} - \theta_e).\end{aligned} \tag{3.30}$$

Where ω_e and θ_e are respectively electrical speed and position, $\hat{\omega_e}$ and $\hat{\theta_e}$ are the estimated ones. When $\hat{\theta_e} - \theta_e < \frac{\pi}{6}$, it is possible to approximate $\sin(\hat{\theta_e} - \theta_e) \approx \hat{\theta_e} - \theta_e$. By minimizing the Δe signal, the electrical position estimation error is also minimized. It is therefore necessary to operate an error rejection on Δe to do it. This is achieved with a PI controller as shown in 3.14.

The PLL schematic represented in 3.14 can be simplified in order to analyze its operation as shown in 3.15. The transfer function of Figure 3.15 is:

$$G_c(s) = \frac{\hat{\theta_e}}{\theta_e} = \frac{KK_p s + KK_i}{s^2 + KK_p s + KK_i}, \tag{3.31}$$

concerning the error transfer function:

$$G_e(s) = \frac{s^2}{s^2 + KK_p s + KK_i}. \tag{3.32}$$

At constant speed, electrical position θ_e is a ramp function, therefore the steady-state error of the (3.32) converges to zero asymptotically:

$$\Delta e(\infty) = \lim_{s\to 0} s\Delta e(s) = \lim_{s\to 0} \frac{s}{s^2 + KK_p s + KK_i} = 0. \tag{3.33}$$

Concerning BEMF signal estimation, a problem associated with the bang-bang control described above is the fact that phase delay introduced by low pass filtering the estimated BEMF is also present in rotor position estimation. Closed loop motor control can not be operated if a phase delay is superposed to position estimation. For this reason, it is necessary to achieve the right trade off between rejected chattering and signal delay. Possible solutions, are the introduction of an additional phase compensation to obtain the exact rotor position and the use of a variable cut-off frequency filter in order to limit the introduced delay

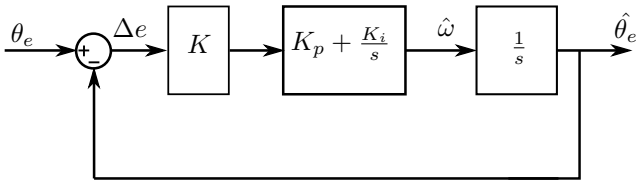

Figure 3.15: Equivalent PLL schematic.

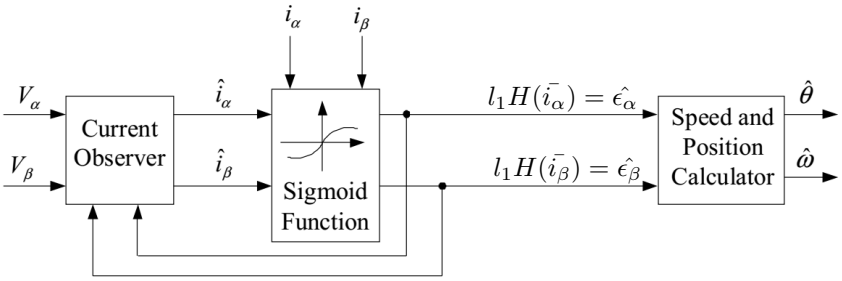

Figure 3.16: SMO estimator schematic with sigmoid instead if $sign(\cdot)$ function.

when the motor operating speed is increased. Other strategies which can be exploited in order to reduce the unwanted chattering in the back EMF waveforms include the use of an asymptotic observer [50] or the substitution of the $sign(\cdot)$ function with a sigmoid function [51]. The replacement of the $sign(\cdot)$ function with a continuous approximation near the sliding surface, is useful to reduce the generation of high frequency harmonics while obtaining a good estimation of the BEMF signals. Hence there is no need to low pass filtering the signal and, as a consequence, to phase compensate the estimated position signal. The resulting estimated signal indeed can be directly processed by the PLL and no filter generated delay is added. The approach which has been adopted in this work makes use of a sigmoid function as shown in Figure 3.16. The expression of this function is formulated in (3.34):

$$\begin{bmatrix} H(\bar{i_\alpha}) \\ H(\bar{i_\beta}) \end{bmatrix} = \begin{bmatrix} \left(\frac{2}{1+exp(-a\bar{i_\alpha})}\right) - 1 \\ \left(\frac{2}{1+exp(-a\bar{i_\beta})}\right) - 1 \end{bmatrix}, \tag{3.34}$$

where a is a positive constant and it can be tuned in order to adjust the slope of the sigmoid function.

3.3 High Frequency Injection Based Position Estimation Techniques

Fundamental model based sensorless estimation methods operate by controlling the fundamental excitation (the motor driving signal) and by estimating the BEMF of the machine. Although they work successfully at medium and high rotor speeds, they fail at very low speed. Indeed, the rotor state information, is due to the BEMF signal, whose amplitude and frequency is proportional to the rotational speed. As a consequence, as the motor speed reduces, also the magnitude and frequency of the induced motor voltage does, causing a loss of information. Hence, with these methods, it is not possible to perform a position control or to run applications requiring operation at low speeds or standstill.

For these reasons, High Frequency Current Injection based control techniques have been investigated in order to operate PMSM in a wider range of speed thus covering special needs such as vehicle propulsion system diagnostics and very low operational speed. They are based on motor anisotropies and they are referred to as signal injection methods, in which a second excitation signal is injected into the motor winding to track the saliency of the motor. The rotor spatial saliencies of permanent magnet machines could derive from the rotor anisotropies (generally IPM - Internal Permanent Magnet motors) or from the saturation induced by the rotor permanent magnets in the stator iron (generally SPM - Surface Permanent Magnet motors). By the way, there is a range of motors in the middle which exploits surface mounted permanent magnets, still showing rotor anisotropies. The work of this PhD thesis, was mainly focused on the improvement of the MARTA AUV which exploits the BlueRobotics T200 described in subsection 6.2.1. These motors are SPM type, as a consequence the methods that have been investigated were selected to be suitable for these kind of machines.

Rotor saliencies are generally estimated through high frequency voltage components which are either due to the PWM phase excitation or to an injected signal superposed to the fundamental excitation. The high frequency components are not meant to influence the electromagnetic torque, although from their interaction with the motor spatial saliencies an information about the rotor position could be extracted. Indeed phase inductances vary during rotor revolution with respect to the fundamental excitation [52]. Signal injection methods essentially monitor this variation through voltage and/or current measurements on the three phases.

Most of SPM motors show a single dominant anisotropy at each pole pair caused by the magnet generated magnetic field and, in the corresponding direction, the stator iron is saturated[52]; hence the synchronous dq reference frame is aligned with it, the d-axis (described in section 2.2) coinciding with the stator most saturated region.

High frequency signal is referred to as a carrier if it is periodical with respect to time. There are two main families of high frequency carriers: rotating car-

rier and pulsating carrier. It is possible either to inject a voltage and monitor the current or to inject a current and to monitor the voltage. By the way, a voltage control loop has better performances in terms of bandwidth and, concerning position estimation, using a current measured carrier to extract position information guarantees a better rejection to nonlinear inverter effects [8]. So in general a voltage carrier injection is operated. Concerning rotating carrier methods, the rotor position is tracked by generating a saliency image that directly highlights rotor position. For pulsating carrier methods, the location of the magnetic axis is estimated by extracting an error signal between the injection (estimated) angle and the magnetic axis itself and by minimizing it.

When operating with HFCI techniques, some approximations of the PMSM model explained in chapter 1 are useful. Starting from the two components stationary reference frame of (2.17):

$$\begin{bmatrix} V_\alpha \\ V_\beta \end{bmatrix} = \left[R^s\right] \begin{bmatrix} i_\alpha \\ i_\beta \end{bmatrix} + \frac{d}{dt}\left[L^s\right] \begin{bmatrix} i_\alpha \\ i_\beta \end{bmatrix} + \omega_e \Lambda_m \begin{bmatrix} -\sin\theta_e \\ \cos\theta_e \end{bmatrix}, \tag{3.35}$$

it is possible to hypothesize a very low motor operating speed. Hence ω_e can be approximated to zero. Furthermore, if the system is excited with a frequency which is much higher than the motor fundamental frequency, it is possible to neglect resistive contribution. Equation (3.35) becomes:

$$\begin{bmatrix} V_\alpha \\ V_\beta \end{bmatrix} = \frac{d}{dt}\left[L^s\right] \begin{bmatrix} i_\alpha \\ i_\beta \end{bmatrix}, \tag{3.36}$$

which can be solved with respect to the currents i_α and i_β by reversing the inductances matrix. L^s has the following expression:

$$\begin{aligned} L^s &= \begin{bmatrix} L_\alpha & L_{\alpha\beta} \\ L_{\beta\alpha} & L_\beta \end{bmatrix} \\ &= \begin{bmatrix} \frac{1}{2}\left[(L_q + L_d) + (L_q - L_d)\cos(2\theta_e)\right] & \frac{1}{2}\left[(L_d - L_q)\sin(2\theta_e)\right] \\ \frac{1}{2}\left[(L_d - L_q)\sin(2\theta_e)\right] & \frac{1}{2}\left[(L_q + L_d) - (L_q - L_d)\cos(2\theta_e)\right] \end{bmatrix}. \end{aligned} \tag{3.37}$$

The expression of L^s is simplified by a transformation involving a change of variables; the following parameters are introduced:

$$L_0 = \frac{1}{2}(L_q + L_d), \tag{3.38}$$

$$L_1 = \frac{1}{2}(L_q - L_d). \tag{3.39}$$

$$\tag{3.40}$$

Equation (3.36) becomes:

$$\begin{bmatrix} V_\alpha \\ V_\beta \end{bmatrix} = \frac{d}{dt} \begin{bmatrix} L_0 + L_1\cos(2\theta_e) & L_1\sin(2\theta_e) \\ L_1\sin(2\theta_e) & L_0 - L_1\cos(2\theta_e) \end{bmatrix} \begin{bmatrix} i_\alpha \\ i_\beta \end{bmatrix}. \tag{3.41}$$

The expression can be easily solved with respect to the currents:

$$\begin{aligned}\begin{bmatrix} i_\alpha \\ i_\beta \end{bmatrix} &= \begin{bmatrix} L_\alpha & L_{\alpha\beta} \\ L_{\beta\alpha} & L_\beta \end{bmatrix}^{-1} \int \begin{bmatrix} V_\alpha \\ V_\beta \end{bmatrix} dt \\ &= \frac{1}{L_0^2 - L_1^2} \begin{bmatrix} L_0 - L_1\cos(2\theta_e) & -L_1\sin(2\theta_e) \\ -L_1\sin(2\theta_e) & L_0 + L_1\cos(2\theta_e) \end{bmatrix} \begin{bmatrix} \lambda_\alpha \\ \lambda_\beta \end{bmatrix}.\end{aligned} \tag{3.42}$$

Where λ_α and λ_β are the components of the stator generated flux. Equation (3.42) can be expressed in synchronous reference frame by applying the Park Transformation:

$$\begin{bmatrix} i_d \\ i_q \end{bmatrix} = \frac{1}{L_0^2 - L_1^2} \begin{bmatrix} L_0 + L_1 & 0 \\ 0 & L_0 - L_1 \end{bmatrix} \begin{bmatrix} \lambda_d \\ \lambda_q \end{bmatrix}. = \frac{1}{L_q L_d} \begin{bmatrix} L_q & 0 \\ 0 & L_d \end{bmatrix} \begin{bmatrix} \lambda_d \\ \lambda_q \end{bmatrix}. \tag{3.43}$$

3.3.1 Rotating Carrier High Frequency Injection

Methods exploiting a high frequency rotating carrier injection operate a scan of the circumferential profile of the machine magnetic anisotropy. This involves a characterization of the spatial displacement of the anisotropy which represents the rotor position information.

A rotating carrier on the stationary reference frame with amplitude V_i and pulsation ω_i can be expressed as:

$$\begin{bmatrix} V_\alpha \\ V_\beta \end{bmatrix} = V_i \begin{bmatrix} \sin\omega_i \\ \cos\omega_i \end{bmatrix} = V_i e^{j\omega_i t}. \tag{3.44}$$

To substitute this expression in (3.43) it is necessary to integrate it and apply a Park Transformation in the rotor reference frame. The expression of the stator generated flux in rotor reference frame is:

$$\begin{bmatrix} \lambda_d \\ \lambda_q \end{bmatrix} = \frac{V_i}{\omega_i - \omega_r} \begin{bmatrix} -\cos(\theta_i - \theta_r) \\ \sin(\theta_i - \theta_r) \end{bmatrix}. \tag{3.45}$$

Hence (3.43) becomes:

$$\begin{bmatrix} i_d \\ i_q \end{bmatrix} = \frac{V_i}{L_q L_d(\omega_i - \omega_r)} \begin{bmatrix} -L_q\cos(\theta_i - \theta_r) \\ L_d\sin(\theta_i - \theta_r) \end{bmatrix}. \tag{3.46}$$

On the motor phase terminals the stationary reference frame currents are available, thus expression (3.46) hast to be transformed in stator coordinates thanks to the reverse Park Transformation:

$$\begin{bmatrix} i_\alpha \\ i_\beta \end{bmatrix} = \frac{V_i}{L_q L_d(\omega_i - \omega_r)} \begin{bmatrix} L_d\sin(\theta_r)\cos(\theta_i - \theta_r) + L_q\cos(\theta_r)\sin(\theta_i - \theta_r) \\ -L_d\cos(\theta_r)\cos(\theta_i - \theta_r) + L_q\sin(\theta_r)\sin(\theta_i - \theta_r) \end{bmatrix}. \tag{3.47}$$

For a better understanding of the problem, (3.47) is expressed in exponential form using L_0 and L_1:

$$\begin{bmatrix} i_\alpha \\ i_\beta \end{bmatrix} = \frac{V_i}{2(L_0^2 - L_1^2)(\omega_i - \omega_r)} \begin{bmatrix} \left\{ L_0 e^{j(\theta_i)} + L_1 e^{j(\theta_i - 2\theta_r)} \right\} - \left\{ L_0 e^{-j(\theta_i)} + L_1 e^{-j(\theta_i - 2\theta_r)} \right\} \\ \left\{ L_0 e^{j(\theta_i)} - L_1 e^{j(\theta_i - 2\theta_r)} \right\} + \left\{ L_0 e^{-j(\theta_i)} - L_1 e^{-j(\theta_i - 2\theta_r)} \right\} \end{bmatrix}. \tag{3.48}$$

Expression (3.48) in turn, can be expressed as a single rotating vector $\boldsymbol{i}^s$:

$$\boldsymbol{i}^s = i_\alpha + j i_\beta = -j \frac{V_i}{(L_0^2 - L_1^2)(\omega_i - \omega_r)} \left[L_0 e^{j(\theta_i)} - L_1 e^{-j(\theta_i - 2\theta_r)} \right]. \tag{3.49}$$

The current rotating vector in stator reference frame, is characterized by two rotating sequences. The positive sequence of the injected signal is:

$$\boldsymbol{i}_p^s = -j \frac{V_i}{(L_0^2 - L_1^2)(\omega_i - \omega_r)} L_0 e^{j(\theta_i)}, \tag{3.50}$$

while the negative sequence is given by:

$$\boldsymbol{i}_n^s = j \frac{V_i}{(L_0^2 - L_1^2)(\omega_i - \omega_r)} L_1 e^{-j(\theta_i - 2\theta_r)}. \tag{3.51}$$

The positive sequence does not contain any interesting information about rotor position and can be filtered off. The negative one does but it is modulated at the injection frequency. As a consequence, it is necessary to operate a Park Transformation into a frame rotating at the injected signal frequency:

$$\begin{aligned} \boldsymbol{i}_p^s &= -j \frac{V_i}{(L_0^2 - L_1^2)(\omega_i - \omega_r)} L_0 e^{j(\theta_i)} * e^{j(\theta_i)} = -j \frac{V_i}{(L_0^2 - L_1^2)(\omega_i - \omega_r)} L_0 e^{j(2\theta_i)}, \\ \boldsymbol{i}_n^s &= j \frac{V_i}{(L_0^2 - L_1^2)(\omega_i - \omega_r)} L_1 e^{-j(\theta_i - 2\theta_r)} * e^{j(\theta_i)} = j \frac{V_i}{(L_0^2 - L_1^2)(\omega_i - \omega_r)} L_1 e^{j(2\theta_r)}. \end{aligned} \tag{3.52}$$

The high frequency component of the positive sequence is easily canceled by operating a low pass filtering. Rotor position can instead be extracted thanks to an observer.
The method although has not been implemented in this work because it presents the following drawbacks [38]:

- Load dependent error compensation is needed;
- Poor signal to noise ratio;
- Not efficient for low saliency machines such as SPM motors;
- A load model is necessary for the implementation of the observer. An a priori knowledge of the working conditions is thus necessary and load uncertainties can compromise the control efficiency.

3.3.2 Pulsating Carrier High Frequency Injection

The principle of operation of Pulsating Carrier Injection techniques is totally similar to the rotating carrier one; a high frequency carrier, is injected by adding it to the fundamental driving components and the resulting signal measured on the motor phases gets modulated by the existing rotor anisotropies. In this case although the injected signal, rotates at the estimated rotor frequency. In this case although, rotor position estimation, is obtained by rejecting the error between the estimated ad actual rotor position. Such error signal is extracted by processing current or voltage phase measurements.
Two similar pulsating carrier high frequency injection techniques have been considered.

A pulsating carrier in the synchronous reference frame is injected along the d-axis in order not to generate any torque. It can be expressed as:

$$\begin{bmatrix} V_d \\ V_q \end{bmatrix} = V_i \begin{bmatrix} \cos(\omega_i t) \\ 0 \end{bmatrix}. \tag{3.53}$$

Although to inject this carrier along the d-axis, it is necessary to know rotor orientation with respect to the stator. Hence the pulsating carrier is injected along an estimated rotor position $\hat{\theta_e}$. The Park Transformation of equation (3.42) along the estimated synchronous reference frame returns the following expression:

$$\begin{bmatrix} i_d^e \\ i_q^e \end{bmatrix} = \frac{1}{L_0^2 - L_1^2} \begin{bmatrix} L_0 - L_1\cos(2\tilde{\theta_e}) & -L_1\sin(2\tilde{\theta_e}) \\ -L_1\sin(2\tilde{\theta_e}) & L_0 + L_1\cos(2\tilde{\theta_e}) \end{bmatrix} \begin{bmatrix} \lambda_d^e \\ \lambda_d^e \end{bmatrix}, \tag{3.54}$$

where $\tilde{\theta_e} = \theta_e - \hat{\theta_e}$. The high frequency component of the stator generated flux in the synchronous reference frame is obtained by time integrating equation (3.53):

$$\begin{bmatrix} \lambda_d \\ \lambda_q \end{bmatrix} = \frac{V_i}{\omega_i} \begin{bmatrix} \sin(\omega_i t) \\ 0 \end{bmatrix}. \tag{3.55}$$

By substituting (3.55) in equation (3.54) the following expression is obtained:

$$\begin{bmatrix} i_d^e \\ i_q^e \end{bmatrix} = \frac{V_i}{\omega_i(L_0^2 - L_1^2)} \begin{bmatrix} L_0 - L_1\cos(2\tilde{\theta_e}) \\ -L_1\sin(2\tilde{\theta_e}) \end{bmatrix} \sin(\omega_i t). \tag{3.56}$$

Under the assumption that the main rotor saliency lies in the direction of the rotor generated flux, the two current components i_d^e and i_d^e contain information about the error between the estimated and the actual rotor flux direction. Basically the position estimation technique consists in injecting a certain signal along the d-axis and minimizing the components of the injected signal along the q-axis [8]. The d and q axis are indeed defined orthogonal. As a consequence, when a sinusoidal voltage signal is injected along the estimated direction of the d-axis a cosinusoidal magnetic flux density distribution is established along the

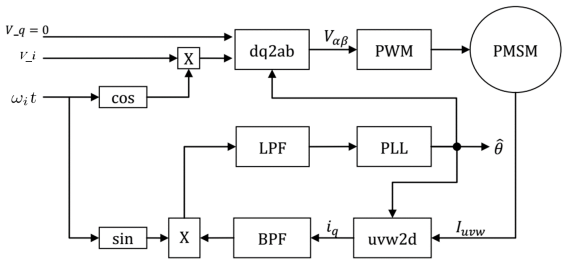

Figure 3.17: High frequency Pulsating Carrier based position estimation scheme according to [8].

same direction; if nothing interacts with the generated magnetic flux density distribution, the flux linkage with the q-axis inductance is zero. This happens when the rotor field is parallel with the estimated d-axis; in case there is an angular displacement between the rotor permanent magnet field and the estimated d-axis, the stator flux is partially deflected and this causes a flux linkage with the q-axis. According to Lenzs law, the oscillating magnetic field through the q-axis induces a BEMF whose amplitude is proportional to the derivative of the flux linkage and, in this case, to the angular estimation error. Hence by minimizing the injected signal components induced along the q-axis, also the displacement between the estimated and actual d-axis is minimized. The main difference among the various signal injection methods for rotor position estimation concerns the processing technique of the currents in (3.56). According to [9] in order to extract this information the measured q-axis current component has to be first separated from the driving components at the fundamental frequency, thanks to a bandpass filter centered on ω_i. The signal is then demodulated at a frequency equal to the injection one:

$$i_q^e \cdot 2 \cdot \sin(\omega_i t) = \frac{-L_1 V_i}{\omega_i (L_0^2 - L_1^2)} \sin(2\tilde{\theta_e})(1 - \cos(2\omega_i t)). \tag{3.57}$$

The demodulated signal contains a high frequency component at twice the injected carrier frequency which is low pass filtered in order to eliminate it.

$$LPF(i_q^e \cdot 2 \cdot \sin(\omega_i t)) \approx \frac{-L_1 V_i}{\omega_i (L_0^2 - L_1^2)} \sin(2\tilde{\theta_e})\Big|_{\tilde{\theta_e}<<1} \approx K_{err}\tilde{\theta_e}, \tag{3.58}$$

where $K_{err} = 2\frac{-L_1 V_i}{\omega_i (L_0^2 - L_1^2)}$. The result is an error signal proportional to the difference between the estimated rotor position $\hat{\theta_e}$ and the actual one θ_e. Hence by operating feedback error rejection a rotor position estimation is performed.

Error rejection is performed thanks to a Phase Locked Loop (PLL) block as shown in Figure 3.15. It is composed by a PI controller followed by an integrator. As visible in Figure 3.17 the estimated position is then fed back to the

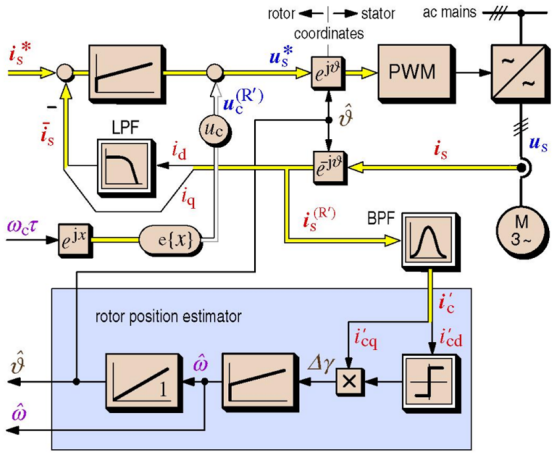

Figure 3.18: High frequency Pulsating Carrier based position estimation scheme according to [8].

system to perform direct and reverse Park Transformation and, if necessary, to perform speed or position control. As explained, for signal demodulation, this technique exploits the injected signal frequency in order to extract the position information contained in the signal expressed in (3.54). Although the delays and non-linearities introduced by the inverter degrade the performances of the estimation technique especially during demodulation phase. Another way to extract the error position information from the estimated synchronous reference frame currents (3.54) is explained in [8]. The main difference with respect to the technique described in [9] is that in this case the position information contained in the signal expressed in (3.54) is extracted by using the d-component measured current carrier. This makes the position estimation less sensitive facing nonlinear inverter effects since both the position information and the reference signal undergo the delays and nonlinear distortions of the inverter. Also in this case, the i_q^e and i_d^e components are separated from the driving components at the fundamental frequency, thanks to a bandpass filter centered on ω_i. The filtered signal i_q^e is then demodulated by multiplying it times $sign(i_d^e)$.

$$K_{err}\tilde{\theta}_e \approx BPF(i_q^e \cdot sign(i_d^e)). \tag{3.59}$$

The resulting signal is proportional to the difference between the estimated and actual rotor angle. The theory under this position signal extraction technique is not described here for brevity and it is reported in [8].

A problematic aspect of this position estimation technique, is that once the d-axis (the direction of rotor magnet in synchronous reference frame) orientation has been estimated, it is not automatically defined if it corresponds to the positive or negative flux direction. Hence it is not possible to operate

position or speed control in the desired direction of rotation. Consequently a preliminary flux polarity identification routine has to be executed before operating the motor. This information can be gathered by exploiting the stator iron magnetization. Motor spatial saliency indeed influences the L_d value and it is determined by stator iron magnetization. If a current is imposed along the d-axis, no resulting torque is generated. However it influences iron magnetization increasing or decreasing it depending on the flux polarity. In brief, if current and rotor flux directions are the same, the magnetization of the stator iron will increase driving the direct axis inductance L_d into deeper saturation [8]. The inductance value is thus reduced. On the contrary, if current and rotor directions are opposite, stator iron saturation will decrease while increasing the value of L_d. This phenomena can be exploited by injecting two opposite direction voltage pulses along the d-axis. If the amplitude and width of these voltage pulses is identical they will generate a corresponding current pulse, whose amplitude is influenced by L_d. The current pulse having the higher amplitude indicates the positive direction of the rotor axis.

Rotor polarity identification routine can be performed by previously activating the high frequency signal injection. The algorithm will consequently estimate rotor orientation making possible to inject two opposite voltage pulses along the d-axis. The resulting current peaks can thus be measured and compared. However, the amplitude difference between the two peaks could be small depending on motor characteristics. Consequently, errors can be made while detecting the highest peak, also due to noise superposed to the current measured signal, sample resolution, electrical constant of motor, sample frequency etc. According to [9] and [8] the identification process of the highest current peak is made by directly processing the current value. In [9] it is proposed a robust method to identify the highest current peak consisting in estimating the current attenuation gradient (due to L_d) during the positive and negative current pulses. In Figure 3.19 the behavior of the current through an inductance as a consequence of two opposite voltage pulses is shown. The blue line is related to a constant inductance, the pink one represents the behavior of a variable value inductance.

Concerning the rotor direction identification problem, in Figure 3.19 the pink line represents the case in which the estimated direction coincides with the flux one, indeed $|I_{pk+}| > |I_{pk-}|$. During the rising pulse edge (positive or negative), the current attenuation behavior is represented by:

$$i_d = \frac{V_{pk}}{R_s}(1 - e^{-\frac{R_s}{L_d}t}), \tag{3.60}$$

where V_{pk} is the peak amplitude. During the falling pulse edge instead:

$$i_d = \frac{V_{pk}}{R_s}e^{-\frac{R_s}{L_d}t}, \tag{3.61}$$

The behavior of (3.61) during a short time interval can be approximated as:

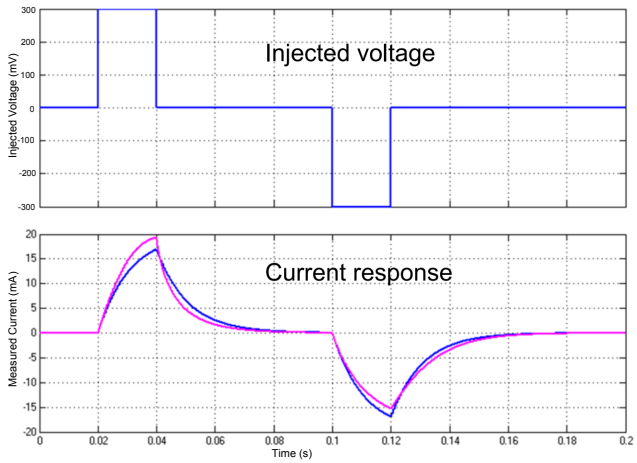

Figure 3.19: Current pulse attenuation through an inductance. Blue: constant inductance, Pink: variable inductance [9].

$$i_d(n+1) = i_d(n)e^{-\frac{R_s}{L_d}T_s} = Ki_d(n), \tag{3.62}$$

Where K represents the attenuation gradient and T_s is the sampling time. Hence the rotor polarity direction can be defined by identifying K during the falling edge of the positive and negative voltage pulses. However the condition $T_s << \frac{L_d}{R_s}$ has to be assumed. In the case of Figure 3.19 ($|I_{peak+}| > |I_{peak-}|$) the positive current peak will be discharged more quickly thus $K(V_{pk+}) > K(V_{pk-})$. The identification is realized through least square estimation. Given the following linear model:

$$y(n) = Kx(n), \tag{3.63}$$

The best estimation by means of least square is:

$$\hat{K}(N) = \frac{\sum_{n=1}^{N} y(n)x(n)}{\sum_{n=1}^{N} x^2(n)}, \tag{3.64}$$

where:

$$y(n) = i_d(n+1), \tag{3.65}$$
$$x(n) = i_d(n), \tag{3.66}$$
$$K = e^{-\frac{R_s}{L_d}T_s}. \tag{3.67}$$

Hence the current gradient attenuation can be performed during the fading edge of the positive and negative peak and by comparing the two results.
In order to simplify and reduce the computational costs of the direction identification algorithm while overcoming noise problems highlighted above, the authors proposed a different technique based on the integration of the current pulse signals. In this case robustness facing electrical and sampling noise is given by the low pass effect of the integration operation. Current integration is operated after the voltage pulse has been triggered for a time that equals the pulse duration. Since the I_d current could be biased due to not perfect rotor magnet symmetry, the bias component has to be sampled before peaks injection and subtracted to the integral measurement.

Chapter 4

Sensorless Control Algorithm Implementation

The selection process of a reliable motor control strategy for underwater vehicle propulsion has to be performed in order to obtain the right tradeoff among control performance, reliability, robustness facing the working conditions, simplicity and space saving. The starting point of this PhD thesis work has been the performance evaluation of the drive system initially mounted on the MARTA AUV. It was a Robbe ROXXY 2827-35 BLDC motor driver. This kind of controller has the advantage of being really cheap, reliable, and of small encumbrance. Although it does not perform any kind of speed or torque control. It is controlled through a servo signal reference which regulates the PWM duty-cycle on the three phases and the rotation direction. For this reason, the propeller speed depends on the torque which is applied to it and only a rough estimation of it can be performed. Hence it has been necessary to find a more performing alternative. Various control techniques have been tested. The selection criteria which have been taken into account were in order of importance:

- Reliability of the control system;
- Motor operating at relatively high and variable torques;
- Need to operate a speed control over a wide range of speed;
- Reduced spaces and harsh operating conditions;
- Importance of a torque and speed feedback for vehicle navigation and diagnostics.

Part of the sensorless algorithm implementation and tests have been carried out in cooperation with the Laboratory of Actuation Technology (LAT) of the Saarland University. In particular their support has concerned the design and implementation of the test bench electronics for the algorithm development and validation.

4.1 InstaSPIN^{TM}-BLDC by Texas Instruments Characteristics

The first technique that has been tested is the InstaSPIN^{TM}-BLDC by Texas Instruments. It has been chosen because it is easy to implement, and because of its robustness facing quick rotor speed variation and measurement noise. Furthermore it makes possible to perform a reliable speed measurement. The technique, described in subsection 3.1.3, can be performed by exploiting the Six Steps control technique explained in section 2.4 and it is based on the BEMF integration. This characteristic, is one of the reasons why it is so robust. Integration indeed acts like a low pass filter thus making the signal used to control the motor less noisy. Essentially it consists in performing the BEMF integration on the floating phase after a zero crossing is detected. The integration value increases until a certain threshold is reached, then the inverter switches to the next step. The threshold is set in order to perform an optimal time switching. This way, the switching is not performed according to a control logic imposed timing but according to the rotor position. This is another reason why the technique is so robust facing abrupt speed changes which could not be detected by the control logic.

The algorithm could be implemented both when driving the motor with unipolar and bipolar PWM. Using star connected motors, bipolar PWM makes the control much easier. For delta connected motors there is almost no difference. By the way, still bipolar PWM seemed easier to implement the control when trying to understand how and were to sample the BEMF and to define the optimal switching time.

The voltage waveform of a delta connected motor driven with bipolar PWM is shown in Figure 4.1. In the figure it is also highlighted the interval in which the integration on the floating phase has to be performed. It starts after the zero crossing (which means that the phase voltage reaches the same level as the star center reference voltage) and ends when the threshold integration level is reached. As explained in subsection 3.1.3 this threshold level does not depend on the speed.

For the development of the control algorithm it has been necessary to implement and test it on a motor. Hence a customized setup has been implemented; in Figure 4.2 a scheme of the control setup is shown. The complete setup is composed of a micro-controller, an interface to the micro-controller, a power supply, and a power stage as illustrated in section 5.2.

4.1.1 InstaSPIN^{TM}-BLDC: Algorithm Parameters Setup

Once the control algorithm has been implemented, parameters tuning has been performed. The first, most important parameter for motor control, is the stator induced flux threshold value. The optimal flux threshold is trimmed in order to perform optimal switching. Optimizing phases switching consists in keeping the BEMF as shown in Figure 2.8, the reason is explained in subsec-

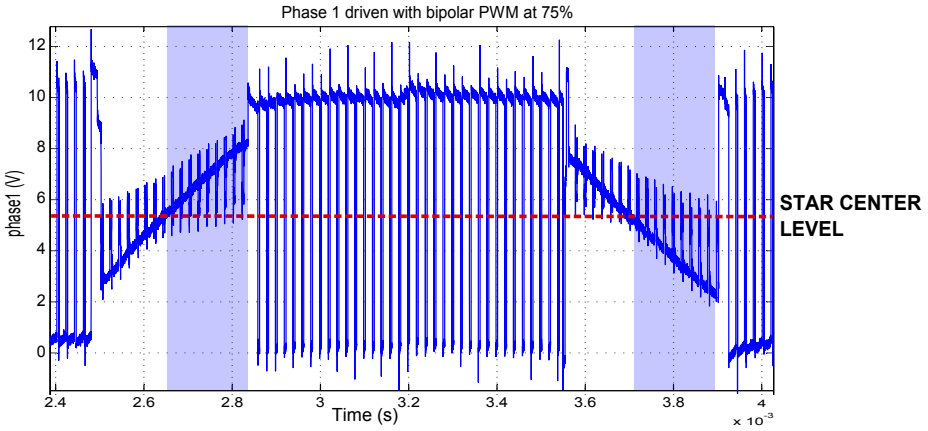

Figure 4.1: Voltage waveform with bipolar PWM.

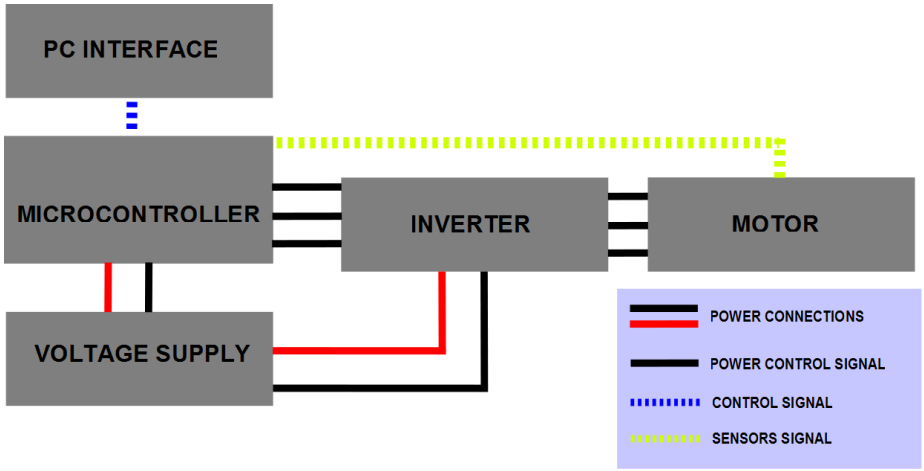

Figure 4.2: Control setup scheme.

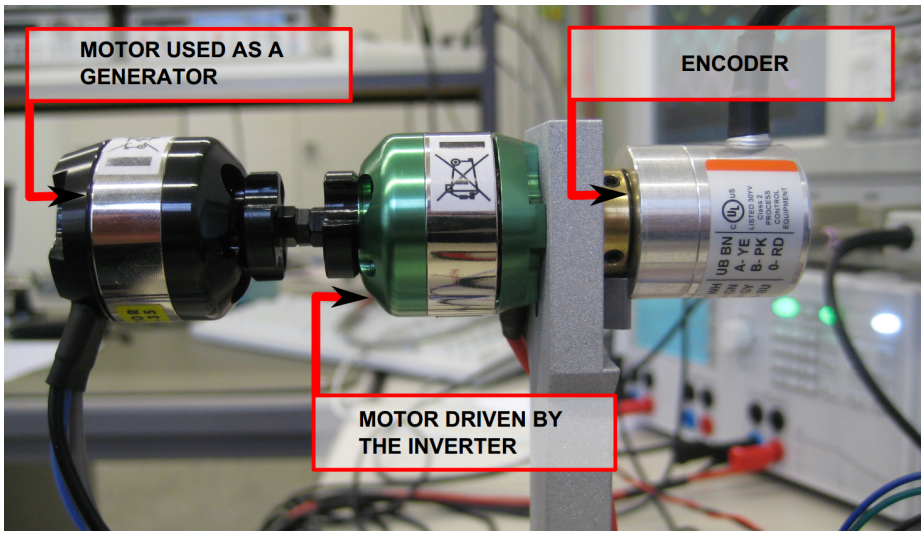

Figure 4.3: Setup for sensorless algorithm tuning.

tion 3.1.3. Initially the motor has been operated through the position feedback of an encoder as shown in Figure 4.3. Doing this, the switching position was controlled through the encoder position information. Thanks to the encoder, optimal phase switching conditions could be defined. By operating the motor in these conditions, it has been possible to measure and define the flux level when the controller has to switch from a phase to another. This level identifies the optimal flux threshold.

In Figure 4.1 it is possible to see that the integration result is not always positive but alternatively positive or negative. At each step it is necessary to define the floating phase on which performing the integration as shown in Figure 3.7. It should be noticed, by magnifying the voltage waveform, that when a phase is floating, the voltage measured on it still depends on the PWM. This is not just due to the noise superposed to the signal but it is mainly due to the switching on the other two active phases.

In Figure 4.4 it is possible to see that it depends on the PWM state. This can be easily explained considering that a delta connected motor was used for algorithm development. In this motor type two windings are connected to a single phase. For this reason, when the PWM signal is high on one phase, there will be another phase set low and the third one floating. If a single ended voltage measurement is performed, on the floating phase it is measured the BEMF induced on the low phase winding. When the PWM signal is set low instead it is measured the BEMF induced in the other one. This is illustrated in Figure 4.5. In step 1 for example phase C is floating while phases A and B switch from V_{DC} to ground according to the PWM duty cycle. When the PWM signal is set high, the phase A is connected to V_{DC} while the phase B is connected to the ground. Figure 4.5 shows that in this case (assuming that

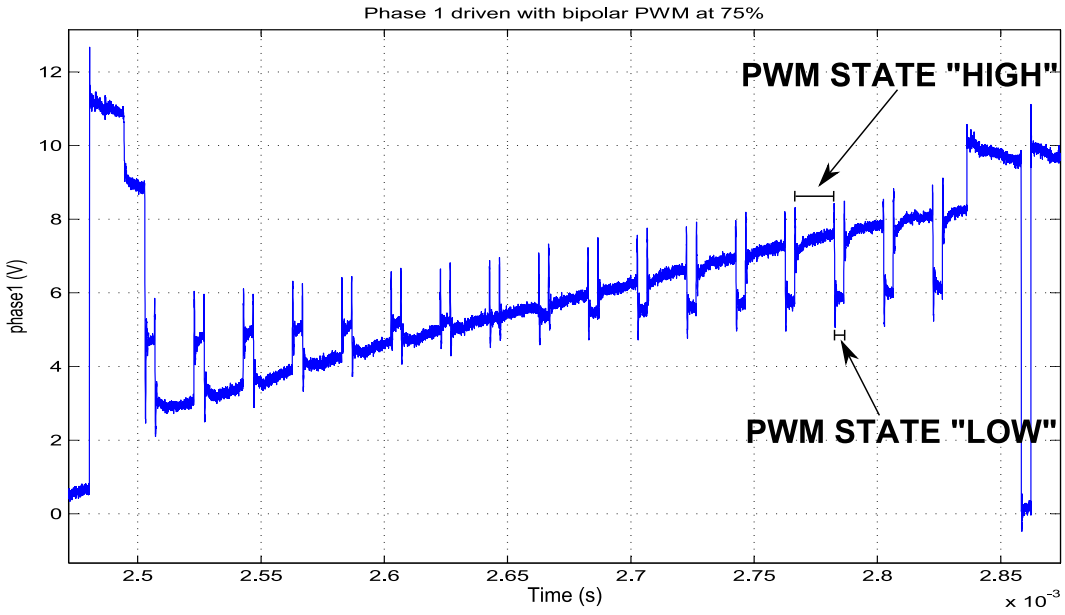

Figure 4.4: BEMF on the floating phase when PWM is set to HIGH and when it is set to LOW.

$L_B = L_C$ and $R_B = R_C$), the voltage sensed on phase C is the sum of the star center reference voltage minus BEMF induced on phase B. When PWM is set low, polarity is inverted and voltage sensed on phase C is the sum of the star center reference voltage plus BEMF induced on phase C. By the way to perform a consistent BEMF integration, just one of the two waveforms has to be sampled and according to it an opportune flux threshold has to be selected. In order do this, it is necessary to trigger the sampler at the right time selecting the right part of the PWM cycle.

4.1.2 InstaSPIN^{TM}-BLDC: Algorithm Operation

The flowchart of the algorithm is illustrated in Figure 4.6. It is divided into two main sections: the startup routine and the normal sensorless operation.

The first part of the startup routine, consist in positioning the rotor, by setting a certain phase step. This because it is necessary to set a defined mutual position between the rotor and the stator. Then the control switches to another step and starts to integrate the BEMF signal on the floating phase. When the flux threshold value is reached, the control switches to sensorless operation and

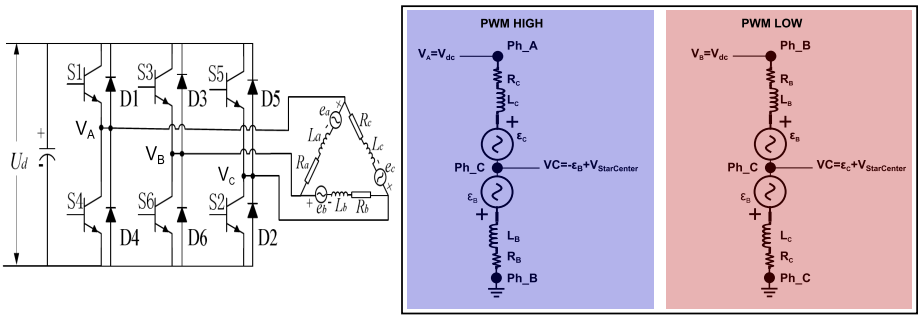

Figure 4.5: Voltage on the floating phase when PWM is set to HIGH and when it is set to LOW.

at the same time the next phase step is set. Sensorless mode consists in a loop in which, after a new step is set, the system starts to integrate on the floating phase. When the threshold is reached, the next step is set and so on. The flowchart also shows that at each step, rotor speed is measured.

4.1.3 InstaSPIN^{TM}-BLDC: Rotor Speed Estimation

As specified at the beginning of this chapter, the aim of this work was not just to design and implement a reliable control of the motor but also to perform speed and torque estimation. As explained in section 2.4, Six Steps control techniques do not allow torque control, speed control can instead be based on an empirical speed estimation. As specified in chapter 2 an entire mechanical rotation corresponds to n_p electrical rotations. Since each electrical rotation is given by 6 phase steps, the inverter has to switch $n_p \cdot 6$ times to complete the mechanical one. So each step rotates the rotor of an angle of $\frac{2\pi}{n_p \cdot 6} rad$. Hence, the speed measurement can be obtained as the ratio between the step angle width and the time between each step. It consists in measuring the time elapsed between two subsequent steps. Each time a new step is set, a timer in the control logic is started and it is reset when the next phase step is set. A time interval Δt is obtained and speed is computed according to (4.1).

$$\omega = \frac{2\pi}{n_p \cdot 6 \cdot \Delta t}. \tag{4.1}$$

Speed measurement flowchart is shown in Figure 4.7

Thanks to the InstaSPIN^{TM}technique, the speed estimation is not based on previous measurement but on the current step. This makes possible to immediately detect an abrupt speed change which is very helpful when designing a feedback control. In Figure 4.8 a comparison between encoder measured speed and the speed estimated through the sensorless technique is shown.

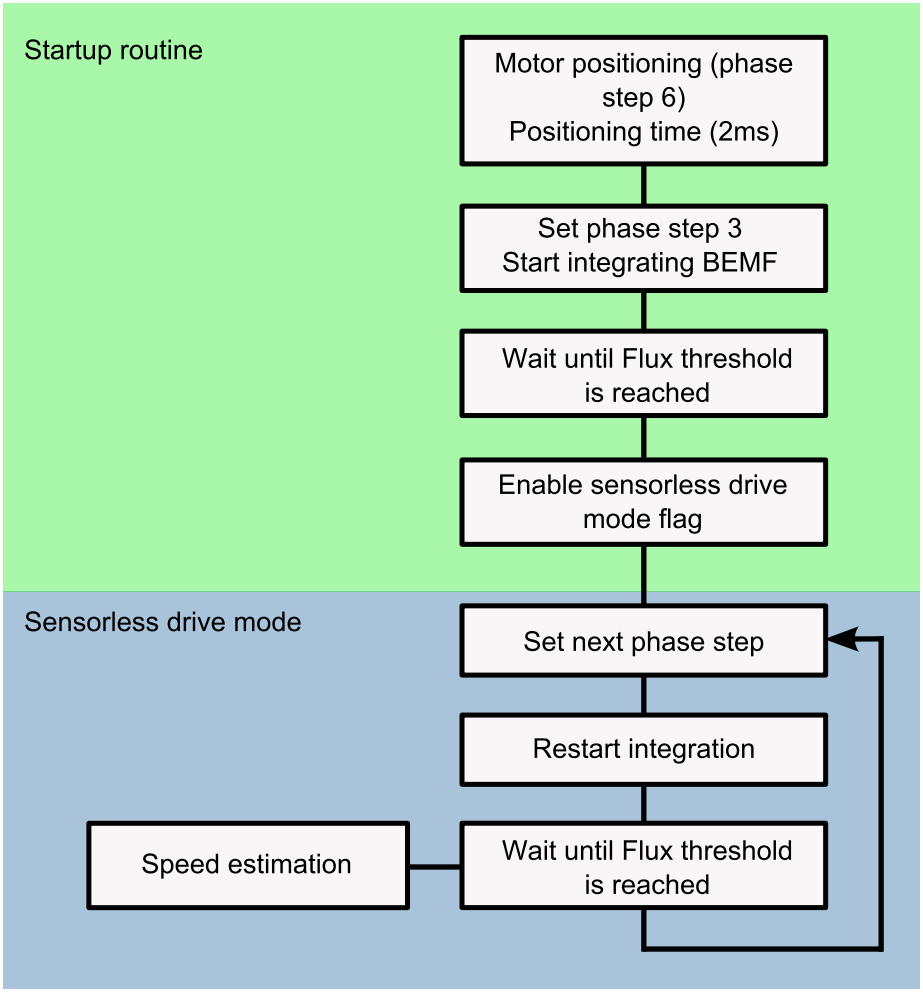

Figure 4.6: Sensorless algorithm flowchart.

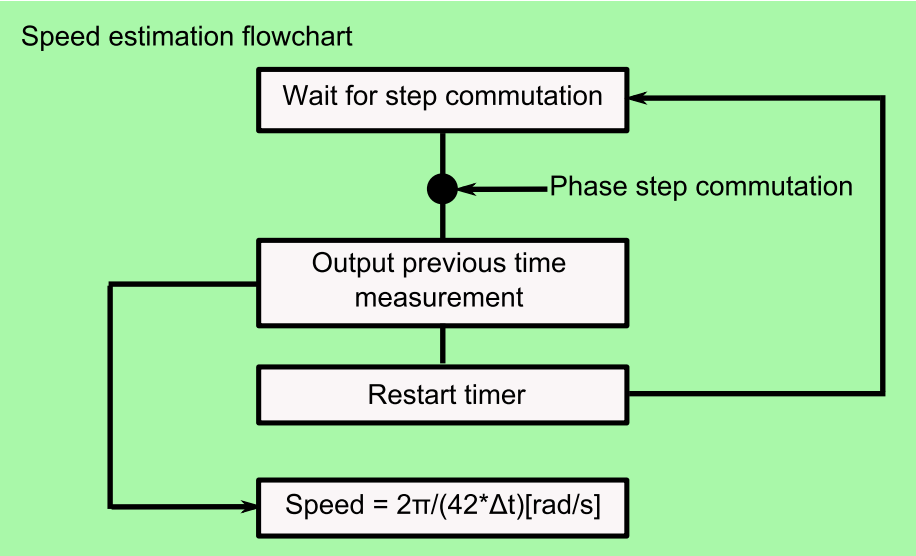

Figure 4.7: Speed estimation algorithm flowchart.

4.1.4 InstaSPIN™-BLDC: Speed Estimation Filtering

Raw signal obtained from the speed estimation technique described in subsection 4.1.3 is quite noisy especially at low speed. This is due to the fact that the phase step duration could be not homogeneous due to signal to noise ratio reduction, not perfect rotor symmetry and quantization error of the ADCs. This results in a high amplitude ripple superposed to the speed estimation. This is visible in Figure 4.9, maximum ripple is verified at low speed while by increasing the speed, the ripple diminishes.

Obviously it is not optimal to operate a feedback control with such a noisy feedback signal. For this reason it is necessary to filter the estimated speed signal that smothers it, thus making it suitable for our purposes. A possible solution is to implement a low-pass Butterworth filter which operates a smoothing of the measured signal. Speed signal has to be filtered in order to cut the high frequency noise without influencing the speed variation dynamics. Butterworth filter has the following attenuation function,

$$H(\omega) = \sqrt{1 + \left(\frac{\omega}{\omega_p}\right)^{2n}}, \tag{4.2}$$

where n is the filter order and ω_p the cutoff pulsation. So implemented the filter attenuates of 3dB at the cutoff frequency. By operating a polynomial approximation of the transfer function and by transforming it to discrete time,

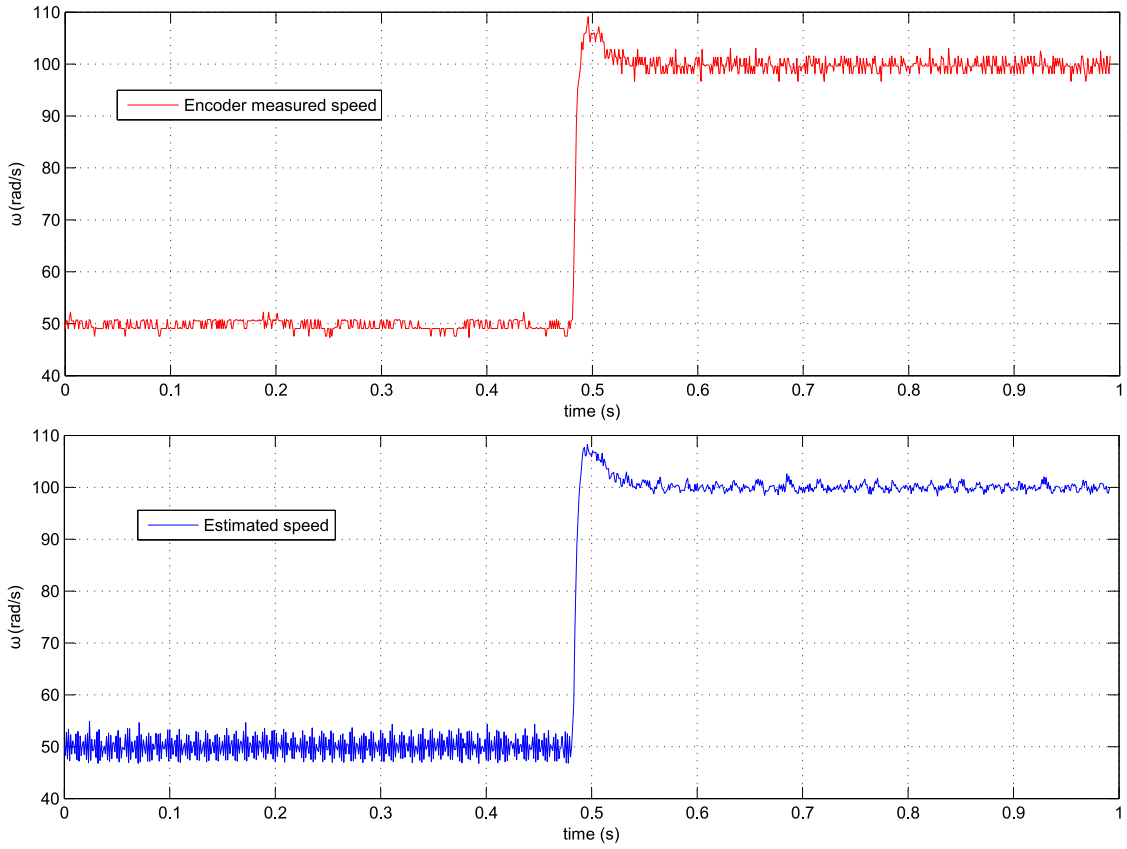

Figure 4.8: Comparison between encoder measured speed and sensorless estimation.

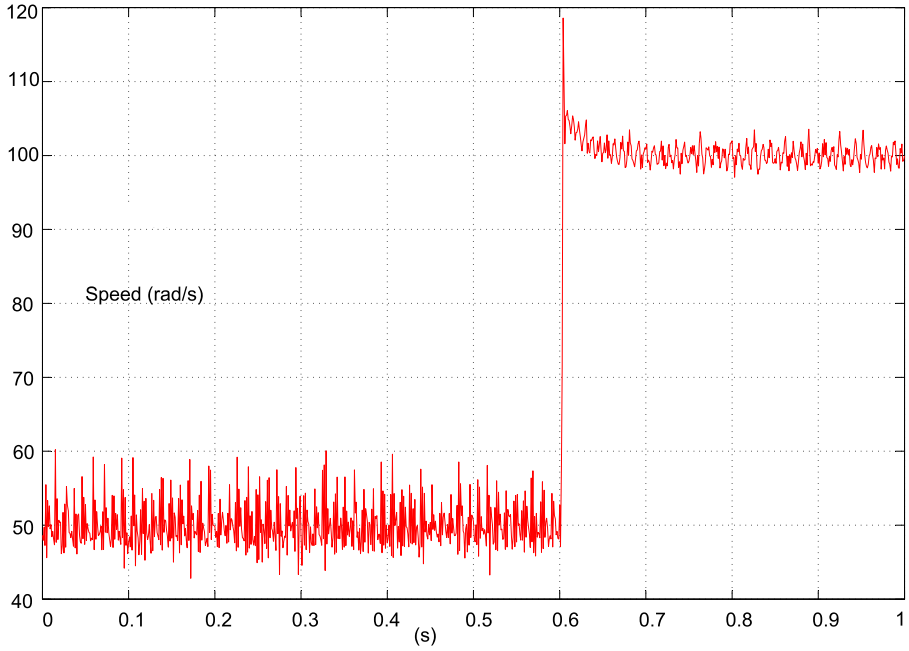

Figure 4.9: Unfiltered speed estimation signal.

$$H(z) = \frac{b_1 + b_2 z^{-1} + \cdots + b_{n-1} z^{-n}}{1 + a_2 z^{-1} + \cdots + a_{n+1} z^{-n}}. \tag{4.3}$$

$H(z)$ can be easily implemented in a micro-controller logic. To test and implement the filter on the micro controller, to decide the filter order, it has been used a Matlab script which computes the filter response to a generic sampled signal and shows it in a graph. It it is possible to set the filter order, the sampling frequency, and the cutoff frequency. The script computes the filter parameters and shows its effects on the sampled signal also by showing a Fourier transformation of the filtered signal frequency components. In Figure 4.10, 4.11 and 4.12 a comparison of the filter signal responses with a cutoff frequency of 100Hz and different filter orders is shown. The right trade-off between filter complexity and optimal response has ended being a third order filter.

4.1.5 InstaSPIN^{TM}-BLDC: Feedback Speed Control Design and Implementation

Once a speed estimation is available, it is possible to design a feedback speed controller. The control that has been implemented is a classical PI controller with feed forward. Controller input is the difference between the desired, and

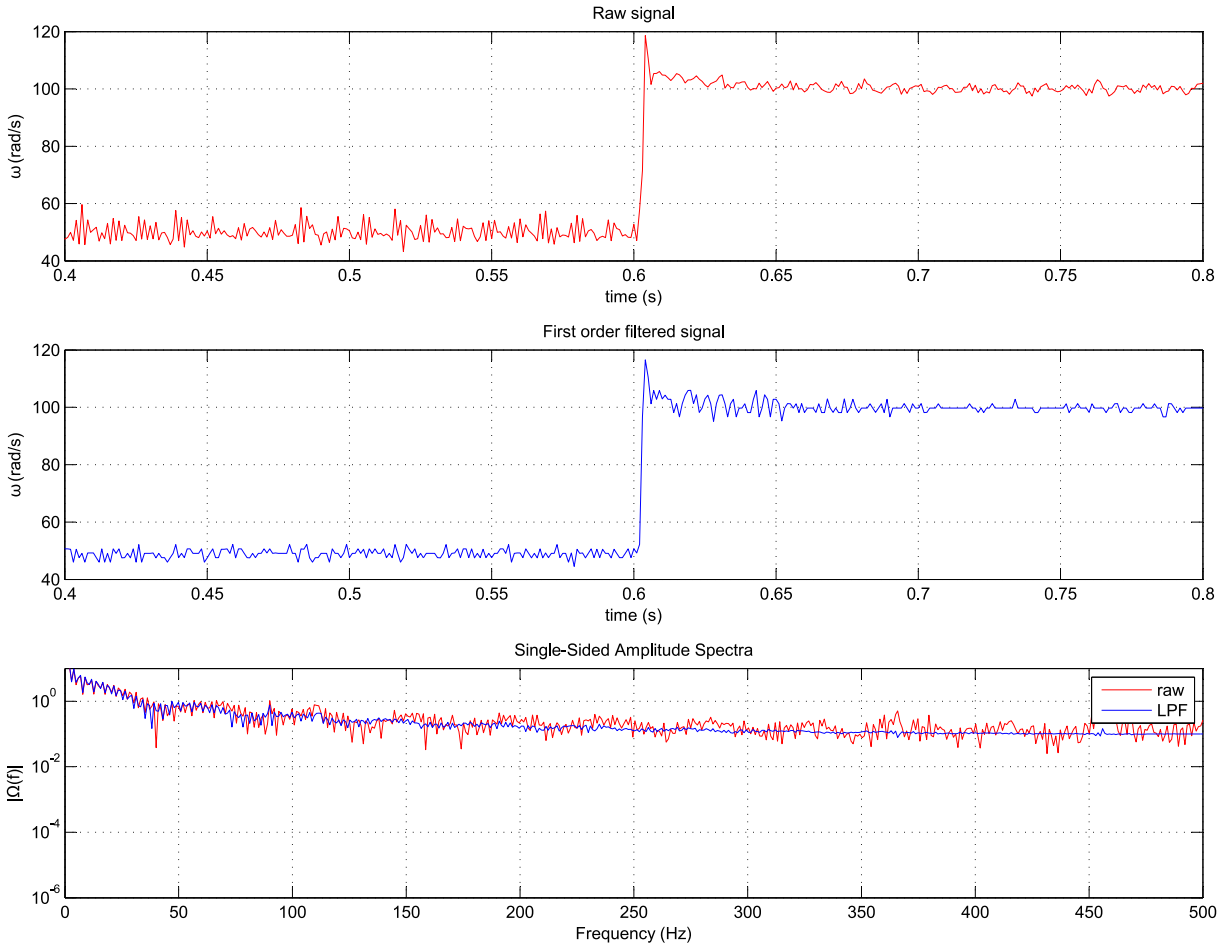

Figure 4.10: First order filtered signal.

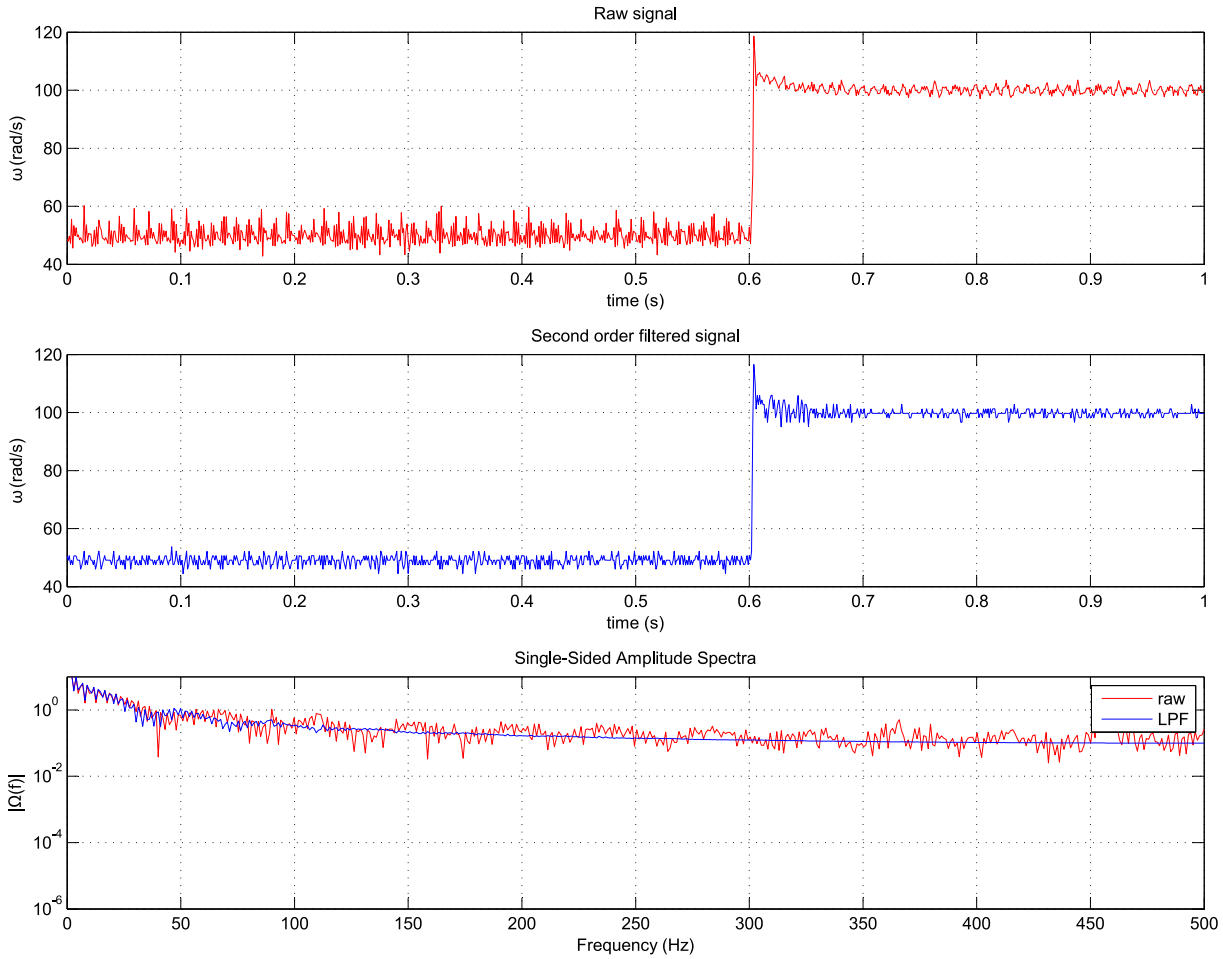

Figure 4.11: Second order filtered signal.

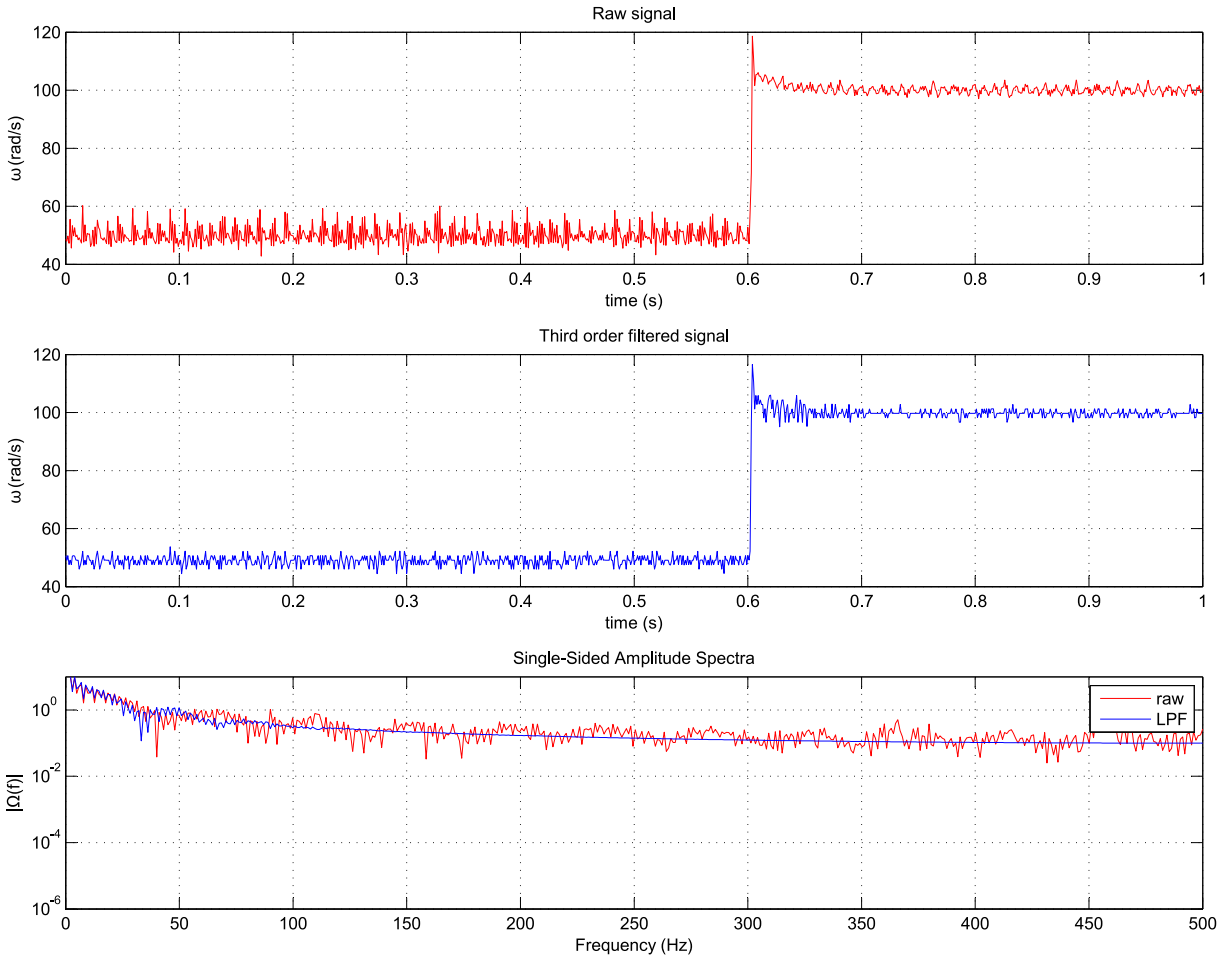

Figure 4.12: Third order filtered signal.

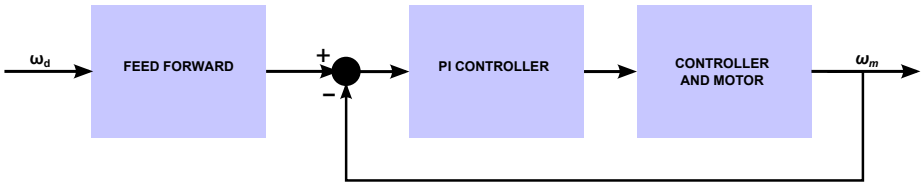

Figure 4.13: Feedback control scheme.

the measured speed, obtained through the sensorless control. Control scheme is shown in Figure 4.13

As specified at the beginning of this chapter, the feedback control provides a tracking of the reference speed signal. It is necessary when a precise speed control is needed not just in steady condition but also when varying the speed. In an open loop control indeed, speed would be influenced by environmental condition, battery level, and motor characteristics thus resulting in an inaccurate control. By operating a constant rejection of the error between the actual speed and the desired one, the control adapts dynamically to those factors that influence the rotor speed. Feedback control scheme is illustrated in Figure 4.13, the speed error between the measured speed and the reference speed is rejected through the PI controller. PI parameters are computed using a BLDC mathematical model.

The system can be described by the angular momentum conservation law:

$$J\dot{\omega}_r = \tau_e - \tau_r, \tag{4.4}$$

where J is the rotor inertia, ω_r is the rotor speed,

$$\tau_e = k_v \left(I_A \sin(\theta) + I_B \sin(\theta + \frac{2\pi}{3}) + I_C \sin(\theta + \frac{4\pi}{3}) \right), \tag{4.5}$$

is the electrical torque and it is the three phase version of (2.9). For what concerns the resistant torque τ_r which appears in (4.4):

$$\tau_r = \omega_r |\omega_r| K_{q0}, \tag{4.6}$$

it is proportional to friction constant which will be discussed later on (in section 6.1) and to the square of the rotation speed.

Assuming I_A, I_B, I_C sinusoidal, with equal modulus I and shifted of $\frac{2\pi}{3}$, (4.5) becomes,

$$\tau_e = \frac{3}{2} k_v I. \tag{4.7}$$

where,

$$I = \frac{1}{R_{tot}}(V_r - k_v\omega_r), \tag{4.8}$$

where R_{tot} is the winding resistance plus the drain to source conduction resistance of the two MOSFETs of the H-bridge, and V_r is voltage amplitude delivered to the motor by the inverter. Thus (4.4) can be rewritten,

$$J\dot{\omega}_r = \frac{3k_v}{2Rtot}(V_r - k_v\omega_r) - \omega_r|\omega_r|K_{q0}, \tag{4.9}$$

let,

$$T_m = \frac{2JR_{tot}}{3k_v^2}, \tag{4.10}$$

(4.9) becomes,

$$T_m\dot{\omega}_r + \omega_r = \frac{V_r}{k_v} - \frac{T_m}{J}\omega_r|\omega_r|K_{q0}. \tag{4.11}$$

The reference voltage V_r can be set through the inverter in order to perform the feed forward and a PI feedback,

$$V_r = k_v(\frac{T_m}{J}\omega_r|\omega_r|K_{q0} + T_m\dot{\omega}_c + \omega_c) - K_P(\omega - \omega_c) - K_I\int(\omega - \omega_c)\,dt, \tag{4.12}$$

where K_I and K_P are the feedback controller gains and ω_c is reference speed. By inserting (4.12) in (4.11) it is possible to obtain the error function of the system,

$$T_m\dot{e} + (K_P + 1)e + K_I\int e\,dt = 0, \tag{4.13}$$

which derived,

$$\ddot{e} + \frac{K_P + 1}{T_m}\dot{e} + \frac{K_I}{T_m}e = 0. \tag{4.14}$$

Let,

$$\frac{2}{T_c} := \frac{K_P + 1}{T_m}, \tag{4.15}$$

$$\frac{D}{T_c^2} := \frac{K_I}{T_m}. \tag{4.16}$$

(4.14) can be rewritten,

$$\ddot{e} + \frac{2}{T_c}\dot{e} + \frac{D}{T_c^2}e = 0. \tag{4.17}$$

The error system has the characteristic equation,

$$s^2 + \frac{2}{T_c}s + \frac{D}{T_c^2} = 0. \tag{4.18}$$

with roots,

$$s = -\frac{1}{T_c}(1 \pm \sqrt{1-D}) = s_+, s_-. \tag{4.19}$$

The error will converge to zero if,

$$Re(s_+) < 0, \tag{4.20}$$
$$Re(s_-) < 0. \tag{4.21}$$

Thus it is necessary to choose $T_c > 0$ and $D > 0$.

In addition to avoid overshoot it is necessary to choose $1 - D > 0$ which means $D < 1$.

With motor characteristic values previously measured, it is possible to define,

$$T_m = \frac{2JR_{tot}}{3k_v^2} = 0.0752. \tag{4.22}$$

According to these value it is possible to define the controller gains K_I and K_P and the feed forward term $\frac{T_m b}{J}$

$$K_P = \frac{2T_m}{T_c} - 1 \approx 1.5, \tag{4.23}$$
$$K_I = \frac{DT_m}{T_c^2} \approx 10.4, \tag{4.24}$$
$$\frac{T_m b}{J} \approx 0.0014. \tag{4.25}$$

From Figure 4.14 and 4.15 it is possible to see how the controller increases the motor performance by making possible not just to track the speed variation but also to do it in a desired time lapse. In this case it is shown a step from 50rad/s to 100rad/ss.

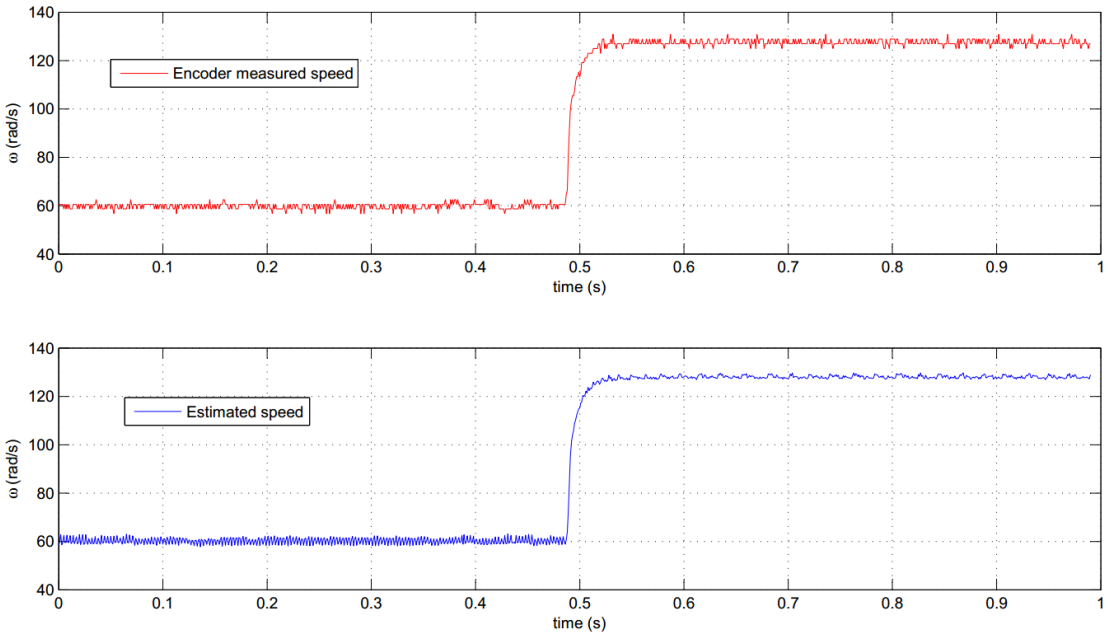

Figure 4.14: Step response without feedback controller.

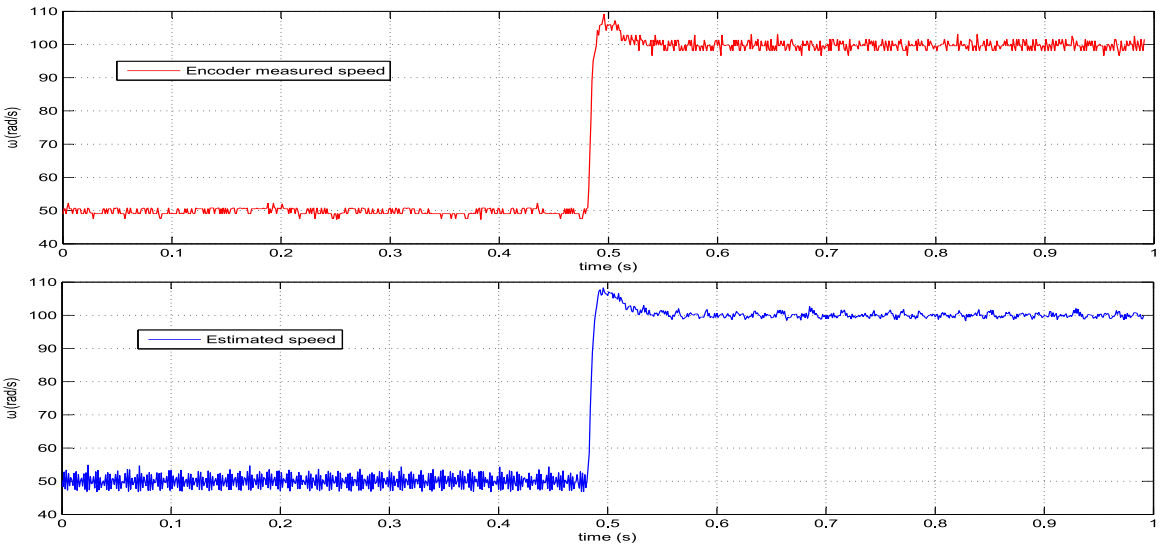

Figure 4.15: Step response with feedback controller.

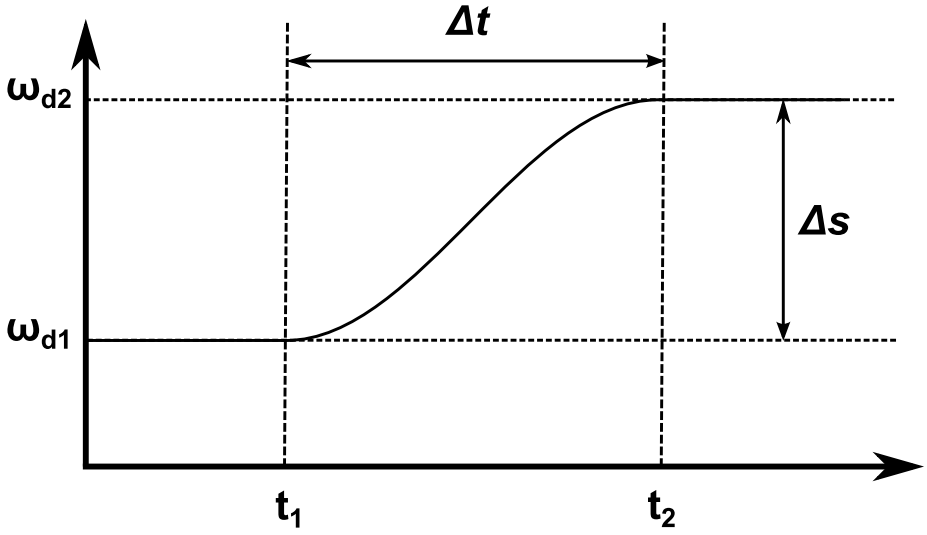

Figure 4.16: Speed transition trajectory graph.

4.2 Motor Control Reference Signal Generation

During the rotational speed variation transients which are imposed to the motor by the speed reference signal, it is important to avoid stress due to abrupt speed changes. This in order to avoid mechanical stresses and excessive current transients. For this reason each time a speed change is set, the control generates a transition trajectory which links the current speed with the desired one. The transition is characterized by Δs which is the difference between the current and the desired motor speed and Δt which is the transition time, computed once a desired acceleration is defined. The transition path is shaped in a way so that the starting and the final accelerations are minimized, and the overall effort is homogeneously distributed throughout the trajectory. In Figure 4.16 a graph of the speed transition trajectory is given; it should be noticed that it consists of a cubic curve which has zero derivative at the beginning (in t_1) and at the end (in t_2).

These conditions can be expressed numerically,

$$\omega_d(t_1) = \omega_{d1}, \tag{4.26}$$
$$\omega_d(t_2) = \omega_{d2}, \tag{4.27}$$
$$\dot{\omega}_d(t_1) = 0, \tag{4.28}$$
$$\dot{\omega}_d(t_2) = 0, \tag{4.29}$$

where ω_{d1} and ω_{d2} are respectively the starting speed and final (desired) speed. The transition could be described numerically starting from a generic cubic curve (4.30).

$$\omega_d(t) = a_3(t-t_1)^3 + a_2(t-t_1)^2 + a_1(t-t_1) + a_0. \tag{4.30}$$

Curves parameters are computed according to the speed variation. It is quite easy to notice that in $t = t_1$,

$$\omega_d(t_1) = a_0, \tag{4.31}$$

which is the speed value before the transition. Deriving (4.30), it is possible to impose the acceleration equal to zero in t_1,

$$\dot{\omega}_d(t) = 3a_3(t-t_1)^2 + 2a_2(t-t_1) + a_1, \tag{4.32}$$
$$\dot{\omega}_d(t_1) = a_1. \tag{4.33}$$

So the acceleration is zero in t_1 if $a_1 = 0$.
Acceleration equal to zero in t_2 is obtained considering that,

$$\dot{\omega}_d(t_2) = 3a_3(\Delta t)^2 + 2a_2(\Delta t). \tag{4.34}$$

So the acceleration is zero in t_2 when:

$$a_3 = -\frac{2a_2}{3\Delta t}, \tag{4.35}$$

a_2 and a_3 are calculated by imposing:

$$\omega_d(t_2) = a_3(\Delta t)^3 + a_2(\Delta t)^2 + \omega_d(t_1), \tag{4.36}$$

where $\omega_d(t_2)$ is given. In equation (4.36), by replacing a_3 with (4.35) the following expression is obtained:

$$\omega_d(t_2) = -\frac{2a_2}{3\Delta t}(\Delta t)^3 + a_2(\Delta t)^2 + \omega_d(t_1) \tag{4.37}$$
$$a_2(\Delta t)^2(1 - \frac{2}{3}) = \omega_d(t_2) - \omega_d(t_1), \tag{4.38}$$

which it is possible to solve with respect to a_2,

$$a_2 = 3\frac{\omega_d(t_2) - \omega_d(t_1)}{(\Delta t)^2}. \tag{4.39}$$

By inserting (4.39) expression in (4.35):

$$a_3 = 2\frac{\omega_d(t_2) - \omega_d(t_1)}{(\Delta t)^3}. \tag{4.40}$$

So each time a new speed is set, the controller computes Δs and calculates the curve parameters. Then the speed transition is performed according to the resulting values. Of course if Δs is smaller than a predefined threshold, the transition path is not computed because the speed variation is limited. An immediate effect of the introduction of this transition trajectory can be remarked by observing the current transient when a step speed variation is entered to the system. Figure 4.17 shows a comparison between current transients with and without the transition trajectory. It is quite clear how the current peaks are limited when the speed is controlled with a variation path. This is of course important for what concerns circuitry stress and conduction losses.

4.3 Implementation of a Field Oriented Control Technique Based on Sliding Mode Observer

As highlighted in section 3.2, trapezoidal control systems cannot operate a continuous position or torque control. In addition to this, with these techniques, it is not possible to control electromagnetic transients, which is necessary for high-performance motor applications that are required to operate smoothly over the full speed range, generate full torque at zero speed, and have high dynamic performance including fast acceleration and deceleration. Position control for what concerns underwater vehicles propulsion is generally unnecessary. Torque control instead could be interesting for several reasons. A torque feedback can be exploited from the navigation algorithms to operate diagnostics and to improve navigation accuracy. For example, if there is a problem in a propeller such as unexpected friction due to dirt or some of the propeller blades are broken, a precise torque and position estimation can help to detect it and appropriate countermeasures can be adopted. Concerning vehicle navigation, an accurate speed and torque feedback can be used to exploit a dynamical model as explained in section 6.3. Hence Field Oriented Control sensorless techniques have been investigated and tested in order to improve vehicle maneuverability, to increase navigation accuracy and fault diagnosis capabilities. Due to the harsh operating conditions and the required system reliability, it has been necessary to select a control method that could guarantee appropriate performances in variable operating conditions. Attention has been focused on a SMO based control algorithm, as described in subsection 3.2.1, because of its robustness facing model variations and or uncertainties.

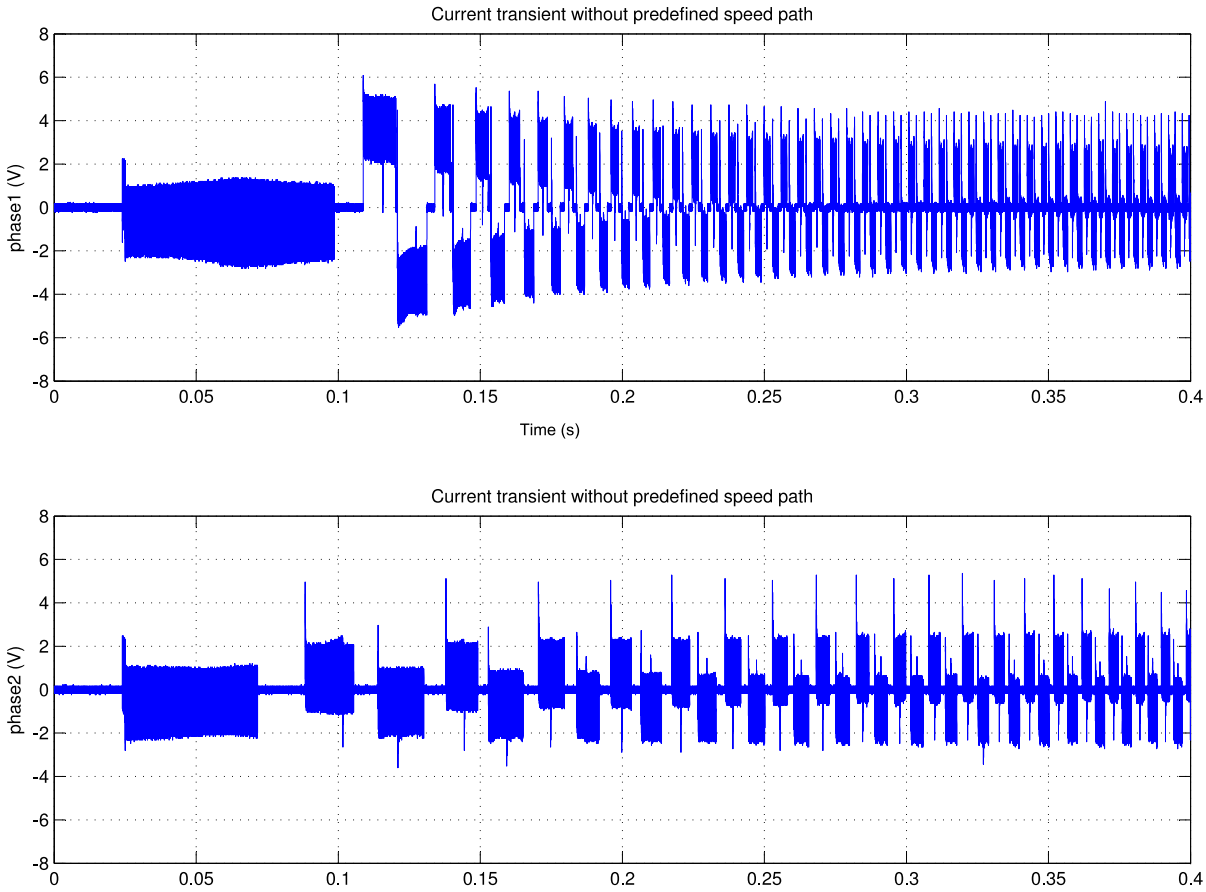

Figure 4.17: Current transient comparison with and without predefined speed path.

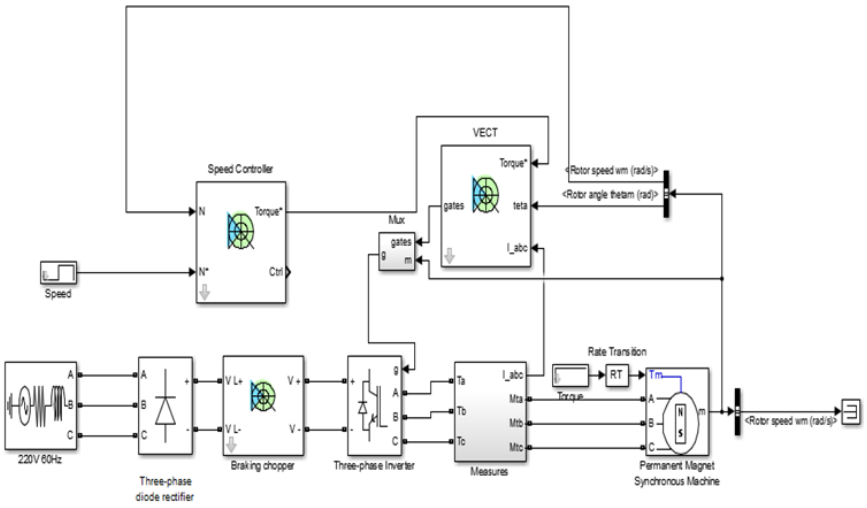

Figure 4.18: Simulink® scheme of a Permanent Magnet Synchronous Motor.

4.3.1 Sliding Mode Observer Algorithm Implementation and Testing with the dSPACE Platform

The first algorithm implementation has been operated in Matlab Simulink® exploiting a mathematical motor as shown in Figure 4.18 [53]. This approach has permitted a quick development of the algorithm which has been implemented first with the Simulink® blocks then in a Matlab function.

A first open loop estimation of the motor generated BEMF has been performed by acquiring motor simulated currents and voltages. As explained in subsection 3.2.1 from ϵ_α and ϵ_β it is possible to extract the rotor position. Hence a good estimation of it is essential. In Figure 4.19 the simulated and estimated BEMF along the two stationary axes at different speed is shown. The two signals have the same trend at each speed. This is remarkable especially at low speed where signal to noise ratio is lower is shown.

The BEMF estimation is then fed to the PLL for the position and speed extraction. In this case a PI controller tuning has been necessary. A preliminary tuning has been performed thanks to a Simulink® self tuning tool. The tool operates a system linearization around the specified working point and calculated PID gains in order to guarantee:

- Closed loop stability;
- Maximum disturbance rejection and input variation tracking;
- Maximum control robustness.

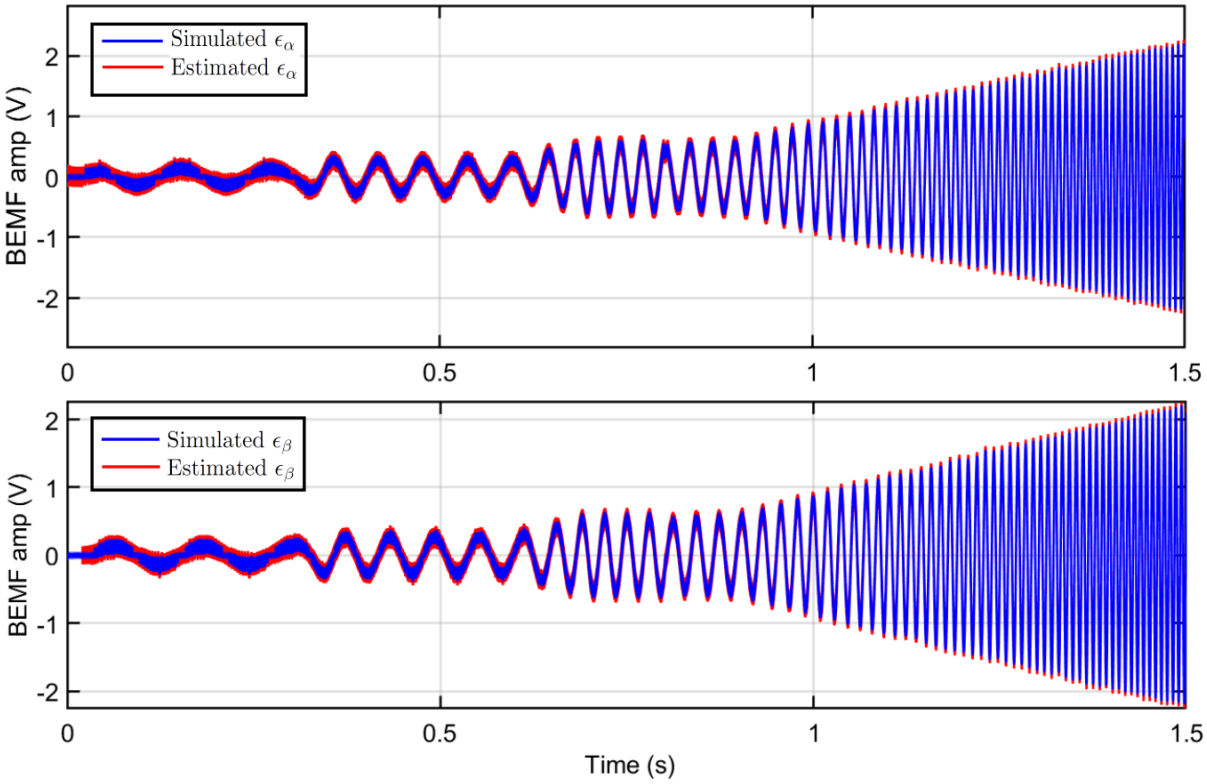

Figure 4.19: BEMF estimation with Simulink® implemented SMO algorithm compared with the simulated one.

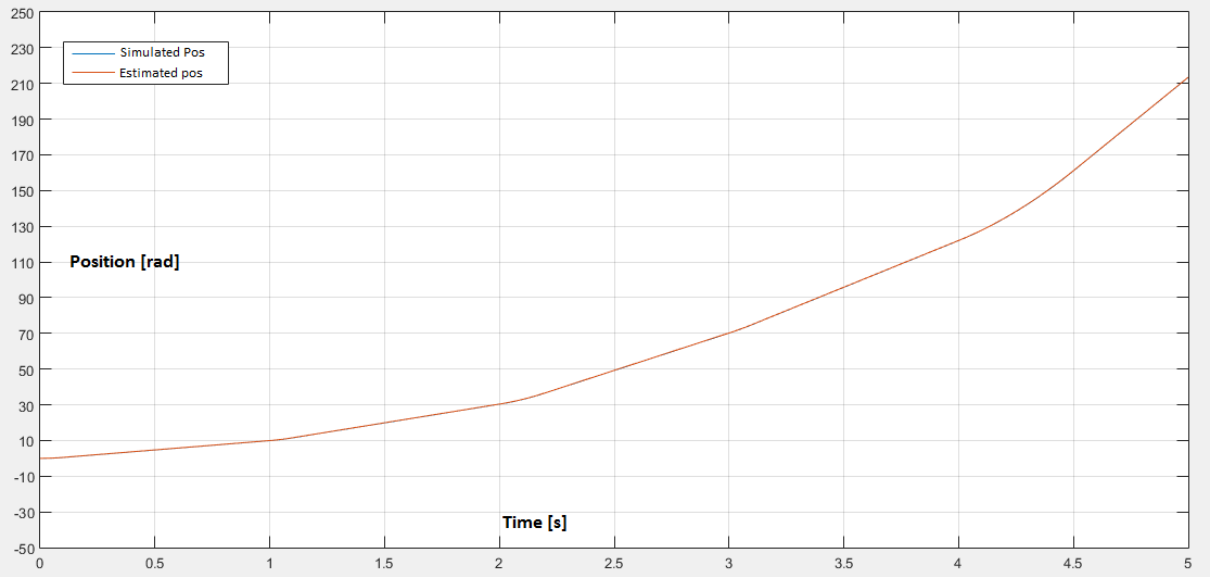

Figure 4.20: Rotor position estimation with Simulink® implemented SMO algorithm compared with the simulated one.

After that, the parameters have been manually adjusted to obtain an optimal output speed and position signal. In Figures 4.20 and 4.21 simulated and estimated rotor position and speed trend is shown according to different rotational speed.

To evaluate the estimation performances, the average error has been evaluated over the speed range. Speed estimation position is shown in Figure 4.22. It is possible to note that speed estimation error in stationary conditions has average value of zero, with a very low ripple amplitude superposed to it ($\leq$ 5rpm). During speed variation instead, there is a transient during which the observer cannot track the position. Although speed error is limited in amplitude.

The following step has been the testing of the observer on a physical motor. To do it, the Maxon386676 motor has been run with an independent test bench driver the Texas Instruments T2000 LAUNCHXL-F28027F control logic plus BOOSTXL-DRV8301 Inverter which performed speed and position measurements. Thanks to the dSPACE MicroAutoBox II 1401/1501 platform, it has been possible to run the Simulink® implementation of the observer by feeding it with real time measurements acquired with the DSPACE ADC peripherals. The setup schematic of the experiment is shown in Figure 4.23. Current measurements have been acquired from the LAUNCHXL-F28027F measurements and conditioning electronics. Voltage measurements instead have been sampled directly from the motor phases then scaled and filtered before feeding it to the dSPACE ADCs. A focus about the dSPACE MicroAutoBox II 1401/1501 platform characteristics is presented in section 5.1.

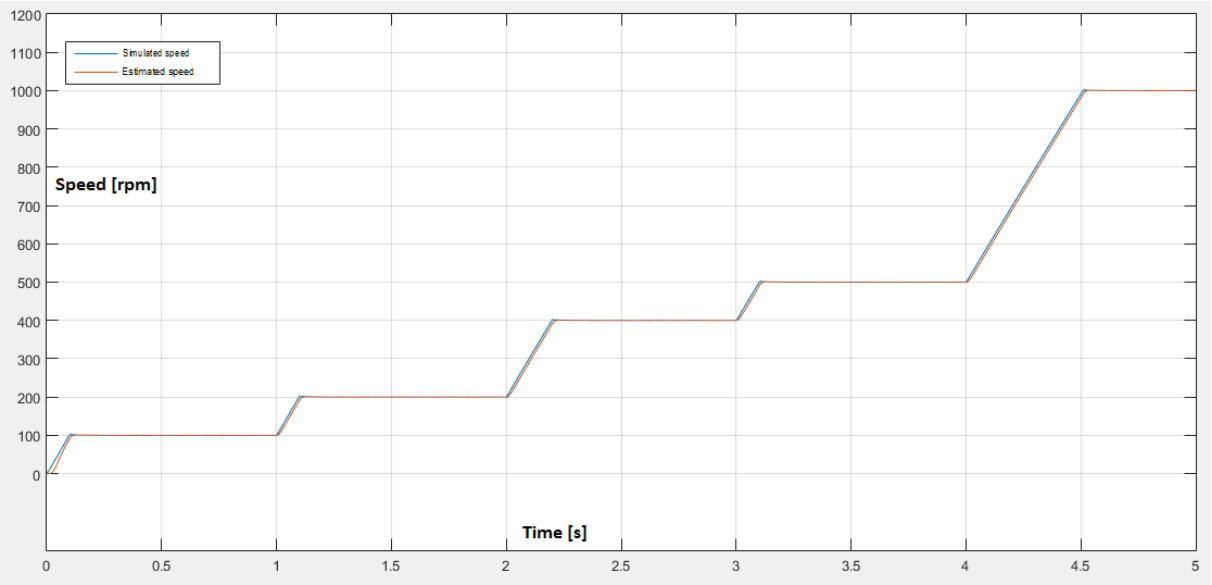

Figure 4.21: Rotor speed estimation with Simulink® implemented SMO algorithm compared with the simulated one.

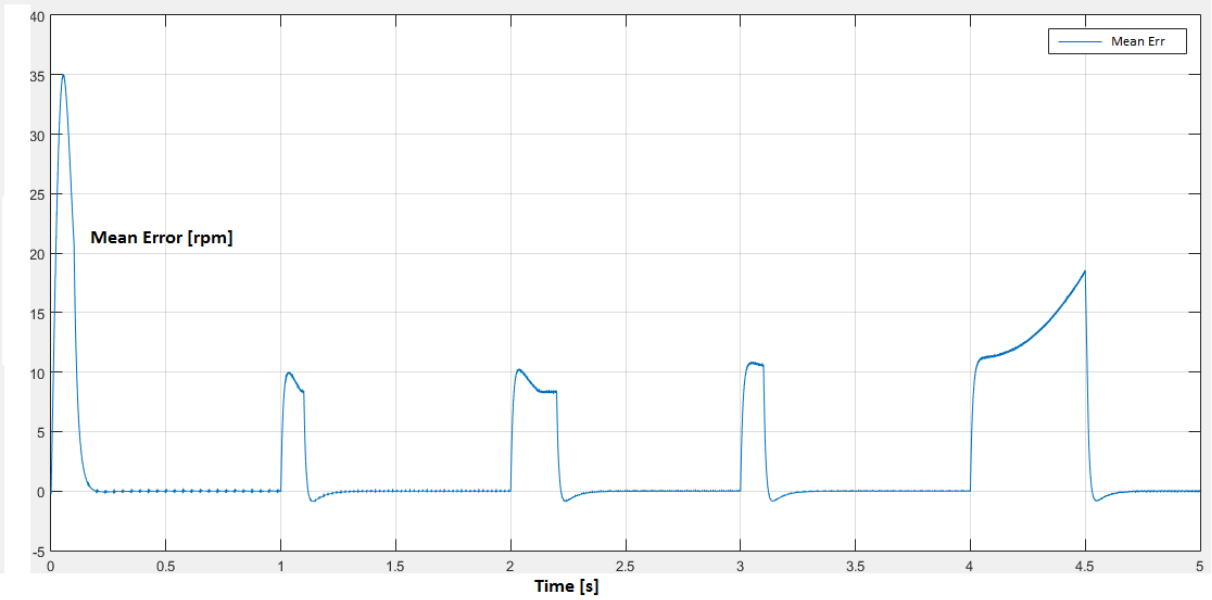

Figure 4.22: Rotor speed error obtained by comparing the Simulink® simulated model speed and the SMO estimated one.

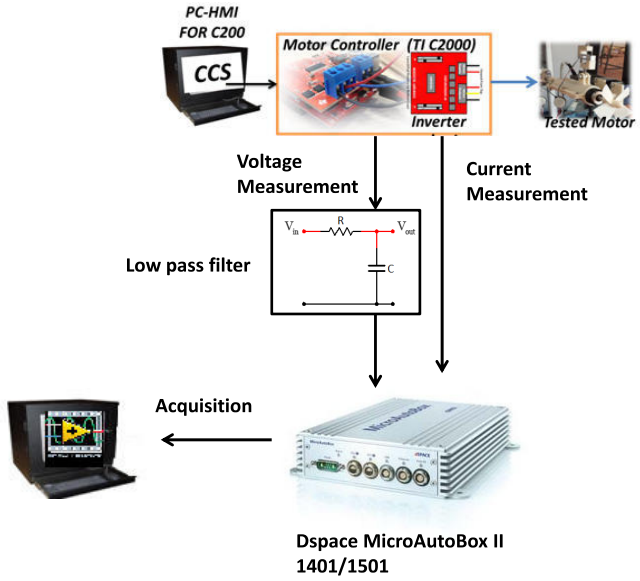

Figure 4.23: Algorithm testing setup with the dSPACE MicroAutoBox II 1401/1501 platform.

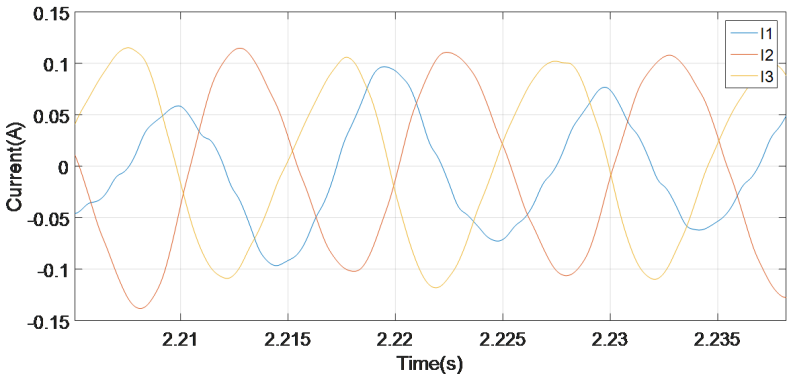

Figure 4.24: Phase current waveforms acquired with the dSPACE MicroAutoBox II 1401/1501 platform.

Speed estimation error with the dSPACE platform acquisitions.				
Ref Speed rpm	Average Est Speed rpm	Mean Err rpm	% Error	Std Dev rpm
2000	2003,30	-3,3029	-0,17%	18,67
4000	4006,93	-6,9367	-0,17%	24,06
6000	6010,51	-10,5131	-0,18%	26,56
8000	8013,19	-13,1935	-0,16%	27,41
10000	10020,13	-20,1314	-0,20%	27,35
12000	12021,12	-21,12	-0,18%	26,10

Table 4.1: Speed estimation error at various speed.

The SMO algorithm in the dSPACE platform has been executed at 10kHz; in figures 4.24 and 4.25 current and voltage waveforms acquired with the dSPACE ADCs are shown. Such a sampling frequency has been high enough to operate speed and position estimation.

In this case, being the estimator operated in open loop it has not been possible to compare the estimated position with the one measured with the test bench. Hence only speed estimation has been compared with the reference speed delivered to the test bench drive. In Figure 4.26 speed estimation error at different speed is shown. Also in this case, error peaks occur in conjunction with reference speed variations. By operating a filtering of the estimated speed, it is clear how the average error is always under the 0.2% as visible in Table 4.1.

In addition to these speed estimation accuracy measurements, the algorithm robustness has been tested. As specified in subsection 3.2.1 the SMO estimator, operated is a model based one, hence it could suffer uncertainties and variations of the motor model parameters. To evaluate the robustness of the developed solution, tests have been carried on by monitoring algorithm performances while

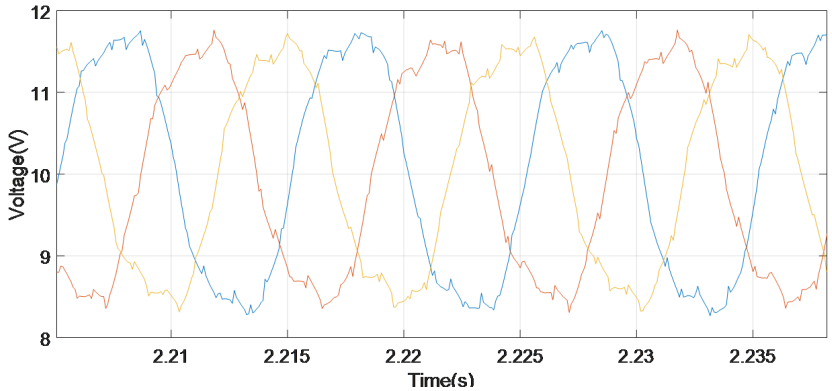

Figure 4.25: Phase voltage waveforms acquired with the dSPACE MicroAutoBox II 1401/1501 platform.

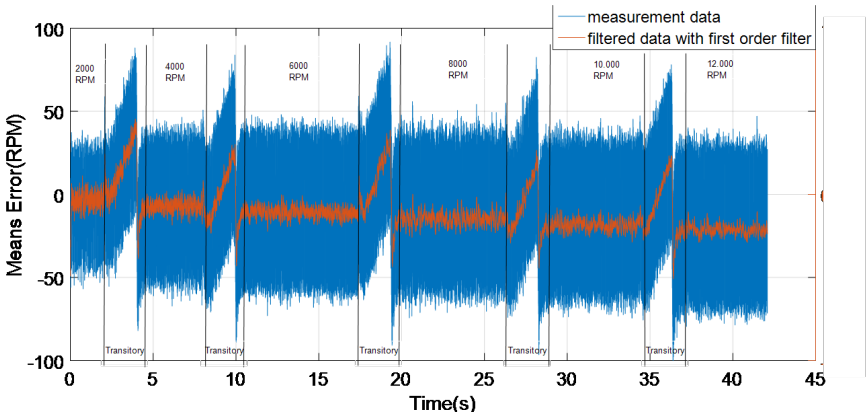

Figure 4.26: Speed estimation error between reference speed and SMO estimated speed.

Robustness test: K = 10.			
Ref Speed rpm	Average Est Speed rpm	% Error rpm	Std Dev rpm
2000	2009	0,448	300
4000	4007	0,175	200
6000	6032	0,531	200
8000	8051	0,633	150
10000	10054	0,537	150
12000	12093	0,769	150

Table 4.2: Speed estimation error with model parameters disturbance. K=10.

Robustness test: K = 20.			
Ref Speed rpm	Average Est Speed rpm	% Error rpm	Std Dev rpm
2000	2010	0,498	600
4000	4007	0,175	350
6000	6031	0,514	350
8000	8052	0,646	300
10000	10055	0,547	300
12000	12094	0,777	300

Table 4.3: Speed estimation error with model parameters disturbance. K=20.

varying model inductances and resistances. For the motor model, symmetric phase impedances have been speculated. Hence, with reference to the motor model described in section 2.2 the following approximations have been done:

- $R_s = R_A = R_B = R_C$,
- $L_s = L_A = L_B = L_C$.

The parameters have been varied starting from the actual one and by multiplying it times K. In tables 4.2, 4.3, 4.4 and 4.5 the results of the robustness test are shown for different values of K. The results of K=1 are listed in Table 4.1.

Robustness errors tests on experimental data, have highlighted that:

- For $K \leq 4$, estimator performances are equal to those relatives to Table 4.1;
- For $4 \leq K \leq 40$ estimation performances degrade with increased amplitude of the ripple superposed to the estimated speed. Although the mean value of the estimated quantity remains correct;

Robustness test: K = 30.			
Ref Speed rpm	Average Est Speed rpm	% Error rpm	Std Dev rpm
2000	2018	0,892	1000
4000	4014	0,349	500
6000	6032	0,531	400
8000	8051	0,633	400
10000	10053	0,527	400
12000	12091	0,753	400

Table 4.4: Speed estimation error with model parameters disturbance. K=30.

Robustness test: K = 40.			
Ref Speed rpm	Average Est Speed rpm	% Error rpm	Std Dev rpm
2000	2022	1,088	1400
4000	4018	0,448	900
6000	6041	0,679	700
8000	8056	0,695	600
10000	10067	0,666	600
12000	12097	0,802	600

Table 4.5: Speed estimation error with model parameters disturbance. K=40.

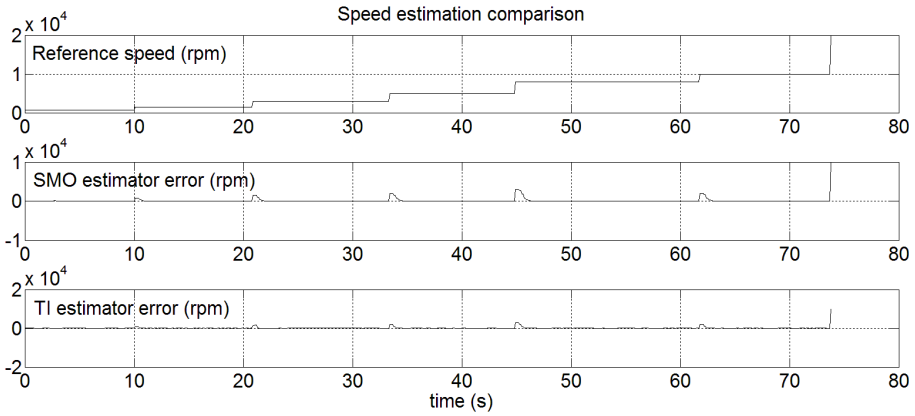

Figure 4.27: Estimated speed error comparison according to a stepped speed reference profile.

- By further increase K, the estimator is no more able to perform speed or position estimation.

According to these results it is possible to affirm that the system operates robust speed position and speed estimation facing parameters uncertainties.

Speed estimation performances have been compared with the Texas Instruments LAUNCHXL-F28027F + BOOSTXL-DRV8301 Inverter ones, The LAUNCHXL-F28027F exploits a T2000 family micro-controller and it is programmed with a proprietary sensorless control technique for PMSM, which is also based on a SMO filter. In the next sections the LAUNCHXL-F28027F board filter will be referred to as the TI filter and the author's developed solution as the SMO filter. Although the complete control algorithm is not accessible for commercial reasons, the TI filter could be considered a good comparison term in order to assess the performances of the developed solution. On this purpose a Matlab based acquisition interface has been developed. Thanks to this interface, it has been possible to acquire in real-time the estimated values (rotor position, speed, and torque) from the TI filter and compare it with the SMO filter ones. Some experimental results of the comparison of the two filters are visible in 4.27, 4.28, 4.29 and 4.30.

In Figure 4.27 it is shown a comparison between the TI filter estimated speed and the SMO filter, according to a stepped speed reference profile. The overall performance of the two filters is similar. By zooming in the graph, it is possible to notice that the ripple amplitude, which affects the estimated signals, varies according to the measured speed for both the TI and the SMO filter. In the performed test, reference speed has been span from 700 to 12000kHz. When dealing with BEMF based sensorless control systems the most critical task, is controlling it at low speed with respect to the nominal speed. This because BEMF signal decreases at low speed. The motor used for the tests, has a

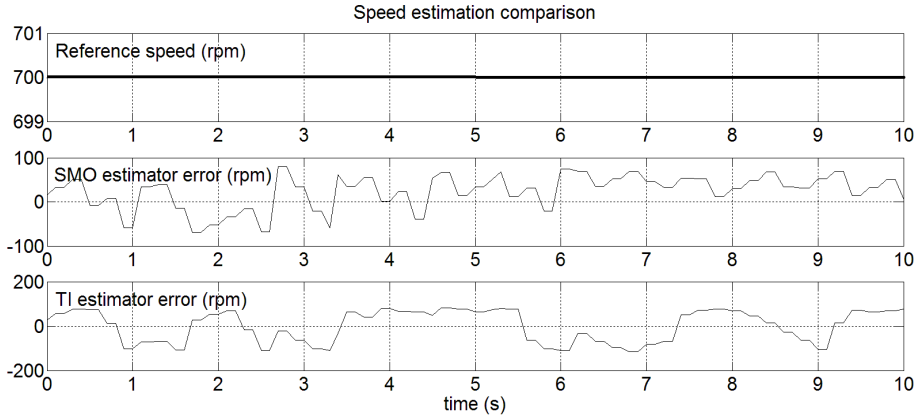

Figure 4.28: Speed measurement error of the two filters given a reference speed of 700rpm.

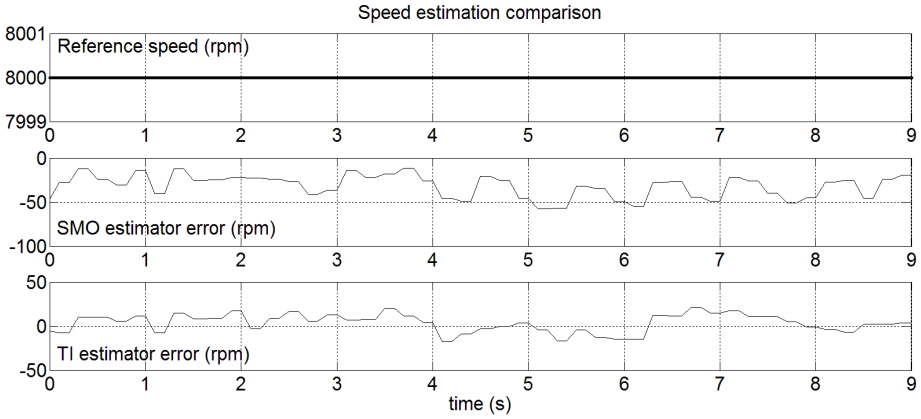

Figure 4.29: Speed measurement error of the two filters given a reference speed of 8000rpm.

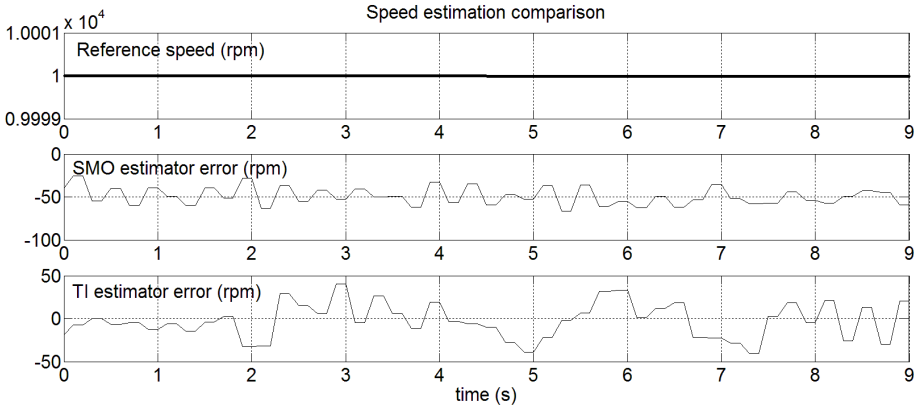

Figure 4.30: Speed measurement error of the two filters given a reference speed of 10000kHz.

Standard deviation of the speed measurement error		
Ref. Speed rpm	SMO filter rpm	TI filter rpm
700	39.0818	71.7796
1500	24.6550	77.3445
3000	16.3979	35.1901
5000	15.9772	10.2908
8000	13.3922	10.9181
10000	10.9927	20.2238

Table 4.6: Speed estimation error standard deviation comparison between TI filter and SMO filter.

nominal speed of 25000rpm so speed estimation is critical when reference speed is below 2000rpm. In Figure 4.28 it is shown the measurement error of the two filters given a reference speed of 700rpm. In this case the SMO filter seems to perform better than the TI filter, although from Figure 4.27 it is clearly visible how the SMO filter is slower when chasing a speed variation. The behavior of the two filters is also highlighted in Table 4.6. In there it has been computed the standard deviation of the speed measurement error at the various speed step. The two filters have similar performances at high speed while from 700 to 3000rpm the SMO filter performs better in terms of average speed error. At higher speed, ripple amplitude decrease as shown in Figure 4.29 and Figure 4.30.

The following step, has been the use of the developed estimation filter in a motor control algorithm. This means that the rotor position estimation operated by the SMO filter, is then fed to a control logic which operates the motor through the power stage. To do this, a test board that could be controlled with the dSPACE platform has been designed. This part of the work has been carried

Test Bench Motor Characteristics	
Nominal Voltage V	12
Pole Pair	6
$R_s\Omega$	0.264
L_dmH	0.004615
L_qmH	0.008214
Inertia $g \cdot cm^2$	15.4
Magnetic Flux Wb	0.00197

Table 4.7: Electrical and mechanical characteristics of the test bench motor.

out in cooperation with the Laboratory of Actuation Technology (LAT) of the Saarland University. The LAT has designed and realized, a dSPACE test bench board, with which it has been possible to operate a PMSM motor control though the dSPACE platform. The testing board is shown in Figure 5.2.

The dSPACE test board has a power stage for motor control, current and voltage sensing electronics, a rotational encoder interface and communication channels to communicate with the dSPACE. A FOC based control has been implemented in Matlab Simulink® with which it has been possible to operate an open loop control of the motor. The control initially has been operated using the rotational encoder measured speed. According to the rotor position, the necessary coordinates transformations were operated and the right phase voltages were imposed on the phases through a PWM generation algorithm. This way the control imposes the orthogonality condition between rotor and stator generated magnetic flux but the motor is operated without any speed or current control. The developed estimator has been included in the control schematic and run in parallel with the motor controller. Once the SMO estimator is activated, the estimated position signal can be feed to the PWM controller in place of the encoder measured one. This is a fundamental step in order to operate a closed loop control of the motor. In these conditions the rotor speed still depends on phase voltage amplitude and on the torque applied to the rotor but a controller can be implemented to operate speed or torque control. After verifying that the controller could be operated correctly in open loop with the position estimated signal, a speed controller has been implemented and tuned according to the technique explained in section 3.2.

The following tests were made exploiting the dSPACE platform as a control and acquisition logic, the dSPACE test board of Figure 5.2 as a power stage, and a PMSM test bench motor coupled with a rotational encoder and a variable torque load. Test bench motor characteristics are listed in Table 4.7:

The setup has been supplied with a bench power supply, delivering a maximum current of 2A, so speed and position measurements were taken imposing low load torque on the motor shaft. In Figure 4.32 the rotor position comparison between measured and estimated position is shown while the motor is spun at 100rpm. The same position comparison is shown at a speed of 500rpm in

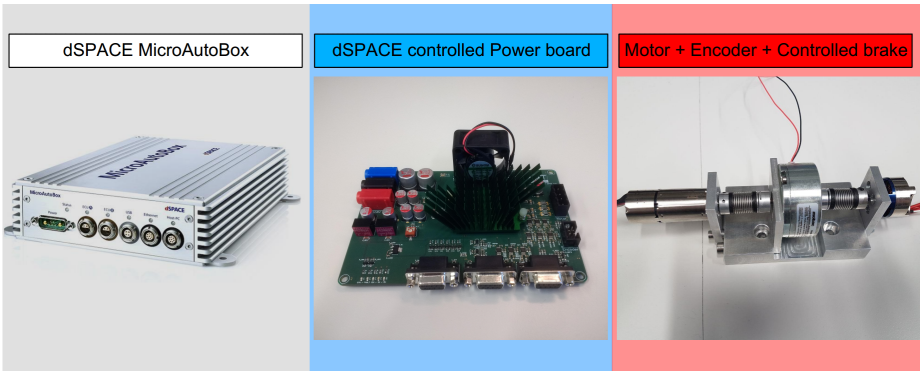

Figure 4.31: Test bench scheme for the implementation of the closed loop sensorless control with the dSPACE platform.

Figure 4.33. Differently from previous measurements, in this case the motor is controlled by exploiting the position and speed estimated signals.

In both graphs of figures 4.32 and 4.33, rotor position is expressed in radians. It can be noticed that some times both the encoder and/or the estimated signal do not reach the full scale value. This is due to the under-sampling of the acquisition interface. The speed estimation comparison is show in figures 4.34, 4.35, 4.36 and 4.37. As seen in the open loop experiments, the ripple superposed to the speed estimation, decreases by increasing the rotational speed.

The amplitude of the noise superposed to the speed estimation signal is similar the one measured in the open loop tests. Although tests were performed with different motors, robustness tests have highlighted that ripple amplitude is highly influenced by model accuracy, so the performances in terms of estimation accuracy are similar. Concerning the speed variation tracking performances in Figure 4.38 it is shown the behavior of the estimator facing a stepped speed reference profile.

In this case, with respect to the open loop measurements the speed estimation is no more delayed with respect to the actual one. This because the motor is controlled with the estimated position signal. Although, this does not interfere with the system readiness. In Table 4.8 the average speed estimation error and ripple amplitude are shown. With respect to the results of Table 4.1 the ripple superposed to the speed estimation is almost the same, while the percentage estimation error is drastically reduced. This means that the estimation error recorded during the previous testing of the SMO filter was due to the open loop estimation.

The same measurements have been taken by operating the motor with an external load of $200\text{mN} \cdot \text{m}$. The simulated load was imposed thanks to the controlled rotational brake of Figure 4.31. Concerning the position estimation, in Figure 4.39 a misalignment between measured and estimated torque is visible but it appears as a ripple disturbance more than a constant error. By increasing the rotational speed the misalignment is reduced; in Figure 4.40 rotor position

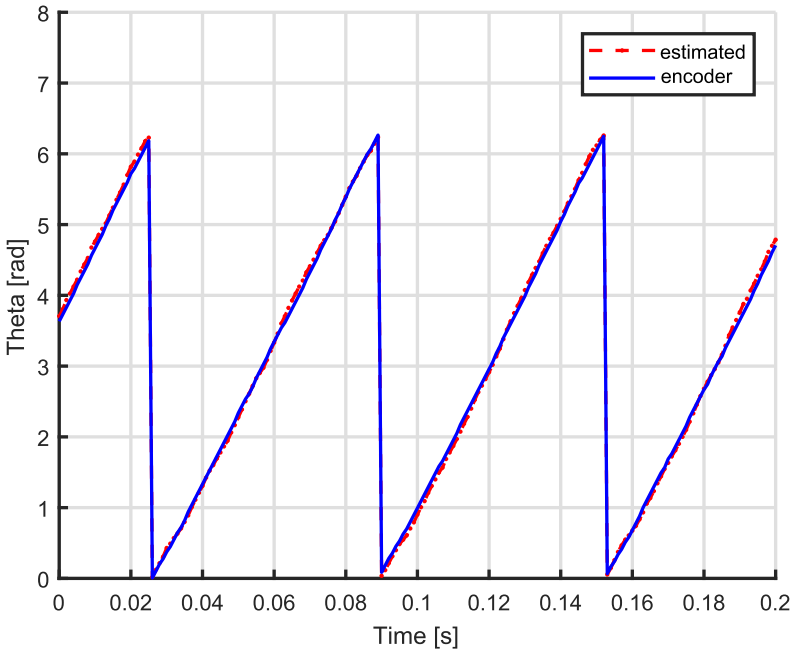

Figure 4.32: Rotor position at 100rpm. Comparison between the encoder measured position and the estimated one.

Speed estimation error.			
Ref Speed rpm	Average Est Speed rpm	% Error rpm	Oscillations Amp. rpm
500	500	0,05071	27,17
1000	1000	-0,02338	19,28
1500	1500	0,01333	14,13

Table 4.8: Speed estimation error at various speed operating the motor in closed loop with the dSPACE platform.

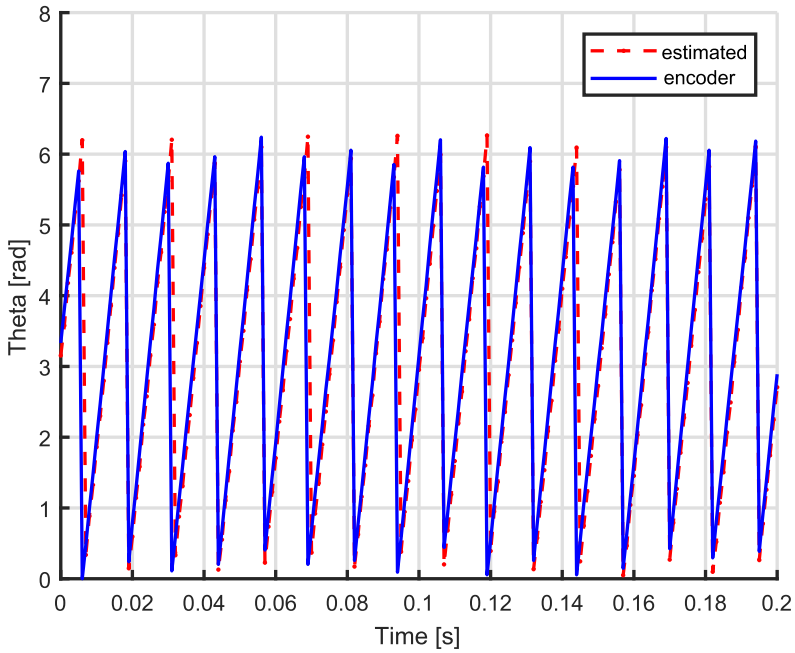

Figure 4.33: Rotor position at 500rpm. Comparison between the encoder measured position and the estimated one.

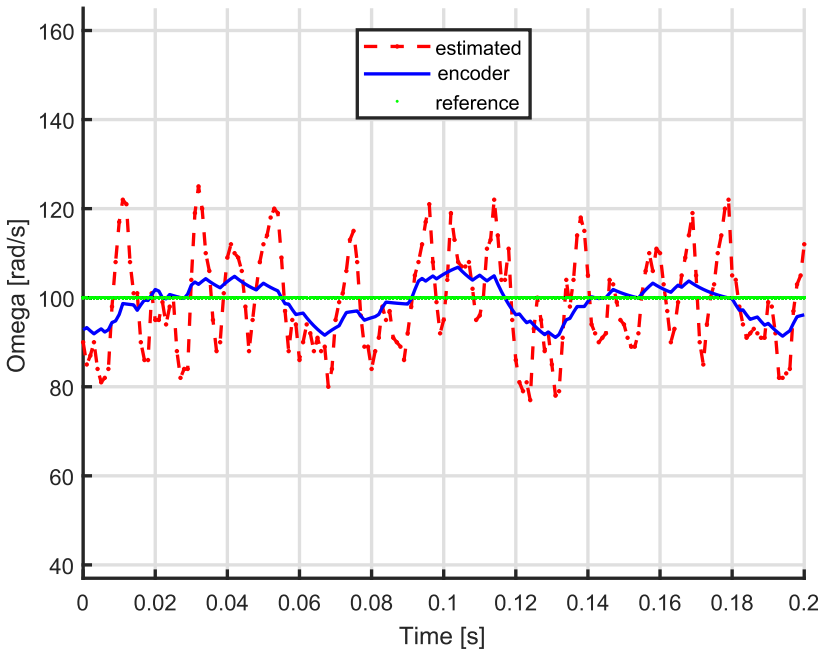

Figure 4.34: Rotor speed estimation at 100rpm. Comparison between the encoder measured position and the estimated one.

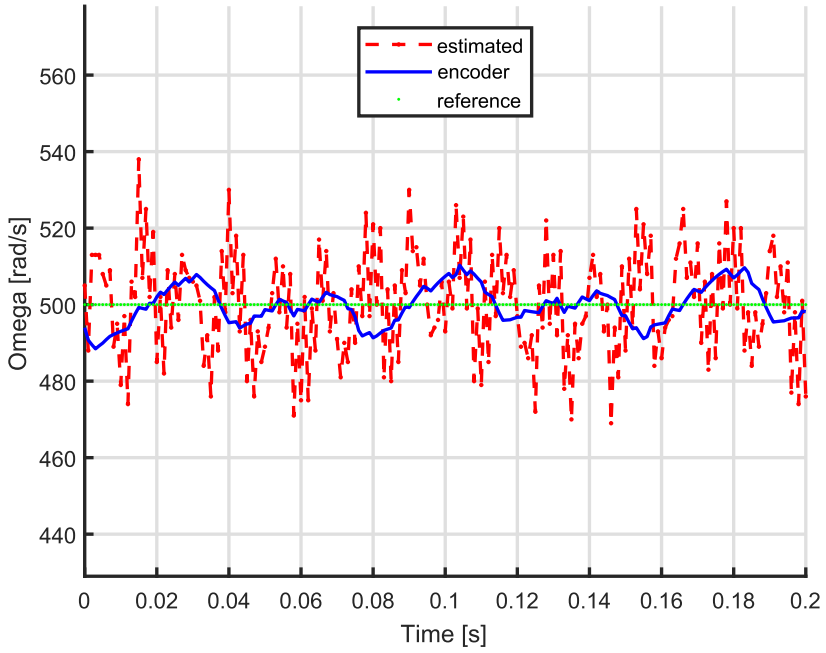

Figure 4.35: Rotor speed estimation at 500rpm. Comparison between the encoder measured position and the estimated one.

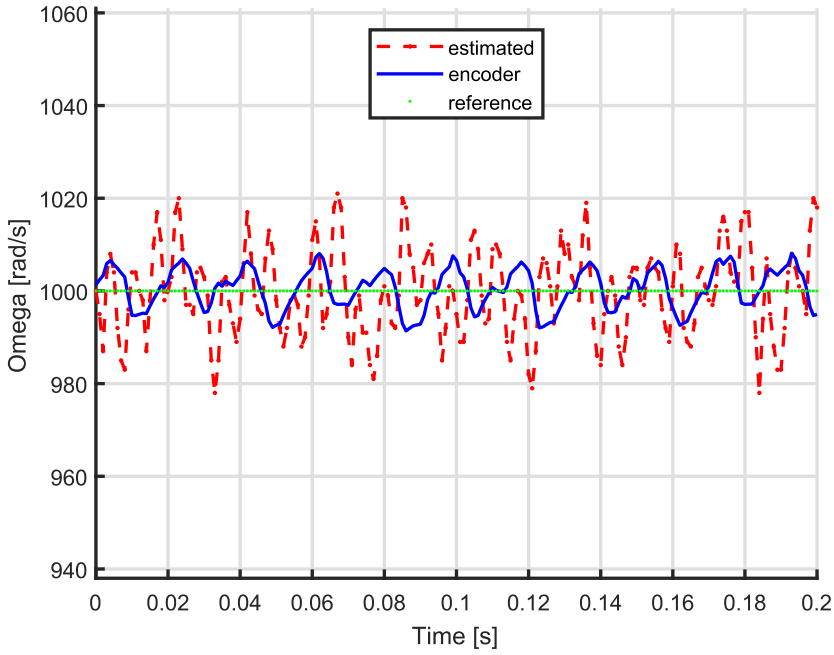

Figure 4.36: Rotor speed estimation at 1000rpm. Comparison between the encoder measured position and the estimated one.

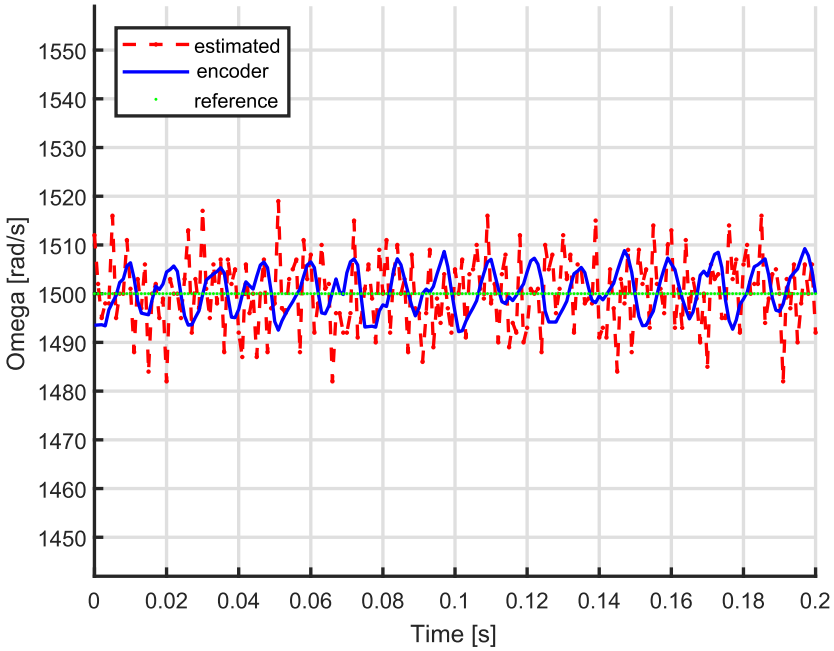

Figure 4.37: Rotor speed estimation at 1500rpm. Comparison between the encoder measured position and the estimated one.

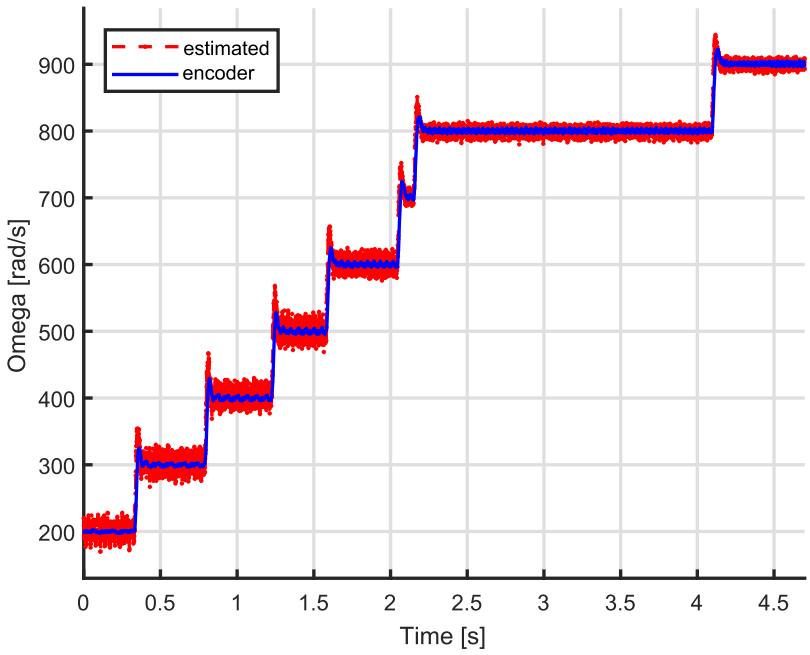

Figure 4.38: Stepped speed reference profile. Comparison between the encoder measured position and the estimated one.

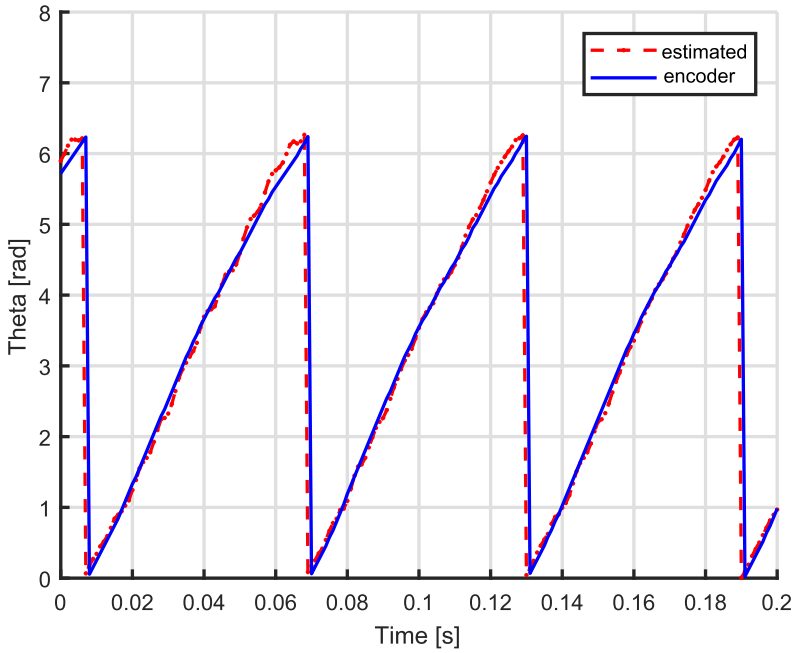

Figure 4.39: Rotor position at 100rpm. Comparison between the encoder measured position and the estimated one operating the motor with an external torque of $200\text{mN} \cdot \text{m}$.

estimation with an external load of $200\text{mN} \cdot \text{m}$ is shown. This is confirmed by speed measurements. In Figure 4.41 and 4.42 a Comparison between the encoder measured position and the estimated one is presented. It is interesting to note that, although a constant speed reference is set, a periodic oscillation appears both on the measured and estimated speed signal. This is due to the speed controller which can not perfectly track the desired speed reference; tracking oscillation amplitude indeed increases when increasing the rotational speed. On the contrary, the misalignment between measured and estimated speed is reduced at higher speed.

4.3.2 Implementation of the Sliding Mode Observer Algorithm in an Embedded System

The final step, concerning the design of the SMO based sensorless control, has been the implementation of the algorithm in an embedded system in C language. For the development of the motor control algorithm a PIC32MZ2048EFH100 has been used. A focus on the selection criteria and micro-controller characteristics is presented in chapter 5.

For the development and testing of the solution, a test board has been designed. The board will be referred to as PIC test board. This part of the work

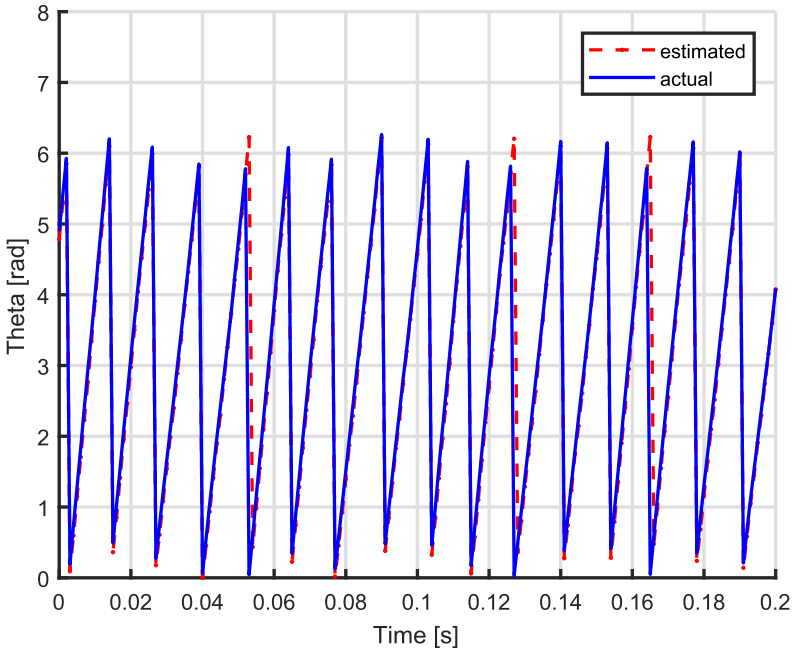

Figure 4.40: Rotor position at 100rpm. Comparison between the encoder measured position and the estimated one operating the motor with an external torque of $200\text{mN} \cdot \text{m}$.

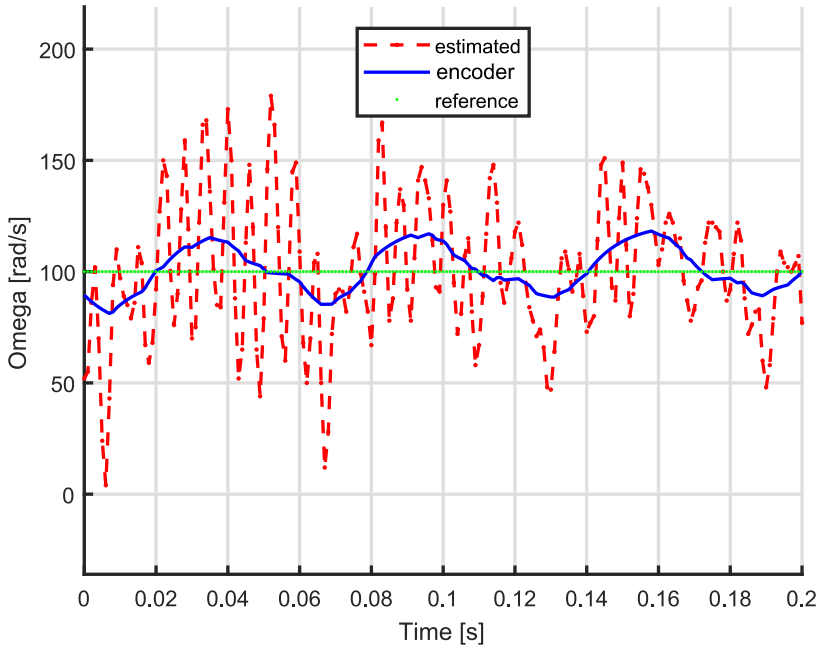

Figure 4.41: Rotor speed estimation at 100rpm. Comparison between the encoder measured position and the estimated one operating the motor with an external torque of $200\text{mN} \cdot \text{m}$.

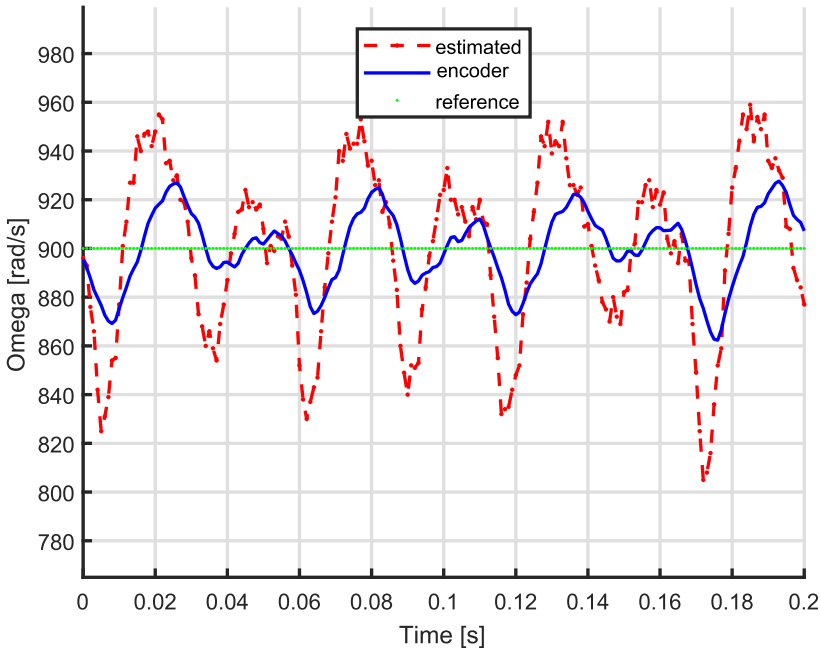

Figure 4.42: Rotor speed estimation at 900rpm. Comparison between the encoder measured position and the estimated one operating the motor with an external torque of 200mN · m.

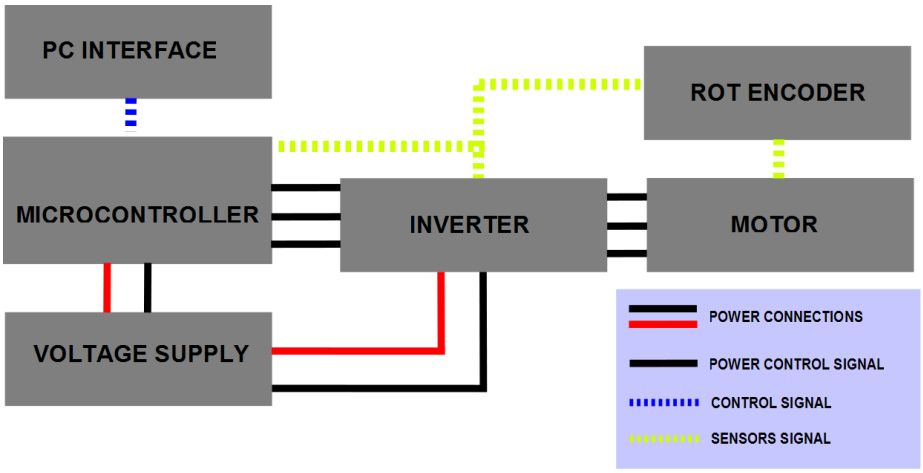

Figure 4.43: Schematic of the development setup of the SMO based sensorless motor control algorithm on an embedded system.

has been carried on with and in the facility of the Laboratory of Actuation Technology (LAT) of the Saarland University. Their support has been fundamental for the development of the embedded code motor control libraries and for the test bench electronics.

The code has been implemented by replicating the Matlab code previously implemented. As a development platform MPLAB R X IDE v3:61 has been used. It is a Microchip free development tool that runs on Windows, Linux, or Mac OS operating systems. As an algorithm debug tool a communication interface has been developed. The interface runs in a Windows environment and communicates with the micro-controller thanks to a USB communication interface at a frequency up to 1kHz. Thanks to it, online analysis of the estimation algorithm operation has been possible since each signal was available in real time for trend analysis and comparison with the Matlab developed algorithm results. The motor has been initially controlled with a sensored FOC without any (position or speed) control. As for the preliminary development in Matlab Simulink® environment, the SMO estimator embedded code algorithm has been first run in parallel with the open loop sensored control. This has permitted the algorithm debug and to tune the estimator parameters. A scheme of the algorithm development setup is shown in Figure 4.43.

This setup, permitted the comparison of the algorithm position and speed estimation, with the encoder measured ones. Once a good position estimation signal has been obtained, a FOC closed loop control has been implemented and tuned according to the system characteristics as explained in section 3.2. Also in this case, to avoid mechanical stresses and excessive current transients, a transition trajectory which links current speed with the desired one has been implemented (See section 4.2).

The entire algorithm schematic is represented in Figure 4.44.

In figures 4.45 and 4.46 a comparison between estimated and measured rotor position is shown with the motor turning at 500rpm and 1000rpm. Concerning rotor speed estimation, in Figure 4.47, estimated, measured and reference speed are shown for a range of speed which goes from 160 to 1800rpm. With respect to the dSPACE implementation, it is interesting to see how the smothered reference trajectory reduced the speed overshoot which is now visible only at high speed.

In figures 4.48 and 4.49 a zoomed view of the estimated speed is shown at 136 and around 1200rpm. In both cases it is interesting to see how the encoder measured and estimated speed coincides, and the displacement with the reference speed is due to speed controller transients. In these graphs the signals have been filtered with a low pass filter of 70Hz to highlight the mean value.

4.4 Implementation of an High Frequency Signal Injection Technique Based on Pulsating Vector

According to [38] and [52], rotating carrier frequency injection techniques, suffer from poor signal-to-noise ratio and sensitivity to small saliencies. The T200 BlueRobotics motor selected for MARTA AUV propulsion is a Surface Mounted type, so it shows low rotor anisotropy and the stator iron saturation is limited by the wide rotor air-gap due to winding sealing. Furthermore rotating carrier techniques generally need to exploit low pass filtering near the fundamental frequency which reduces the bandwidth for the control of the machine torque. Using a pulsating carrier instead, more sensitivity to small saliencies is achieved [38],[52]. As a consequence a pulsating carrier frequency injection method has been selected and implemented. In particular the technique illustrated in subsection 3.3.1 from [8] shows less sensitivity facing the additional induced saliencies, injected signal distortion and disturbances caused by the dead time effect.

4.4.1 Pulsating Carrier High Frequency Injection Based Rotor Position Estimation Technique Implementation and Testing with the dSPACE Platform

Also concerning this technique, the first algorithm implementation has been executed in Matlab Simulink® exploiting a mathematical motor as shown in Figure 4.18. This approach has permitted a quick development of the algorithm. Also in this case, the algorithm can be operated in parallel with the motor model control without interfering with it. The simulation permitted to understand how the two algorithms performed the misalignment error estimation and to evaluate its performances. Initially, a simulation frequency of 10kHz has been selected with an injection carrier frequency of 1kHz. The selection criteria of the simulation and carrier frequency was in accordance with examples in

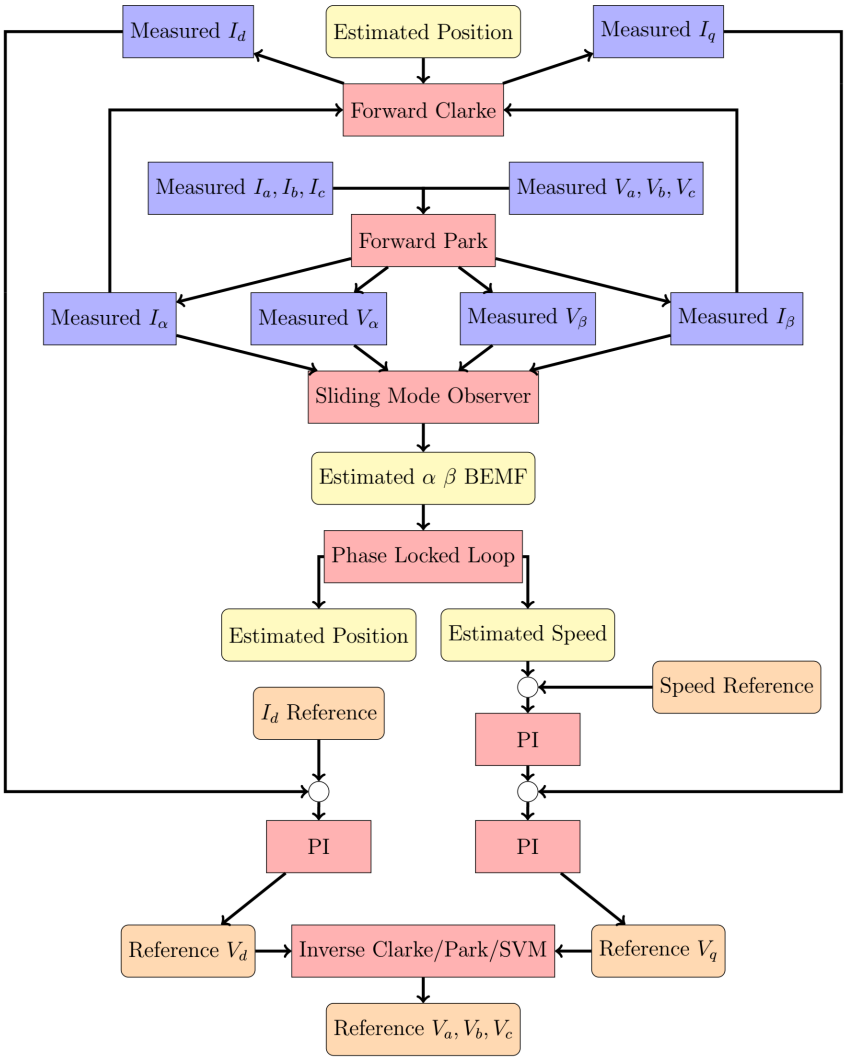

Figure 4.44: Flow schematic of the SMO based FOC control.

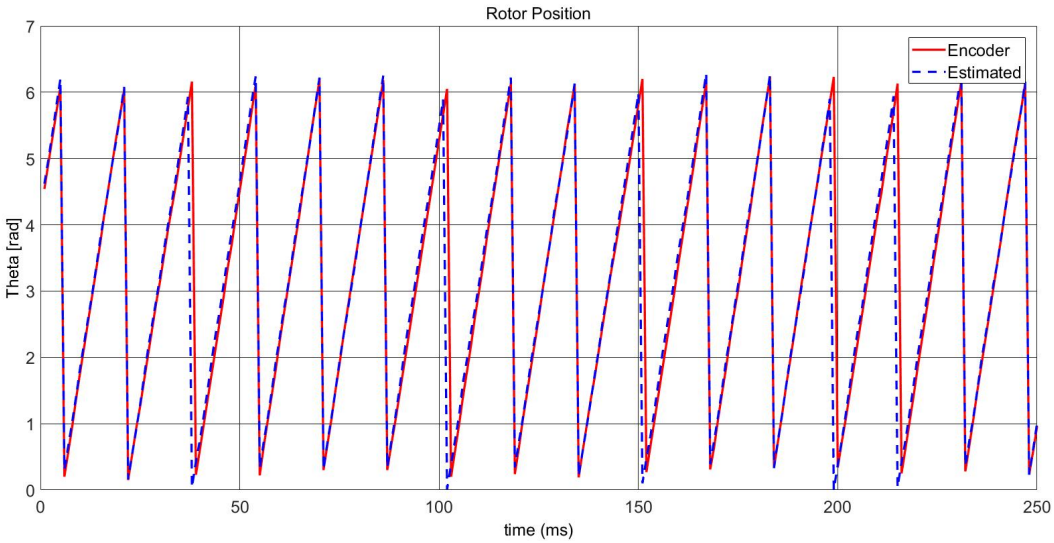

Figure 4.45: Rotor position estimation at 400rpm.

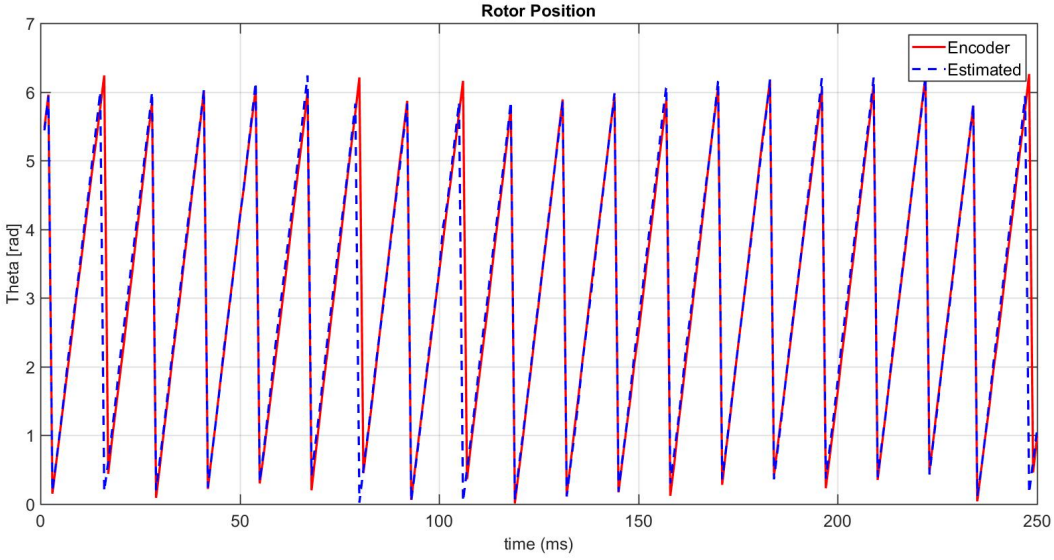

Figure 4.46: Rotor position estimation at 850rpm.

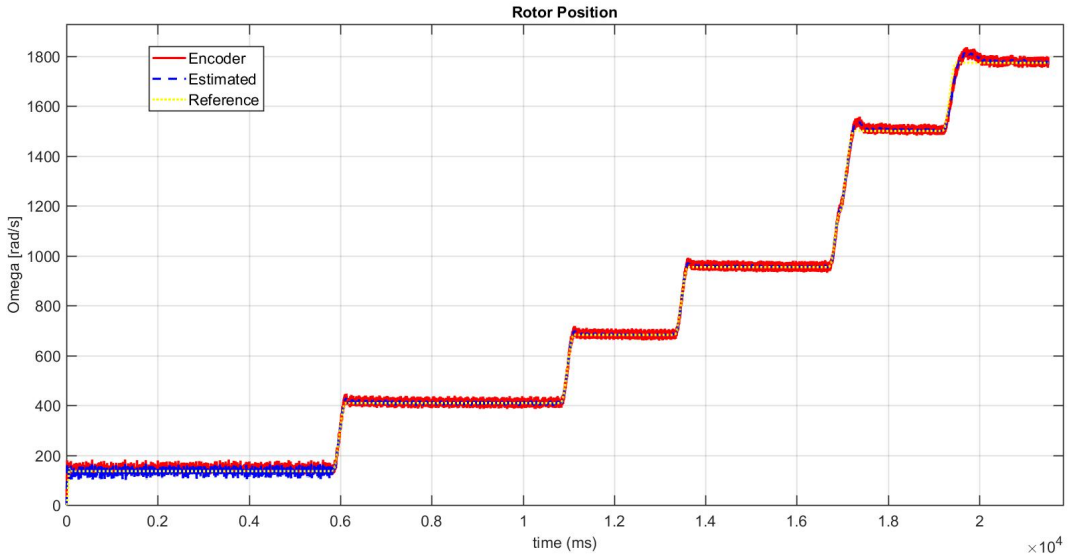

Figure 4.47: Estimated and encoder measured rotor speed from 130 to 1800rpm.

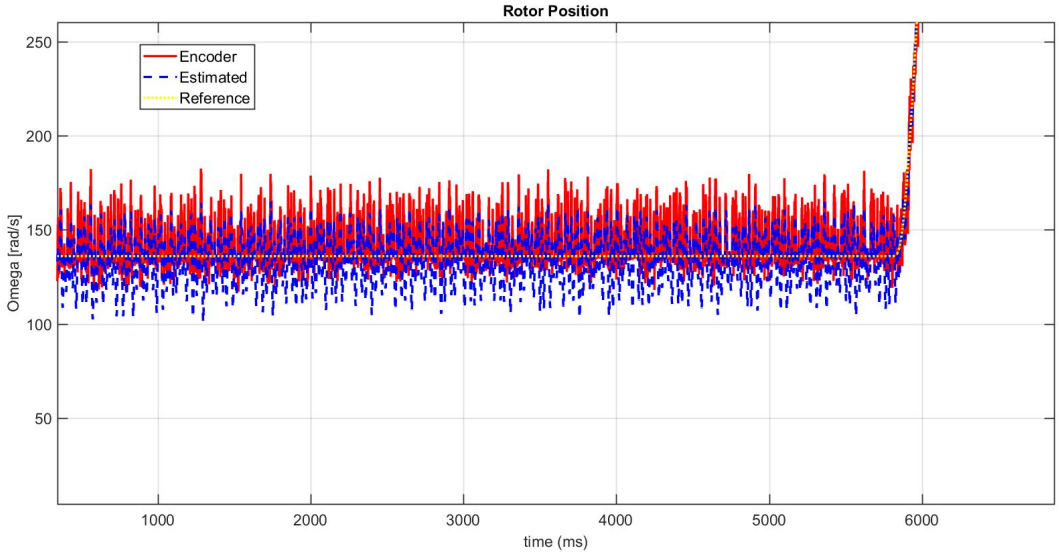

Figure 4.48: Estimated and encoder measured rotor speed at 136rpm.

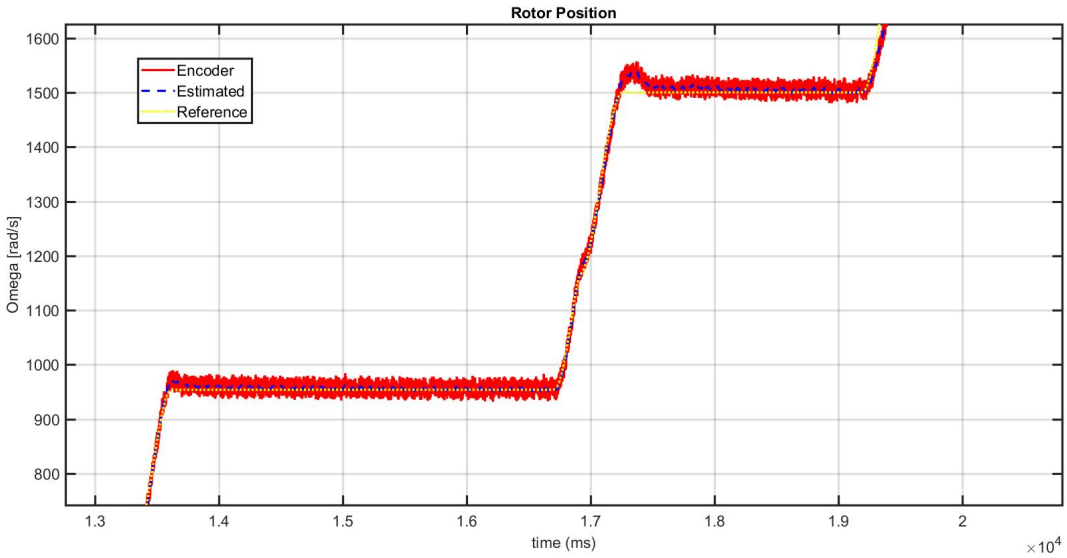

Figure 4.49: Estimated and encoder measured rotor speed at 960 and 1500rpm.

literature see [8], [9], [52]. Both the methods explained in subsection 3.3.2 have been simulated. On the first phase of the work, the position estimation algorithm has been implemented and run in parallel with the motor. This means that initially, the motor control has been performed with the rotor position information provided by the motor model and the High Frequency Injection algorithm performed his own position estimation. This has permitted to tune the Phase Locked Loop (PLL) parameters for an optimal position tracking. A comparison between the simulated and estimated rotor position is shown in Figure 4.50. In this case, rotor position is obtained by using the technique described in [8]. In it, it is possible to see that initially, the HF (High Frequency) pulsating signal is injected along a fixed direction, thus a sinusoidal signal is produced as a misalignment estimation.

Once the position estimation algorithm is activated (in $t = 1.5$s of Figure 4.50), the position error tracking is started and the estimated position aligns with the simulated one. After that, the simulated motor model has been controlled in open loop with the HF estimated rotor position. This means that no speed or torque control is performed, and a certain voltage is applied along the q-axis of the motor synchronous reference frame. To do this, the rotor position information is necessary for the stationary to synchronous transformation and vice versa and it has been provided by the HF position estimator. In Figure 4.51 a comparison between the simulated and estimated rotor position is shown. In Figure 4.52 the same signal are shown, in this case the technique described in [9] has been used. In simulation, the two techniques showed similar performances. Although, due to the less sensitivity facing nonlinear inverter effects,

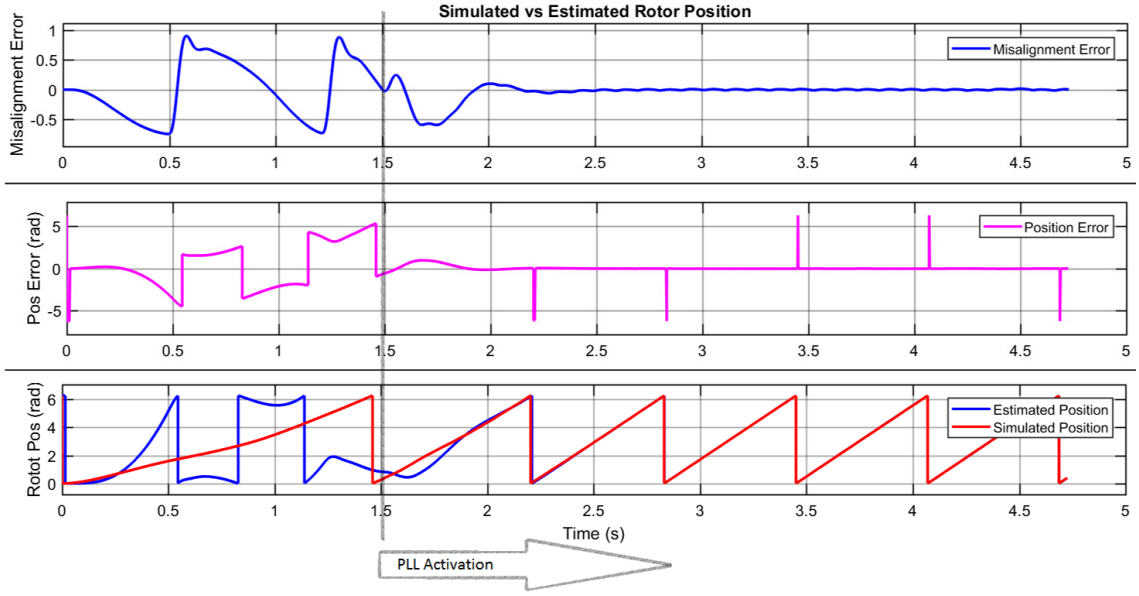

Figure 4.50: HF estimation algorithm: rotor position estimation and simulated one.

the technique described in [8] has been selected for the experimental scenario implementation.

Once the HF position estimation algorithm has been simulated successfully, it has been possible to operate it in a motor control algorithm. This means that the rotor position estimation obtained by the HF estimator, is fed to a control logic which operates the motor through the power stage. By exploiting the dSPACE based algorithm development setup shown in Figure 4.31, it has been possible to test the Simulink^{TM}schematic which had been previously simulated. Switching from the simulated to the experimental scenario in this case it has been quite simple. The algorithm indeed does not exploit a mathematical motor model, and the algorithm tuning has mainly concerned the injection frequency and PLL parameters. The motor that has been used, is the out-runner PMSM described in Table 4.7. For that kind of motor, the best estimation results have been obtained with an excitation carrier of 2.6kHz frequency and 0.6V amplitude. In Figure 4.53 reference and estimated speed during motor operation is shown. In Figure 4.54 also position estimation is shown during a motor change of rotation. It is possible to notice that the position estimation is performed also at standstill. It is important to remark that using this kind of algorithms, motor control is limited at around the 3% of the motor nominal speed [8].

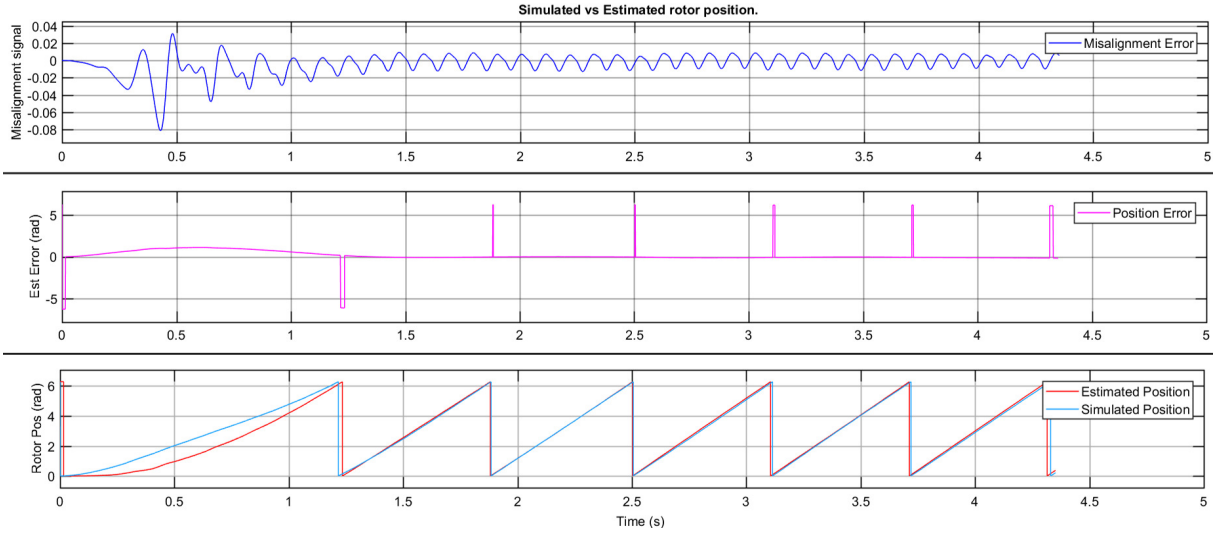

Figure 4.51: Motor model controlled with HF estimation algorithm according to [8] technique. Rotor position estimation and simulated one.

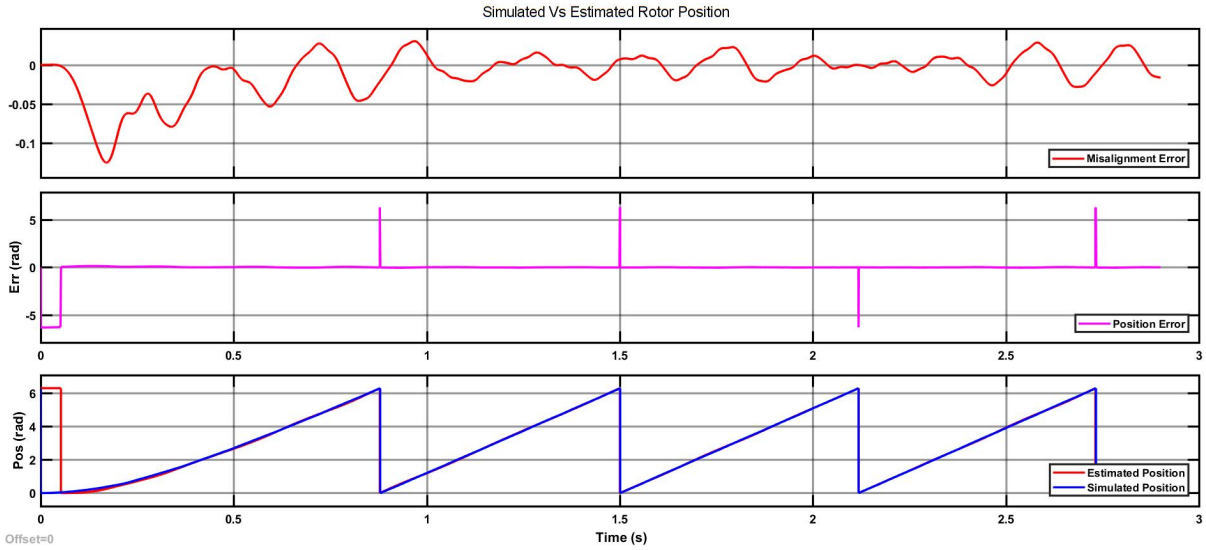

Figure 4.52: Motor model controlled with HF estimation algorithm according to [9] technique. Rotor position estimation and simulated one.

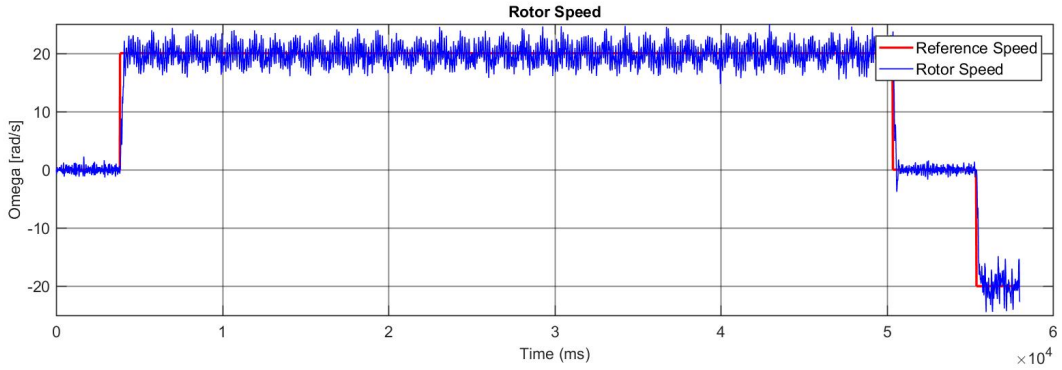

Figure 4.53: High frequency injection technique, reference and estimated speed.

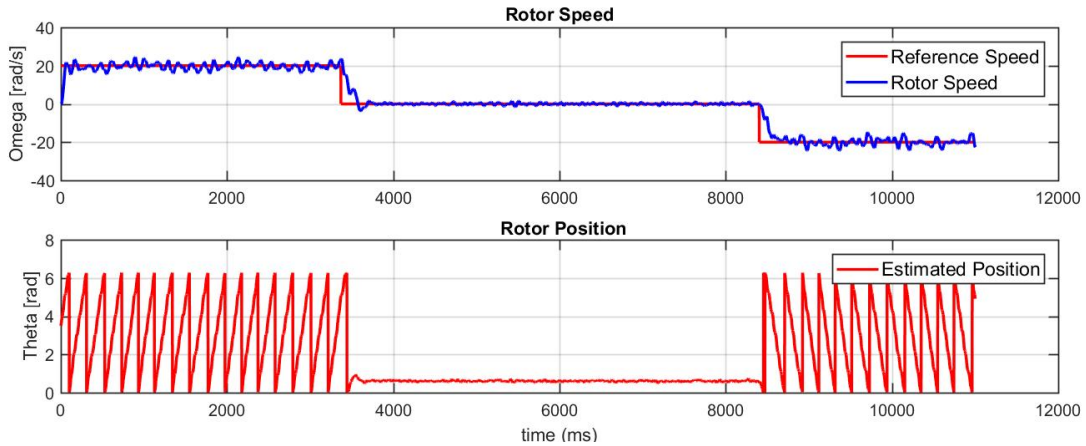

Figure 4.54: High frequency injection technique, estimated speed and position.

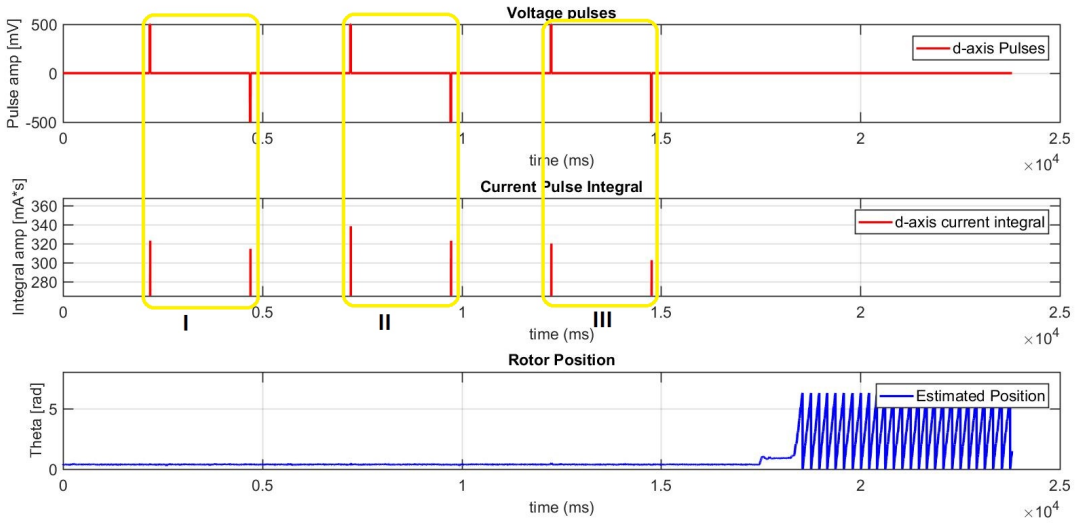

Figure 4.55: High frequency injection technique, rotor polarity identification routine.

4.4.2 Embedded Code Implementation and testing of the Pulsating Carrier High Frequency Injection Based Rotor Position Estimation Technique

Once it has been possible to operate a reliable estimation of the rotor position, the algorithm has been implemented in embedded C language for the PIC32MZ2048EFH100 micro-controller. The board that has been used for code development and control testing is the one in Figure 5.6. The algorithm has been completed by introducing the rotor polarity identification routine. For the final implementation of the position estimation algorithm, the technique described in [8] has been used. For the polarity identification the solution proposed by the author in subsection 3.3.2 has been used because of its reliability and low computational effort. The polarity identification routine consists in three couples of opposite direction voltage pulses along the d-axis of the synchronous reference frame. The corresponding current is then measured and integrated. In Figure 4.55 the three couples of pulses and the corresponding current integrals are highlighted. In this case, the estimated flux direction corresponds to the positive rotor flux direction. Hence the positive voltage pulse results in a higher current peak. Consequently, when a positive reference is set the rotor start rotating in the positive direction.

Chapter 5

Testing Appliances Developed and Used for the Experimental Tests

In the present chapter, an overview of the testing appliances and control solutions which have been developed during the PhD thesis work is presented. These appliances have been implemented in order to test and produce experimental results of the developed solutions. The work has involved the design and implementation of customized prototype electronic boards for the development of sensorless control techniques; this permitted the study and comparison of several motor control techniques, data acquisition and performance assessment of these techniques.

Concerning the design of the vehicle propellers, two test bench have been implemented for the characterization of the propulsion system in a testing pool of the MDM Lab of the Florence University.

Finally an integrated motor control drive has been developed; the controller is able to perform sensorless control of PMSM over a wide range of speed, to operate motor speed control and torque estimation.

5.1 dSPACE MicroAutoBox II 1401/1511 Platform Characteristics

MicroAutoBox is a real-time system for performing fast function prototyping in fullpass and bypass scenarios. It operates without user intervention, MicroAutoBox can be used for many different rapid control prototyping (RCP) applications such as:

- Powertrain;
- Chassis control;

- Body control;
- Electric drives control;
- X-by-wire applications;
- Advanced driver assistance systems (ADAS);
- Aerospace applications.

It is essentially a real-time prototyping system that allows a rapid control and monitoring of automation systems. It is characterized by great computing power, small dimensions and good robustness facing mechanical and thermal shocks. This makes it optimal for those applications where a complex and high performance control logic has to be operated in harsh conditions. It can also be controlled through the most common communication buses such as CAN, LIN, K/L line, FlexRay, and Ethernet. The system is associated with ControlDeskNG®, a programming environment that allows the creation of control interfaces that are executed on a host system. Through this interface, a real-time parameter tuning and signal monitoring can be operated allowing to monitor and control mechanical and electrical systems in few easy steps. Concerning the implementation of a motor control logic, the dSPACE prototyping system has been selected because it can be programmed through Simulink™schematics and it can be interfaced in semi-automatic mode with various types of sensors and actuators such as encoders, load cells and positioners. Finally, acquisition and storage of simulation quantities and measured signals can be easily performed.

All of these factors considerably increase the speed and simplicity of system deploying by simplifying the steps related to the implementation of the interface between electronics and control system, filtering design of the acquired signals and control code design. System peripherals such as actuators, sensors, relays and switches are controlled through the IO peripherals of the dSPACE which connect the outputs and inputs of the control algorithm to the "real" outputs and inputs of the peripherals.

The main characteristics of the dSPACE MicroAutoBox II 1401/1511 are listed in Table 5.1:

The dSPACE system although is not provided with a motor control power stage. Hence a prototyping motor control board has been designed dy the Laboratory of Actuation Technology (LAT) of the Saarland University. The board is illustrated in Figure 4.31. In it, it is possible to identify the power stage, the signal conditioning electronics and the connectors to communicate with the dSPACE peripherals. The board exploits the Texas Instrument Three phase PWM motor driver DRV8332 which is a fully integrated three-phase driver, including logic and the three phase H-bridge in a single package. It can supply up to $8A$ continuous phase current per phase with peaks up to 13A. It can manage supply voltages up to 50V. It could reach an efficiency up to 97% and its internal logic manages by itself the switching of the 6 power MOSFETs of the H-bridge managing autonomously shoot through problems. The developed

Figure 5.1: dSPACE MicroAutoBox II 1401/1511 platform.

Board characteristics	
Producer	dSPACE GmbH
Processor	IBM PPC 750GL, 900 MHz (incl. 1 MB level 2 cache)
Operating Frequency	150MHz
Supply Voltage	3.3V
Program Memory	16 MB main memory 6 MB MicroAutoBox/Host Communication 16 MB nonvolatile ash memory
Communication Peripherals	RS232, USB, LIN, K / L line, FlexRay, Ethernet.
ADC Channels	16 * 16 Bit res
Analog Outputs	0-4.5V - 12 Bit
PWM outputs	40
Pin GPIO	80
On-board sensors	3-axis accelerometer Pressure sensor

Table 5.1: Main characteristics of the dSPACE MicroAutoBox II 1401/1511.

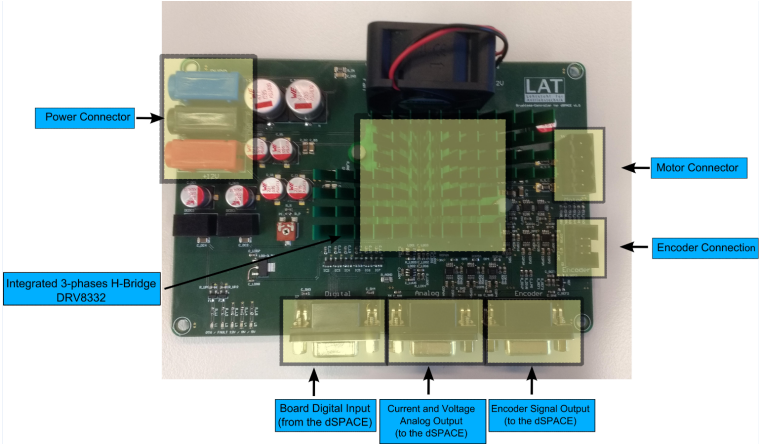

Figure 5.2: Power stage and acquisition test board with controllable via dSPACE platform.

system, compared with other dSPACE commercial devices for signal acquisition proved to be a less noisy, compact and flexible solution.

5.2 Control Setup and Communication Interface for the Development of the InstaSPIN^{TM}-BLDC Control Technique

To develop the InstaSPIN^{TM}-BLDC sensorless control technique, an electrical setup has been implemented on which the algorithm has been tested. The control algorithm has been written in C++ and run on a Texas Instrument TMS320F28335 micro-controller. It is a 32 bit microprocessor core and it is internal clock can run up to 150MHz. The characteristics of this micro-controller are listed in Table 5.2:

The TMS320F28335 has been exploited using an apposite prototyping board provided by Texas Instruments (see Figure 5.3).

An apposite development board has been designed and realized to develop the control. A top view of the board is shown in Figure 5.4. The board exploits the Texas Instrument Three phase PWM motor driver DRV8332 which is a fully integrated three-phase driver, including logic and the three phase H-bridge in a single package. It can supply up to $8A$ continuous phase current per phase with peaks up to $13A$. It can manage supply voltages up to $50V$. It could reach an efficiency up to 97% and its internal logic manages by itself the switching of the 6 power MOSFETs of the H-bridge managing autonomously shoot through problems. [1]

[1]The development board has been designed and realized by Dott. Ing. Emanuele Grasso

TMS320F28335 characteristics	
Producer	Texas Instruments
Model	TMS320F28335
Operating Frequency	150MHz
Supply Voltage	3.3V
On-Chip Flash Memory	256K x 16 bytes
PWM outputs	18
CAN modules	2
SCI Modules	3
ADC Channels	16 * 12 Bit
Pin GPIO	88

Table 5.2: TMS320F28335 micro-controller characteristics.

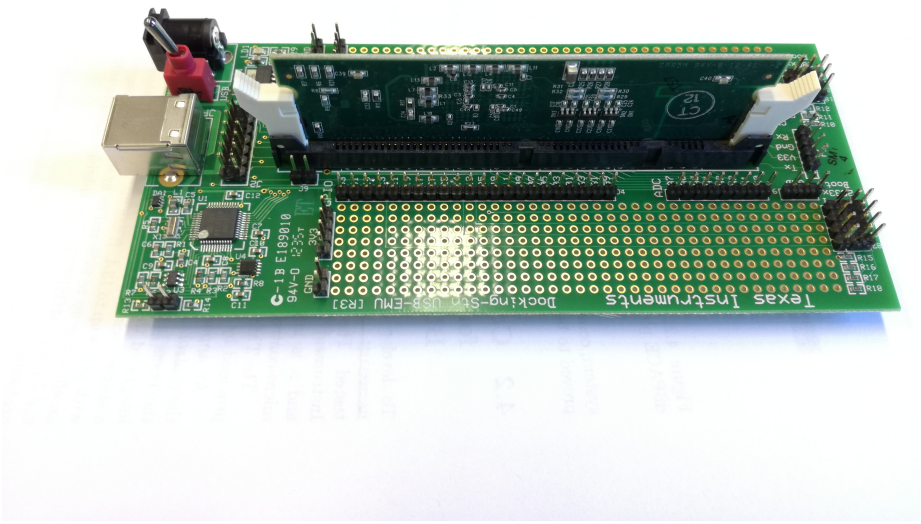

Figure 5.3: TMS320F28335 prototyping board by Texas Instruments.

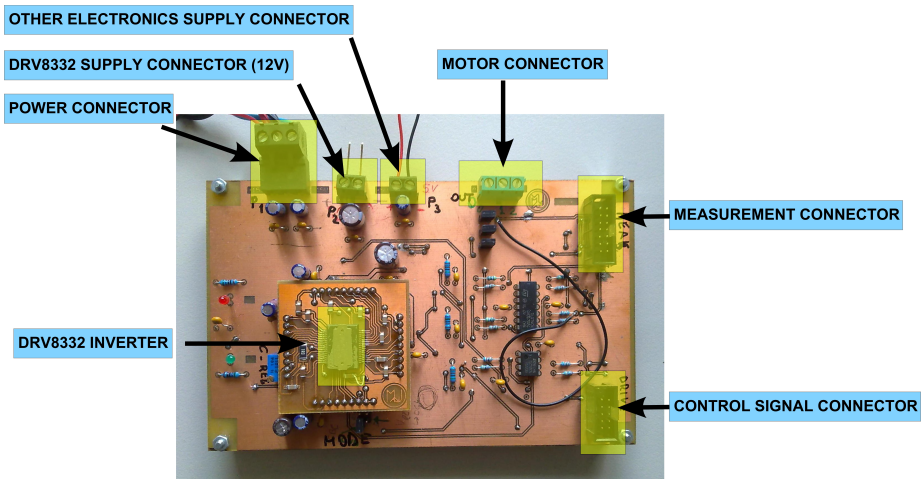

Figure 5.4: Top view of the prototype control board containing the DRV8332.

To control the motor speed, to monitor the control parameters and the measured values (current, voltage, timing) a Matlab interface has been written. It enables to communicate in real time with the micro controller, sending commands and receiving the desired information. Received data can be displayed in a graph or just numerically. This made easier to develop and debug the motor control algorithm.

The complete board setup is illustrated in Figure 5.5. The micro-controller, controls the DRV8332 inverter with three PWM signals and three Reset signals, one for each branch of the three phase H-bridge. PWM signals control the switching of the two MOSFETs of the corresponding branch (A, B or C). Reset signals disable the corresponding branch of the inverter turning off both of the MOSFETs. Voltage measured signals are then fed back to the micro controller in order to perform the sensorless control. Before being fed to the micro-controller, signal is filtered and scaled through a conditioning electronics.

5.3 PIC Test Bench Board Characteristics

For the development of the final implementation of the SMO based sensorless control algorithm it has been necessary to design a new test board. This in order to develop and test the algorithm in a micro-controller embedded code. The processing unit selection is of key importance when designing a motor controller. The factors influencing this choice are among all: device cost, performances, encumbrance and reliability. Obviously the right trade-off among these parameters have to be selected, tuning the choice according to the application needs

of the Laboratory of Actuation Technology of the Saarland University

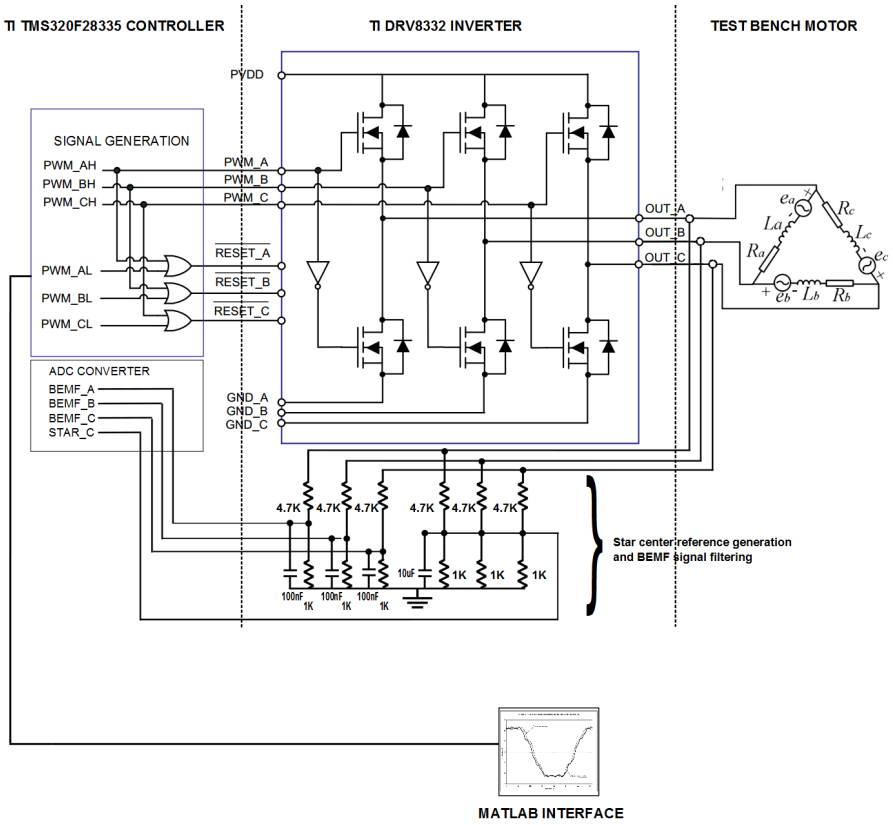

Figure 5.5: Control setup circuit.

PIC32MZ2048EFH100 characteristics	
Producer	Microchip Technology
Hardware Architecture	32 bit with FPU
Operating Frequency	252MHz
On-Chip Flash Memory	2048 KB
ADC resolution	12 Bit
Communication Peripherals	UART, USB, SPI, CAN, I2C
Operating Voltage	3,3V
Number of Pin	100
Dimensions	16*16mm

Table 5.3: PIC32MZ2048EFH100 micro-controller characteristics.

and constraints. For small underwater vehicles such as MARTA AUV, reduced encumbrance and low costs are important parameters together with high system reliability demand. In the last 10 years, small size, high performances micro-controllers such as the Microchip PIC32MZ family have been developed and intensively used for industrial and automotive processes. Hence these devices offer relatively high performances and reliability at low costs. For these reasons for the development of the motor control algorithm a PIC32MZ2048EFH100 has been used. The characteristics of this micro-controller are listed in Table 5.3.

The board in Figure 5.6 is composed of two layers, a control logic and a power stage layer. The control logic layer is composed of the following elements:

- Control unit (PIC32MZ2048EFH100 micro-controller);
- Signal conditioning electronics for filtering and scaling of the measured quantities;
- USB communication interface for real time acquisition and monitoring of the signals of interest;
- Control unit programming port.

The power stage layer is composed by the following elements:

- Power MOSFETs for phase current and voltage control;
- Integrated MOSFET controller interface (TI DRV8301);
- Voltage and current sensing electronics;
- Board voltage supply connector;
- Motor connector;
- Rotational encoder interface and connection;

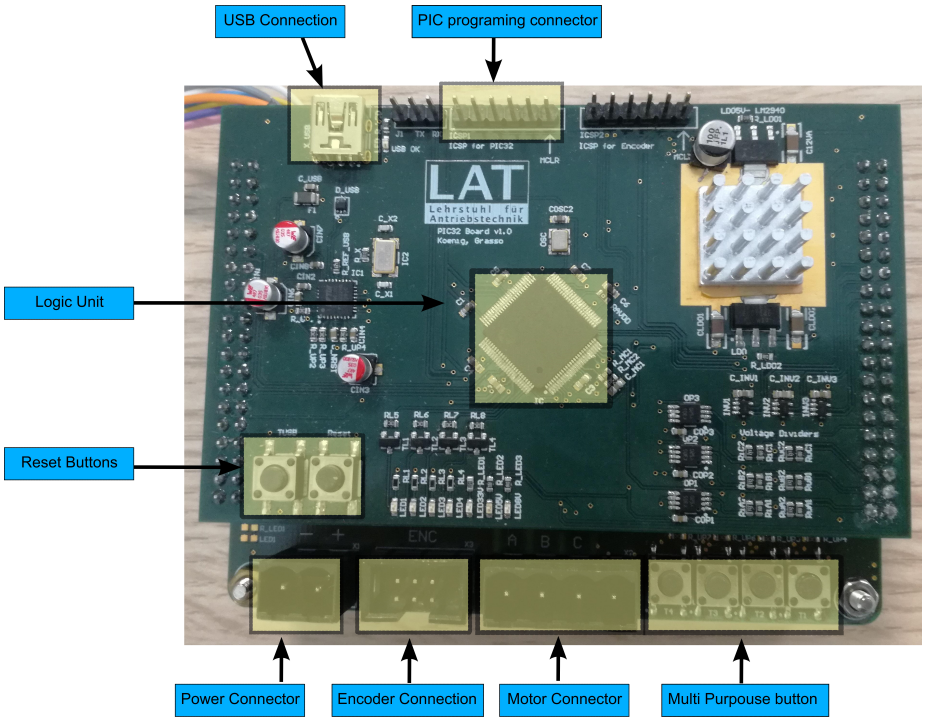

Figure 5.6: Algorithm development and testing board with the PIC32MZ2048ECH100 micro-controller.

- Multipurpose buttons for board control.

The board can operate motors at up to 350W. The particular two layers design makes the power stage board suitable for different control logics and configurations.

Starting from the design layout of Figure 5.6 a smaller motor control drive has been designed. This board has basically the same structure as the PIC test bench board but without all the diagnostic and communication peripherals of a testing device. The board has been designed and assembled in the MDM Lab of the Department of Industrial Engineering of the University of Florence in cooperation with the Laboratory of Actuation Technology (LAT) of the Saarland University. It was designed to control 350W motor power with minimized board encumbrance and is meant to be a multipurpose low-cost motor drive solution for any kind of application. Also in this case, a logic and power stage layer were implemented as shown in Figure 5.7. The board is provided with CAN bus communication peripheral in order to guarantee robust bi-directional communication. The logic layer is provided with a computational unit, the PIC32MZ2048ECH100 which operates the sensorless motor control and the external communication; also part of the signal conditioning electronics is placed

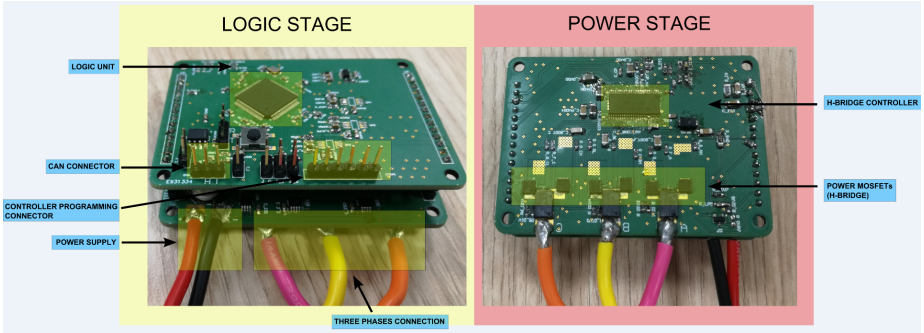

Figure 5.7: Final motor drive design.

in the logic layer. This electronics consists in voltage and current analog signal filtering and rescaling. On the power stage layer, the three phase H-bridge described in section 2.3 is controlled by a three phase H-bridge driver which acts as an interface between the logic unit and the MOSFETs of the H-bridge. Current measurement is preformed through shunt resistors placed in series with the motor phases. Due to time constraints, field test campaigns and the integration of the developed solution on an operating vehicle has not been possible yet. As a future work, it will be necessary to extensively test the device in various operating conditions in order to asses its reliability and robustness facing temperature stress, electrical noise, and long time operation.

5.4 Test Bench for Bollard Thrust Test in a Pool

For the estimation of the Bollard thrust coefficients related to a certain propulsion system, it has been necessary to perform Bollard thrust tests in a testing pool. This is one of the most common way to identify the first quadrant response of a propeller and consequently to characterize its performances. To execute these tests, it has been necessary to design and realize a measurement test bench which operates a measurement of the propeller thrust.

The first solution that has been developed is a cheap and simple test bench described in figures 5.8, 5.9, 5.10 and 5.11. The tested thruster is constrained using an isostatic structure, composed of three joints, a cylindrical one (able to suppress 4 degrees of freedom) and two links (each one able to suppress 1 degree of freedom).

Neglecting the friction on all the other joints and referring to the scheme of Figure 5.8, the longitudinal thrust of the propeller is balanced only by the constraint of the longitudinal link L1, which is given by a simple traction-compression load cell. With the same principle the torque Q applied to the propeller can be measured by estimating the reaction torque on constraints. In particular the force that can be measured with a traction-compression cell on link L2 is directly proportional to the applied torque Q and inversely to the

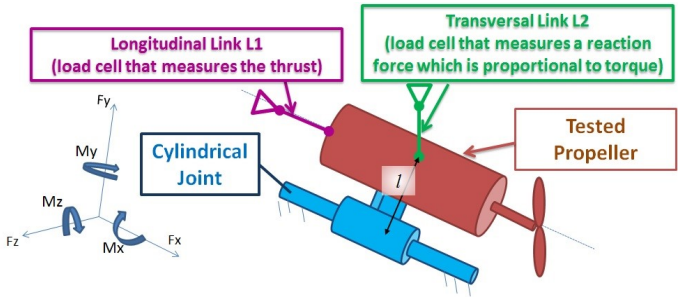

Figure 5.8: Scheme of the proposed testing device.

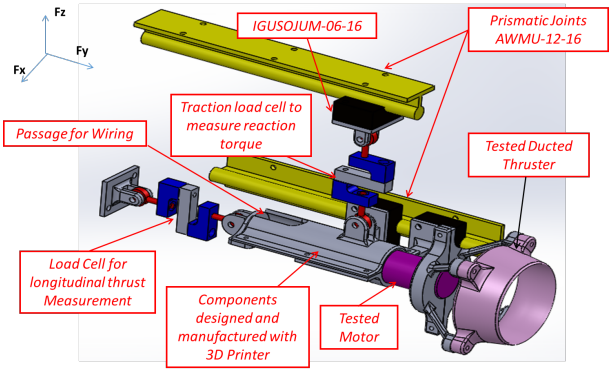

Figure 5.9: CAD of the proposed testing device.

Figure 5.10: Bollard Thrust Test Bench. First version.

distance l between the axis of the link and the one of the cylindrical joint.

The main advantages of the proposed approach can be clearly understood looking at the schemes of Figure 5.8, Figure 5.9 and at the photo of the testing system (Figure 5.10):

- Modularity and Easy Customization: the system is modular and the measurement range can be easily customized by changing the range of the adopted traction-compression load cells or even by adjusting the distance l. As a consequence, it is quite easy to adapt and replicate the same measurement layout for the testing of different propulsion systems.

- Costs and Availability: the cost of a standard traction load cell is quite lower with respect to torque sensors and more in general to corresponding multi-axis sensors (especially water proof sensors).

- Design optimized for the using of fast prototyping techniques: as visible in Figure. 6, the design of the system is optimized to exploit as much as possible the usage of 3D printing.

Low cost anodized aluminum load cells have been used: since they are not designed for underwater applications, they were protected using a plastic spray film. The mechanical interface of the cell with the link was customized as visible in Figure 5.11. In order to improve the measurement quality, signal-conditioning units (cell amplifiers) had to be placed near to the cells. In this case, miniaturized amplifiers were used (Figure 5.11). On the first implementation transducer generated voltages were measured with a voltage meter.
Since rotor position sensors (generally Hall Sensors or Encoders) are not always present, in the proposed testing layout the rotational speed is estimated through electric measurements directly performed on motor drive phases. In particular, the fundamental harmonic drive component is extracted from the driving voltage waveform through a spectrum analyzer. Additional measurements performed on the tested motor and the corresponding sensors are mean temperature of motor windings through a thermocouple in the stator windings and the power absorbed by the motor drive through voltage and current sensors on the DC source used to supply the motor.

Although this setup has been widely used for preliminary characterization of the MARTA AUV propulsion system, the measurements showed a not sufficient repeatability, especially in order to asses the performances of the developed sensorless control described in chapter 4. The cause of measurements inaccuracy were due to joint frictions and low repeatability of load cells measurements, low flexibility facing different motor types that caused load cell misalignment. Furthermore using that measurement configuration, the load cell and signal conditioning electronic had to operate underwater. At low depth this was not optimal and eventually caused a load cell malfunction, due to deteriorated sealing. Another important problem related to that configuration was that the cell measured the thrust in just one direction. This slowed measurement operations,

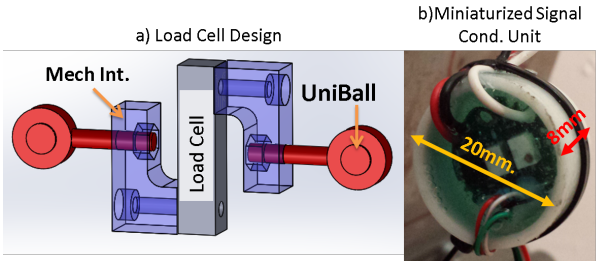

Figure 5.11: Customized load cell interface (a) and miniaturized signal conditioning unit (b).

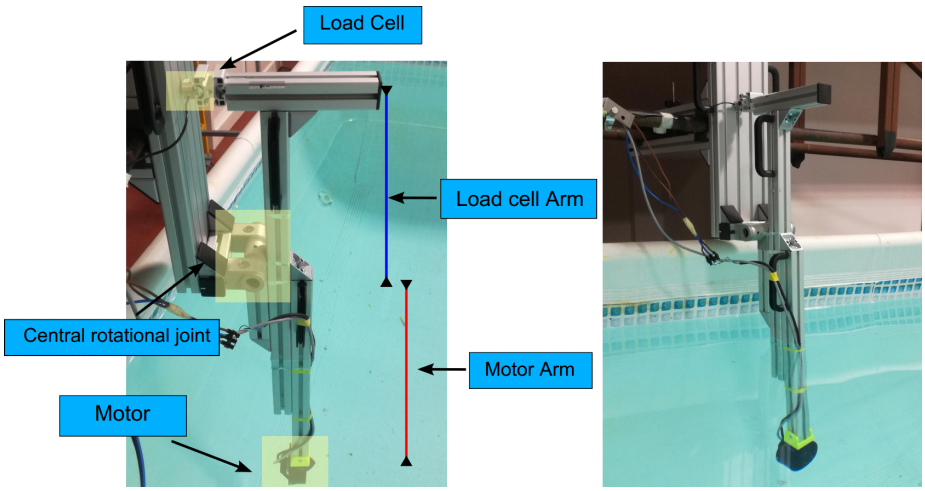

Figure 5.12: Bollard Thrust test bench, second version

since each time the propeller rotation direction was changed, the bench had to be partially disassembled and re-assembled for the new measurement. Hence, in order to increase measurement accuracy, a new test bench has been designed changing the test bench structure. The new design has a main rotational joint in the center as shown in Figure 5.12 [2]. In this case, the thrust measurement is obtained as the result of the ratio between the motor arm and the cell arm (as highlighted in Figure 5.12) of the force exerted on the central joint. This way the load cell do not have to operate in the water, there is no need to move or replace it each time a new motor is tested and different arm ratios between motor and cell arm can be configured in order to test propellers of different size. The length of both arms indeed can be easily regulated in order to set different force ratios. This improves test bench flexibility and accuracy.

As regards the load cell, a factory calibrated one has been selected, able to

[2] A special thank to Per.Ind. Andrea della Valle of the DIEF for his precious help designing and assembling the test bench.

Load cell characteristics		
Specification	unit	Results
Capacity	kg	30
Rated Output	VDC	0±10
Combined Error	%FS	±0.1
Non Linearity	%FS	±0.1
Hysteresis	%FS	±0.1
Repeatability	%FS	±0.1
Creep (30 min)	%FS	±0.1
Zero Balance	%FS	±0.1
Temp Effect on SPAN	%FS/10C	±0.1
Temp Effect on ZERO	%FS/10C	±0.1
Input Resistance	Ω	725±25
Output Resistance	Ω	700±1
Recommended Excitation	VDC	24
Insulation Resistance	MΩ	≥5000
Compensated Temp Range	C	-10 to 40
Operating Temp Range	C	-20 to 55
Safe Overload	%FS	120
Ultimate Overload	%FS	150

Table 5.4: TAS510 load cell characteristics.

perform load measurements both in compression and traction. The characteristics of the TAS510 load cell shown in Figure 5.13 are listed in Table 5.4. The cell is provided with the SIC-A2, a factory calibrated cell amplifier.

For what concerns rotor speed estimation, the measurement of the fundamental motor excitation frequency performed in the previous test bench, was quite inaccurate with a measure uncertainty of the 10%. Hence a different method has been adopted, placing an Hall sensor by the motor shaft as shown in Figure 5.14. Thanks to rotor permanent magnet generated field, hall sensor generates a square wave whose duty-cycle is proportional to the rotational speed. In this case speed uncertainty is due to motor magnet asymmetry; anyway for the T200 BlueRobotics motors presented in subsection 6.2.1, the measurement error is under 5%. Another improvement with respect to the previous measurement setup has concerned the measured signals acquisition method. In this case, a custom load cell and rotor speed signal acquisition board has been designed together with a graphical user interface. Thanks to this interface, it is possible to monitor and store the measured quantities for further processing.

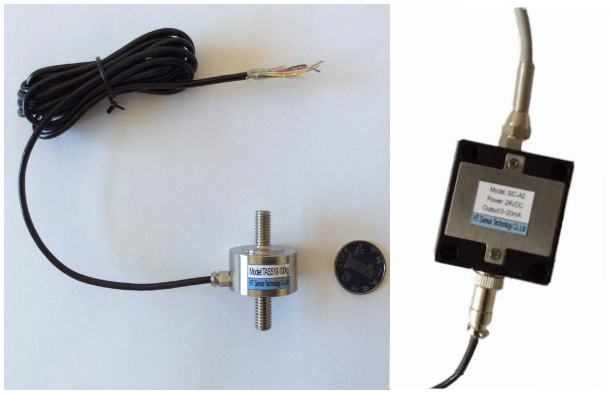

Figure 5.13: TAS510 load cell and related SIC-A2 amplifier.

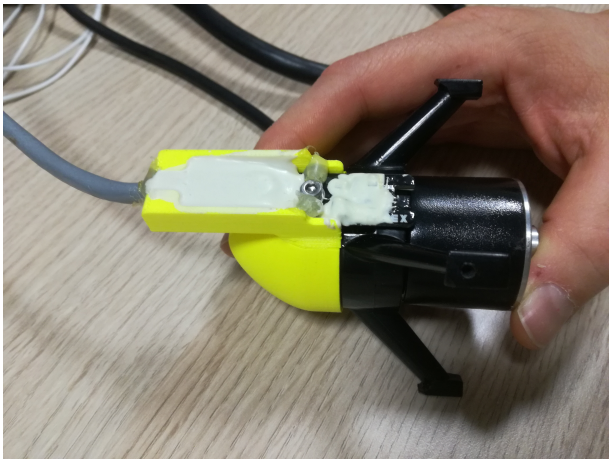

Figure 5.14: Hall sensor placed by rotor magnets for speed estimation.

Chapter 6

Propulsion System Characterization: Parameter Identification and Modeling

The work regarding this thesis was initially focused on the improvement of the existing propulsion system of MARTA AUV. For this reason, comparative field tests have been carried out to demonstrate the improvement which could have been reached with the solutions proposed during the PhD research activity.

In particular, when a new propulsion layout is designed or it is necessary to test an newly implemented one, testing assessment campaigns are performed to evaluate the performance of the developed solutions.

For these reasons, concerning the vehicle propulsion system, it has been necessary to set-up a test bench to measure its performances in static conditions. The implementation of this test bench is described in section 5.4. Other field test experiments exploiting the on board sensors of the AUV have been performed to highlight the proposed improvement and to validate the test bench results.

The first implementation of the MARTA AUV propulsion system is illustrated in Figure 6.2. It is composed of six thrusters used to control all the degrees of freedom of the vehicle, except the roll one. This propulsion layout is quite similar to other existing torpedo-shaped vehicles, e.g. the Folaga AUV produced by Graaltech [33]. A PMSM motor coupled with a fixed pitch propeller through an epicycloidal gearbox controls each thruster. The two rear propulsion thrusters are intended to perform surge and yaw motions. They are not incorporated in the hull as the vertical and lateral thrusters are. For this reason, the propellers used for the rear thrusters are different from the lateral and vertical ones. Rear thrusters are equipped with Ka-4-70 propeller type ducted with a 19-A nozzle; the other four thrusters, due to the particular con-

Main Features of the Motor	
Property	Value
Model	Maxon386676
No-load speed	31000rpm
Nominal Speed	28300rpm
Torque Constant	5.53 mNm/A
Speed/torque Gradient	48.4 rpm/mNm
Nominal Voltage	18V
Nominal Current	9.11A
Nominal Torque	49mNm
Speed Constant	1730rpm/V
Planetary gearbox reduction ratio	1:3.8 or 1:14

Table 6.1: Maxon386676 Motor electrical and dynamic characteristics [54].

ditions they work in, are equipped with customized propellers type. In order to obtain a modular system, with simplified maintenance, on the first propulsion setup each propeller exploits the same electric motor and actuation system: a PMSM 100W Maxon motor with main data reported in Table 6.1.

Each motor is controlled with a commercial hobby sensorless drive system performing a very robust sensorless motor control based on the BEMF zero crossing technique explained in subsection 3.1.1. This kind of controller has the advantage of being really cheap, reliable, and of small encumbrance. Although it does not perform a real speed or torque control. It is controlled through a servo signal reference which regulates the PWM duty-cycle on the three phases and the rotor direction. For this reason, the propeller speed depends on the torque which is applied to it and only a rough estimation of it can be performed.

Concerning the motor sealing, MARTA AUV has an operating depth of over 100 meters, hence these kind of motors have to be protected from the external pressure and from the contamination of the surrounding water. External pressure compensation and protection of the electrical and mechanical components from corrosion and excessive overheating is obtained with an inert liquid. This solution corresponds to the layout of Figure 6.1. The motor case is filled with an inert fluid such as an halogenated hydrocarbon (as example Florinert), a dielectric oil (silicon or carbon based) or a bio-compatible organic oil in order to preserve the surrounding environment from any contamination.

Finally, attention has to be payed to MARTA AUV navigation system. Initially it was implemented without a vehicle dynamical model and based on a kinematic one with the support of other navigation sensors such as DVL (Doppler Velocity Log), FOG (Fiber Optic Gyro), IMU (Inertial Measurement Unit) and a pressure sensor. Although this navigation strategy proved to be accurate and efficient, it is strongly dependent on the on board sensor data and could be improved thanks to the knowledge of the AUV dynamics [55].

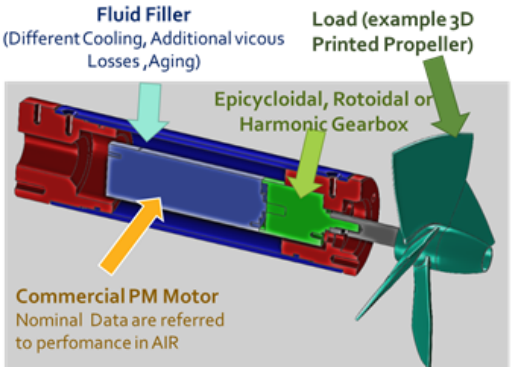

Figure 6.1: MARTA AUV motor sealing, first implementation.

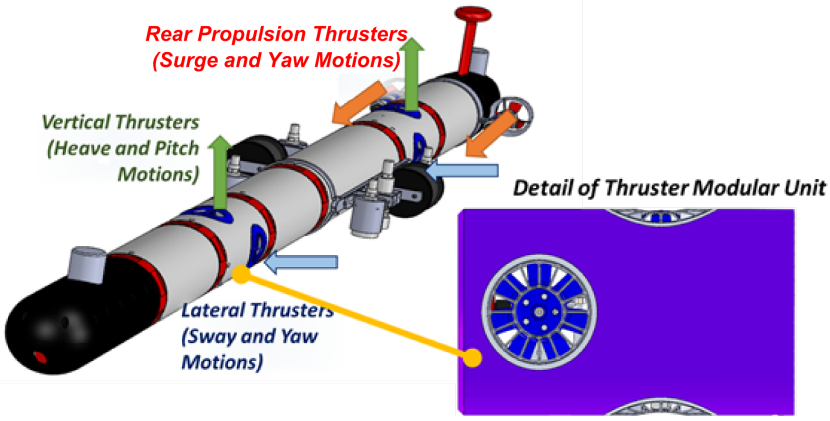

Figure 6.2: MARTA AUV propulsion layout.

6.1 Propulsion System Modeling

Navigation strategies of underwater vehicles are mainly based on on board sensors such as GPS, DVL, Depth Sensor, Acoustic Positioning Sensor and inertial sensors. A common approach is the fusion of the data provided by these sensor to operate an estimation of the vehicle position and an adequate navigation strategy. With the inertial on board sensors it is possible do develop a vehicle kinematic model and operate a dead-reckoning navigation. However purely kinematic based model simplifies too much the real behavior of the vehicle thus is unsuitable to accurately describe the evolution of its navigation state and, in absence of other sources of information, frequent resurfacing are needed to reset the position estimation filter. More information can be gathered by exploiting a dynamic model of the vehicle; these informations concern the force and the moment exerted on the vehicle by the propellers and they are obtained by modeling the hydrodynamics and the propulsion system of the vehicle itself. The latter is achieved by an experimental characterization of the propeller behavior on the four quadrant of operation and by defining a relation between the propeller rotational speed and the corresponding generated thrust and torque. The thrust delivered by a propeller along the shaft direction, can be expressed by the following equation:

$$T_p = \rho n^2 d^4 K_t(J), \tag{6.1}$$

while the resistant torque needed to move the propeller is expressed by the following:

$$\tau_r = \rho n|n| d^5 K_q(J), \tag{6.2}$$

where the following symbols are adopted:

- n Hz rotation speed;
- ρ $\frac{\text{kg}}{\text{m}^3}$ is the fluid density;
- u $\frac{\text{m}}{\text{s}}$ advance speed;
- d m is the propeller diameter;
- $J = \frac{u}{nd_e}$ is a dimensionless advance coefficient;
- p m is the propeller pitch.

Concerning K_t and K_q are respectively the thrust and torque dimensionless coefficients. Another important coefficient is the efficiency coefficient η:

$$\eta = \frac{K_t J}{K_q 2\pi}, \tag{6.3}$$

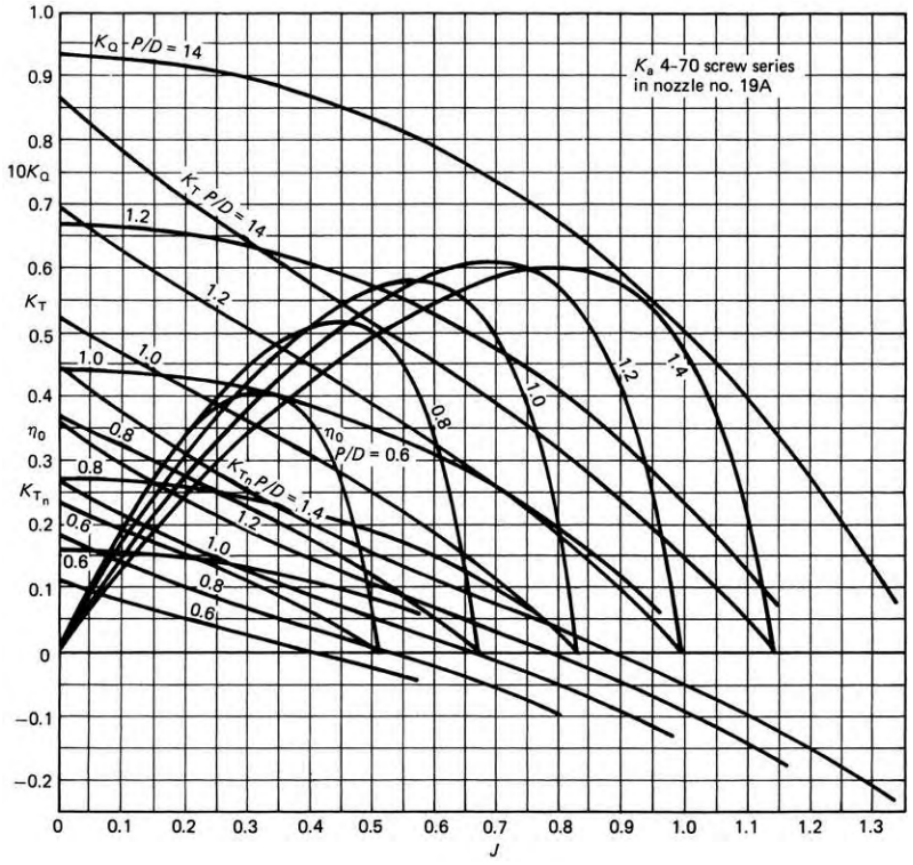

Figure 6.3: Thrust, torque and efficiency coefficient patterns of a $Ka-4-70$ screw series propeller ducted with a 19-A nozzle as a function of J and the $\frac{p}{d}$[10].

In (6.1), (6.2) and (6.3) it is highlighted the dependency of these coefficients on the advance one. According to the propeller type, experimentally derived curves of these coefficients exist in literature. In Figure 6.3 the coefficient patterns obtained with a Ka-4-70 screw series propeller for different pitch/diameter ratios are shown. It is important to highlight that being dimensionless coefficients there is no unit of measure in the ordinates axis and for sake of readability of the graph, the K_q coefficient has been plotted ten times its actual value. Compared with the K_t and efficiency coefficients indeed, K_q is significantly smaller. With these values it is possible to obtain an estimation of the propeller delivered torque and thrust according to the rotational and advance speed of the propeller itself.

A possible approach, starting from these charts, is the generation of three-dimensional look-up tables depending on the advance and rotational speed. Although the use of these reference curves is not always convenient in order to

develop a navigation strategy. The results would be hardly exploitable in a mathematical model in which, as an example, function derivatives should be calculated at each iteration. Furthermore, in literature just a limited range of the coefficient is represented. Negative advance speed range is not represented as well as the values of J higher than the ones for that K_t or K_q are null. As a consequence, another possible approach, is the generation of an analytical expression of these coefficients in order to achieve a trade-off between computational efficiency and model accuracy [56], [55]. In particular, since the propeller generated moments can be neglected if appropriate vehicle design criteria are followed, the analysis is concentrated on the definition of a function expressing the generated propeller thrust as a function of J and n:

$$T_p = f(n, J). \tag{6.4}$$

From Figure 6.3 it can be noticed that the trend of K_t as a function of J, can be approximated with a negative slope linear function in the positive rotational and advance speed range. For this reason, an approximated expression of $K_t(J)$ can be determined by properly identifying the parameters of:

$$K_t(J) = -aJ + b. \tag{6.5}$$

By solving (6.1) with respect to K_t the following expression is obtained:

$$K_t = \frac{T_p}{\rho n^2 d^4}, \tag{6.6}$$

which can be substituted in (6.6):

$$\frac{T_p}{\rho n^2 d^4} = -aJ + b. \tag{6.7}$$

Hence the resulting expression of the propeller thrust is given by a linear function whose parameters depend on the rotational speed n while the independent variable J is a function of the advance speed:

$$T_p(n, J) = -a\rho n^2 d^4 J + b\rho n^2 d^4 = m_t(n)J + q_t(n). \tag{6.8}$$

To define $m_t(n)$ and $q_t(n)$ it is necessary to define where the function crosses the abscissa and ordinate axes. The intersection with the x-axis is obtained for a null value of the propeller thrust $T_p = 0$ which is verified when the propeller is not rotating ($n = 0$) or when $K_t = 0$ which means that the fluid linear momentum is not modified by the propeller. The first case is obviously not of interest, the second case instead corresponds to $J = \frac{p}{d} \Leftrightarrow u = pn$. Hence, the function defined in (6.8) crosses the abscissa in $(\frac{p}{d}, 0)$. The intersection with the y-axis is obtained for a null value of the advance coefficient $J = 0$. $T_0(n)$ is called Bollard Thrust and it is the propeller thrust delivered at a given n when

$u = 0$, as a consequence it is only dependent on the rotational speed. Thus the ordinate axis is crossed in $(0, T_0(n))$. It is possible to define the parameters of (6.8) as:

$$q_t(n) = T_0(n) = K_{t0}\rho n^2 d^4, \tag{6.9}$$

$$m_t(n) = \frac{-T_0(n)d}{p} = \frac{-K_{t0}\rho n^2 d^4 d}{p}, \tag{6.10}$$

with which the following expression of $T(n, u)$ is obtained:

$$\begin{aligned} T_p(n,u) &= \frac{-T_0(n)d}{p} J + T_0(n)\Big|_{\left(J=\frac{u}{nd}\right)} = \\ &= \frac{-T_0(n)du}{pnd} + T_0(n) = \\ &= \frac{-T_0(n)u}{pn} + T_0(n). \end{aligned} \tag{6.11}$$

An analytical expression of $T_0(n)$ is obtained by experimental measurements of the propeller thrust in bollard conditions. From (6.10) it can be seen that it has a parabolic trend with respect to the propeller rotational speed and it is proportional to a constant K_0:

$$T_0(n) = K_{t0}\rho n^2 d^4 = K_0 n^2, \tag{6.12}$$

Equation (6.11) becomes

$$T_p = \left(K_0 n^2 - \frac{K_0 n u}{p}\right). \tag{6.13}$$

where

$$K_0 = \frac{T_0}{n^2}\Big|_{u=0}. \tag{6.14}$$

The expression of (6.13) is still relative to the propeller first quadrant of operation. By making a set of assumptions [55], it is possible to define a more general expression of the thrust. Concerning the second quadrant of operation $(J < 0, n > 0)$ it is reasonable to assume that the working point is close to the ordinate axis indeed it is generally an unwanted condition. For this reason, the thrust in that region can be considered constant and equal to $T_0(n)$. Concerning the behavior of the propeller, when $(J > \frac{p}{d}, n > 0)$, it is a condition in which the propeller does not deliver any thrust because the propeller is not able to modify the flow direction; still, this condition does not impose a negative thrust, for this

reason the propeller contribution can be considered null in that range of advance speed. The third and the fourth quadrants can be obtained by mirroring the behavior of the propeller in the first and second quadrant respectively. This condition is true in case the propeller has a symmetrical behavior concerning both the reverse and the forward thrust. In case a not symmetrical propeller is used, two thrust coefficients can be identified: a positive thrust coefficient K_{0+} concerning quadrants I and II and a negative coefficient thrust K_{0-} concerning quadrants III and IV. Under these assumption it is possible to obtain an expression of the propeller thrust on the four quadrants [55]:

$$T(n,u) = \left(K_{0_{+/-}} - \frac{K_{0_{+/-}} |n| g(sign(n) \cdot u)}{p} \right). \tag{6.15}$$

Where $g(x)$ is a piecewise function defined in the following way:

$$g(x) = \begin{cases} 0 & if \quad x \leq 0 \\ x & if \quad 0 < x \leq |n| \cdot p \\ |n| \cdot p & if \quad x > |n| \cdot p \end{cases} \tag{6.16}$$

The resulting function is continuous but not differentiable and it makes possible to determine the thrust on the longitudinal direction as a function of the propeller rotational speed n and the velocity of the fluid along the thrust direction u.

6.2 Propulsion Field Test and Parameter Identification

A first improvement of the initial navigation strategy of MARTA AUV has been the introduction of a dynamic model. For this reason in addition to the identification of the propeller characteristic parameters described in section 6.1, a rough estimation of a law which would relate the propeller speed and the motor reference has been performed thanks to pool tests. It consisted in measuring the rotational propeller speed with an external Hall sensor placed on the rotor shaft, and in creating a function interpolating the measured speed as a function of the reference servo signal fed to the motor controller. Clearly the actual propeller speed is influenced by several factors as water density, vehicle battery level, rotor friction and vehicle advance speed. As a consequence the level of accuracy of this estimation is quite low and highly dependent on environmental conditions. Other propulsion layout improvements have concerned the propeller design. This in order to establish the optimal shape and dimensions of MARTA AUV rear propellers and thrusters. It has been necessary to test different propellers of various dimensions and pitch over diameter (p/d) ratio. Concerning the structure of MARTA AUV shown in Figure 6.2, in the next sections, the author will refer to the two motors on the vehicle tie deputed to the *surge* and *yaw* motion as *"rear propellers"*. The other motors incorporated on the hull deputed to the *pitch*, *heave* and *yaw* motion will be called *"thrusters"*.

6.2.1 Bollard Thrust Test for the Characterization and Optimization of MARTA AUV Propellers

Concerning propulsion layout optimization, the choice of the optimal propeller shape depends on various factors. The propeller type has been chosen in order to obtain a good performance at a relatively low advance speed by minimizing the design and testing costs. There is a wide and complete literature about Ka-4-70 series propellers ducted with a 19-A nozzle [10], [57], [58]; for this reason it can be easily adapted to a specific application without sophisticate fluid dynamics testing. The propeller parameters which have been investigated were the diameter, the number of blades and the pitch over diameter (p/d) ratio. These parameters had to be tuned according to the motor characteristics. Clearly given a fixed rotational speed, the more the propeller diameter and pitch over diameter ratio are high, the higher the thrust is. Although the optimal layout depends also on the motor electrical power consumption, the working condition (maximum current, thermal stress) and desired advance speed. With the test bench illustrated on section 5.4 the following measurements have been taken. In Figure 6.4 and Figure 6.5 the delivered thrust is plotted as a function of the power absorbed by the motor and of the rotor speed considering different propeller diameters. For these measurements, it has been used a gearbox with a reduction ratio of 1:14 and a p/d ratio of the propellers of 1.4. These measurements made possible to define optimal propellers dimensions. Obviously, the main criteria is to maximize the thrust delivered by the propeller while maintaining optimal working conditions of the motor and minimum power consumption. The Maxon motor described in Table 1 reaches its optimal working point at a speed around 28000rpm. According to Figure 6.4 the best performance in terms of power consumption is obtained with a propeller of 85mm in diameter. Of course the use of propellers with lower diameter guarantee better working conditions as shown 6.5 but power efficiency has been privileged. According to Figure 6.4 the optimal choice is thus a 85mm diameter propeller.

It is important to notice that the thrust measurements of Figure 6.4 and Figure 6.5 were performed without a nozzle. By adding it, it is possible to obtain an increase in terms of thrust which is between 20% and 30%, as shown in 6.6 and Figure 6.7. The same can be observed considering the thrust delivered by the propeller as a function of the power absorbed by the motor driver; in that case at a fixed current value, the use of nozzle causes an increase in terms of thrust of more than 90%.

Vertical and lateral thrusters are incorporated in the hull of MARTA AUV as shown in Figure 6.8. This limits the water flow conveyed by the propeller and it complicates the design a proper nozzle in order to maximize the thrust. In these conditions a Ka-4-70 propeller was not efficient: for this reason it has been designed a customized propeller like the one showed in Figure 6.9.

For the selection of thruster propeller, a fixed propeller diameter has been used because it had to fit the vehicle thruster tunnels. These holes are partially clogged by the motor itself and its supports, for this reason it has been used the largest possible propeller diameter to maximize the conveyed flow. Hence to

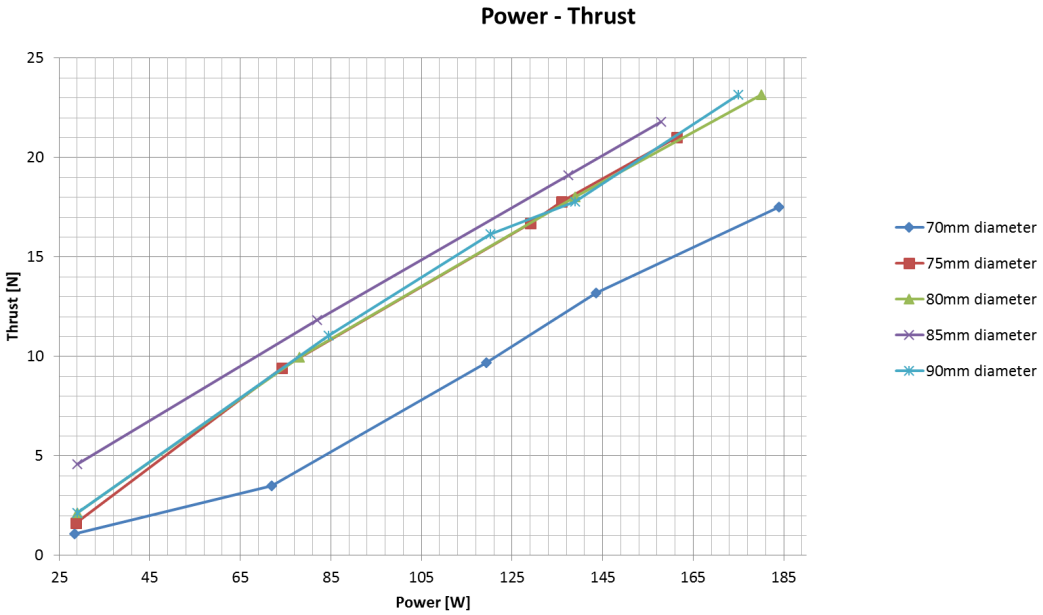

Figure 6.4: MARTA AUV rear propellers: delivered thrust as a function of the electrical power absorbed by the motor for various propellers diameters.

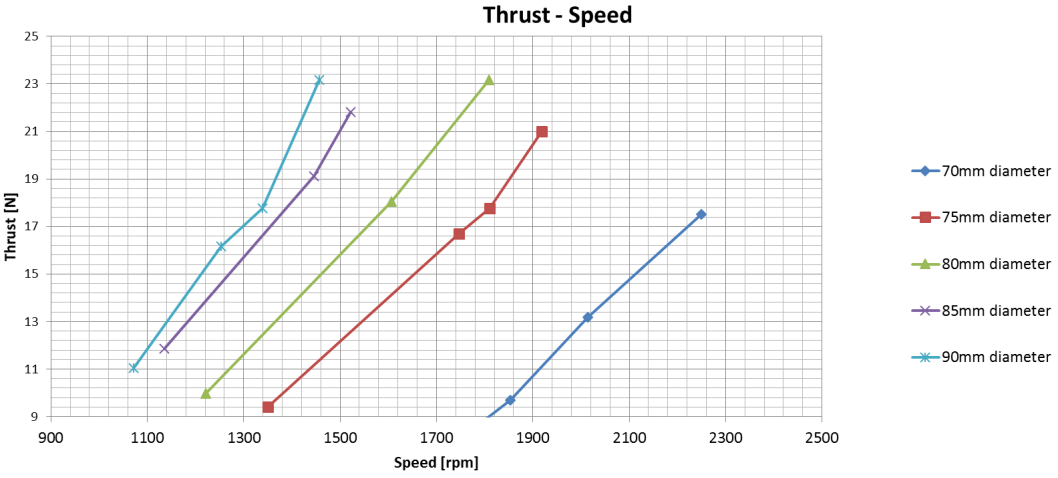

Figure 6.5: MARTA AUV rear propellers: delivered thrust as a function of the speed for various propellers diameters.

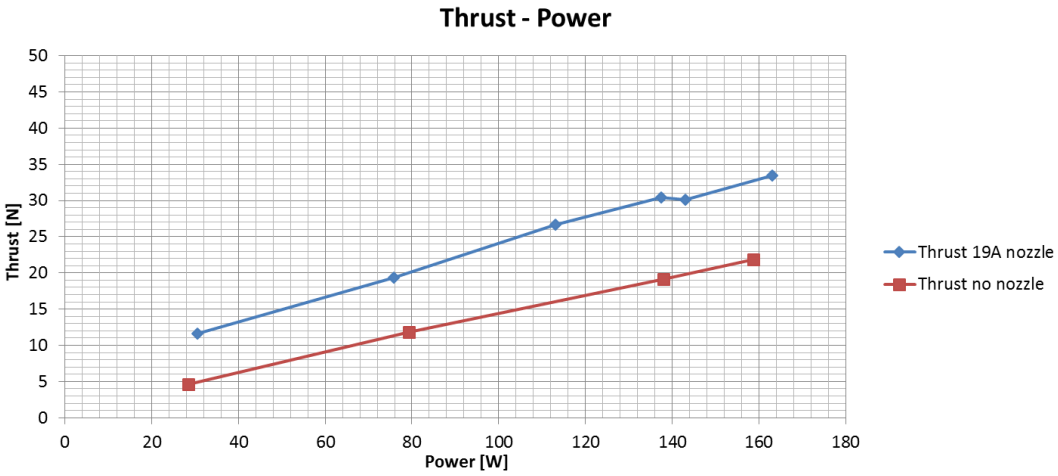

Figure 6.6: MARTA AUV rear propellers: delivered thrust as a function of the electrical power absorbed by the motor for an 85mm diameter propeller.

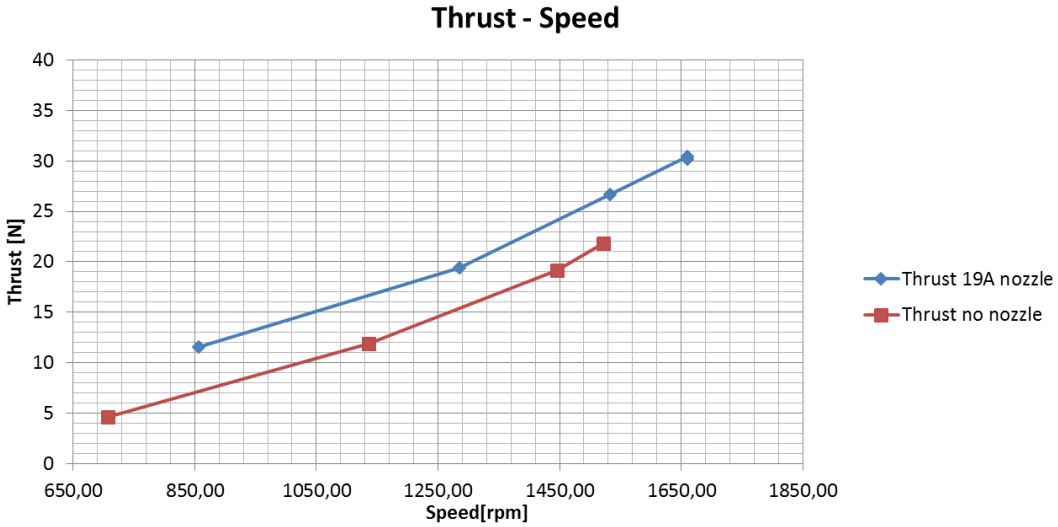

Figure 6.7: MARTA AUV rear propellers: delivered thrust as a function of the speed for an 85mm diameter propeller.

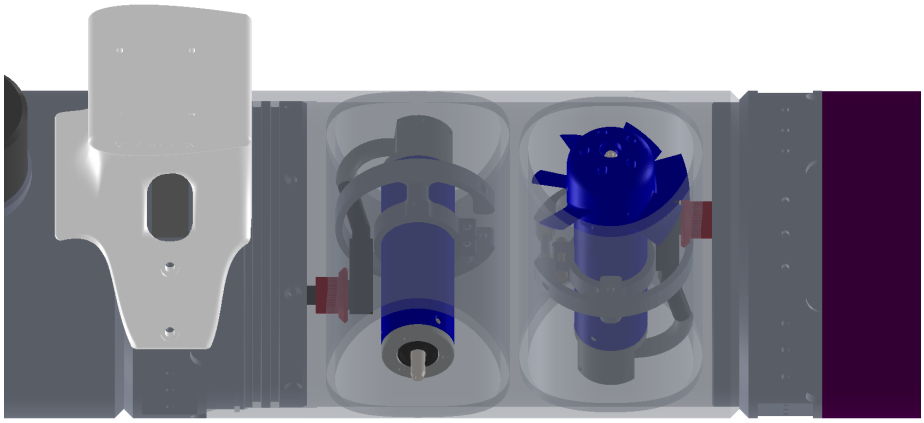

Figure 6.8: Thruster incorporated in the hull of the vehicle.

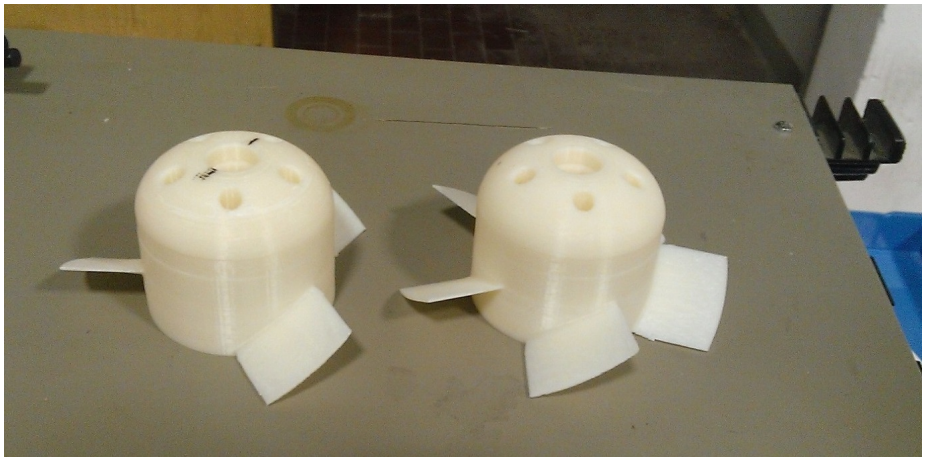

Figure 6.9: Thruster propellers design.

Figure 6.10: Thrust measurement configuration for thruster propellers.

determine the optimal propeller geometry, various shapes have been tested, by varying just the number of blades and the p/d ratio. To simulate the effects of the hull, in which the propeller is incorporated, measurements have been taken with the propeller turning inside a mockup of the hull channel. Measurement setup is shown in Figure 6.10. Due to the working conditions and to the particular shape of the propeller, it is difficult to achieve the thrust delivered by the Ka-4-70 propeller ducted with the nozzle. Figure 6.11 and Figure 6.12 show the thrust delivered by various configurations of the thruster propellers. According to Figure 6.12 the propeller which delivers the higher thrust for a given motor electrical power is the 86mm diameter, 5 blades propeller with a p/d ratio of 1.4. It is also the one which delivers the highest thrust as a function of the speed.

The execution of bollard thrust tests in a testing pool is one of the most common way to identify the first quadrant response of a propeller, calculating the values of the thrust coefficient $K_t(J)$ for a null value of the advance coefficient J. These information can be exploited if the propeller speed information is available during navigation in order to feed a dynamical model of the vehicle for pose estimation during navigation as described in section 6.3. According to the bollard tests described above, for the rear thrusters, it has been selected the Ka-4-70 series propeller ducted with a 19-A nozzle with 85mm diameter and a

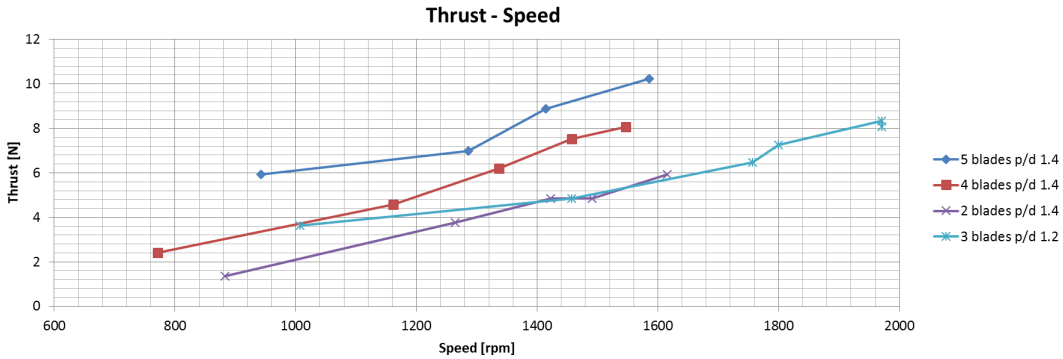

Figure 6.11: MARTA AUV thrusters: thrust as a function of the rotor speed for various propellers configurations.

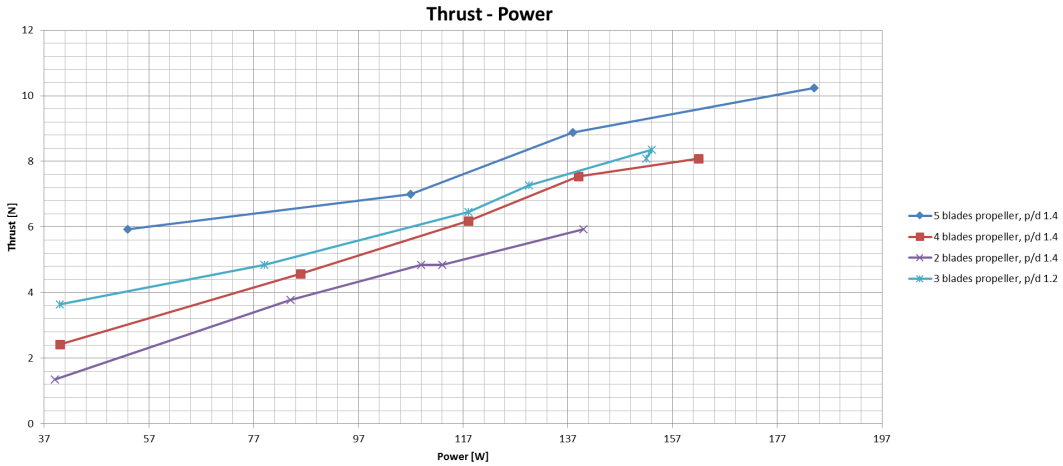

Figure 6.12: MARTA AUV thrusters: thrust as a function of the motor electrical power for various propellers configurations.

Figure 6.13: Thrust coefficient of the Ka-4-70 series propeller, 85mm diameter ducted with a 19-A nozzle.

p/d ratio of 1.4. A 86mm diameter 5 blades propeller with a p/d ratio of 1.4 has been selected for the thrusters. The parameters of interest can be sourced by using the speed thrust measurements above shown according to (6.14). The Ka-4-70 series propeller has a symmetric layout, for this reason the behavior of the first and third quadrant can be considered equivalent[55]. Thus a single value of K_0 is identified by taking into account the thrust measurement of the propeller operating in the positive direction. From Figure 6.13 a value of $K_0 \approx 0.044$ is measured.

The same parameter is estimated by taking into account the above selected propeller for the vehicle thrusters. In Figure 6.14 it is shown that for a thruster propeller with 86mm diameter, 5 blades and a p/d ratio of 1.4, a value of $K_0 \approx 0.017$ is measured. The value highlights the difference in terms of thrust between the two propellers. The thruster propeller is clearly less performing in terms of maximum thrust. This is due to the non optimal shape of the propeller itself and to the clogging effect of the motor which limits the fluid flow through the tube. The low performance of the thrusters limits the maneuverability of the vehicle also due to its length which is approximately 3.7m. Also concerning the rear propeller maximum thrust, it has often being found not sufficient to operate in scenarios where moderate current drift were present.

Consequently, more performing motor control systems have been investigated and tested in order to obtain higher performances in terms of maximum thrust, reliability, encumbrance and cost.
As regards the propulsion layout, a further improvement concerned the introduction of a new propulsion system. The BlueRobotics T200 thruster is a commercial complete propulsion system with its own electrical motor, propeller and duct. It is shown in Figure 6.15.

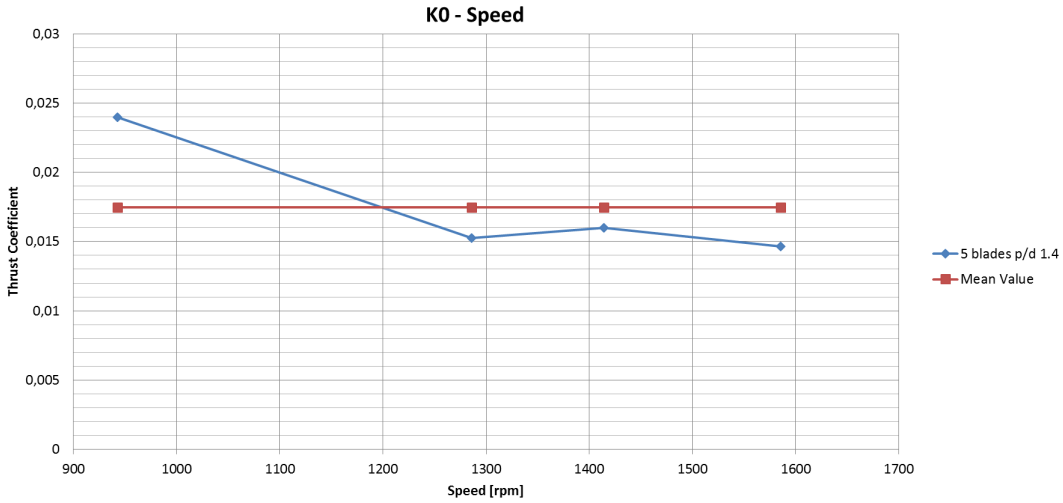

Figure 6.14: Thrust coefficient of the thruster propeller.

Figure 6.15: BlueRobotics T200 Thruster.

Main Features of the Motor	
Property	Value
Model	BlueRobotics T200
Speed Range	300-3800rpm
Nominal Speed	28300rpm
Nominal Voltage	20V
Maximum Power	350W
Coil Resistance	$0.18 \pm 0.01\Omega$
Coil Inductance	$0.077 \pm 0.008mH$

Table 6.2: BlueRobotics T200 Thruster electrical and dynamic characteristics [59]

6.2.2 Bollard Thrust Test for the Characterization of the T200 Thruster System

Differently from the Ka-4-70 series propeller, the BlueRobotics T200 has its own customized propeller that is not symmetric, for this reason different values of thrust are measured when operating the motor in positive or negative direction. Also for the T200 thrusters Bollard Thrust tests have been performed in order to asses the performances of the propulsion system and to identify its dynamic parameters. In Figure 6.16 it is shown the thrust delivered by the propeller as a function of the rotational speed. These results are in accordance with the results presented in the BlueRobotics official website. By comparing 6.17 and 6.6 it is clear how the behavior of the T200 propeller and the previous one is not really different in terms of efficiency. Concerning the Bollard thrust instead, it is interesting to note that compared to the behavior of the Ka-4-70 series propeller above measured there is a remarkable increase in terms of maximum thrust. This is due to the higher power of the T200 motor which permits operate at higher currents with respect to the Maxon386676 motor.

The T200 thruster can be operated at up to 350W continuously while the windings of Maxon386676 would quickly be damaged in these operating conditions. In addition to that, the epicycloidal gearbox which is mounted on the rotor shaft of the Maxon in order to reduce the motor generated torque, reduces the conversion efficiency and limits the rotational speed of the propeller. The gearbox indeed has an efficiency of 80%, needs to be lubricate and its optimal input rotational speed is 8000rpm. To reach a thrust of around 50N it would be necessary to impose an input speed of around 30000rpm which would quickly degrade the gearbox itself. The T200 thruster, instead, can operate in direct drive thanks to a lower K_v coefficient thus avoiding the limits imposed by a gearbox. It has sealed woundings and operates directly in contact with the water, so it has good heat dissipation properties and do not need to be lubricate. Another important advantage is the compact design of the T200 thrusters and the fact that they do not need oil filling for the motor seal housing. The previous and

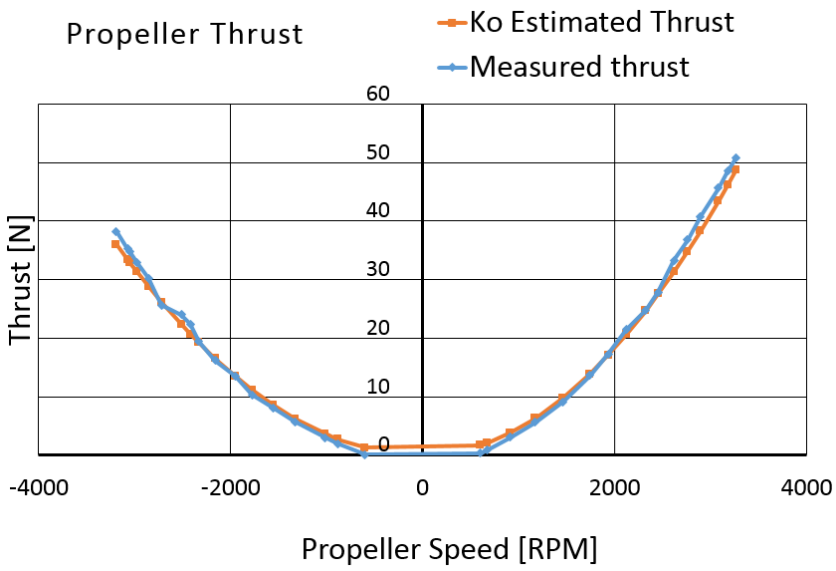

Figure 6.16: Bollard thrust of the T200 thruster as a function of the propeller rotational speed.

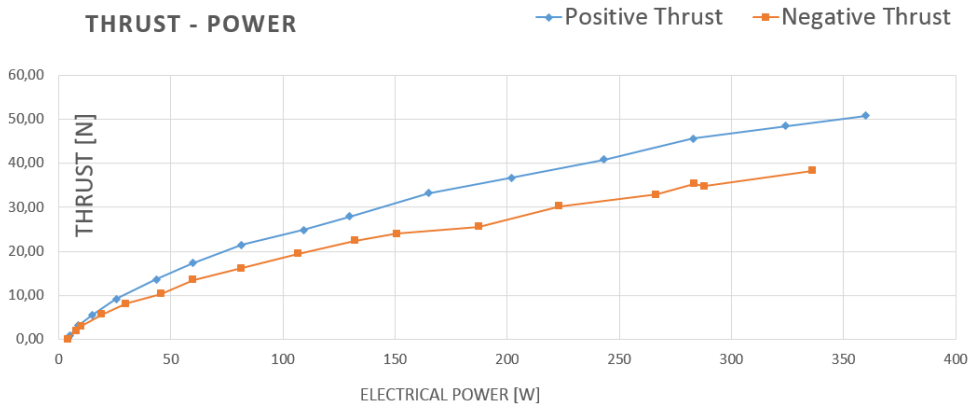

Figure 6.17: Bollard thrust of the T200 thruster as a function of the motor electrical power.

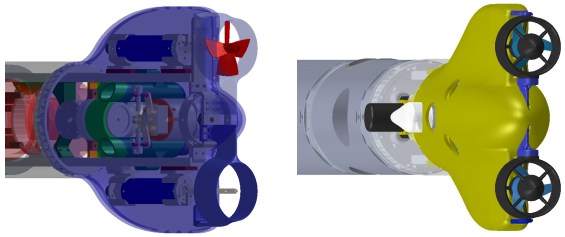

Figure 6.18: Rear propeller setup. With Maxon386676 motor on the left and with T200 BlueRobotics on the right.

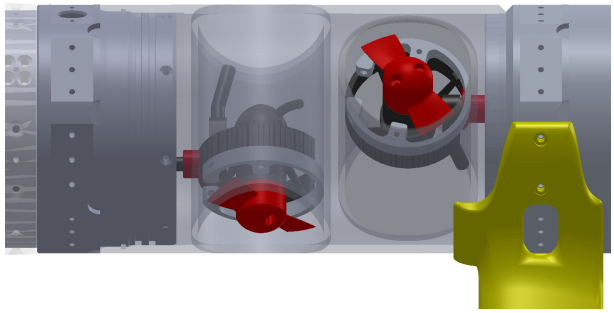

Figure 6.19: Thruster setup. Motor fastening system exploiting an expansion clamp.

the proposed setups are shown in Figure 6.18.

The same motors have been used for the thrusters propellers. In this case it has not been possible to use the nozzle and the propeller of the T200 system. A propeller similar to the one used for the previous configuration has been designed because symmetric propeller was needed. Two solutions have been designed. The first one was based on the design of the previous implementation, as shown in Figure 6.8. The motor is held through an expansion clamp which is fixed to the hull thanks to friction as shown in Figure 6.19.

Bollard thrust measurements of this configuration were performed using the same setup as in Figure 6.10. Three different propellers have been tested: a three blades propeller with $\frac{p}{d} = 1.2$ ratio, a three blades propeller with $\frac{p}{d} = 1.4$ ratio and a two blades propeller with $\frac{p}{d} = 0.6$ ratio. As visible in Figure 6.20 the improvement in terms of maximum thrust with respect to Figure 6.11 is remarkable; compared with the results of the previous configuration the maximum trust is almost doubled.

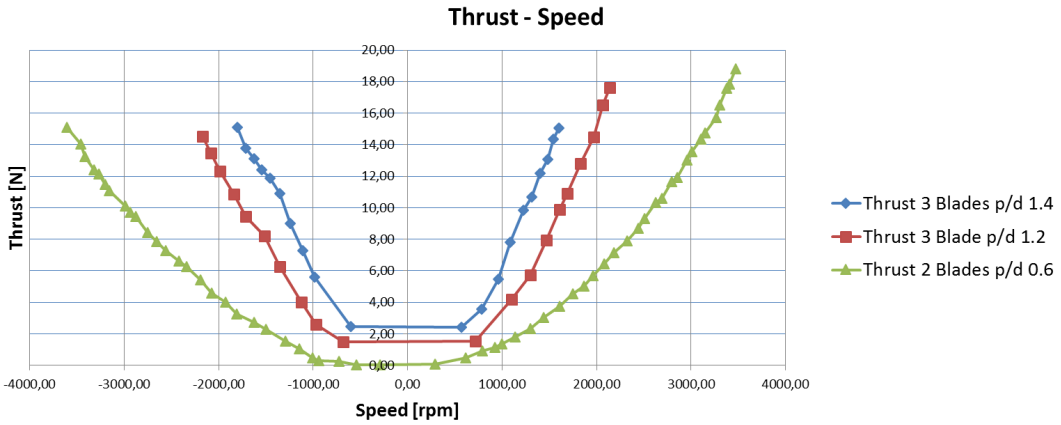

Figure 6.20: First configuration. Bollard thrust of the T200 motor in the tube for various propeller configurations as a function of the propeller rotational speed.

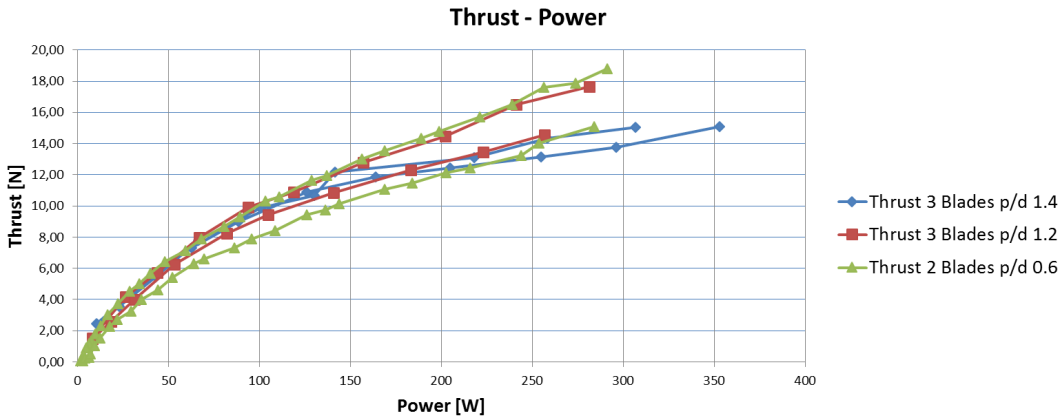

Figure 6.21: First configuration. Bollard thrust of the T200 motor in the tube for various propeller configurations as a function of motor electrical power.

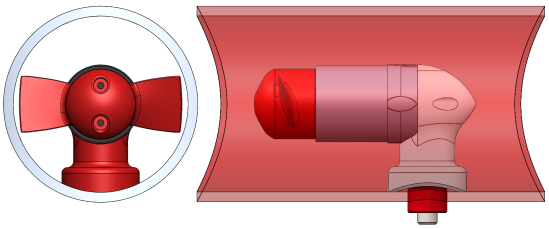

Figure 6.22: Second configuration proposed for the MARTA AUV thrusters.

The two blades propeller with $\frac{p}{d} = 0.6$ ratio has been selected, being the one which delivers the highest thrust. By comparing the thrust trend as a function of the motor electrical power of Figure 6.21 with the one of Figure 6.12 it is interesting to note an improvement in terms of efficiency of around the 12%. The improvement in terms of maximum thrust is mainly due to the increased motor power. Concerning the efficiency, the new setup does not use any gearbox and the motor encumbrance is reduced. Hence the power conversion efficiency is increased as well as the water flux through the hull hole. A further improvement of the thruster setup has been designed and tested in the pool. It exploits a different fastening system of the motor to the vehicle hull as shown in Figure 6.22. Pool tests have been performed with the two blades, $\frac{p}{d} = 0.6$ ratio propeller. Compared to the configuration shown in Figure 6.19 the clogging effect due to the motor supports is further reduced. This implies just a slight increase of the maximum bollard thrust but it makes the thrust trend in the two propeller direction more symmetric as visible in Figure 6.23.

The rear propellers are mainly operated to deliver a positive advance thrust to the vehicle, so a reduced negative direction thrust is not really important. The thrusters instead are operated in both directions, so the proposed improvement increases the vehicle maneuverability. The solution is thus quite promising but it has not been implemented on the vehicle yet.

Also for the T200 thrusters and rear propellers, it has been calculated the advance coefficient K_0. Being the thrust trend not symmetrical in the two rotating directions, two coefficients have been estimated K_{0+} for the positive thrust and K_{0-} for the negative one. K_0 trend as a function of the rotor speed is plotted in Figure 6.24.

The two coefficients have been computed according to Figure 6.24 as an average of the various thrust and speed samples, thus resulting in $K_{0+} \approx 0,016$ and $K_{0-} \approx 0,012$. The same measurements have been computed for the thrusters. Also in this case, the resulting K_0 is lower with respect to the rear propellers one. From Figure 6.25 an average value of $K_{0+} \approx 0,0052$ and $K_{0-} \approx 0,0039$ was obtained in the testing pool.

Once the propeller parameters are identified it is possible to estimate the

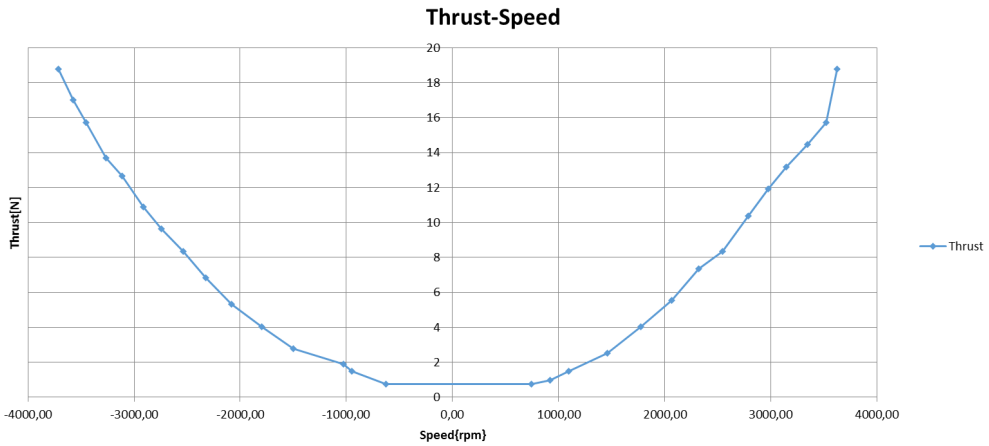

Figure 6.23: Second configuration. Bollard thrust of the T200 motor in the tube as a function of motor electrical power.

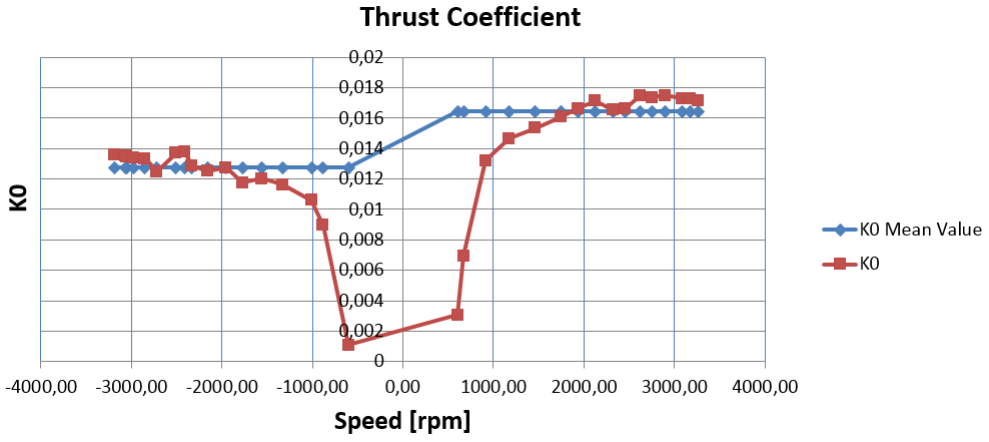

Figure 6.24: First configuration. Thrust coefficient of the T200 rear propeller in the two operating direction.

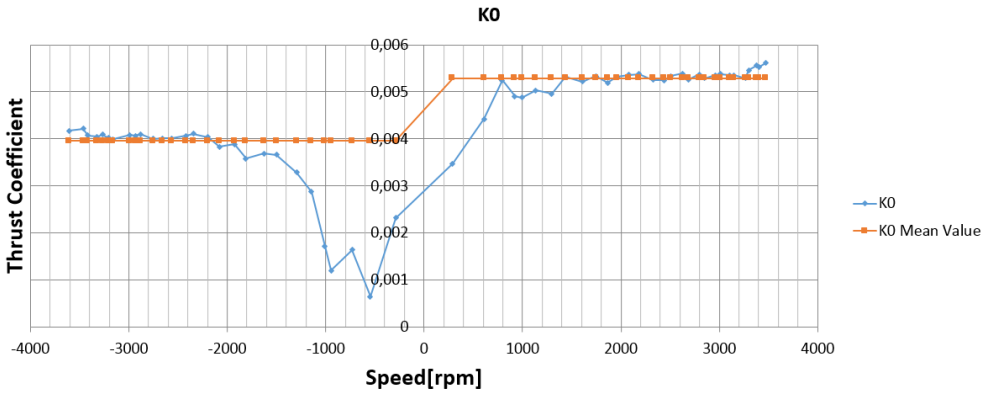

Figure 6.25: First configuration. Thrust coefficient of the T200 thruster in the two operating direction.

thrust delivered by the propeller if the propeller speed is known. With the commercial hobby drive systems described at the beginning of the chapter, it is not possible to precisely operate a propeller rotational speed control. Indeed it does not just depend on the reference value imposed to the drive but also on the operating propeller conditions such as applied torque and battery level. In Figure 6.3 the graph shows that when the propeller advance speed in the positive direction increases, the torque applied to the propeller decreases. This means that with the commercial hobby drivers, a reliable estimation of the propeller thrust can be obtained only at low advance speed. By operating the motor with a drive which performs a feedback speed control it is possible to set a desired speed regardless of these conditions. Furthermore, if also the torque delivered to the propeller by the motor is known, it is possible to operate an estimation of the advance speed of the propeller itself by relating the propeller rotational speed with the generated torque.
On this purpose a sensorless control algorithm has been implemented and tested as presented in section 4.3. The testing of the SMO based control solution has been performed through pool tests to evaluate its performances and potential. In figures 6.26 and 6.27 the thrust delivered by the T200 propeller with respect to the rotational speed in the first and third quadrant of operation respectively it is shown. The measurement has been performed with the test bench presented in section 5.4. In figures 6.28 and 6.29 the same measurements are presented but in this case they are estimated values. The propeller thrust is estimated thanks to the T200 propeller thrust coefficients previously identified. Although test bench measured values are quite noisy, it is interesting to see the good matching between measured and estimated values. The tests were carried out with the PIC test bench board presented in section 5.3 which cannot manage large current loads. So it has not been possible to perform a test over the entire speed range of interest.

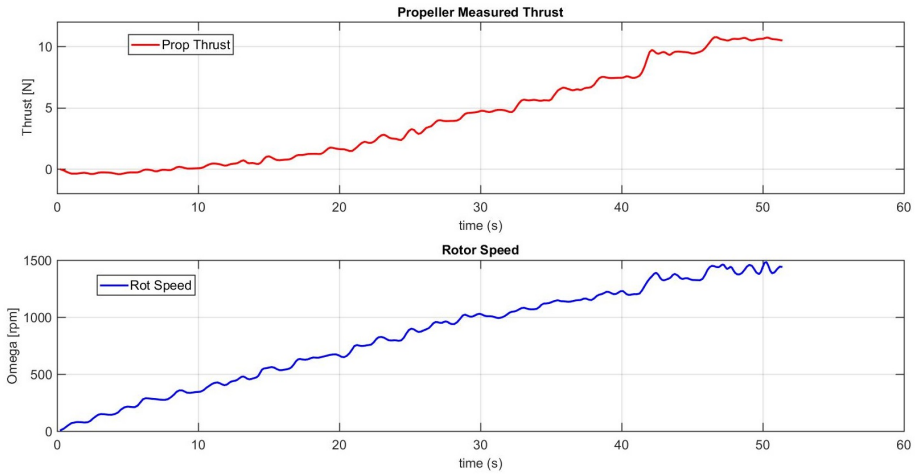

Figure 6.26: Bollard Thrust bench measurement. T200 propeller measured thrust with respect to measured rotational speed. First quadrant of operation.

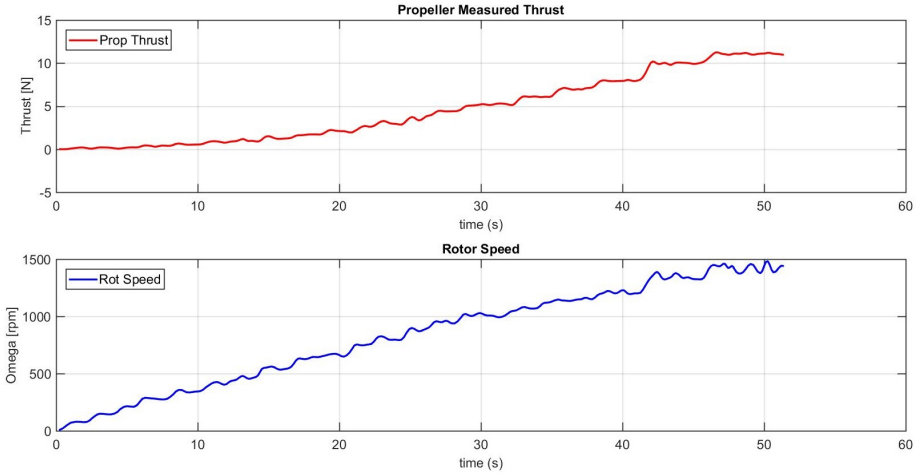

Figure 6.27: Bollard Thrust bench measurement. T200 propeller measured thrust with respect to measured rotational speed. Third quadrant of operation.

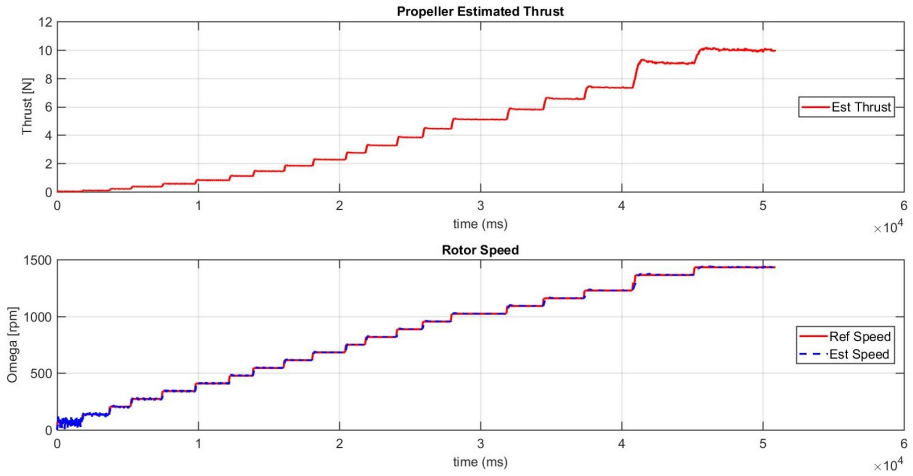

Figure 6.28: T200 propeller estimated thrust with respect to the estimated rotational speed. First quadrant of operation.

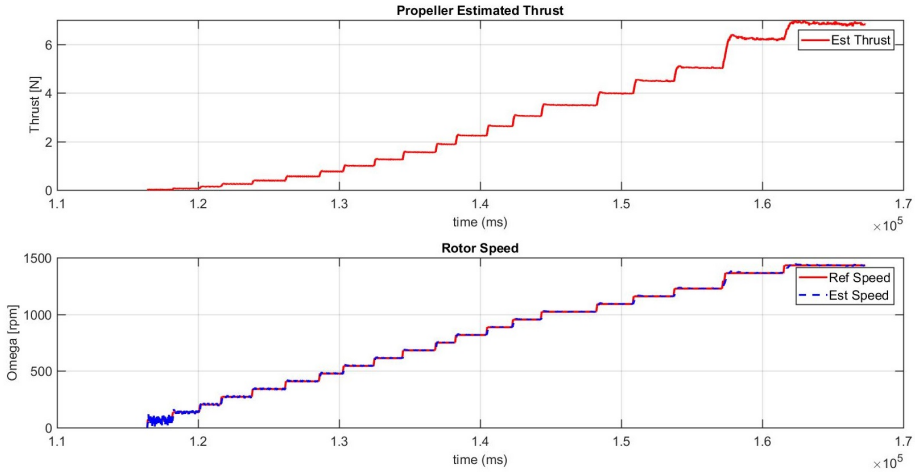

Figure 6.29: T200 propeller estimated thrust with respect to the estimated rotational speed. Third quadrant of operation.

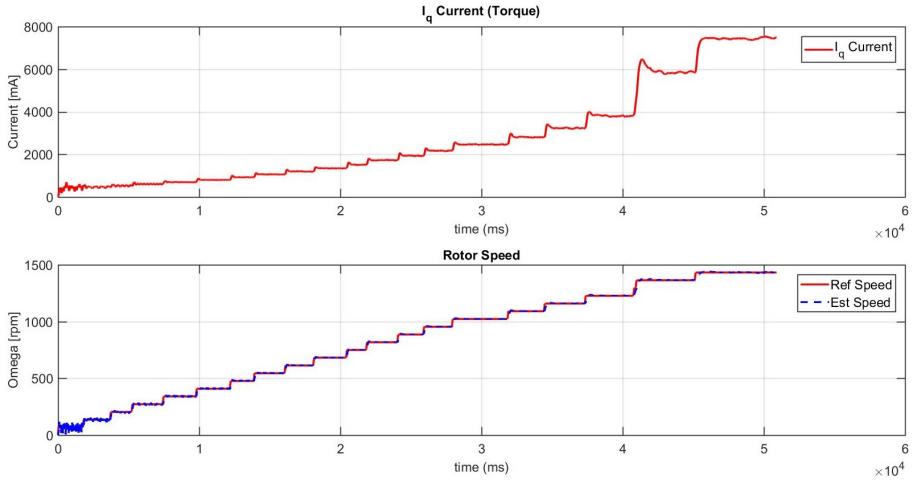

Figure 6.30: T200 q-axis drive current with respect to the estimated rotational speed. First quadrant of operation.

Concerning the torque estimation, in figures 6.30 and 6.31 it is possible to see how the rotating frame q-axis current described in subsection 3.2.1 is related to the rotational speed at a null value of the advance speed. Synchronous frame q-axis current, as explained, is proportional to the motor generated torque.

Hence it is possible to identify a coefficient which relates the rotational speed with the motor generated torque. As a reference for the identification of this parameter, the LaunchXL-F28027 + Boostxl-DVR8301 driver has been used. The controller which is produced by Texas Instruments, is a complete test bench motor control solution and it performs sensorless position, speed and torque estimation. In figures 6.32 and 6.33 a comparison of the torque estimation as a function of the propeller rotational speed between the two systems is shown. In the two graphs, the results obtained with the developed experimental set-up are referred to as "SMO torque" while the results obtained with the Texas Instruments set-up are referred to as "Texas torque".

In (6.2) the dependence of the resistant torque needed to move the propeller from the rotational and advance speed is highlighted. Hence a law expressing the vehicle advance speed as a function of the generated torque and of the rotational speed can be experimentally extracted by performing navigation test fields. Concerning this thesis, it has not been possible to operate these tests but further investigation could be carried on to obtain an improvement of the vehicle navigation accuracy due to additive information availability. Another important information that can be obtained by monitoring the q-axis current is related to unwanted propeller frictions due to dirt or rust. These factors could damage the propeller and motor and diminish the overall vehicle efficiency. In this case current monitoring could be used as a real time diagnostic.

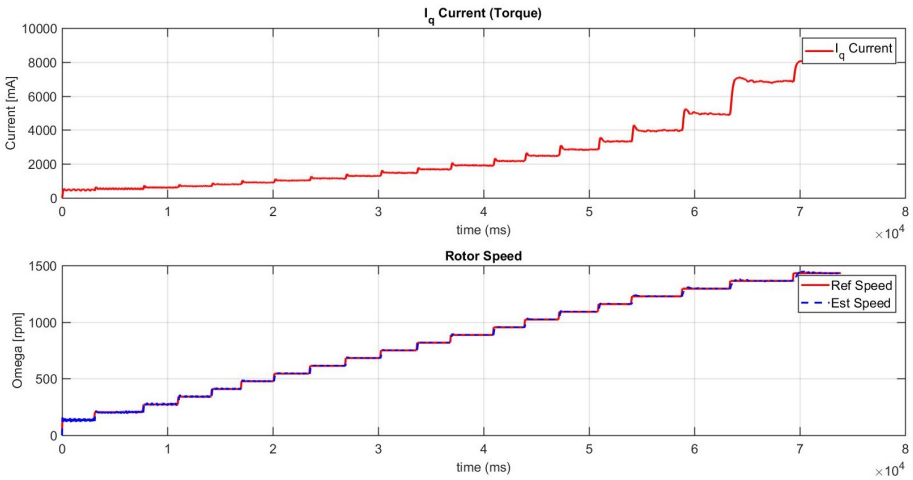

Figure 6.31: T200 q-axis drive current with respect to the estimated rotational speed. Third quadrant of operation.

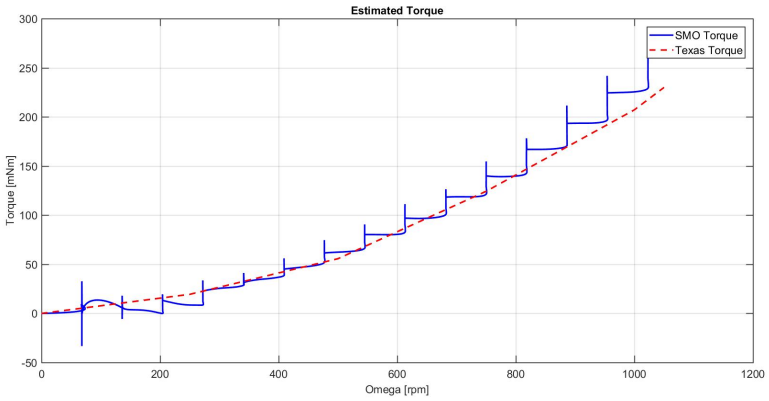

Figure 6.32: T200 motor estimated torque with respect to the estimated rotational speed. First quadrant of operation.

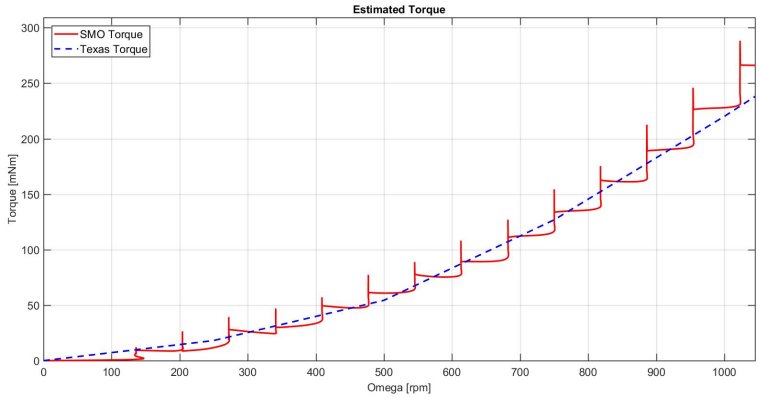

Figure 6.33: T200 motor estimated torque with respect to the estimated rotational speed. Third quadrant of operation.

6.3 Vehicle Dynamics: Modeling and Parameters Estimation

In order to model the behavior of an underwater vehicle, a kinematic and dynamic model of a rigid body is defined. The body freely moves into a fluid with which interaction cannot be considered negligible as water. Two different reference frames are introduced:

- **"Body" frame** $< b >$ **:** reference frame with origin O^b placed in the center of mass of the body and axes lined up to the main inertia axes of the body itself. In case of a vehicle of regular shape, x^b axis is longitudinal, pointing to the forward motion, z^b axis is vertical downward and y^b axis is set out in order to form a right-handed frame with the other two axes;

- **"Fixed" frame** $< n >$**:** inertial reference frame, described for the analyzed scene as the frame with origin O^n placed on the surface and axes lined up to the ones of a NED (North-East-Down) frame. x^n axis heads to the north, y^n axis heads to the east and z^n axis to the bottom.

The modeling is based on the SNAME notation (1950), that defines the following different quantities:

$$\begin{aligned}
\boldsymbol{\eta} &= \left[\boldsymbol{\eta}_1^\top \; \boldsymbol{\eta}_2^\top\right]^\top \quad \text{with} \quad \boldsymbol{\eta}_1 = [x\; y\; z]^\top \quad \boldsymbol{\eta}_2 = [\varphi\; \vartheta\; \psi]^\top \\
\boldsymbol{\nu} &= \left[\boldsymbol{\nu}_1^\top \; \boldsymbol{\nu}_2^\top\right]^\top \quad \text{with} \quad \boldsymbol{\nu}_1 = [u\; v\; w]^\top \quad \boldsymbol{\nu}_2 = [p\; q\; r]^\top \\
\boldsymbol{\tau} &= \left[\boldsymbol{\tau}_1^\top \; \boldsymbol{\tau}_2^\top\right]^\top \quad \text{with} \quad \boldsymbol{\tau}_1 = [X\; Y\; Z]^\top \quad \boldsymbol{\tau}_2 = [K\; M\; N]^\top ,
\end{aligned} \tag{6.17}$$

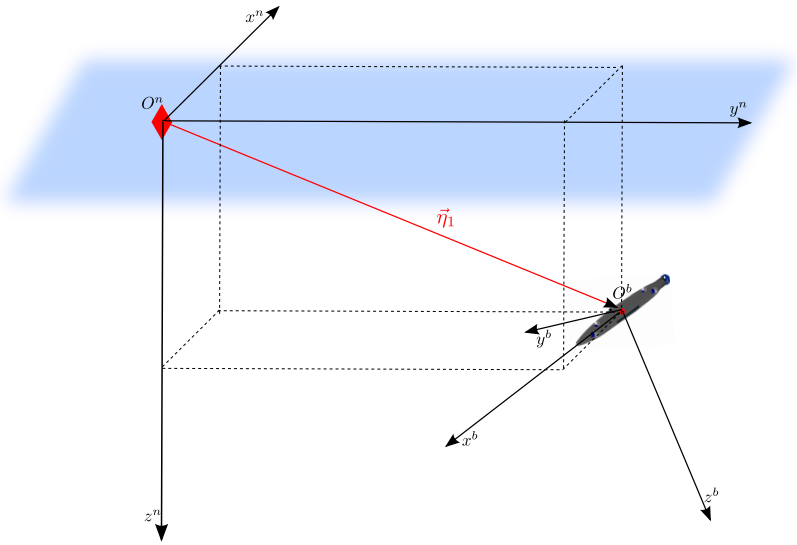

Figure 6.34: Reference frames for underwater vehicle modelling.

where $\boldsymbol{\eta}$ represents the vector of position ($\boldsymbol{\eta}_1$) and orientation ($\boldsymbol{\eta}_2$) in the fixed frame $< n >$, $\boldsymbol{\nu}$ includes the components of linear ($\boldsymbol{\nu}_1$) and angular ($\boldsymbol{\nu}_2$) speeds, expressed in the body frame $< b >$ and $\boldsymbol{\tau}$ are the forces ($\boldsymbol{\tau}_1$) and torques ($\boldsymbol{\tau}_2$) applied to the vehicle, expressed in the body frame $< b >$.
As concerns the nomenclature of the degrees of freedom:

- x motion along x^b axis is defined *surge* motion;
- y motion along y^b axis is defined *sway* motion;
- z motion along z^b axis is defined *heave* motion;
- φ rotation around x^b axis is defined *roll* motion;
- ϑ rotation around y^b axis is defined *pitch* motion;
- ψ rotation around z^b axis is defined *yaw* motion.

It is easily possible to link the quantities expressed in the fixed frame $< n >$ and the quantities given in the body frame $< b >$ at "speed level". As regards the translational part:

$$\dot{\boldsymbol{\eta}}_1 = R_b^n \left(\boldsymbol{\eta_2}\right) \boldsymbol{\nu_1} \ , \tag{6.18}$$

where $R_b^n(\boldsymbol{\eta_2})$ is the rotation matrix between $< b >$ and $< n >$ that, as a function of the Euler Roll-Pitch-Yaw angles (RPY) $[\varphi, \vartheta, \psi]^T$, is equal to:

$$R_b^n(\boldsymbol{\eta_2}) = \begin{bmatrix} c_\psi c_\vartheta & -s_\psi c_\varphi + c_\psi s_\vartheta s_\varphi & s_\psi s_\varphi + c_\psi c_\varphi s_\vartheta \\ s_\varphi c_\vartheta & c_\psi c_\varphi + s_\psi s_\vartheta s_\varphi & -c_\psi s_\varphi + s_\psi c_\varphi s_\vartheta \\ -s_\vartheta & s_\varphi c_\vartheta & c_\varphi c_\vartheta \end{bmatrix} , \tag{6.19}$$

using for the generic angle α

$$c_\alpha = cos(\alpha) \ , \ s_\alpha = sin(\alpha) \ . \tag{6.20}$$

As regards instead the orientation part:

$$\dot{\boldsymbol{\eta}}_2 = T_b^n(\boldsymbol{\eta_2}) \ \boldsymbol{\nu_2} \ , \tag{6.21}$$

where the transform matrix $T_b^n(\boldsymbol{\eta_2})$ is defined as function of RPY angles as:

$$T_b^n(\boldsymbol{\eta_2}) = \frac{1}{c_\vartheta} \begin{bmatrix} c_\vartheta & s_\varphi s_\vartheta & c_\varphi s_\vartheta \\ 0 & c_\varphi c_\vartheta & -c_\vartheta s_\varphi \\ 0 & s_\varphi & c_\varphi \end{bmatrix} . \tag{6.22}$$

As notable from (6.22), the RPY angle representation has a singularity when $\vartheta = (2n+1)\frac{\pi}{2}$, with $n \in \mathbb{N}$. This problem could be overcome by introducing an alternative representation of the orientation of redundant type, e.g. using the components of the unitary quaternion. In short, the relationship linking vectors $\dot{\boldsymbol{\eta}}$ and $\boldsymbol{\nu}$ is expressed like this:

$$\dot{\boldsymbol{\eta}} = J_b^n(\boldsymbol{\eta_2}) \ \boldsymbol{\nu} \ , \tag{6.23}$$

where

$$J_b^n(\boldsymbol{\eta_2}) \ = \begin{bmatrix} R_b^n(\boldsymbol{\eta_2}) & 0_{3\times3} \\ 0_{3\times3} & T_b^n(\boldsymbol{\eta_2}) \end{bmatrix} . \tag{6.24}$$

Using equation (6.23) it is possible to write also relationships between the time derivatives of the same quantities:

$$\begin{aligned} &\dot{\boldsymbol{\eta}} = J_b^n \ \boldsymbol{\nu} && \Leftrightarrow \quad \boldsymbol{\nu} = (J_b^n)^{-1} \ \dot{\boldsymbol{\eta}} \\ &\ddot{\boldsymbol{\eta}} = J_b^n \ \dot{\boldsymbol{\nu}} + \dot{J}_b^n \ \boldsymbol{\nu} && \Leftrightarrow \quad \dot{\boldsymbol{\nu}} = (J_b^n)^{-1} \ \left(\ddot{\boldsymbol{\eta}} - \dot{J}_b^n \ (J_b^n)^{-1} \ \dot{\boldsymbol{\eta}} \right) \ , \end{aligned} \tag{6.25}$$

leaving out the explicit dependence from the variables to simplify the notation.

Vehicle dynamic model of an underwater vehicle is used in conjunction with the kinematic one to perform position estimation during navigation. To obtain it, some fluid-dynamic parameters characterizing the vehicle have to be identified. These parameters are needed in order to define a mathematical expression of an analytical model which relates forces and moments acting on the AUV to vehicle speed and propeller rotational speed.

The motion of an AUV is governed by the following dynamic equations:

$$M\dot{\boldsymbol{\nu}} + C(\boldsymbol{\nu})\boldsymbol{\nu} + D(\boldsymbol{\nu})\boldsymbol{\nu} + \mathbf{g}(\boldsymbol{\eta}) = \boldsymbol{\tau}(\boldsymbol{\nu}, \boldsymbol{u_c}), \tag{6.26}$$

where M is the mass matrix, C is the centrifugal and Coriolis matrix, D is the drag matrix, $\mathbf{g}$ is the gravity and buoyancy vector and $\boldsymbol{\tau}(\boldsymbol{\nu}, \boldsymbol{u})$ are the resultant forces and torques acting on the vehicle ($\boldsymbol{u_c}$ are the control signals of the vehicle motors, i. e. the motor rotational speeds). These physical quantities, not reported here for reasons of brevity, are reported in [60] and [61]. Under the assumption of uniform motion of the vehicle, it is possible to neglect Coriolis and inertial contributions. If the vehicle moves on an xy plane in earth fixed reference frame, also the gravitational contribution is negligible along the x direction in body-fixed reference frame. Consequently the dynamics equation is simplified:

$$D(\boldsymbol{\nu})\boldsymbol{\nu} = \boldsymbol{\tau}(\boldsymbol{\nu}, \boldsymbol{u_c}). \tag{6.27}$$

Damping force contributions, in the x direction of the body-fixed reference frame are expressed in (6.28), see [62]:

$$D(u)_x = \frac{1}{2}\rho A u C_x. \tag{6.28}$$

Where $\rho\frac{kg}{m^3}$ is sea water density, Am^2 is the reference area of the AUV, $u\frac{m}{s}$ is the advance speed along x and C_x is a dimensionless damping coefficient of the vehicle along x. According to [63], when dealing with torpedo shaped bodies, the reference area of the AUV, could be computed as the product of the vehicle length times its diameter $A = Ld$. MARTA AUV has a length of $L = 3,7m$ and a diameter of $d = 0.18m$. The thrust along the x direction in body-fixed reference frame is given by two rear propellers together delivering:

$$\tau_x = f(n, u) = T_p^{right} + T_p^{left}. \tag{6.29}$$

Where T_p^{right} and T_p^{left} are the right and left propeller thrust, as described in section 6.1. By solving (6.27) with respect to (6.28) and to (6.13) the following expression is obtained

$$2\left(K_0 n^2 - \frac{K_0 n u}{p}\right) = \frac{1}{2}\rho L d u^2 C_x. \tag{6.30}$$

The thrust coefficients relative to the various thruster configurations have been estimated through pool tests described in subsection 6.2.1. The missing parameter of (6.30) is the C_x previously described. By having measurements or good estimations of u and n while the vehicle navigates, it is possible to solve (6.30) with respect to C_x. An estimation of the advance speed is given by the on board DVL while a law relating the propeller rotational speed with the servo signal used to control the motors has been extracted thanks to the pool measurements. In order to acquire all the necessary quantities, field tests have been performed being MARTA AUV navigating at different known constant

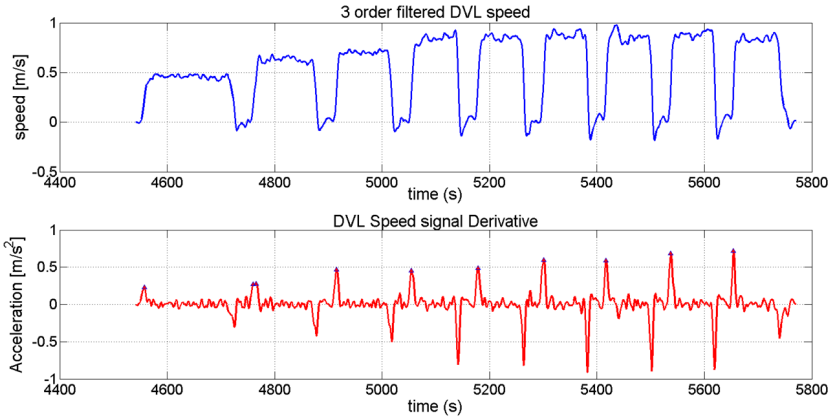

Figure 6.35: Graph of the vehicle advance speed measured with the on board DVL during field test in Roffia Lake.

longitudinal speed. In Figure 6.35 it is shown the advanced speed measurement obtained thanks to the DVL.

The C_x is a constant value and it is computed for different speed to increase the accuracy of the estimation. Clearly the DVL measured speed is not constant, so an average value of it has been extracted in these sectors in which a constant speed reference had been set. The expression of the C_x as a function of u and n is:

$$C_x = 2(2K_0)\frac{(n^2 - n\frac{u}{p})}{\rho L d u^2}. \tag{6.31}$$

The average results of advance speed and propeller rotational speed measurements are listed in table 6.3. According to these values, it is possible to compute an average $C_x = 0.11$.

Table 6.3: Advance speed and propeller rotational speed measurements.

Acquisition	Advance speed m/s	Propeller speed Hz
1^{st}	0,4546	19,6
2^{nd}	0,5972	24,38
3^{rd}	0,7371	29,10
4^{th}	0,8388	32,24
5^{th}	0,9286	35,4

The advance speed measurements taken during the field tests in Roffia Lake can be used also for a partial validation of the vehicle model parameters estimation and $T(n, u)$ estimation described in (6.15). The measurements shown in

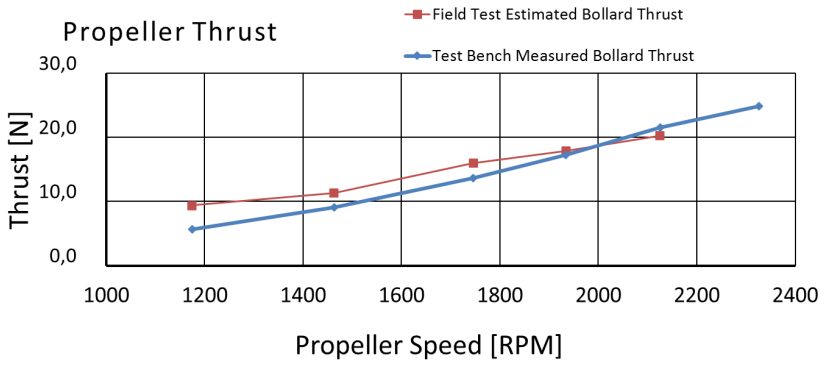

Figure 6.36: Vehicle thrust delivered in bollard condition and measured with the test bench.

Figure 6.35 were taken, being vehicle started several times from a null advance speed, by imposing different cruise speed. As shown in Figure 6.35 each time a new speed is set, the vehicle is initially accelerated until it reaches the target cruise speed. In the initial phase, the advance speed is null or very low, so the thrust delivered by the two rear propellers can be approximated to the bollard thrust measured in a test pool. In these condition (6.26) can be approximate by considering just the inertial contribution along the x-axis in the in body-fixed reference frame.

$$M_x\dot{u} = m\dot{u} = \tau_x(n,u)\Big|_{u\approx 0}. \tag{6.32}$$

Where m is the vehicle mass of about 80kg. By solving (6.32) with respect to (6.12) the following expression is obtained:

$$m\dot{u} = K_0 n^2, \tag{6.33}$$

which in turn can be solved with respect to the K_0

$$K_0 = \frac{m\dot{u}}{n^2}, \tag{6.34}$$

According to (6.15) the maximum thrust delivered by a propeller is when $u \leq 0$ and it corresponds to the previously measured bollard thrust value. This condition can be approximated to the condition of maximum measured acceleration which is obtained by operating a time derivative of the DVL measured speed. Of course being the vehicle equipped with two rear propellers, the thrust is twice the one measured in the pool.

In Figure 6.36 a comparison between the thrust measured with a test bench and estimated through the time derivative of the advance speed is presented.

6.4 Parameter Validation: Navigation Field Tests

Once the dynamic parameters are estimated, it is possible to operate a navigation strategy based on a dynamical model of the vehicle. Most of the AUV navigation system filters described in literature and used on several vehicles, are based on the Kalman Filter (KF) [64]and on the Extended Kalman Filter (EKF) [65], [66], [67], a KF extension which can be employed on nonlinear dynamical systems. In general these methods make use of kinematic or dynamic vehicle models.

These methods often exploit sets of sensors for the navigation, including Inertial Measurement Units (IMU) [68], [69], or Fiber Optic Gyros (FOG) [70], [19] to measure vehicle orientation, Pressure Sensors (PS) for depth measurements, Doppler Velocity Logs (DVL) [68] to measure the vehicle translational velocity and acoustic localization systems based on range measurements [71], [72], [73], or on Ultra-Short BaseLine (USBL) [74], [75], [76].

In the MDM Lab of the Department of Industrial Engineering of Florence, an innovative navigation technique has been developed exploiting an UKF [55], [77]. Such filter is based on the Unscented Transform (UT), a deterministic sampling technique which allows the propagation of a Random Variable (RV) undergoing a generic non-linear transformation without requiring the computation of derivatives. This filter makes use of simplified kinematic and dynamic models of the vehicle and it is aimed to offer a good trade-off between the accurate reproduction of vehicle motion and the demand for computational resources. By doing this, the filter can be exploited in real-time without simplifying too much the physical behavior of the AUV.

The filter was experimentally validated exploiting the data acquired during several test field with the TifOne and TifTwo vehicles [67], [28]. The two vehicles exploit sensored motors for the propulsion, so an accurate rotational speed estimation is performed and the necessary vehicle physical parameters have been estimated in order to use the dynamical model of the vehicle. In Figure 6.37 [77], the TifOne AUV, navigating in dead reckoning, performs an autonomous mission through five way-points which form a square-shaped path. In this case, navigation is performed thanks to a DVL, an IMU and an USBL which operates as an underwater GPS.

With the data gathered during these test, the proposed UKF-based navigation filter has been validated offline in a Matlab environment. The UKF based navigation algorithm has been compared with the standard EKF-based ones using different sensor combinations. In the first combination called “Configuration One” (Figure 6.37), the DVL, the USBL, the IMU and the depth sensor were used for position estimation. In the second one called “Configuration Two” (Figure 6.38), the USBL data was not provided for the estimation algorithm, in the third one (Figure 6.39), neither the USBL and the DVL data was provided to the algorithm. As a ground truth, the GPS fix are also highlighted as well as the USBL fix. In Figure 6.37 the performances of the two filters are totally similar, the two dotted lines concerning the EKF and the UKF based algorithm are superposed. The same happens when the DVL, the pressure sensor and the

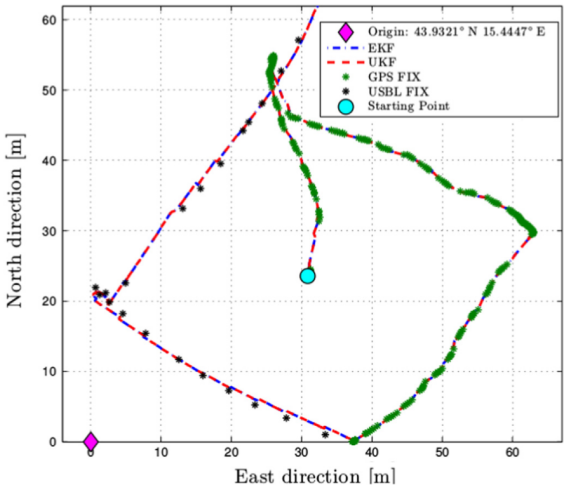

Figure 6.37: AUV position estimation comparing an UKF and an EKF based algorithm. Configuration One.

IMU are used for position estimation as visible in Figure 6.38. In Figure 6.39 the position estimation operated by the two algorithms is shown. It is the case in which only the IMU and pressure sensor data are used. In this case the UKF-based navigation algorithm turns out to be more robust than the EKF-based one. The proposed algorithm thus can be exploited especially when reduced sets of sensors are employed, reduced measurements are available and the navigation algorithm relies more on the model-based prediction step[77]. This is particularly important in order to reduce vehicle cost and facing sensors failures. On board navigation sensors above listed indeed, highly affect the final cost of the vehicle when dealing with low size AUVs and for non military purposes.

According to these results, the solution has been applied also to MARTA AUV. Also in this case, an identification of the dynamic parameters of the vehicle has been necessary (section 6.3). In addition, since the motors mounted on the vehicle do not have any position or speed sensor, it has been necessary to estimate a law which would relate the propeller speed and the motor reference (subsection 6.2.1). The validation of the proposed algorithm has been carried on exploiting a data-set of sensors acquisitions including Doppler Velocity Log - DVL, Pressure Sensor, Inertial Measurement Unit - IMU, single-axis Fiber Optic Gyro - FOG, and Global Positioning System - GPS on surface. The data was gathered during a mission performed in La Spezia (Italy) in October 2016. With the results obtained during these measurements campaigns, the authors validated (offline) an UKF-based navigation state estimation algorithms for underwater vehicles [78]. In this case also an estimation of the direction and the magnitude of a priori unknown marine currents was performed [79]; the currents estimation is performed during the navigation of the AUV together

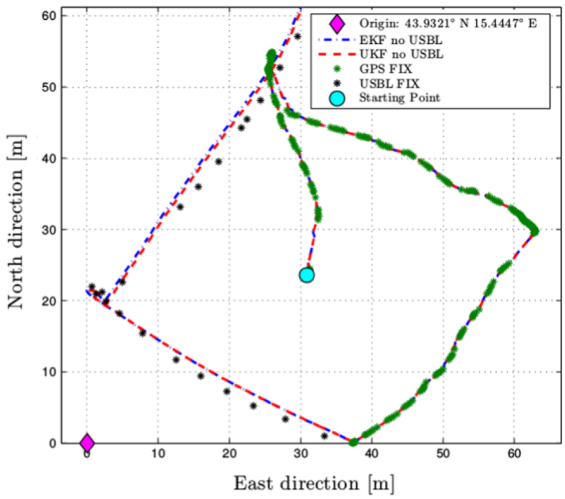

Figure 6.38: AUV position estimation comparing an UKF and an EKF based algorithm. Configuration Two.

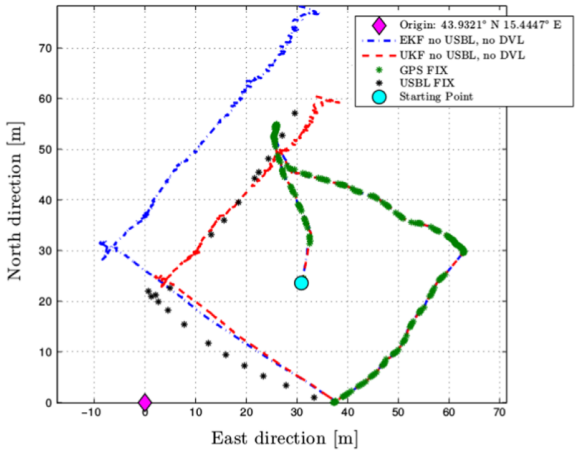

Figure 6.39: AUV position estimation comparing an UKF and an EKF based algorithm. Configuration one.

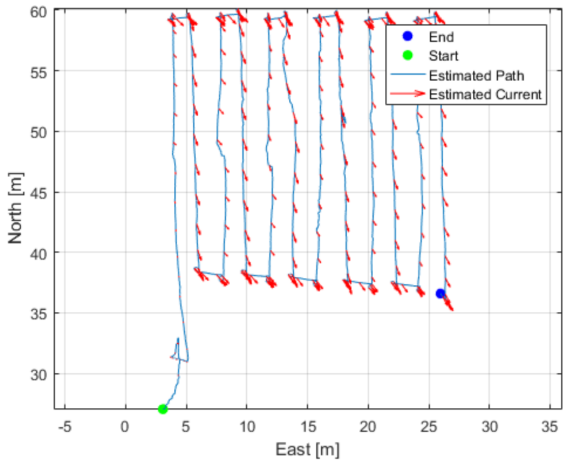

Figure 6.40: Simultaneously estimated vehicle trajectory and sea currents during the field test.

with the estimation of the vehicle navigation state. The performed mission consisted of a lawn-mower path at a constant depth. A very low current was present on the surface during the demonstration day. The mission lasted about 1300s with a starting point indicated with a green dot in Figure 6.40. MARTA AUV reached the desired depth of about 7m before starting to move towards the first way-point of the lawn-mower path, it traveled the whole path controlling its depth and then it surfaced on the ending point (the blue dot). In Figure 6.40 the estimated path is shown along with the estimated direction of the sea current during the mission represented at intervals of 5 seconds (for the sake of plot intelligibility) by the red arrows. After a first period of transient behavior corresponding to the immersion phase, the estimated direction of the sea current remains, during the whole mission, approximately at a constant value (both magnitude and direction) coherent with what expected from the on-field experience. Direction and the low intensity of the estimated current are coherent with what observed during the experimentation. Regarding the vehicle propulsion side, an improvement could came from a better estimation of the propeller rotational speed and thus on the delivered thrust. This clearly would influence the accuracy of the navigation algorithm dynamic model which, as shown above, plays an important role in the reliability and robustness of the system.

Chapter 7

Conclusions

The development of underwater appliances for exploration, patrolling and study of sub-sea environment is growing in importance and the field of operation concerns a wide spectrum of applications, from industrial application (mainly Oil&Gas) fields, to military, underwater archeology, underwater geology, tourism, etc.
In the Mechatronics and Dynamic Modeling Laboratory (MDM Lab) of the Department of Industrial Engineering of the Florence University, research activities regarding the development of UUVs (Unmanned Underwater Vehicles) are carried on since 2010. The activity involves several research fields and expertise, from mechanical design, to computer vision, control theory, soft and power electronics design. The activities described in this thesis work have been developed mainly in the framework of the European FP7 project ARROWS, and concerned the development of the propulsion system of the MARTA AUV, an Autonomous Underwater Vehicle for underwater archeology exploration and mapping.

The work was intended to develop a customized propulsion system from the propeller selection and design, to the selection of the actuation strategy, electronic design and control strategy.

Several commercial AUV, similar to MARTA AUV, exploit PMSM actuators for vehicle propulsion. It is a motor technology that can be considered mature and which is often exploited thanks to its performances in terms of efficiency and reliability. Hence, in chapter 1 an overview of PMSM operation and control techniques was presented. It is also highlighted the possibility of operating the motor with a customized sensorless technique, this in order to reduce actuation system costs, maintenance and encumbrances and to improve its reliability. In chapter 3 several sensorless control techniques were presented highlighting the pros and cons of each one with respect to the application of interest. Some of these techniques have been implemented and tested in order to evaluate their performances and compare the results. The implementation process of these techniques is described in chapter 4 with the experimental results. In particular the most interesting results have been obtained with a Sliding Mode Observer

based sensorless control technique which showed interesting performances concerning the operational speed range, speed and torque estimation, robustness facing system parameters variations and efficiency. In chapter 5 an overview of the testing appliances and control solutions which have been developed during the work is presented. These appliances have been implemented in order to test and produce experimental results of the developed solutions. In chapter 6 experimental results of the developed propulsion system were given. In particular, in the first part of the chapter, it is shown the propeller selection process. Subsequently, propeller parameters identification theory is explained with the related experimental results. Finally, it is explained how the possibility of operating the propulsion system by performing propeller rotational speed and torque estimation improves navigation performances. The additional information provided thanks to this control techniques indeed permits a more accurate position estimation also in absence of very important navigation sensors like the DVL or the USBL.

As a result of this thesis work, a sensorless control algorithm and a custom motor drive controller have been designed and implemented. The system was designed to be integrated in underwater vehicles, it operates PMSM in sensorless control performing speed control and providing an estimation of the rotor generated torque.
Due to time constraints it has not been possible to extensively test the developed solution in real scenarios such as AUVs navigation field test campaigns. Hence as a further development of this work it will be necessary to perform endurance and stress test of the motor drive in order to verify its reliability and highlight possible failure causes. This process will consist both in pool test and navigation field campaigns. Finally, further attention has to be paid to the exploitation of the torque estimation in order to integrate this information in the vehicle navigation algorithm and improve its performances.

Concerning my personal work experience, this activity has represented an important step in terms of acquired expertise in the promising field of electric motor sensorless control. The theoretical and applied operational approach involved the development of several skills both related to practical and theoretical issues. This expertise hopefully will be applied to further development of underwater propulsion applications and to other fields of interest.

Bibliography

[1] *http://www.arrowsproject.eu.*

[2] *https://www.wartsila.com/.*

[3] Parviz G. Roya S. Mahdi Y F. Performance assessment of the waterjet propulsion system through a combined analytical and numerical approach. *International Journal of Physics, 2013 1 (2), pp 22-27.*, 2013.

[4] F. Cupertino. Macchina singola a magneti permanenti (brushless DC). Technical report, DEE, POlitecnico Bari, 2006.

[5] Ward Brown. Brushless DC motor control made easy. Technical report, Microchip Technology Inc., 2002.

[6] S. Bowling C. Elliott. Application note 901 - using the dspic30f for sensorless BLDC control. Technical report, Microchip, 2004.

[7] Jiacai H. Hongsheng L Qinghong X Di L. Sensorless vector control of PMSM using sliding mode observer and fractional-order phase-locked loop. *Proceedings of the 31st Chinese Control Conference*, 2012.

[8] Holtz J. Initial rotor polarity detection and sensorless control of PM synchronous machines. *1-4244-0365-0/06 (c) 2006 IEEE*, 2006.

[9] Cypress Semiconductor. FM3 family, position estimation of PMSM with signal injection - AN204470. Technical report, Cypress Semiconductor, 2016.

[10] J Carlton. *Marine Propellers and Propulsion, 2nd edition.* Springer-Verlag, Heidelberg, Germany., 2007.

[11] et al Allotta B. Costanzi R. Meli E. Pugi L. Ridolfi A. Cooperative localization of a team of AUVs by a tetrahedral configuration. *Robotics and Autonomous Systems 62: 1228-1237*, 2014.

[12] Allotta B. Costanzi R. Gelli J. Paolucci L. Pugi L. Ridolfi A. Development and testing of the propulsion system of marta AUV. *VI International Conference on Computational Methods in Marine Engineering MARINE 2015*, 2015.

[13] SAUC-E student program. http://www.ing-mel.unifi.it/upload/sub/studenti/sauce.pdf, 2013.

[14] Bartolini F. Costanzi R. Ridolfi A. Vettori G. Allotta B. SAUC-E 2012 - UNIFI team - turtle vehicle. In *Proceedings of SAUC-E (Student Autonomous Underwater Vehicle Challenge - Europe)*, 2012.

[15] Bartolini F. Conti R. Costanzi R. Gelli J. Meli E. Ridolfi A. Allotta B. Toni P. SAUC-e 2013 - UNIFI team - feelhippo vehicle. In *Proceedings of Student Autonomous Underwater Competition - Europe*, 2013.

[16] Bartolini F. Conti R. Costanzi R. Gelli J. Meli E. Ridolfi A. Allotta B. D'Adamio P. Fanelli F. Gori L. Monni N. Natalini M. Paolucci L. Ridolfi A.. Bianchi M. Capitani S. Corrieri A. Montagni M. Nocentini A. Topini A. Urbani G. Vagli S. Allotta B. UNIFI team euRathlon 2015 sea + air sub-challenge. 2015.

[17] Allotta B. Casagli N. Costanzi R. Mugnai F. Monni N. Natalini M. Ridolfi A. Development of nemo remotely operated underwater vehicle for the inspection of the costa concordia wreck. *Proceedings of the Institution of Mechanical Engineers, Part M: Journal of Engineering for the Maritime Environment Vol 231, Issue 1, pp. 3 - 18*, 2015.

[18] Allotta B. Costanzi R. Ridolfi A. The ARROWS project: Adapting and developing robotics technologies for underwater archaeology. *IFAC Workshop on Navigation Guidanceand Control of Underwater Vehicles, Girona, Spain*, 2015.

[19] Allotta B. Costanzi R. Fanelli F. Monni N. Ridolfi A. Single axis FOG aided attitude estimation algorithm for mobile robots. *Mechatronics 30 July 2015 DOI: 10.1016/j.mechatronics.2015.06.012*, 2015.

[20] Allotta B Ridolfi A. Bianchi M Fanelli F. Gelli J. Monni N. Nocciolini D. Pagliai M. Paolucci L. Pecorella T. Employment of an autonomous underwater vehicle as mobile bridge among heterogeneous acoustic nodes. *20th IFAC World Congress*, 2017.

[21] Bellavia F. Fanfani M. Pazzaglia F. Colombo C. Allotta B. Costanzi R. Monni N. Ridolfi A. Piecewise planar underwater mosaicing. *Proceedings of OCEANS15 MTS/IEEE GENOVA*, 2015.

[22] Allotta B. Colombo C. On the use of linear camera-object interaction models in visual servoing. *IEEE Transactions On Robotics And Automation*, 1999.

[23] Fioravanti D. Allotta B. Rindi A. Image based visual servoing for robot positioning tasks. *Meccanica*, 2008.

[24] Allotta B. 3D motion planning for image based visual servoing tasks. *IEEE International Conference on Robotics and Automation (ICRA '06) Barcelona, Spain*, 2005.

[25] Fioravanti D. Allotta B. Rindi A. Robot positioning via image based visual servoing. *AIMETA 2007 Atti del XVIII Congresso dellAssociazione Italiana di Meccanica Teorica e Applicata*, 2007.

[26] *http://www.archeosub.eu*.

[27] Christ R.D. Wernli R. L. *The ROV Manual A User Guide for Remotely Operated Vehicles*. Elsevier, 2014.

[28] Allotta B. Caiti A. http://thesaurus.isti.cnr.it. official site of the italian THESAURUS ;project2013. Technical report, 2013.

[29] Christ R.D. Wernli R. L. Observation class ROVs come of age. *Sixth International Symposium on Underwater Technology UT2009, Wuxi, China, April 2009*, 2009.

[30] Zhao J. Yu Y. Brushless DC motor fundamentals AN047. Technical report, MPS, 2011.

[31] *http://cirs.udg.edu*.

[32] *https://www.atlas-elektronik.com*.

[33] Caiti A. Caffaz A Casalino G. Turetta A. The hybrid glider/AUV folaga. *IEEE Robotics & Automation Magazine 17(1):31 - 44 April 2010*, 2010.

[34] *www.km.kongsberg.com*.

[35] Luca Pugi Benedetto Allotta. *Modellistica e Controllo di Sistemi Elettrici*. 2010.

[36] Adriano Faggion. *Algorithms and Rotor Designs for the Position Estimation of PM Synchronous motors at Zero and Nonzero Speed*. PhD thesis, Universit Delgi Studi Di Padova - Scuola di Dottorato di Ricerca in Ingegneria Industriale, 2011.

[37] Duesterhoeft Clarke, Schulz. Determination of instantaneous currents and voltages by means of alpha, beta, and zero components. *Transactions of the American Institute of Electrical Engineers*, 1951.

[38] Rami Krishnan. *Permanent Magnet Synchronous and Brushless DC Motor Drives*. CRC Press, 2010.

[39] Park R. H. Two reaction theory of synchronous machines. 1929.

[40] *https://www.tm4.com/blog/electric-motor-topologies-101/*.

[41] *http://empoweringpumps.com/ac-induction-motors-versus-permanent-magnet-synchronous-motors-fuji/.*

[42] Jim Murphy. Understanding ac induction, permanent magnet and servo motor technologies: Operation, capabilities and caveats. Technical report.

[43] Titus J. Careful designers get the most from brushless DC motors. *ECN*, 2012.

[44] Lewin C. Field oriented control deep dive. Technical report, Engineering of Performance Motion Devices.

[45] Texas Instruments Europe. Field orientated control of 3-phase AC-motors. Technical report, Texas Instruments Europe, 1998.

[46] B.R. Menezes Z.M.A. Peixoto Sa F.M Freitas P.F. Seixas. Application of sliding mode observer for induced EMF, position and speed estimation of permanent magnet motors. *Proc.Power Electronics and Drive Systems Int. Conf., pp.599 604.*, 1995.

[47] T. Furuhashi S. Sangwongwanich S. Okuma. A position and velocity sensorless control for brushless DC motors using an adaptive sliding mode observer. *IEEE Trans. Industrial Electronics, Vol.39, pp. 89 95*, 1992.

[48] Massoum A. Khouidmi H. Reduced-order sliding mode observer-based speed sensorless vector control of double stator induction motor. 2014.

[49] Allotta B. Paolucci L. DAdamio P. Nocentini L. Pugi L. Rindi A. Next generation of smart sensorless drives for sustenaible underwater vehicles. *2016 IEEE 16th International Conference on Environment and Electrical Engineering (EEEIC) 7-10 June 2016, Florence, Italy Conference Proceedings pp.1-6. - ISBN:978-1-5090-2319-6*, 2016.

[50] Vadim U. Hoon L. Chattering problem in sliding mode control systems. *Proceedings of the International Workshop on Variable Structure Systems*, 2006.

[51] Konghirun M. Paponpen K. An improved sliding mode observer for speed sensorless vector control drive of PMSM. *IPEMC 2006*, 2006.

[52] Linke M. Kennel R. Holtz J. Sensorless position control of permanent magnet synchronous machines without limitation at zero speed. *0-7803-7474-6/02 02002 IEEE*, 2012.

[53] Allotta B. Pugi L. Paolucci L. DAdamio P. Nocentini L. Niehaus M. Grasso E. Kanapari E. Development of sensorless pm servo-system for harsh environments. *Proceedings of 2015 AEIT International Annual Conference - pp.1-6.*, 2015.

[54] *https://www.maxonmotor.it/maxon/view/content/index.*

[55] Costanzi R. *Navigation Systems for Unmanned Underwater Vehicles*. PhD thesis, Florence University, 2014.

[56] Pivano L. Johansen T. Smogeli N. A four-quadrant thrust estimation scheme for marine propellers: Theory and experiments. *Control Systems Technology, IEEE Transactions on, 10.1109/TCST.2008.922602*, 2009.

[57] Oosterveld M W C. *Wake adapted ducted propellers, Wageningen: Netherlands Ship Model Basin*. PhD thesis, Delft University of Technology, 1970.

[58] Oosterveld M W C. Ducted propeller characteristics. In *RINA symposium on ducted propellers, London*, 1973.

[59] *http://www.bluerobotics.com/*.

[60] Fossen T I. *Guidance and Control of Ocean Vehicles*. John Wiley and Sons, London, UK, 1994.

[61] Fjellstad O. Fossen T. Nonlinear modelling of marine vehicles in 6 degrees of freedom. *Journal of Mathematical Modelling of Systems, 1.*, 1995.

[62] Barros E.D. Pascoal A. de Sac E. Investigation of a method for predicting AUV derivatives. *Ocean Engineering.*, 2008.

[63] Munson B.R. Okiishi T.H. Huebsch W.W. Rothmayer A P. *Fundamentals of Fluid Mechanics*. 2013.

[64] Kalman R E. A new approach to linear filtering and prediction problems. *Trans. ASME J. Basic Eng., 82 (Series D), 3545*, 1960.

[65] Kirubarajan T. Bar-Shalom Y, Li X R. *Estimation with Applications to Tracking and Navigation: Theory Algorithms and Software.* Wiley (July), Hoboken, New Jersey, USA., 2001.

[66] Evensen G. *Data assimilation.* Heidelberg, Germany: Springer Verlag;, 2009.

[67] Allotta B. Costanzi R. Monni N. Pugi L. Ridolfi A. Vettori G. Design and simulation of an autonomous underwater vehicle. *In: Proceedings of the European Congress on Computational Methods in Applied Sciences and Engineering (ECCOMAS), Vienna, Austria, pp. 1014 (September)*, 2012.

[68] Fallon M. Bahr A, Leonard J. Cooperative localization for autonomous underwater vehicles. *Int J Robot Res 2009;28:71428.*, 2009.

[69] Yun X. Bachmann E. McGhee R. Whalen R. Roberts R. Knapp R. et al. Testing and evaluation of an integrated GPS/INS system for small AUV navigation. *IEEE J Oceanic Eng 1999a;24:396404.*, 1999.

[70] Pflimlin J. Mahony R, Hamel T. Nonlinear complementary filters on the special orthogonal group. *IEEE Trans on Autom Control 2008;53:120318*, 2008.

[71] Arrichiello F. Antonelli G. Aguiar AP. Pascoal A. Observability metric for the relative localization of auvs based on range and depth measurements: Theory and experiments. *IEEE/RSJ international conference on intelligent robots and systems (IROS); 2011. San Francisco, CA, USA*, 2011.

[72] Oliveira P. Batista P, Silvestre C. Single range aided navigation and source localization: observability and filter design. *Syst Control Lett 2011;60:66573*, 2011.

[73] Gebre-Egziabhern D. *Design and performance analysis of a low-cost aided dead reckoning navigator.* PhD thesis, Standford University, CA, USA; 2004. Ph.D. Thesis., 2004.

[74] Williams S. Rigby P, Pizarro O. Towards geo-referenced AUV navigation through fusion of USBL and DVL measurements. *In: Proceedings of MTS/IEEE OCEANS 2006; 2006. Boston, MA, USA*, 2006.

[75] Singh S. Grund M. Bingham B. Eustice R. Singh H. Freitag L. Underwater acoustic navigation with the WHOI micro-modem. *In: Proceedings MTS/IEEE conference and exhibition OCEANS 2006; 2006. Boston, MA, USA*, 2006.

[76] Larsen M. Synthetic long baseline navigation of underwater vehicles. *In: Proceedings of MTS/IEEE OCEANS 2000; 2000. Providence, RI, USA*, 2000.

[77] Allotta B. Caiti A. Costanzi R. Fanelli F. Fenucci D. Meli E. Ridolfi A. A new AUV navigation system exploiting unscented kalman filter. *Ocean Engineering 113 (2016) 121132*, 2016.

[78] Allotta B. Costanzi R. Fanelli F. Monni N. Paolucci L. Ridolfi A. Sea currents estimation during AUV navigation using unscented kalman filter. *IFAC 2017*, 2017.

[79] Allotta B. Costanzi R. Fanelli F. Ridolfi A. Simultaneous navigation state and sea current estimation through augmented state unscented kalman filter. *OCEANS 2016 MTS/IEEE Monterey*, 2016.